FUSING OPTICAL COHERENCE TOMOGRAPHY AND ANGIOGRAPHY TO MODEL CORONARY BRANCHES AND SIMULATE FLOW

Nada Ghorab (MEng)

The Mathematical Modelling in Medicine Group

Department of Clinical Medicine

School of Medicine, Dentistry and Population

University of Sheffield

A thesis submitted in partial fulfilment of the requirements for the degree of Doctor of Philosophy

May 2025

Thesis Abstract

Background. To diagnose, assess severity and guide treatment, currently, most patients with ischaemic heart disease undergo 2-dimensional, x-ray angiography (CA). During CA, optical coherence tomography (OCT) can provide high-resolution, intravascular images of the lumen. Coronary physiology is used to assess various pressure- and flow-based metrics. CA, OCT and physiology have a class 1A indication in international guidelines yet are rarely used together.

Aims. To develop a novel, prototype computational method that fused all three assessments generating high-resolution, 3D, bifurcation anatomy models, to simulate physiology.

Methods. The novel toolchain fused 3D arterial centrelines (paired CA-images) and lumen contours (OCT), creating three reconstruction sets: CA-only and fused CA-OCT single vessels and CA-OCT branched vessels. Novel approaches to centreline torsion correction, bifurcation merging, rotational OCT optimisation and fusion of vessel surfaces were developed. CFD simulations were performed computing virtual fractional flow reserve (vFFR), absolute flow and microvascular resistance. Anatomical and physiological results were compared with state-of-the-art modelling techniques and against in vivo data.

Results. The prototype model successfully reconstructed twenty coronary arteries and eight bifurcations, from twelve different patients with stable coronary artery disease, from two tertiary cardiology centres. Single cases were processed in sub-four hours. Convergence rate was 100% and 75% for single and branched models, respectively. Branching-CA-OCT vFFR had the best agreement with clinical FFR, followed by the single-CA-OCT, followed by the branching-CA models (all suggesting a trend towards superiority to previous state-of-the-art) (Bland Altmann overall bias [limits of agreement]: -0.02 [-0.22 0.18] vs -0.034 [-0.25 0.18] vs -0.001 [-0.24 0.25] respectively). These were statistically non-significant differences.

Conclusions. The novel toolchain and prototype model fused CA-OCT data, generating high-resolution, branched 3D anatomy and simulating clinically useful physiological data. Accuracy was comparable to existing, state-of the art techniques. Further work should focus on reducing processing time, validation in a larger cohort, and improving the graphical user interface.

Acknowledgements

I am very grateful to my supervisors **Dr Paul Morris** and **Professor Rod Hose** for the opportunity to work on this project and their constant tuition and guidance. Thank you for being supportive and understanding during my (two) times of injury. **Dr Dan Taylor**, thank you for being the angiography and statistics expert on this project. I am very grateful for all the hours you put in and your support. **Krzysztof Czechowicz**, **Dr Giulia Pederzani** and **Dr Alberto Biancardi**, your technical support was invaluable. **Dr Andrew Narracott**, **Dr John Fenner**, and **Professor Ian Halliday**, thank you for providing support whenever I needed it. Thank you to everyone in the Mathematical Modelling in Medicine Group for their friendly company.

The data for this thesis was mostly collected by our collaborators in The Norfolk and Norwich University Hospitals: **Dr Simon Eccleshall** and **Dr Natasha Corbalis**, this work would not have been possible without your thorough data collection and dedication. Thank you.

I was lucky to be hosted by the ANSYS team in their office in Lyon for a month to perform the fluid dynamic simulations required for this thesis, and the welcoming and support they've given me was over-the-top. **Dr Michel Rochette** and **Dr Antonio Martinez Pascual**, I am immensely grateful for everything. Thank you for the highlight of my PhD journey.

I am also grateful to the UK Research and Innovation council which has funded me.

Last but not least, thank you to my family, **Mama**, **Papa**, **Kareem** and **Gedo** for being there through it all. Thank you for being my backbone, my home and the support system that I am always grateful for. **Setto**, it is for you that I am doing this. I hope you can see me and are proud of me. It is not even close to being the same without you. Thank you, **Adel** for being my cool uncle and a very good friend. **Tante Rim**, thank you for taking care of me over the past 8 years. And to my friends, you've been my home away from home. Thank you.

Publications

Pederzani, G., Czechowicz, K., Ghorab, N. et al. (5 more authors) (2022) *The use of digital coronary phantoms for the validation of arterial geometry reconstruction and computation of virtual FFR.* Fluids, 7 (6). 201. ISSN 2311-5521

Conferences

LE STUDIUM Conference Cardiovascular Modelling: Basic Science to Clinical Translation (Tours, France) 2022 – Talk

Insigneo Showcase (2023, 2024 and 2025) – Poster/Slide

British Cardiovascular Society Annual Conference (June 2025) – Poster

Collaborative Work Abroad

Ansys Inc., Lyon, France (October/November 2024)

Awards

Postgraduate Symposium – The School of Medicine and Population Health – Third place presentation winner

Table of Contents

Appendix 2: Pressure Contours for the Eight Branching Reconstructions

List of Figures

Chapter 1

The distal image demonstrates the trilaminar structure of the arterial wall. Stent struts can be seen in (b) which are well expanded and well opposed to the arterial wall. (Courtesy of the Mathematical Modelling in Medicine Group at The University of Sheffield).

Figure 1.7. Coronary OCT showing (A) the main vessel and (B) the main vessel with the emergence of a side vessel (at a bifurcation). The straight line that transects the lumen has dots at 1 mm distances to aid size interpretation. The dark (black) lumen is outlined by thickened (bright yellow /gold colour) and atheromatous plaque. The catheter is seen as a series of circles at the 8 o'clock position and there is a wire shadow seen in the 10 o'clock position. (Courtesy of the Mathematical Modelling in Medicine Group at The University of Sheffield).

Figure 1.8. Example of an OCT case in a diseased left anterior descending artery. In each, the central dark colored region is the lumen. In each image, there is a wire shadow caused by the presence of the angioplasty wire which occludes the light signal. The dots on the straight line are spaced at 1 mm intervals. (a) is a distal frame showing an approximately 2.25 mm diameter vessel with clearly visible circumferential atheroma (yellow coloring at luminal border). (b) shows two side-branches emanating from the main vessel at the 2 and 10 O'clock positions. (c) shows a stenosed region. The diameter here is approximately 1 mm by 2 mm. Invasive angiography would be unable to represent this asymmetry. (d) shows a proximal section. Here the OCT is unable to detect the entire luminal border due to the size of the proximal vessel and some blood swirl artefact. These are recognized limitations of OCT, especially in large proximal arteries. Panel (e) is a screen capture from the clinical graphical user interface. The two horizontal images demonstrate the diameter as a function of the length (average top and in-plane bottom). As can be seen, OCT renders the artery completely straight, even though this is never the case. The green lines demarcating the luminal border (a, c, e) are the system-generated capture of the luminal border. The equivalent amber lines (b, d) indicate where the system is not sufficiently confident in identifying the luminal border. Images courtesy of the Mathematical Modelling in Medicine Group at The University of Sheffield.

Figure 1.9. An example of a fractional flow reserve measurement. The red and green lines (y axis) chart the time-dependent changes in distal (green) and proximal (red) pressures (x axis). The continuous horizontal lines track the corresponding moving average (over three cardiac cycles) of these pressure waveforms which are also displayed in numbers at the top right. The proximal and distal pressures separate with time due to the administration of adenosine which indices maximal coronary blood flow. The FFR is 0.92, indicating that the pressure transducer

is positioned distal to physiologically non-significant coronary artery disease and so PCI is not indicated. Image courtesy of the Mathematical Modelling in Medicine Group at The University of Sheffield.

Chapter 2

Figure 2.1. A Venn diagram that illustrates the benefits of coronary intravascular imaging, invasive angiographic imaging and physiological assessment, how they have been integrated and fused thus far, and how the current project attempts to bring the benefits of all these methods together in a single platform.

Chapter 3

Figure 3.1. The image acquisition procedure. Patient is on the table in the catheterisation lab, and the C-arm, holding the x-ray source and detector units is rotated both right to left and top to bottom, to acquire images from two distinct views.

Figure 3.2. The 3D centreline of a coronary artery. It is fully described by a set of 3D points (X, Y, Z), and a set of normal (n), tangent (t) and binormal (b) vectors at every point. s is the cumulative distance (s) along the centreline.

Figure 3.3. Rotation of the tangent vector. T_{i+1} and T_j are the tangent vectors at the point on the curve, and the point before it, respectively. R is the radius of the circle formed by the two points and α is the angle of rotation.

Figure 3.4. (top) Centreline with tangent, normal and binormal vectors for a typical artery before (left) and after (right) using the Frenet frame to compensate for torsion. The figure on the top right exhibits more consistency of its vectors. (bottom) CA-derived vessel contours projected back onto angiogram for illustration of the segmented section. This can be a clinically useful tool, especially when the angiogram image is lacking sufficient resolution.

Figure 3.6. (Top) An illustration of the forward (green) and backward (orange) triangulations joining consecutive circles that make up the surface mesh and (Bottom) The first ring joining the first two circles on the main vessel with the directions of their normal vectors.

Figure 3.7. Triangulated surface of the main vessel.

Chapter 4

Figure 4.1. (A) OCT frame acquired from within the catheter. This, and similar frames, do not contain meaningful anatomical information from the vessel and are thus disregarded from this work. Similarly for frames such as (B) which exhibit the 'swirl' artefact due to incomplete blood displacement at the catheter tip.

Figure 4.2. (left) The red CA-centreline (segmented) and blue OCT-centreline (joins cross-sectional centroids). (right) An OCT cross-section on the centreline.

Figure 4.3. This is an illustration, of cases 1-3, whereby the diameter data from CA and OCT were acquired, aligned and then examined for correspondence. The non-corresponding sections for each were discarded to produce the last image in every series. The corresponding set of diameters were used to quantify any systematic differences between the image acquisition of the two imaging modalities.

Figure 4.4. Three OCT frames; the reference frame is in red. The goal is to rotate the second frame (purple = unrotated, green = rotated) through several angles to find the rotation angle to produces the minimum non-overlapping area between both frames.

Figure 4.5. Difference between lumen area and overlapping area for every lumen and its preceding lumen, before (top) and after (bottom) linear interpolation was performed for frame 27, which has an overlapping difference of zero.

Figure 4.6. The angio-optimisation method. (A) Shows the OCT-cross section in 3D with the Frenet normal, tangent and binormal vectors as well as the OCT x and y-axis. (B) Shows the projected OCT frame on the relevant angiogram (zoomed in), with the vessel edges as seen on the angiogram marked in yellow. (C) Shows the extreme OCT points along the centreline normal vector which (D) are compared to the extreme points as identified from the greyscale of the angiogram, which then allows the computation of the error in radius for the positive and

negative extremes. The error values are what is minimised in the cost function for this orientation optimisation method.

Figure 4.7. The change in the value of optimisation angle of orientation using the area-overlap and angio-optimisation for the first 53 frames of the OCT run.

Figure 4.8. Area of OCT cross-sections with respect to the longitudinal OCT pullback. (A) Start of diffuse stenosis, characterised by sharp area decrease. (B) Sharper area decrease, continuation of stenotic region. (C) Recovery and start of second stenotic region. (D) Recovery and stable area region pre-bifrucation. (E) Bifurcation: Transition from main vessel to side branch and start of post-bifurcation stenotic region. (F) Healthy tapering region.

Figure 4.9. Graph showing the ratio of the moment of area about the principal axes for each of the 333 frames. Two frames are chosen to demonstrate ellipticity as shown, which are those with the larger ratio values.

Figure 4.10. The Fourier expansion of an elliptical and non-elliptical frame. The 2theta term (red) is more pronounced for the elliptical frame and can be used to identify non-circularity.

Figure 4.11. A graph of the ratio between the 2-theta and 1-theta coefficients of the Fourier decomposition of each frame. The graph shows two clear peaks that refer to elliptical frames. The frames are also included in the figure.

Chapter 5

Figure 5.1. This is a visualisation of the data presented in Table 5.1, showing the mean value for the percentage of equivalent OCT vessel length that is discarded wither due to imaging the catheter or to the swirl artefact.

Figure 5.2. Agreement as a function of vessel size. Both figures display binned data. Panel A: Bland Altman plot: The overall positive bias means that OCT measures the arterial diameter larger than CA; mean bias = 0.23 mm (95%LOA -0.13 to 0.59). Panel B: Simple linear regression analysis demonstrating how this effect is more pronounced in regions of artery with larger diameter.

Figure 5.3. Agreement as a function of vessel length. At more proximal positions in the artery, there is a greater underestimation of diameter by angiography compared with OCT ($P_{interaction}<0.0001$)

Figure 5.4. The cross-sections having the maximum (Case 10) and minimum maximum (Case 4) ellipticity values across all twenty cases. The cross-section from Case 10 appears to be stenosed at the bifurcation, contrary to that from Case 4 (healthy bifurcation), thus it is expected that the combination of bifurcation and stenosis will produce the largest value of ellipticity

Figure 5.5. (top) The ellipticity for all frames in case 1 (bottom) frame with the global maximum peak ellipticity.

Figure 5.6. (top) The ellipticity for all frames in case 4 (bottom) frame with the global maximum peak ellipticity.

Figure 5.7. (top) The ellipticity for all frames in case 6 (bottom) frame with the global maximum peak ellipticity.

Figure 5.8. Example of a frame from the Abbott OCT machine, where the edge detection algorithm misses the true edge of the vessel yet is still shown in green.

Figure 5.9. 3D reconstructions of coronary vessels from cases 6, 7 and 14. The reconstructions are presented here before any additional smoothing has been performed on the surface prior to CFD. (OCT = purple. CA = green).

Chapter 6

Figure 6.1. The two CA views chosen for the flagship case (LAD-Diagonal): LAO 0.24 CRA 35 and LAO 42 CRA 32.47. this is a NGH case, that was specifically chosen for demonstration because it exhibits a combination of stenotic and bifurcation regions, which challenged the mathematics of the protocol being presented here

Figure 6.2. The raw 3D centrelines of the main and side vessels as extracted from the segmentation tool. As seen, the proximal common stem section does not overlap in both vessels.

Figure 6.3. The joined centrelines (blue) and bifurcation points (green) when projected back on the two angiographic views.

Figure 6.4. The centrelines joined at the common stem, showing the ideal circles with CA-derived radii positioned along the lengths of both centrelines.

Figure 6.5. The targeted area of tightness at the bifurcation point, replaced by interpolating using Hermite Cubic patches between a point proximal and a point distal to the bifurcation point, to produce a smoother curvature that mitigates issues of overlap. (top) full model, (bottom) close-up of bifurcation area.

Figure 6.6. The final patched centrelines of both vessels (left) and the centrelines with the idealised circles representing the vessel wall on the centreline points (right).

Figure 6.7. An illustration of a bifurcation exhibiting post-bifurcation curvature discontinuity, demonstrating radii (the short black segments) overlapping in areas where the radius of curvature is smaller than the radius of the vessel.

Figure 6.8. Triangulated surface of the side branch.

Figure 6.9. The full model with surface triangulations (main vessel in blue and side branch in red).

Figure 6.10. The procedure involved in identifying internal nodes and thus triangles and deleting them. The points of intersection of the edges on one vessel and the triangles of the other are stored for use in stitching the vessel together at a later step.

Figure 6.11. The three scenarios for criterion 1. Scenario1 is when the two endpoints of the line segment DE are on opposite sides of the plane containing triangle ABC. Scenario 2 is when one of the endpoints of segment DE are on the plane containing triangle ABC. Scenario 3 is when both endpoints are on the same side of the plane containing triangle ABC.

Figure 6.12. The scenarios that can occur if the endpoints of a line segment are on opposite sides of a plane containing a triangular surface.

Figure 6.13. Contour plots of both vessels showing, in blue the points of the main vessel that were inside the side branch (top) and the points of the side branch that were inside the main vessel (bottom) and the points in yellow that were not inside a specific vessel. In this case, the side branch starts off fully inside the main branch, hence the points starting off all blue.

Figure 6.14. (Left) Main vessel surface after overlapping sections with the side branch in the bifurcation region were deleted and (Right) Side branch surface after the overlapping sections with the main vessel in the bifurcation region were deleted.

Figure 6.15. (Left) A close-up of the cut surfaces of the main vessel (blue) and side branch (red) in the bifurcation region, and the intersection curve (green), at which both vessels were stitched (next step).

Figure 6.16. An example of a case where two intersection points can be exceptionally close to each other. In this case, the black edges of the triangle are intersecting the interior of the blue triangle at the points marked in red. Since, these points happen to be in the region close to a vertex of the triangle containing the black edges, the points are exceptionally close to each other and are targeted by the decimation procedure to refine the intersection curve.

Figure 6.17. The final and stitched branched model.

Figure 6.18. An illustration of the case where a hole can be formed in the stitched area of the triangulated surface. The black triangle belongs to the main vessel, thew orange triangle belongs to the side branch, and the curve of red stars represents the intersection curve. This case occurs when a point (A in this case) is 'skipped' by a vessel (the side branch in this case) because it is not the closest point to any of the points on this vessel. This results in the point not being connected to any of the surface triangulations, leaving a hole in the final model.

Figure 6.19. Sealing the holes by dividing the triangle that skips a point on the intersection curve in two, so it joins at every point.

Figure 6.20. (Top) Volume mesh of the fluid domain and (Bottom) An example of a CFD simulation with pressure boundary conditions performed on this bifurcating model.

Figure 6.21. Bifurcation Cases 2-4, which are cases that have exhibited entanglements of the surface mesh at the bifurcation region and have been subjected to Fluent’s wrapping and smoothing function.

Chapter 7

Figure 7.1. A scatter plot showing the agreement between the volumetric flow rate as obtained in silico, using the novel fusion method versus the CA-only method, with the line of best fit.

The ideal $R^2 = 1$ line is also plotted as a reminder that ideally, both lines of best fit should be the same.

Figure 7.2. Analogy between a single coronary vessel with a characteristic resistance to flow connected with a network of microvasculature and an electric circuit with two in-series resistances.

Figure 7.3. A scatter plot showing the agreement between the microvascular resistance as obtained in silico, using the novel fusion method versus the CA-only method, with the line of best fit. The ideal $R^2 = 1$ line is also plotted as a reminder that ideally, both lines of best fit should be the same.

Figure 7.4. Pressure-drop versus volumetric flow rate plots, showing a quadratic relationship. The green points are the pressure drops at the 1 and 3ml/s values, which are the estimated boundaries of the physiological range expected in the coronary arteries. The red point is the actual volumetric flow rate through the vessel and the corresponding simulated pressure drop. (left) Shows a case where the volumetric flow rate through the vessel is within the 1-3 ml/s range, thus having a pressure drop accurately estimated by the quadratic relationship, which is less so in the (right) case where the volumetric flow rate is outside the range and thus the pressure value is extrapolated.

Figure 7.5. Scatter plots of the clinically measured FFR, $vFFR_{Fused}$ and $vFFR_{CA\text{-}only}$ using $CMVR_{avg\text{-}fused}$, to study their concordance. The black lines at 0.80 mark the critical threshold of stenting. The points in the top right and bottom left quadrants are concordant points, indicating that both the FFR and vFFR values either both indicate the need to stent or not to. The points in the top left and bottom right show discordance between the FFR and vFFR values, whereby one indicates the need to stent and the other does not. $vFFR_{Fused}$ shows better concordance with the FFR than the $vFFR_{CA\text{-}only}$ with (six discordant cases vs ten).

Figure 7.6. Scatter plots of the clinically measured FFR, $vFFR_{Fused}$ and $vFFR_{CA\text{-}only}$ using $CMVR_{avg\text{-}CA}$, to study their concordance. The black lines at 0.80 mark the critical threshold of stenting. The points in the top right and bottom left quadrants are concordant points, indicating that both the FFR and vFFR values either both indicate the need to stent or not to. The points in the top left and bottom right show discordance between the FFR and vFFR values, whereby one indicates the need to stent and the other does not. $vFFR_{Fused}$ shows better concordance with the FFR than the $vFFR_{CA\text{-}only}$ with (six discordant cases vs nine).

Figure 7.7. Scatter plots of the vFFR from both the fused and CA-only reconstructions using $CMVR_{avg\text{-}fused}$ and $CMVR_{avg\text{-}CA}$, to study their concordance. The black lines at 0.80 mark the critical threshold of stenting. The points in the top right and bottom left quadrants are concordant points, indicating that both the FFR and vFFR values either both indicate the need to stent or not to. The points in the top left and bottom right show discordance between the FFR and vFFR values, whereby one indicates the need to stent and the other does not. $vFFR_{Fused}$ and $FFR_{CA\text{-}only}$ show better concordance with the $CMVR_{avg\text{-}CA}$ boundary condition (three discordant cases vs six).

Figure 7.8. Bland Altmann plots of the FFR and $vFFR_{Fused}$ and the limits of agreement using both $CMVR_{avg\text{-}fused}$ and $CMVR_{avg\text{-}CA}$. All the points lie within the 95% limits of agreement.

Figure 7.9. Bland Altmann plots of the FFR and $vFFR_{CA\text{-}only}$ and the limits of agreement using both $CMVR_{avg\text{-}fused}$ and $CMVR_{avg\text{-}CA}$. All the points lie within the 95% limits of agreement.

Figure 7.10. Bland Altmann plots of $vFFR_{Fused}$ and $vFFR_{CA\text{-}only}$ and the limits of agreement using both $CMVR_{avg\text{-}fused}$ and $CMVR_{avg\text{-}CA}$. All the points lie within the 95% limits of agreement.

Figure 7.11. The electrical circuit representation of a branching coronary vessel. The vessel is regarded as a three-section circuit, each with a characteristic resistance and the daughter branches being in series to microvascular resistances.

Figure 7.12. Scatter plots of the clinically measured FFR and $vFFR_{branching\text{-}fused}$ using $CMVR_{avg\text{-}fused}$ and $CMVR_{avg\text{-}CA}$ to study their concordance. The orange lines at 0.80 mark the critical threshold of stenting. The points in the top right and bottom left quadrants are concordant points, indicating that both the FFR and vFFR values either both indicate the need to stent or not to. The points in the top left and bottom right show discordance between the FFR and vFFR values, whereby one indicates the need to stent and the other does not. $vFFR_{branching\text{-}fused}$ computed using $CMVR_{avg\text{-}fused}$ produced better concordance with the FFR (two discordant cases vs four).

Figure 7.13. Scatter plots of the clinically measured FFR and $vFFR_{branching\text{-}CA}$ using $CMVR_{avg\text{-}fused}$ and $CMVR_{avg\text{-}CA}$ to study their concordance. The orange lines at 0.80 mark the critical threshold of stenting. The points in the top right and bottom left quadrants are concordant points, indicating that both the FFR and vFFR values either both indicate the need to stent or not to. The points in the top left and bottom right show discordance between the FFR and vFFR values,

whereby one indicates the need to stent and the other does not. $vFFR_{branching\text{-}CA}$ produced comparable concordance using both boundary conditions (three discordant cases vs three).

Figure 7.14. Scatter plots of the $vFFR_{branching\text{-}fused}$ and $vFFR_{branching\text{-}CA}$ using $CMVR_{avg\text{-}fused}$ and $CMVR_{avg\text{-}CA}$ to study their concordance. The orange lines at 0.80 mark the critical threshold of stenting. The points in the top right and bottom left quadrants are concordant points, indicating that both the FFR and vFFR values either both indicate the need to stent or not to. The points in the top left and bottom right show discordance between the FFR and vFFR values, whereby one indicates the need to stent and the other does not. The best concordance between the two vFFR sets was produced when the $CMVR_{avg\text{-}CA}$ was applied (five discordant cases vs four), although most of the discordant cased were at the threshold.

Figure 7.15. Bland Altmann plots of the FFR and $vFFR_{branching\text{-}fused}$ and the limits of agreement using both $CMVR_{avg\text{-}fused}$ and $CMVR_{avg\text{-}CA}$. Most points lie within the 95% limits of agreement.

Figure 7.16. Bland Altmann plots of the FFR and $vFFR_{branching\text{-}CA}$ and the limits of agreement using both $CMVR_{avg\text{-}fused}$ and $CMVR_{avg\text{-}CA}$. Most points lie within the 95% limits of agreement.

Figure 7.17. Bland Altmann plots of $vFFR_{branching\text{-}Fused}$ and $vFFR_{branching\text{-}CA}$ and the limits of agreement using both $CMVR_{avg\text{-}fused}$ and $CMVR_{avg\text{-}CA}$. All the points lie within the 95% limits of agreement.

Chapter 8

Figure 8.1. LAD vessel segmented twice by the same user. The top images show the segmented centrelines from the two attempts, which were reconstructed using different sets of start, end and co-registration points. The bottom images show the resulting geometries from both attempts.

List of Tables

Chapter 1

Chapter 3

Chapter 5

Table 5.5. Description of how OCT and CA data were fused for modelling, starting from data acquisition and data processing to the final 3D product.

Chapter 6

Table 6.1. Outline of the patient cases that were modelled as branching vessels, each main vessel and its corresponding side branch, in this thesis. The eight cases were imaged in the Norfolk and Norwich University Hospital.

Chapter 7

Table 7.1. The boundary conditions for the pressure-pressure simulations used to compute the volumetric flow rate for each of the twenty single vessel models.

Table 7.2. The simulated volumetric flow rates for all twenty cases. The volumetric flow rate was simulated using 3D coronary reconstructions from fused OCT-CA and from CA-only.

Table 7.3. The computed distal resistance values for all twenty single vessel cases, computed using the clinically measured distal pressure and the simulated volumetric flow rate for both the novel fusion method and the angiography only methods.

Table 7.4. The vFFR using the $CMVR_{avg\text{-}fused}$ and $CMVR_{avg\text{-}CA}$, for both the fused OCT-CA and CA-only geometries. The clinically measured FFR is also included for in the table for comparison. Dark green cells indicate FFR ≤ 0.80 and a vFFR ≤ 0.80. Light green cells indicate FFR > 0.80 and vFFR > 0.80. These make up the concordant scenarios. Blue indicates an FFR > 0.80 and a vFFR ≤ 0.80. Orange indicates an FFR ≤ 0.80 and a vFFR > 0.80. These are the discordant cases. The entries in bold are those that lie inside the grey zone (0.78≤FFR≤0.83).

Table 7.5. The four combinations of boundary conditions, with their corresponding sensitivity, specificity, negative and positive predictive values (NPV and PPV) and accuracy, for the single vessel reconstructions.

Table 7.6. The overall bias, Bland-Altmann limits of agreement and their width for the six combinations comparing FFR, $vFFR_{Fused}$ and $vFFR_{CA\text{-}only}$ using $CMVR_{avg\text{-}CA}$ and $CMVR_{avg\text{-}fused}$. The last column shows the scoring for the first four combinations to rank their agreement with the clinical FFR.

Table 7.7. The correlation analysis between clinically measured FFR and the single vessel vFFR simulated using both the fused and CA-only reconstructions using $CMVR_{avg\text{-}fused}$ and $CMVR_{avg\text{-}CA}$. All correlations are clinically non-significant.

Table 7.8. The $vFFR_{branching}$ computed using the distal resistance values, $CMVR_{avg\text{-}fused}$ and $CMVR_{avg\text{-}CA}$, for the fused OCT-CA and CA-only geometries. The clinically measured FFR is also included for in the table for comparison. Dark green cells indicate FFR ≤ 0.80 and a vFFR ≤ 0.80. Light green cells indicate FFR > 0.80 and vFFR > 0.80. These make up the concordant scenarios. Blue indicates an FFR > 0.80 and a vFFR ≤ 0.80. Entries in bold are within the 'grey zone' for stenting (0.78≤FFR≤0.83).

Table 7.9. The four combinations of boundary conditions, with their corresponding sensitivity, specificity, negative and positive predictive values (NPV and PPV) and accuracy, for the branching vessel reconstructions.

Table 7.10. The overall bias, Bland-Altmann limits of agreement and their width for the six combinations comparing FFR, $vFFR_{branching\text{-}Fused}$ and $vFFR_{branching\text{-}CA}$ using $CMVR_{avg\text{-}CA}$ and $CMVR_{avg\text{-}fused}$. The last column shows the scoring for the first four combinations to rank their agreement with the clinical FFR.

Table 7.11. The correlation analysis between clinically measured FFR and the branching vessel vFFR simulated using both the fused and CA-only reconstructions using $CMVR_{avg\text{-}fused}$ and $CMVR_{avg\text{-}CA}$. All correlations, but one are clinically significant.

Table 7.12. Clinically measured FFR increased using the percentages computed by Yan et al. which account for the impact of the catheter and pressure wires on the measurement of FFR. The orange-highlighted cases are those that become discordant, and those highlighted in green have become concordant.

Table 7.13. The $Q_{branching}$ computed using the distal resistance values, $CMVR_{avg\text{-}fused}$ and $CMVR_{avg\text{-}CA}$, for the fused OCT-CA and CA-only geometries. The single vessel Q values are also included for in the table for comparison.

Table 7.14. Compilation of the FFR, single vessel vFFR and branching vFFR for all the cases that were modelled as single and as branching vessels (sixteen cases, constituting eight branching cases). Dark green cells indicate FFR ≤ 0.80 and a vFFR ≤ 0.80. Light green cells indicate FFR > 0.80 and vFFR > 0.80. These make up the concordant scenarios. Blue indicates

an FFR > 0.80 and a vFFR ≤ 0.80. Orange indicates an FFR ≤ 0.80 and a vFFR > 0.80. These are the discordant cases.

Table 7.15. General comments regarding the eight branching cases, regarding the interpretation of the angiograms, and whether the data from the angiograms and the OCT runs correspond and are reflected in their corresponding reconstructions. The FFR and vFFR values are also commented on, with regards to whether they reflect the imaging data and how the results have changed using different models with different boundary conditions.

List of Equations

Chapter 1

Chapter 3

Chapter 4

Equation 4.2. Computing the effective diameter of an OCT cross-section from its area

Equation 4.3. Shifting the OCT effective diameter curve a distance 'shift' to achieve maximum correspondence with the CA diameter curve.

Equations 4.4 and 4.5. Finding the x limits of the overlapping sections of the OCT and CA diameter curves.

Equation 4.6. A cost function with an optimal solution θ_{opt}.

Equation 4.7. The OCT lumen orientation composite cost function that includes a term for each: area-overlap optimisation, angio-optimisation and smoothing. Each term has a weighting factor to scale its impact on the overall optimisation.

Equation 4.8. Area-overlap cost function

Equation 4.9. Finding the difference between the area of a lumen and the difference between that and the overlapping area with its preceding lumen.

Equation 4.10. Positive and negative extreme point distances (radii) from the centroid of the OCT cross-section.

Equation 4.11. Angio-optimisation cost function

Equation 4.12. Smoothing cost function

Equations 4.13-4.15. The three components of the second moment of area of a 2D shape about the x and y axes.

Equation 4.16. Moment of area about the principal axes of a 2D shape

Equation 4.17. The Fourier decomposition equation

Chapter 5

Equation 5.1. Computing the norm of the difference vector between CA and OCT diameters.

Equation 5.2. Computing the ellipticity of the OCT cross-sections as the ratio between the magnitude of the second harmonic and the fundamental frequency of the Fourier decomposition of the vector of radii.

Chapter 6

Equation 6.1. Shift of the main vessel so the bifurcation points on both the main vessel and side branch coincide.

Equation 6.2. The Hermite Cubic Spline

Equation 6.3. Checking for Criterion 1: Do the endpoints of the segment lie on opposite sides of the plane containing the triangular surface?

Equation 6.4. Checking for Criterion 2: Does the point of intersection of the line segment and the plane lie inside the triangular surface?

Equation 6.5. The aspect ratio of a triangle

Chapter 7

Equation 7.1. The hydraulic equivalent of Ohm's Law in the context of distal coronary microvascular resistance.

Equation 7.2. The first coefficient in the quadratic equation to compute the vFFR for coronary vessels.

Equation 7.3. The second coefficient in the quadratic equation to compute the vFFR for coronary vessels.

Equation 7.4. The distal volumetric flow rate computed using the computed coefficients in Equations 3 and 4.

Equation 7.5. vFFR computation from measured proximal pressure and computed distal pressure.

Equation 7.6. Scoring the Bland-Altmann overall bias and limits of agreement to determine which combination of reconstruction method boundary condition produces vFFR values that agree the most with the FFR.

Equation 7.7. The four simultaneous equations that allow the computation of pressure and flow everywhere in a branching model.

Abbreviation List

2D	Two-Dimensional
3D	Three-Dimensional
ACS	Acute Coronary Syndrome
ALARA	As Low As Reasonably Achievable
ANOCA	Angina with No Obstructive Coronary Arteries
CA	Coronary Angiography
CABG	Coronary Artery Bypass Graft
CAD	Coronary Artery Disease
CFD	Computational Fluid Dynamics
CFR	Coronary Flow Reserve
CI	Confidence Interval
cMRI	cardiac Magnetic Resonance Imaging
cPET	cardiac Positron Emission Tomography
CRA	Cranial
CTCA	Computed Tomography Coronary Angiography
DICOM	Digital Imaging and Communications in Medicine
DSA	Digital Subtraction Angiography
ECG	Electrocardiogram
EET	Exercise Electrocardiography Testing
eGFR	estimated Glomerular Filtration Rate
FD-OCT	Frequency Domain – Optical Coherence Tomography
FFR	Fractional Flow Reserve
HMG-CoA	3-hydroxy-3-methyl-glutaryl-coenzyme A
iFR	Instantaneous Wave-Free Ratio
IHD	Ischemic Heart Disease
IMR	Index of Myocardial Resistance
IVUS	Intravascular Ultrasound
CCS	Chronic Coronary Syndrome
LAD	Left Anterior Descending
LAO	Left Anterior Oblique

LCX	Left Circumflex
LMS	Left Main stem
LCA	Left Coronary Artery
LV	Left Ventricle
LVEF	Left ventricular ejection fraction
MACE	Major Adverse Cardiac Event
MI	Myocardial Infarction
NGH	Northern General Hospital
NNUH	Norfolk and Norwich University Hospitals
NSTEMI	Non-ST-Elevation Myocardial Infarction
OCT	Optical Coherence Tomography
OM	Obtuse Marginal
PCI	Percutaneous Coronary Intervention
QCA	Quantitative Coronary Angiography
RAO	Right Anterior Oblique
RCA	Right Coronary Artery
SPECT	Single-Photon Emission Computerized Tomography
STEMI	ST-Elevation Myocardial Infarction
vFFR	virtual Fractional Flow Reserve
WSS	Wall Shear Stress

Chapter One:

Background

1.1 The heart and the coronary arteries

The human heart is a complex muscular pump. Its main function is to transport oxygenated and nutrient rich blood to the systemic organs and deoxygenated blood to the lungs. To perform this function, the heart must contract and relax, during systole and diastole, both of which are energy consuming processes. Unlike all other muscles, the heart can never rest. Even under resting conditions, the cardiac myocytes extract up to 75% of the oxygen present in blood, much higher than other muscles. Consequently, any increase in oxygen demand, associated with exercise and high output states, requires an increase in blood supply. In short, the cardiac myocardium needs an excellent blood supply itself, and this is conducted from the proximal aorta to the myocardium via the coronary arteries.

The coronary arteries originate from the aortic root sinuses as the left and right coronary arteries (LCA and RCA). The left coronary artery arises from the left coronary sinus as the left main stem (LMS) and branches into the left anterior descending (LAD) and left circumflex arteries (LCX). The LAD usually reaches the apex of the left ventricle (LV). Along its course, it supplies diagonal branches which are numbered sequentially and supply the lateral left ventricular wall. The LAD also supplies the interventricular septum with septal branches. The LCX artery lies in the left atrioventricular groove and provides obtuse marginal (OM) branches to the lateral left ventricular wall. The artery that arises from a point exactly between the LAD and LCX is called the ramus intermedius (or intermediate) artery. The RCA arises from the right coronary sinus and lies in the right atrioventricular groove where it supplies sinoatrial and conus (right ventricular outflow) and right ventricular branches. The RCA usually reaches the inferior surface of the heart where it supplies posterior descending and posterior left ventricular branches. Coronary anatomy is naturally highly variable in terms of the diameter, length and course of individual arteries and branches. Despite anatomical variation, there is always balance as is evidenced in the dominance of the coronary arteries: the inferior LV wall is supplied by the RCA in approximately 80% of people, by the LCX in around 10%, and by both RCA and LCX in 10%. This is known as right, left and co-dominance respectively. However, even in those with right-dominance the LCA conducts around 80% of all coronary arterial blood flow. In addition, LCA has larger and therefore more important proximal branches. This is reflected in the work presented in this thesis in that both the left and right coronary circulations are imaged, modelled and reconstructed, but the greater focus is on the left coronary arteries, mainly the LMS bifurcation (into the LAD and LCX) and the major LAD-

diagonal bifurcations. Not only do these bifurcations experience the highest coronary flow rates, they are prone to the development of obstructive atherosclerotic plaque and are common locations for percutaneous coronary intervention (PCI) (Chatzizisis et al., 2007). Figure .1 shows the 'standard' coronary anatomy, highlighting the vessels of greater focus in this thesis. Beyond naturally occurring variation, coronary anatomy can be 'anomalous' if a certain anatomical variation is found in less than 1% of the general population (Angelini, 1989).

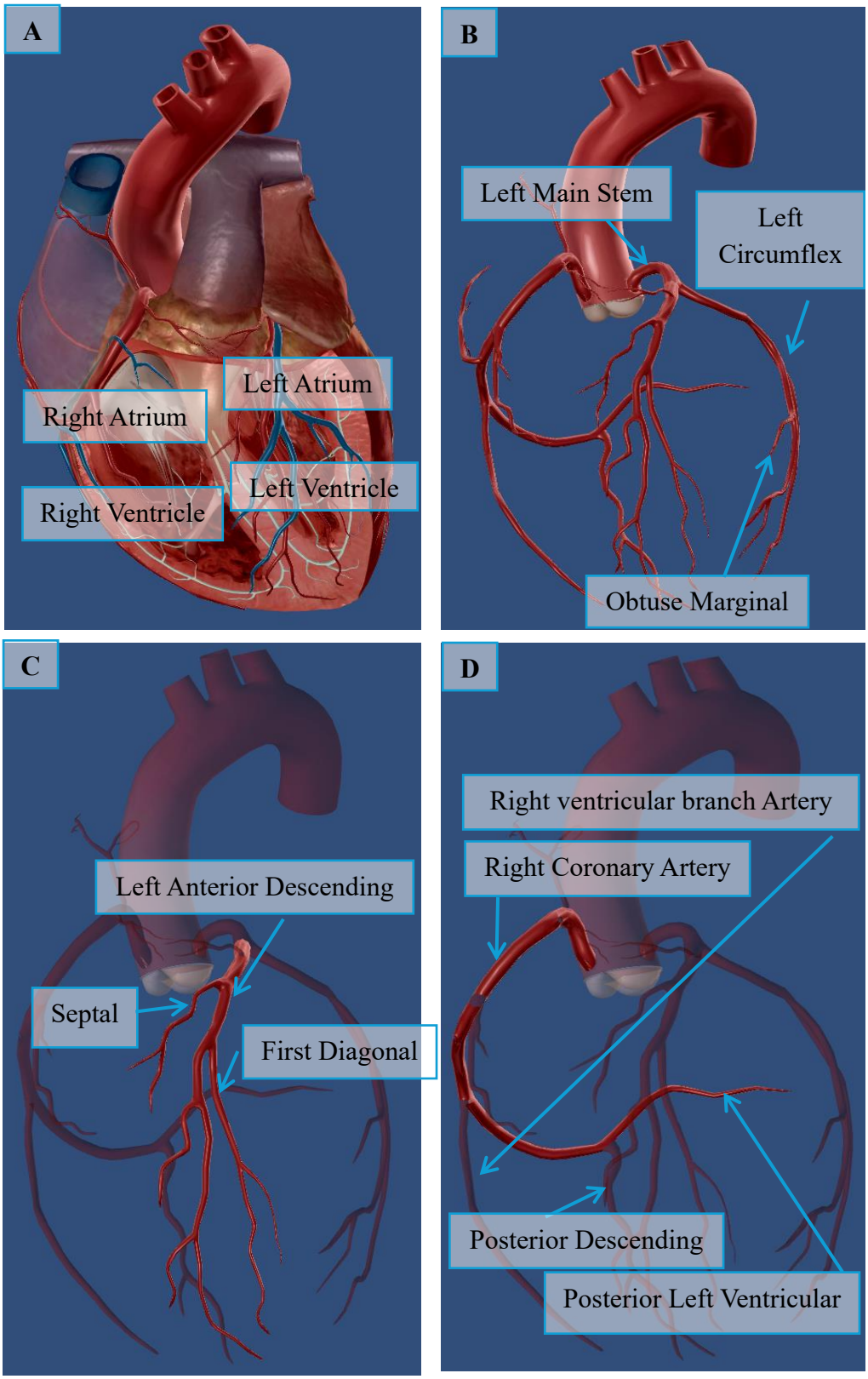

Figure 1.1. (A) The heart and its four compartments: the atria and ventricles, (B) The coronary arteries present on the surface of the heart with a focus on the left main stem, left circumflex and obtuse marginal arteries, (C) Continuation of the left coronaries with a focus on the left anterior descending artery, diagonal and septal branches, (D) The right coronaries: Right ventricular branch, right coronary, posterior descending and posterior left ventricular arteries.

1.2 Ischemic heart disease

1.2.1 Ischemic heart disease and its burden

Cardiovascular disease is the leading cause of death globally. Worldwide, coronary heart disease caused a total of nine million deaths in 2021 (BHF, 2025b). Although the UK is not one of the top five countries with cardiovascular death rates in the world, by January 2024, IHD was reported to account for the deaths of 150 individuals a day in the UK (BHF, 2025a). According to Public Health England and the Centre of Disease Control and Prevention in the USA, cardiovascular disease is responsible for a death every four minutes in the United Kingdom resulting in an annual financial burden of £15.8 on the economy (PHE, 2019).

Ischaemia occurs when the supply of oxygenated arterial blood to the myocardium is insufficient to meet the needs of the myocardium. Unless ischaemia is resolved quickly, it develops rapidly, in minutes, into myocyte necrosis and myocardial infarction (MI). IHD comprises acute coronary syndromes like unstable angina and myocardial infarction, and stable coronary disease. The latter is the focus of this thesis. Ischaemia is a physiological phenomenon, but it is usually caused by anatomical pathology; coronary artery disease (CAD). CAD is caused by the presence of atherosclerotic plaque inside the coronary arterial wall, that causes a narrowing of the lumen area thus restricting myocardial blood flow. Stable angina results when blood flow rate at rest is sufficient but the plaque becomes flow limiting under exercise or higher flow states. Typical symptoms include a heavy or constricting central chest discomfort or pain that may radiate to the arms, jaw or neck, and that resolves relatively quickly, within five minutes, with rest (NICE, 2010). Acute coronary syndromes occur when an atherosclerotic plaque ruptures or erodes, exposing constituents of the plaque and arterial wall to the blood which results in platelet activation, followed by occlusive thrombus formation and then myocardial infarction. Symptoms may occur at any time, whether rest or exercise, and do not resolve with rest.

1.2.2 Treatment

Management of IHD is quite different for chronic (stable) and acute coronary syndromes (CCS and ACS). Suspected CCS is managed on an outpatient basis, whereas suspected ACS is managed as an emergency with immediate assessment and treatment in in secondary care. The focus of this thesis is CCS and unless otherwise stated, IHD refers to stable coronary syndromes.

Treatment categories for IHD include risk factor modification, medical therapy and coronary revascularisation. The latter comprises PCI and coronary artery bypass graft surgery (CABG). When a diagnosis of IHD (due to CAD) is made, all patients are advised on lifestyle changes to modify their risk factor profile (smoking cessation, weight loss, regular aerobic exercise, blood pressure and glucose control) and are offered antithrombotic drug treatment which is usually an antiplatelet drug like aspirin, and a lipid modifying drug like a 3-hydroxy-3-methyl-glutaryl-coenzyme A (HMG-CoA) reductase inhibitor, more commonly known as a statin, used to optimise circulating lipid levels and stabilise atherosclerotic plaque. Both these measures help to reduce the risk of progression to ACS. Beyond these prognostic treatments, further tablet therapy can be offered to reduce the symptoms of angina, i.e. antianginal therapy. Antianginal therapy includes nitrates, calcium channel antagonists, betablockers, nicorandil, ranolazine and ivabradine. These mediations work by reducing the work of the heart via a variety of mechanisms including reducing pre-load, afterload, sympathetic activation and heart rate.

PCI involves inserting catheter into the patient's radial or femoral artery and guiding it to the aortic root where it engages the coronary ostia. Through this, a wire is passed into the coronary artery, over which a balloon can be passed, used to dilate areas of stenosis. After this, a balloon-mounted stent can be positioned and deployed to maintain a healthy luminal area and to restore flow through the artery. PCI is performed in a cardiac catheterization laboratory, and although it is invasive, it only requires a local anaesthetic and a small puncture (4-6 French, 1.3-2 mm) in a peripheral artery. Patients usually go home the same day and resume normal activities within a couple of days. Coronary artery bypass surgery involves a median sternotomy (opening the chest cavity) under a general anaesthetic and bypassing the stenosed arterial regions with a conduit (vein or artery) from another part of the body which is sutured from the aorta to the coronary artery at a point distal to the stenosis. This procedure can take up to six hours and requires around a week in hospital with a prolonged recovery times relative to PCI. The decision to offer PCI or CABG is usually made based on a combination of factors including the extent of CAD, age, comorbid conditions, frailty, patient choice and feasibility (Neumann et al., 2018, Gunn and Morris, 2022). Broadly, PCI is used in single and double vessel disease, selected (lower complexity) triple vessel disease and in patients not suitable for CABG (ungraft-able distal vessels or not fit enough to tolerate the operation). CABG is favoured in triple vessel disease in those with suitable coronary anatomy who are physiologically fit enough to undergo the procedure. For patients, wherever feasible, PCI is a more attractive option,

mainly due to it being less invasive, with fewer side effects and fast patient recovery. For all these reasons, PCI procedures far exceed those of CABG surgery. In the UK in 2022 there were nearly 100,000 PCI procedures, compared with around 15,000 CABG operations (Mamas A, 2023).

1.3 Investigating coronary artery disease

How patients with IHD are treated depends on clinical assessment and the results of investigations, which are used to support the diagnosis and to establish the extent and severity of CAD, all in the context of a patient's general condition and lifestyle. Investigations can be divided into invasive and non-invasive, and into functional and anatomical. Aside from invasive coronary angiography (CA) (considered below), all other investigations are non-invasive, and these tend to be used as first line tests. Anatomical investigations include invasive and computed tomography-based coronary angiography (CTCA) which delineate epicardial coronary luminal anatomy, and specifically, the presence, location and extent of stenoses. Thus, anatomical tests are good at diagnosing or excluding CAD. Functional tests include stress echocardiography, single-photon emission computerized tomography (SPECT), stress perfusion cardiac magnetic resonance imaging (cMRI), cardiac positron emission tomography (cPET) and exercise electrocardiography (ECG) testing (EET). The basic premise of these tests is to compare images of the ventricles with and without stress, that can be induced with exercise or pharmacologically to identify areas of relative under perfusion. The EET uses exercise to induce electrocardiographic evidence of ischaemia. Thus, functional tests are good at diagnosing (or excluding) IHD and quantifying and localising areas of ischaemia to a coronary territory. Despite considerable overlap, there is a distinction between CAD and IHD. Which investigation a clinician chooses depends on a variety of factors including clinical likelihood (Vrints et al., 2024), as well as local availability and experience, radiation exposure, patient frailty, cost, and what precisely the clinician wishes to know: i.e. are they seeking to diagnose CAD or IHD. The general approach to the investigation of patients with suspected stable CAD is outlined in Figure 1.2.

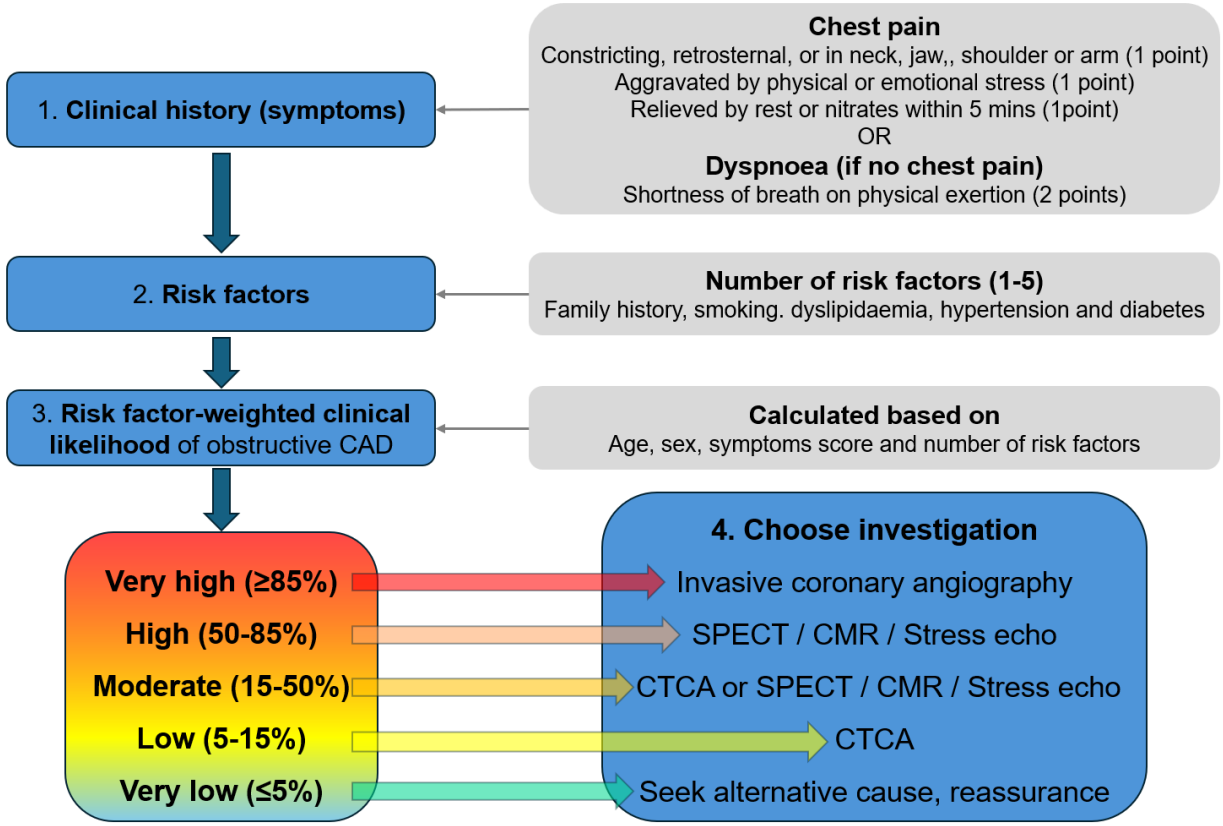

Figure 1.2. An overview of the clinical assessment and investigation of patients with suspected chronic coronary syndrome. Clinicians must consider the anginal nature of symptoms, burden of risk factors, age and sex of the patient before considering which investigation to best support or exclude a diagnosis. Other factors like local availability, cost and radiation exposure must also be considered, based on the UK National Institute for Health and Care Excellence (NICE, 2010, Vrints et al., 2024) and the European Society of Cardiology guideline documents. (CAD = Coronary Artery Disease, SPECT = Single Photon Emission Computed Tomography, CMR = Coronary Cardiovascular Magnetic Resonance Imaging, CTCA = Computed Tomography Coronary Angiography).

Traditionally, investigations have provided either coronary anatomical information *or* functional evidence of ischaemia. This is outlined in Table 1.1.

The ideal investigation for patients with suspected IHD, would provide both anatomical *and* functional data because this would allow for more a more comprehensive assessment and better-informed diagnostic and treatment decisions. This ideal is the focus of this thesis. The presence and magnitude (amount of myocardium affected) of ischaemia determine whether intervention is indicated and the anatomy (focality, extent, location, plaque composition) influence how it is treated (bypass surgery versus PCI) and the strategy (bifurcation stenting, calcium modification etc). Even more ideal, would be a test that provided anatomical and physiological information, was non-invasive, with no associated risk, was inexpensive and did not involve exercise or radiation exposure. Whilst the ideal test does not exist, recent work has made some progress in this regard because it is now possible to estimate coronary blood flow, and other physiological parameters, during CA. This can be based on data derived from transducer tipped angioplasty wires or from computational modelling.

The following sections consider in more detail how coronary arteries can be imaged and how these methods can be complemented by adjunctive physiological assessment in an effort make the assessment of patients more comprehensive in terms of providing anatomical and physiological data in a single test.

Investigation	Anatomical or Functional?	Invasive?	Radiation exposure
Invasive coronary Angiography	Anatomical	Yes	Yes
Computed Tomography coronary angiography*	Anatomical	No	Yes
Optical Coherence Tomography*	Anatomical	Yes	No
Intravascular Ultrasound	Anatomical	Yes	No
Exercise ECG testing	Functional	No	No
Stress echocardiography	Functional	No	No
Myocardial perfusion scintigraphy	Functional	No	Yes
Perfusion magnetic resonance imaging	Functional	No	No
CT perfusion	Functional	No	Yes
Fractional Flow Reserve*	Functional	Yes	No
Instantaneous wave-free ratio*	Functional	Yes	No
Index of Microvascular Resistance*	Functional	Yes	No
Hyperaemic Stenosis Resistance*	Functional	Yes	No

Table 1.1. Guideline-indicated investigations for the diagnosis of chronic coronary syndromes. *Indicates adjunctive tests that are done at the same time as invasive coronary angiography. Echocardiography and MRI demonstrate cardiac anatomy but not coronary arterial anatomy.

1.4 Coronary anatomical imaging

Coronary anatomical imaging modalities include CA and CTCA. The former is based on multi-projection, single-plane, 2-dimensional (2D) x-ray imaging in various coronal and hybrid sagittal/axial planes). The latter is a computed tomographic x-ray assessment in the axial plane. More recently, intravascular imaging techniques have been developed using light- or ultrasound transducers placed inside the coronary artery during invasive angiography. These adjunctive tests provide much greater resolution of the coronary luminal anatomy, including the detail regarding the arterial wall and atherosclerotic plaque constituents. Although

cardiologists rely mainly on CA, these emerging modalities are useful adjuncts, especially for planning, guiding and optimizing PCI strategy.

CAD reduces the coronary artery lumen diameter and, hence, coronary blood flow, i.e., it affects both the anatomy and physiology. It is aberrations of the latter that cause ischemia and symptoms. Ideally, diagnostic imaging methods should integrate relevant information on both aspects, either directly, or indirectly. Unfortunately, no routinely used tools do this. However, with modern 3D reconstruction and segmentation techniques, coronary imaging can be used to transform standard 2D angiographic images of anatomy into representative 3D models, which can be used to simulate coronary physiology. Routinely used imaging modalities mainly include CA, CT, OCT and IVUS, all of which capture different aspects of coronary anatomy. Recent developments have advanced towards multi-modal imaging, that spatially co-registers, and three-dimensionally fuses complementary information from different modalities, to provide a more comprehensive anatomical picture. The following sections review the range of coronary imaging modalities used in routine clinical practice and explore their potential for integration, specifically spatial co-registration of the OCT luminal images onto its corresponding coronary angiogram, and fusion of both modalities to produce 3D models that use information from both.

1.4.1 2D imaging: Invasive coronary angiography

CA was introduced in 1959 and remains the gold-standard technique for assessing CAD and guiding PCI in the catheterization laboratory, because of its high temporal and spatial resolution and its widespread availability (Collet et al., 2017). It involves inserting a catheter through the radial or femoral arteries, to reach the aortic root where radio opaque contrast medium is injected into the left and right coronary ostia. The procedure is guided by live x-ray imaging, to monitor the catheter position, and guide catheter manipulation, until the catheter tip sits at the arterial ostium. The x-ray source and detector are housed in a C-arm which hangs from a ceiling-mounted gantry, that rotates around two separate axes to acquire a series of 2D images from a range of different modified coronal projection angles, relative to the patient (Frison, 2018a). In the catheterization laboratory, the radiographer, with guidance from the clinician, can manipulate the x-ray C-arm to adjust the angle between the targeted section of the arterial tree and the source/detector in the x-ray machine. Due to the complexity and variability of the arterial anatomy, certain projections are more suitable to view different sections of different

arteries and are thus favored in the catheterization lab during a PCI (Green et al., 2005b). The resulting silhouettes or ‘luminograms’ reveal areas of healthy artery and stenoses reflecting CAD. Figure 1.3 shows the 2D projection of the same anatomy pre- and post-PCI highlighting the stenosed and then stented regions, the areas where the vessel is expected to be foreshortened in this projection, vessel overlap, and the catheter.

During standard CA, cardiologists reconstruct the 3D anatomy from visual interrogation and understanding of (i) the 2D images, (ii) the projection angles and (iii) knowledge of coronary anatomy - all in their ‘mind’s eye’. This is a subjective and inaccurate process. Being x-ray-based, detection of stenoses is critically dependent on the grey-scale contrast between the contrast-filled lumen and the surrounding arterial, cardiac and thoracic tissues and other factors, such as obesity and vessel overlap. X-ray images are pixelated images and diagnosis based on such images is highly dependent on their quality (Figure 1.4) and interpretation is user dependent. This may lead to sub-optimal vessel edge detection, which is a vital part of any modelling process, particularly around stenosed regions.

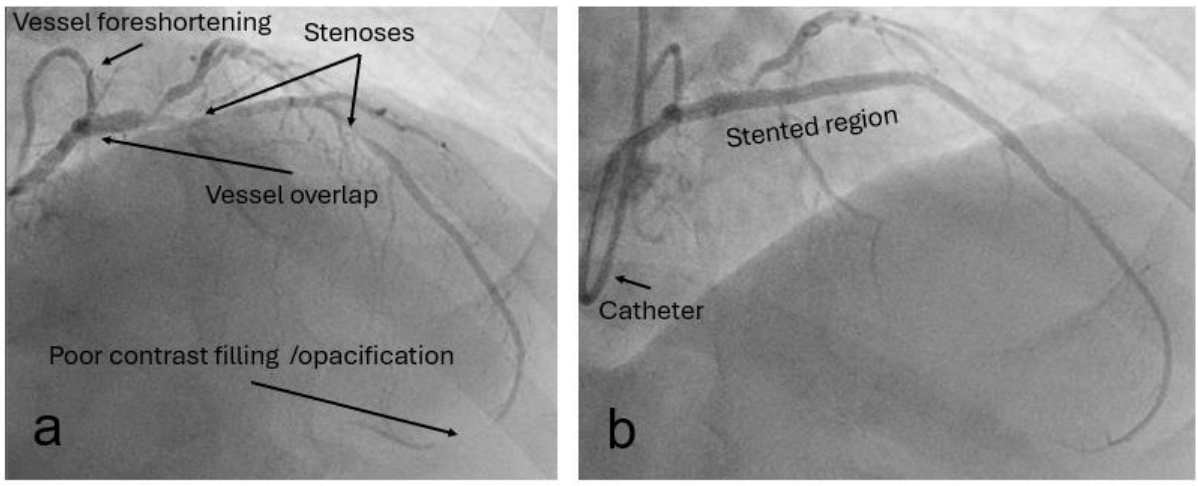

Figure 1.3. An example of a 2D invasive angiogram. The left coronary artery is seen pre- (a) and post- (b) PCI. The images are both acquired in the right anterior oblique angle. Some of the key features and limitations of this imaging modality are highlighted. Images courtesy of the Mathematical Modelling in Medicine Group at The University of Sheffield.

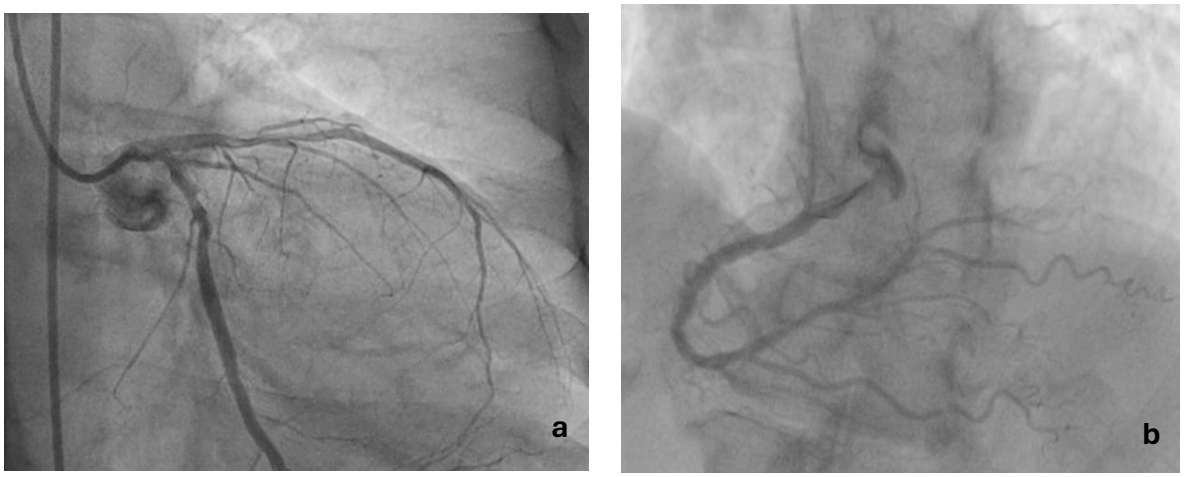

Figure 1.4. Coronary angiograms with (a) high and (b) low vessel edge grey-scale contrast. In (a) the vessel edge contrast is clearer than (b) due to a higher voltage (kV) setting resulting in a higher x-ray radiation dose. (Courtesy of the Mathematical Modelling in Medicine Group at The University of Sheffield).

In the UK, the radiation dose per patient per angiographic procedure is regulated and must be kept as low as reasonably achievable (ALARA), and so ultra-high image quality must be balanced against patient and staff safety. The interpretation of the appropriate proximal and

distal points, borders, bifurcation points and the apparent significance of stenoses include a degree of uncertainty and subjectivity that, in some cases, may influence treatment decisions. Angiograms are analogous to 2D shadows of a 3D tree, produced by a point source of light. Since the tree exhibits both curvature and tortuosity, imaging the same vessel from different angles is required to fully delineate the true shape of the vessel. Depending on the choice of imaging angle, known as the projection angle, a curved section of vessel might appear straight, for instance, if the plane of curvature of the vessel is exactly perpendicular to the projection plane, thus showing a vessel that is shorter than its actual length, in a phenomenon called 'vessel foreshortening'. Figure 1.5 shows an LAD viewed from four separated angles. Each angle produces a vessel that is either less/more curved or is longer/shorter. How can two 2D angiograms completely capture the anatomy of 3D tortuous vessels such as coronaries?

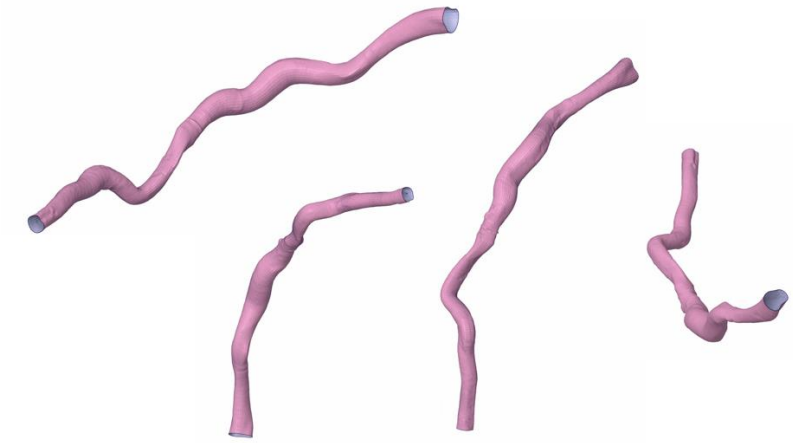

Figure 1.5. Four different views of the same coronary artery (LAD). Despite multiple views, 2D imaging modalities are often insufficient to characterise 3D anatomical structures.

Accordingly, it is not guaranteed that a single planar angiographic view represents an entire spatially curved artery, without some degree of foreshortening (Green et al., 2005b). This presents a challenge to CA-based 3D reconstruction, as the reconstructed arteries can be imaged with distorted lengths depending on the view they were captured from (Frison, 2018a, Pederzani et al., 2022).

During the 1980's, quantitative coronary angiography (QCA) was introduced (Brown et al., 1977). QCA calibrates the pixel/size ratio from the catheter tip (known dimensions) to enable objective measurements of distance, resulting in more accurate predictions of stenosis diameter and lesion length, although the latter is still susceptible to foreshortening. In some centers, QCA

is used routinely as a clinical decision support tool for interventional cardiologists to decide when to intervene (Garrone, 2009). 3D QCA is now available, based on a 3D reconstructed coronary model derived from two orthogonal projections (Masdjedi et al., 2020).

Until recently, most studies reconstructed only the main vessel in so-called *single conduit* models. Not only is it computationally challenging to model side-branches, but smaller vessels are not fully resolved even with excellent quality CA (Figure 6). Moreover, smaller side branches (≤ 2 mm) are clinically less interesting because it is not possible to intervene upon them and they subtend small areas of myocardium. Unlike intravascular imaging, CA cannot resolve plaque composition, beyond a relatively crude prediction of the presence or absence of calcium deposits. CA is also vulnerable to 'noise' from nearby and overlapping organs and tissues (lungs, mediastinum, ribs, diaphragm) creating inconsistent shadowed greyscale background (Lyu et al., 2020) (Figure 1.4a and 1.4b). There were attempts to tackle image background noise using techniques such as digital subtraction angiography (DSA) (Yamamoto et al., 2009, Zhu et al., 2021). DSA is a fluoroscopy-based technique that removes, as much as possible, background noise present in an angiogram due to other anatomical structures, such as the ribs, lungs, heart etc by subtracting the pre-contrast image, also called the masque, from the subsequent post-contrast images. DSA is used in several clinical applications, the most common of which are cerebral and pulmonary diseases. However, the challenge when using DSA to process angiograms of the coronaries is motion artefacts from breathing and cardiac motion making the post-contrast images different from the masque, complicating the subtraction process. Yamamoto et al. have attempted to measure the relative translation vector and rotation between the masque and the post-contrast images yet have concluded that this technique might have reduced motion artefact for main branches, the combination of motion and artefact and background anatomical structures such as the ribs, rendered the visualization of smaller vessels a still existing challenge (Yamamoto et al., 2009).

Coupled with its benefits, CA has other limitations. It is invasive and is associated with a low risk of major complication (~1:1000). It only demonstrates the contrast-filled lumen, it provides very little information regarding plaque composition or arterial wall structure. Accordingly, CA-based 3D arterial reconstructions lack any arterial wall detail. In addition, because they are almost all reconstructed from just two angiographic projections, the result is an assumed circular (axisymmetric) arterial lumen shape, as a most logical first assumption (Frison, 2018a). Galassi et al. have diverted from using just two angiographic projections for reconstruction. They based their reconstructions on more than two angiographic projections

and control points to reconstruct the lumen wall structure (Galassi et al., 2018). Foreshortening due to projection angle choice and table movement during PCI, lead to errors in the final reconstruction, which is irreducible. Clearly, this and other sources of error impact any CA-based modelling. Even while using the 'standard' angiographic views which are known to optimally view specific vessels, in their study, Green et al. reported 7.4% and 10.2% foreshortening in the proximal and middle sections of the left anterior descending artery, respectively, even using the optimal (right anterior oblique cranial) view (Green et al., 2005b). Their study also highlighted the subjectivity of CA-based coronary viewing by reporting up to 50% versus 0.5% vessel foreshortening from clinician-selected angles and computer-chosen "optimal" angles based on a 3D reconstruction, respectively, which were more than ten degrees apart for most vessels. Although clinicians do attempt to position the C-arm perpendicular to the inherently tortuous targeted segment in the catheter laboratory, it remains impossible to acquire paired images that truly represent the stenosis and the remainder of the proximal and distal arterial sections without any degree of vessel overlap or differential relative foreshortening. Inaccuracy is therefore introduced, depending on the angiographic projections selected. In cases with eccentric plaques, two images will never fully capture the plaque, because the best that can be generated from two images is an axisymmetric reconstruction. Other errors may be introduced by temporal and spatial inconsistencies due to patient and/or table movement which may occur between image acquisitions, which has been flagged as a source of error since the early years of imaging (Zir et al., 1976b, Galbraith et al., 1978a). Biplane angiography, which takes both images simultaneously in 'stereo', avoids the errors introduced due to patient and/or table movement, but is not widely available and increases patient and operator radiation exposure (Sadick et al., 2014). During CA, different structures are differentially magnified due to the variable distance between the source and the tissue plane in which they lie, all within a diverging x-ray beam (Tafti and Byerly, 2025). Thus, the LCX artery often appears larger than it is due to it being closer to the x-ray source than the catheter and LAD. Intravascular imaging, as will be presented in a later section, is not susceptible to this.

The CA limitations, addressed previously, have been the target of technological advancements such as the introduction of biplane or rotational angiography. The former has been described. The latter acquires angiograms as the C-arm pans around the patient's thorax, reducing contrast and radiation. However, it restricts the viewing time per viewing angle, which is a barrier to 3D reconstruction. This is because 3D reconstruction requires at least two images that

adequately represent the stenosis, and artery, with adequate opacification, with minimal foreshortening and overlap, both in the same phase of the cardiac cycle. As the C-arm pans around the heart, it captures images continuously meaning that it is almost impossible to satisfy all these criteria (Morris et al., 2013, Morris et al., 2016). In any case, neither is available widely. Developments in QCA hardware, such as flat panel detectors and adaptive image processing, and software, such as automatic calibration, have led to decreased signal distortion and noise and improved resolution (Collet et al., 2017), but none can resolve the aforementioned limitations.

1.5 2D imaging: Computed tomography coronary angiography (CT)

Since 2005, CT scanning emerged as a diagnostic test for CAD. It is non-invasive and has a high sensitivity (91% - 97%) and negative predictive value (97%- 99%) and produces a stack of 2D images with negligible movement artefact due to rapid acquisition (Min et al., 2010). It has been adopted widely, particularly as a rule-out tool in patients deemed to have low-moderate probability of CAD (NICE, 2010). CT is accurate and reliable in ruling-out non-obstructive stenoses (<50% stenosis), and therefore, in reducing unnecessary invasive CA procedures (Miller et al., 2008). According to the Society of Cardiovascular Computed Tomography 2021 Expert Consensus Document on Coronary Computed Tomographic Angiography, CT is deemed a suitable gatekeeper for symptomatic patients, with or without prior CAD history (Narula et al., 2021). The 2D axial image stack lends itself to 3D image reconstruction which, in turn, is ideal for physiological modelling of FFR measurements (as discussed in section 1.8 and 1.9). Developments in CT technology reduced the original 20 millisieverts radiation dose by up to 70%, with the introduction of the 640- slice CT scanner further reducing it to less than one millisievert. This is compared with seven millisieverts exposure from an invasive coronary angiogram, which naturally affects image resolution due to pixel intensity being less defined (Crowhurst et al., 2014). For many years CTCA has been used as an effective gatekeeper to invasive catheterisation, but has been limited in its ability to quantify disease significance in the presence of coronary calcification (causing blooming artefact) and arrhythmia (especially tachycardia) and, in such cases, CA has had the upper hand in regards to spatial and temporal resolution (Van Mieghem, 2017). These limitations may be resolved by the latest photon-counting scanners that can detect and quantify x-ray energy more directly and with less background artefact. Conventional CTCA provides a resolution of ~0.4–

0.5 mm, whereas photon counting detectors provide a resolution ~0.20 mm. Photon-counting detectors are made of a semiconducting material that absorb all x-ray quanta and transform them to electrical signals. The electrical signals are proportional to the energy of the x-ray quanta that created them, and by using different energy thresholds, a spectrum of CT data can be obtained while allowing the detector to 'count' the pulses at each threshold. Photon-counting CTCA is associated with significantly reduced blooming artefact which improves quantitative analysis of calcified and previously stented coronary segments and improved analysis of plaque composition, all at comparable radiation doses (Flohr et al., 2023).

1.6 Intravascular imaging: IVUS and OCT

Whereas CA and CT view the coronary anatomy from the outside, 'looking' through the body, OCT and IVUS acquire images from inside the coronary arteries and generate cross-sectional images (Reiber et al., 2011, Terashima et al., 2012, Carpenter et al., 2022). This resolves many of the limitations of CA, such as providing significantly more detail on internal lumen morphology and plaque composition. Cohort studies and meta-analyses have reported the benefit of using intravascular imaging to guide PCI, co-registered with CA in terms of clinical outcomes, specifically in reducing major adverse cardiac events (Jones et al., 2018, Hong et al., 2020, Park et al., 2020, Zhang et al., 2018, Elgendy et al., 2019, Chiastra et al., 2018). IVUS emerged in the 1980s, followed a decade later by OCT (Huang et al., 1991, Yock et al., 1989, Brezinski et al., 1996). Both techniques depend on the interpretation of reflected waves transmitted from inside the coronary artery. IVUS (Figure 1.6) uses ultrasound whereas OCT (Figure 1.7) uses visible light to delineate intraluminal anatomy. Both techniques are used to assess coronary luminal anatomy and plaque composition, and both are used pre-PCI to determine indication for PCI and then strategy and post-PCI to check the result of intervention in terms of stent deployment and apposition and to rule out any dangerous edge dissections. The wavelengths of visible light and ultrasound are very different, and this influences the spatial image resolution and the level of arterial wall penetration. The choice between IVUS and OCT is therefore nuanced. The factors that influence the choice between IVUS and OCT are summarized in Table 1.2.

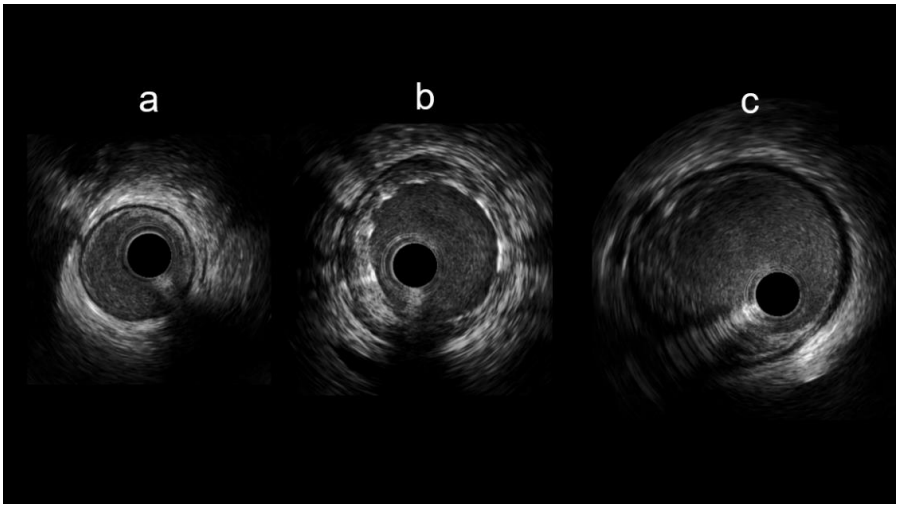

Figure 1.6. Example of IVUS images from a distal (a), mid (b) and proximal (c) left coronary artery. The dark black circle in each is the catheter itself. The dark shadow caused by the angioplasty wire is visible at the bottom right, bottom center and bottom left in each image. The distal image demonstrates the trilaminar structure of the arterial wall. Stent struts can be seen in (b) which are well expanded and well opposed to the arterial wall. (Courtesy of the Mathematical Modelling in Medicine Group at The University of Sheffield).

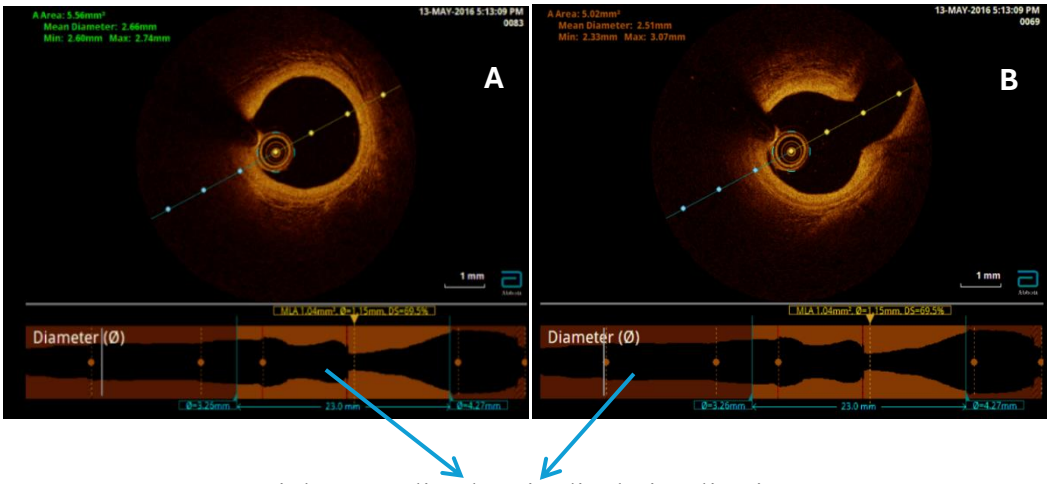

Figure 1.7. Coronary OCT showing (A) the main vessel and (B) the main vessel with the emergence of a side vessel (at a bifurcation). The straight line that transects the lumen has dots at 1 mm distances to aid size interpretation. The dark (black) lumen is outlined by thickened (bright yellow /gold colour) and atheromatous plaque. The catheter is seen as a series of circles at the 8 o'clock position and there is a wire shadow seen in the 10 o'clock position. (Courtesy of the Mathematical Modelling in Medicine Group at The University of Sheffield).

	OCT	IVUS
Mechanism	Automatic lens retraction through target artery	Camera moved manually or with motorised transducer pull-back at 0.5-2 mm/s
Radiation type	Near infrared light	Ultrasound
Wavelength, μm	1.3	35-80
Frequency	20-45 MHz	190 THz
Penetration Depth, mm	1-3	4-10
Resolution, μm	Axial: 10-20 μm Lateral: 20-90 μm	Axial: 100-150 μm Lateral: 150- 300 μm
Frame rate (per second)	100	30
Blood flushing needed?	Yes	No
Field of view diameter, mm	10-15	7-10

Table 1.2. Comparison between IVUS and OCT signal properties and captured features.

Being the older technique and more widely available, IVUS has been evaluated by more studies than OCT for PCI guidance. Zhang et al. performed a meta-analysis involving over 16,600 patients undergoing CA and IVUS to guide drug-eluting stent implantation. With IVUS, they showed significantly reduced rates of stent thrombosis, major adverse cardiac events (MACE) and death compared to cases guided with standard angiography (Zhang et al., 2018). Other studies led to similar conclusions (Ali et al., 2016, Elgendy et al., 2016, Hong et al., 2015, Bavishi et al., 2017, Tan et al., 2015). Jones et al. reported significantly lower rates of mortality in patients who underwent OCT-guided PCI (7.7% of 1,149 cases) when compared with IVUS-guided and CA guided patients (12.2% of 10,971 cases and 15.7% and 75,046 cases, respectively, $p<0.0001$) (Jones et al., 2018). Studies have also explored the diagnostic accuracy of the second-generation frequency domain OCT (FD-OCT) and IVUS when classifying lipid-rich, fibrocalcific, or fibrous plaque and reported FD-OCT superiority in classifying fibrous plaque, in terms of sensitivity and specificity (Shimokado et al., 2019, Guo et al., 2012, Rieber et al., 2006).

Figure 1.8 shows an example OCT case of a diseased LAD highlighting an area of healthy vessel, bifrucation, stenosis, and what the OCT monitor displays in the clinic.

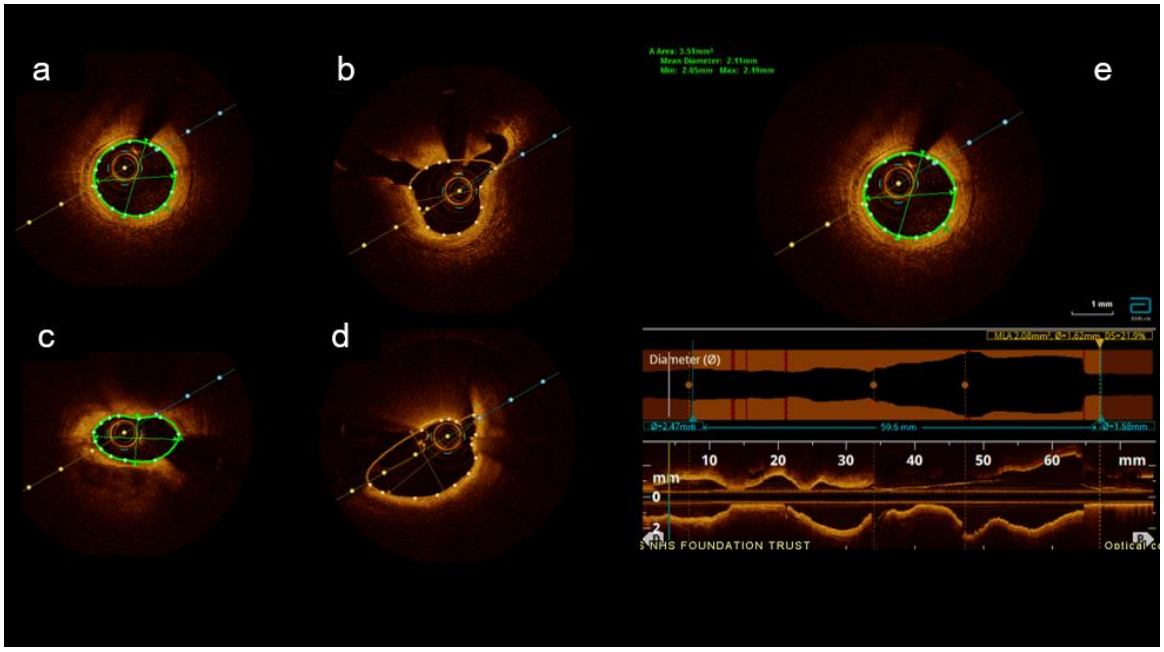

Figure 1.8. Example of an OCT case in a diseased left anterior descending artery. In each, the central dark colored region is the lumen. In each image, there is a wire shadow caused by the presence of the angioplasty wire which occludes the light signal. The dots on the straight line are spaced at 1 mm intervals. (a) is a distal frame showing an approximately 2.25 mm diameter vessel with clearly visible circumferential atheroma (yellow coloring at luminal border). (b) shows two side-branches emanating from the main vessel at the 2 and 10 O'clock positions. (c) shows a stenosed region. The diameter here is approximately 1 mm by 2 mm. Invasive angiography would be unable to represent this asymmetry. (d) shows a proximal section. Here the OCT is unable to detect the entire luminal border due to the size of the proximal vessel and some blood swirl artefact. These are recognized limitations of OCT, especially in large proximal arteries. Panel (e) is a screen capture from the clinical graphical user interface. The two horizontal images demonstrate the diameter as a function of the length (average top and in-plane bottom). As can be seen, OCT renders the artery completely straight, even though this is never the case. The green lines demarcating the luminal border (a, c, e) are the system-generated capture of the luminal border. The equivalent amber lines (b, d) indicate where the system is not sufficiently confident in identifying the luminal border. Images courtesy of the Mathematical Modelling in Medicine Group at The University of Sheffield.

Conclusions regarding the imaging technique better suited to classify calcified plaque are contradictory. Rieber et al. reported higher sensitivity and specificity for detecting calcified plaque with IVUS and Guo et al. reported similar values for both. A concrete differentiation of strengths between the two techniques is not yet confirmed. Some studies have concluded that OCT is better suited for detecting coronary dissection assessment and for analyzing plaque composition (Ali et al., 2016, Rieber et al., 2006), while others deem IVUS to be the better choice (Peters et al., 1997, Windecker et al., 2014). It has even been suggested that the high resolution of OCT can give "too much detail" (Prati et al., 2016, Prati et al., 2018, Van Zandvoort et al., 2020) luring some operators into over-diagnosis and intervention of what are actually insignificant dissections (Ali et al., 2021). In 2018, the consensus paper from the European Association of Percutaneous Cardiovascular Interventions stated that OCT was more user-friendly and superior in identification of in-stent restenosis and thrombosis. IVUS was recommended for patients with significant renal impairment due to the lack of requirement for contrast displacement of the blood pool (Räber et al., 2018).

Both OCT and IVUS images are recorded during a pullback of the lens /transducer. The catheter is placed distally to the region of interest. When recording commences, the lens /transducer is retracted and spatially ordered cross-sectional images are acquired in the plane perpendicular to the guidewire are acquired. Software is then used to visualize the imaged lumen assuming a straight line (longitudinal horizontal section in Figure 8e) i.e. the curvature tortuosity of the artery cannot be captured, and this remains a limitation, especially in the context of 3D modelling.

For effective imaging and reconstruction, artefacts should be minimized. Because blood cells attenuate light, cardiologists displace the blood pool by injecting viscous contrast medium. In cases with severe stenosis or tortuosity, the OCT catheter may occlude blood flow and interfere with contrast displacement impairing image quality and even causing ischemia.

Unlike OCT, IVUS can be used manually (without automated pullback) with the operator advancing or withdrawing the catheter in a distal or proximal direction. This provides insight into the local luminal anatomy but cannot be reconstructed because the time and direction data are unknown.

Recently (September 2024), intracoronary imaging with either IVUS or OCT gained a class 1, evidence base A (both are the highest level) indication in the international guidelines for guiding PCI in the context of anatomically complex lesions (Vrints et al., 2024). Of importance

to this thesis, the guidelines specifically indicate intracoronary imaging in *bifurcation* PCI, along with LMS and long lesions. This promotion for intracoronary imaging was based on three randomized controlled trials and two metanalyses. In the RENOVATE-COMPLEX PCI trial, IVUS (74%) and OCT (26%) imaging, in the context of long, bifurcation, and chronic total occlusion lesions was associated reduced mortality, target vessel MI, or target-vessel revascularization when compared with standard angiography-guided PCI over two years (7.7% vs. 12.3%; HR 0.64; $P = 0.008$) (Lee et al., 2023). In the OCTOBER trial, OCT-guidance in true bifurcation lesions was associated with reduced cardiovascular death, culprit-lesion MI, or ischaemia-driven revascularization compared with angiography guidance, again, over two years (10.1% vs. 14.1%; HR 0.70; $P = 0.035$) (Holm et al., 2023). The third trial was ILUMIEN IV, which investigated the benefit of OCT-guided PCI which did not reduce the primary outcome measure of target-vessel failure (cardiovascular death, culprit-vessel MI, or ischaemia-driven culprit vessel revascularisation) compared with angiography (7.4% vs. 8.2%; HR 0.90; 95% $P = 0.45$), but did reduce the rate of stent thrombosis (0.5% vs. 1.4%; HR 0.36; $P = 0.02$) (Ali et al., 2023). These results were corroborated by a metanalysis by Kuno et al of 32 trials of intracoronary imaging versus standard angiography (Kuno et al., 2023). This included 22,684 patients and found that imaging was associated with reduced cardiovascular death, MI and culprit lesion revascularisation (RR 0.75; 95% CI 0.57-0.9). A similar network metanalysis by Stone et al of trials comparing IVUS and/or OCT against angiography guidance included 15,964 patients and also found that imaging was associated with reduced culprit lesion failure (cardiovascular death, culprit vessel MI or culprit lesion revascularisation) (Stone et al., 2024).

Thus, using intravascular imaging to guide PCI is associated with improved outcomes and is now guideline-indicated, particularly in bifurcation lesions.

1.7 Multimodality imaging

Multimodality imaging seeks to incorporate the strengths of individual imaging methods in a synergistic manner, to provide more comprehensive anatomical data (Greulich and Sechtem, 2015). Most commonly, multimodality imaging spatially co-registers or fuses CA with OCT or IVUS. Co-registration refers to relating information from different modalities to each other, such as indicating the position on an angiogram where a specific OCT frame was taken from etc. The information remains separate. Fusion refers to the process of combining information

from multiple modalities together to produce a model; the information is combined into a single set of anatomical data sources from different modalities. Some investigators have experimented with fusing OCT with IVUS (Ono et al., 2020, Sheth et al., 2018, Huang et al., 2021). Recent studies have investigated the benefits of multimodal imaging (Greulich and Sechtem, 2015, Hebsgaard et al., 2015, Daubert et al., 2021) and have focused on researching two main aspects: (i) whether co-registration/fusion generates data which might result in a change in treatment decisions, and (ii) whether co-registration/fusion improves post-PCI results (e.g. stent deployment, apposition, restenosis, edge dissection) compared with single modality imaging. Studies have used multi-modal imaging for several purposes, such as WSS computation, (Krams et al., 1997), to capture non-uniform lumen morphology post-PCI, (Bourantas et al., 2014), and to study the impact of scaffolds implanted in side branch ostia, (Karanasos et al., 2015). (Kubo et al., 2021) Kubo et al. analysed frequency of untreated lipid-plaques at the stent edges (16% vs 26% for the co-registered cases) while Schneider et al. (Schneider et al., 2021) analysed rates of longitudinal geographic mismatch (4.2% for fused CA OCT co-registered cases, compared to 17% and 22.9% for OCT- and CA-guided PCI, respectively). Koyama et al. analysed rates of co-registration on stent geographic miss frequency and edge dissection (27.6% vs 34% for with versus without co-registration) and (11.1% vs 20.8% for co-registered cases, when compared to OCT-guided PCI) (Koyama et al., 2019). (Migliori et al., 2017) Migliori et al. compared lumen area and volume between OCT-based reconstructions and micro-CT reconstructions and found a difference of 17.5% and 7.1%, respectively, with the micro-CT values being higher. Hebsgaard et al. studied the impact of co-registration on decision-making. They reported that in 70% of lesions, without co-registration, parts of the diseased vessel sections areas where left uncovered (Hebsgaard et al., 2015).

Several researchers have described the way they extracted and used OCT data for coronary reconstruction (Li et al., 2024). Wu et al extracted the catheter centre and lumen contours, stacked the contours in a straight-line using catheter centre, and rotated the contours around the catheter centre to minimise outside frame overlap between any two consecutive contours (Wu et al., 2020). Ellwein et al segmented the OCT images and giving each lumen a z-coordinate corresponding to the pullback distance and stacked them in a straight-line (Ellwein et al., 2011). Chiastra et al reconstructed the wire pathway by minimising bending energy then position the ‘landmark lumens’ on the pathway and the remaining lumens according to inter-frame space (Chiastra et al., 2018). The wire pathway is reconstructed by assuming that the wire follows the straightest pathway within any tortuous and curved vessel (minimising

bending energy, by optimisation of the set of possible wire pathways). Andrikos et al used back projection onto the angiograms to extract catheter path with centroids used as the centreline points (Andrikos et al., 2017). Mutha et al. segmented the centreline from the angiogram images and the contours from the OCT images and mapped the contours onto the centreline (Mutha et al., 2013). Li et al corrected for longitudinal and rotational mismatch of OCT contours by matching the side branch ostia with CA ('landmark contours') and the longitudinal positions of the OCT contours by interpolation between landmark contours (Li et al., 2015). They modelled the main vessel using fused CA and automatic OCT pullback. The side branches were modelled directly using CA only and indirectly using information on the position and orientation of the side-branches from the main vessel OCT sequence. This is not an exception, as until recently, many studies that incorporated multi-modal imaging for 3D modelling branches, only used multiple imaging modalities for the main branch while the side branch was modelled using a single modality. However, Li et al. reported that four out of 21 patients lacked side branches that were greater than 1mm in diameter (their pre-specified threshold for segmentation). This is an interesting finding because studies usually specify diameter thresholds that are larger than this to study epicardial coronary arteries and primary branches (i.e. ≥1.5mm) (Kim et al., 2017). This may indicate that a more inclusive segmentation might require diameter thresholds that capture smaller vessels. Clearly, the question of 'how significant is flow sequestered from a vessel of that size' is important. Indeed, since the focus of this thesis is modelling major side branches, it is essential to consider: how small is too small? When does a 'branch' become insignificant to model? On this topic, Li et al. and Ishibashi et al. reported that the absence of a side branch could cause underestimation of the functional significance of proximal stenoses (Ishibashi et al., 2015). Modelling side branches therefore serves two purposes. The first is anatomical, i.e. it may provide a clinician with 3D images that may be beneficial in guiding interventional strategy. For this indication the threshold for 'significance is widely considered as any side branch ≤2.5 mm (Neumann et al., 2018). The second is physiological, i.e. to ensure flow simulations are accurate, because underestimating or neglecting side branch flow may underestimate the physiological significance of main vessel stenoses (Gosling et al., 2020).

It is impossible to resolve all small side branches for 3D modelling, and so laws of physiology and morphometric scaling (like Murray's law) can infer side branch sequestration flux from healthy vessel taper (Taylor et al., 2024). This is discussed later in this report. However, it is out of the question that modelling major bifurcations (side branch ≥2.5 mm) as accurately as

possible is important due to the frequent occurrence of bifurcation stenoses and the need for bifurcation stenting (Lefevre, 2001).

To summarize, multi-modal imaging is of increasing interest and the studies that focus on CA and OCT co-registration and fusion are more common than those that do CA and IVUS. To use multiple imaging modalities to model branching vessels, some researchers have, for instance, used a combination of CA and OCT to model the proximal and distal ends of the vessels, while limiting the bifurcation region to CA only or to statistical shape models. This indicates a gap regarding fully modelling branching vessels from multiple modalities, not just the sections away from the bifurcations (Morlacchi and Migliavacca, 2013).

1.8 Physiological assessment

Coronary imaging provides anatomical data, but this does not necessarily predict flow limitation. Studies have consistently shown that coronary anatomy is a poor predictor of blood flow restriction and thus the ischemia-causing potential of CAD (Mehta et al., 2022). Over the last two decades seminal studies have reported improved outcomes when coronary physiological assessment is used to guide PCI, compared with angiographic guidance alone (Tonino et al., 2009, De Bruyne et al., 2012). Physiological assessments can be invasive (performed during angiography) or non-invasive. Non-invasive physiological tests of ischaemia include stress echocardiography, exercise electrocardiography, myocardial perfusion imaging and cardiac magnetic resonance imaging (Mieres et al., 2014), but these are beyond the scope of this report which is focused on invasive imaging and assessment.

Being due to insufficient myocardial blood flow, ischaemia is a physiological (not anatomical) phenomenon. It is, therefore, unsurprising that IHD is better predicted with *physiological* rather than *anatomical* assessment. Invasive physiological assessment of IHD involves the insertion of sensor-tipped guidewires into the patient's coronary artery to measure haemodynamic metrics such as pressure and surrogate markers of flow. These metrics can be used to calculate indices of coronary physiology like fractional flow reserve (FFR), coronary flow reserve (CFR) and the index of myocardial resistance (IMR). The FFR is the maximal myocardial blood flow during hyperaemia in the presence of a stenosis in the epicardial artery, expressed as a fraction of its normal/healthy value. Because coronary blood flow is not routinely measured due to a lack of appropriate method, this is derived from the ratio between

the distal (Pd) and aortic (Pa) pressures as outlined in Equation 1.1 (Pijls et al., 1996, De Bruyne et al., 1995).

$$FFR = \frac{P_d}{P_a}$$

Equation 1.1. Fractional Flow Reserve

For a detailed derivation of FFR from pressure measurements see (Morris et al., 2016). FFR is used in the clinic to identify stenoses that may cause ischaemia, as shown in Figure 1.9. The threshold for physiological significance is ≤0.80 (Tonino et al., 2009, Cuisset et al., 2013, Chahour et al., 2020). FFR measures a lesion's effect on flow as a fraction of an unknown and hypothetical maximum. The actual flow in a stenosed vessel does not influence the numerical value of FFR. Notwithstanding these limitations, FFR is widely used to guide intervention, with the current clinical guidance being that FFR≤0.80 is an accepted threshold for PCI intervention. The Fractional Flow Reserve versus Angiography for Multi-Vessel Evaluation (FAME) study reported reduced stent implantation (2.7 vs 1.9, $p<0.001$) and rates of MACE (death, myocardial infarction, and repeat revascularization) (18.3% vs 13.2%, $p=0.02$) in the FFR-guided group (Tonino et al., 2009). (Tonino et al., 2009, De Bruyne et al., 2012). These benefits persisted in the two year follow up (Pijls et al., 2010) but beyond this, developed similarly for both groups (van Nunen et al., 2015). In the follow-on FAME-2 trial, the authors compared FFR-guided revascularisation of physiologically significant lesions (FFR ≤0.80) against best medical therapy. The rate of urgent revascularisation was significantly reduced in the FFR arm (Bruyne et al., 2012). Despite these proven clinical benefits, FFR remains underused, due to the associated additional time, effort and expense of measuring FFR with a pressure wire (Mamas A, 2023).

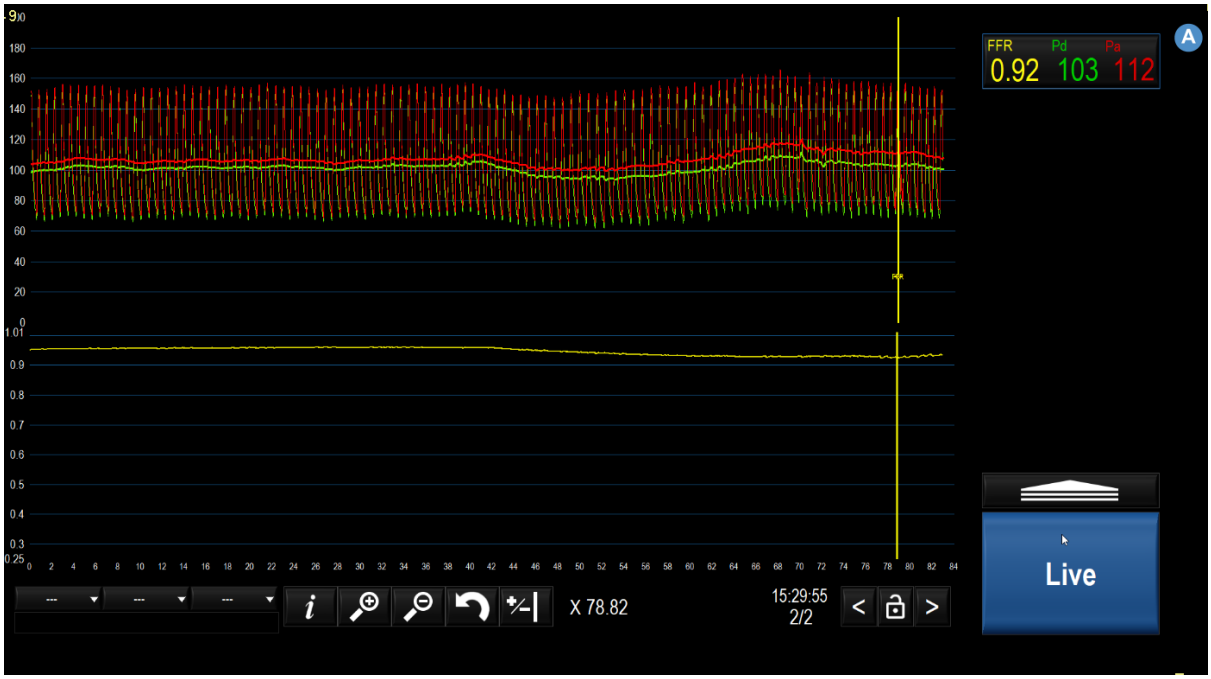

Figure 1.9. An example of a fractional flow reserve measurement. The red and green lines (y axis) chart the time-dependent changes in distal (green) and proximal (red) pressures (x axis). The continuous horizontal lines track the corresponding moving average (over three cardiac cycles) of these pressure waveforms which are also displayed in numbers at the top right. The proximal and distal pressures separate with time due to the administration of adenosine which indices maximal coronary blood flow. The FFR is 0.92, indicating that the pressure transducer is positioned distal to physiologically non-significant coronary artery disease and so PCI is not indicated. Image courtesy of the Mathematical Modelling in Medicine Group at The University of Sheffield.

The use of adjunctive physiological assessment has been granted a class 1 indication in the international guidelines to assess the ischaemia causing potential of arteries with intermediate (40-90%) lesions (Vrints et al., 2024). This indication is supported by the strongest evidence base (class A), based largely on the studies described above. FFR can also be used in an ACS setting where it significantly reduces the number of lesions and vessels undergoing PCI (38% of intended lesions differed) with no difference in MACE rates (Van Belle et al., 2017).

The instantaneous wave free ratio (iFR) is a resting, pressure-derived metric that is like FFR but only considers the Pd/Pa ratio during diastole and does not need the induction of hyperaemia. Early results comparing it against FFR were non-inferior (Davies et al., 2017,

Götberg et al., 2017) but longer term metanalysis of the same study results after five years suggested an excess of mortality and MI in the iFR group (Eftekhari et al., 2023).

Use of intracoronary physiology has also proven beneficial in those with angina and no obstructive coronary artery disease (ANOCA). Increasingly, ANOCA is considered a common cause of angina, that often escapes diagnosis and affects women considerably more than men. In ANOCA, the epicardial arteries are disease free (hence negative FFR) and the angina is caused by disease or dysfunction of the distal microcirculation (Morris et al., 2022). For the assessment of ANOCA a metric of coronary blood flow (not pressure) is required in combination with a pressure assessment, and this can be derived from a Doppler flow velocity wire, thermodilution mean-transit time or from continuous thermodilution. These measurements are used to derive the coronary flow reserve (ratio of hyperaemic to baseline flow) and index of myocardial resistance (ratio of Pd and flow), both of which are central to the diagnosis of macrovascular angina (Perera et al., 2023). Assessment of microvascular angina has also received a high-level indication in the most recent European guidelines (class 1, level of evidence B), but currently, assessment is largely restricted to specialist, tertiary centres. Absolute (volumetric) coronary blood flow can also be estimated using a continuous thermodilution method requiring a dedicated microcatheter (Candreva et al., 2021). This is an emerging technique and is yet to enter routine clinical practice or the guideline documents. A large number of other physiological metrics and assessment methods exist but are beyond the scope of the current focused summary but are reviewed by Perera et al. and Ghobrial et al. (Perera et al., 2023, Ghobrial et al., 2021).

1.9 Modelling physiology from anatomy

Attempting to model the coronary anatomy as a standard singular ‘typical’ artery would disregard considerable natural variation. Modelling must therefore capture patients’ specific variation and anomalies. Moreover, it is imperative that any potential model can also capture luminal narrowing, known as stenosis, because this is the principal cause of CAD. It is important to note that, in recent years, so-called model databases and statistical shape models of the coronaries and myocardium have been developed based upon cardiovascular imaging, which attempt to quantitatively assess cardiac anatomy and the relationship between that and pathophysiological dynamics (Medrano-Gracia et al., 2016b, Tekle, 2025, Costa, 2024).

Despite the strong evidence base and proven benefits of using physiology to guide coronary intervention, and its deferral, uptake of physiology has been low due to several factors, all based on the additional required effort, time and economic cost. Use of a pressure wire in the UK remains at around 8% of all PCI procedures (Mamas A, 2023). Therefore, over the last decade, researchers have investigated and developed computer-based models that aim to provide coronary physiology and therefore its associated benefits, without the drawbacks that have hampered its use so far. Computer modelling is software based and does not need an intracoronary wire, hyperemia induction and therefore, the associated cost, time and effort.

Computational modelling techniques that simulate coronary physiology are based on the laws of fluid dynamics and use computational fluid dynamics (CFD) methods (Lodi Rizzini et al., 2020, Biglino et al., 2017). Typically, models require anatomical information which comes from clinical imaging as the basis for reconstructing the anatomy of a coronary artery. Physiological CFD simulation, based on the governing equations of fluid dynamics (Navier-Stokes laws), is then used to generate metrics of intracoronary physiology similar to those derived from sensor-tipped wires during invasive coronary angiography. These computational modelling approaches negate the need for an invasive angioplasty wire which makes them more applicable, lower in cost and lower in risk. They can also generate novel data that traditional sensor-based analysis cannot (see wall sheer stress below). Like any model, however, they are not perfect. Models require several boundary conditions, which affect model accuracy. In the context of computed FFR, the main accuracy-limiting factor is the choice of the boundary condition that represents microvascular resistance (Morris et al., 2020a) which is variable in health and disease. Currently, in most models of coronary physiology, 3D coronary anatomy is reconstructed from 2D angiographic images (Morris et al., 2016), before CFD analysis is performed. This is the basis for all commercially available models of computed FFR. Aside from CT-derived FFR, all other models of FFR are therefore based on invasive coronary angiographic data as their main input. As described above, this lacks the high-resolution anatomical assessment that intravascular imaging techniques provide. Integration and fusion of multiple, complementary imaging modalities may increase the accuracy of the anatomical reconstruction, and this may enable higher fidelity and more accurate hemodynamic simulation results. Each imaging modality has certain strengths in capturing a particular feature of anatomy, along with certain weaknesses and shortfalls. Naturally, the imaging of the coronaries using a combination of these modalities would provide a wealth of anatomical information that no single modality can provide on its own. When using a combination of modalities, for

example angiography and OCT, clinicians then face a new challenge regarding how to relate all the anatomical information to reconstruct the anatomy, either in their 'minds' eye' or *in silico*, i.e. using computer software to co-register or reconstruct the different techniques. A clinician's experience is the key to the minds' eye reconstructions, but this is subjective and can be misleading.

Developments in cardiac imaging have allowed researchers to model and simulate several aspects of cardiac anatomy and physiology, from fluid flow to cardiac biomechanics and, possibly, disease progression, and delve deeper into intricate aspects such as 3D mesh structure (Krishnamurthy et al., 2016, Thondapu et al., 2016, Morris et al., 2016). More specifically, advancements in coronary imaging and 3D modelling have allowed researchers to develop CFD-based models which simulate and predict blood pressure, wall shear stress (WSS), flow and velocity, along in silico geometries derived from clinical imaging patient-specific proximal, distal and along the stenotic region are predicted. This allows indices like FFR to be simulated and predicted, thus providing the benefits of FFR without involving the factors that limit its use. FFR only predicts the percentage flow changes in a single coronary artery; however, it still does not provide information on how absolute flow changes. When FFR is computed using the laws of haemodynamics, it is known as virtual-FFR (vFFR). Morris et al. developed the first model of vFFR in 2013. They described a close correlation between their CFD-derived vFFR and the invasive FFR measurements (R=0.84) (Morris et al., 2013). This initial method took over 24 hours per case for CFD computation, highlighting the absence of a time-efficient solution. Over the years, several software suites such as VIRTUheart by The University of Sheffield (Morris et al., 2013), CAAS by Siemens Healthcare (Stähli et al., 2019) and others by MedisMedical Imaging (Fearon et al., 2019) and CathWorks (Masdjedi et al., 2020) combined the knowledge on the anatomy, physiology and produced anatomically representative 3D models to simulate coronary physiology. Although the systems mentioned above were all developed for coronary simulations, the differences between the results of their modelling was previously reviewed (Ghobrial, 2021), which highlights the impact of the underlying assumptions and model personalization on the simulated physiology. FFR has also been modelled from CTCA-derived reconstructions (Celeng et al., 2019). This has improved the specificity and negative predictive value of CT and enhanced its ability to act as an outpatient-based gatekeeper for CA (Curzen et al., 2021) and led to a 1B indication in the ESC guidelines for investigating those at low-moderate probability of CAD (Vrints et al., 2024).

Over the last decade, almost all the modelling research and development effort has been directed towards modelling FFR. However, more recently, software tools that predict absolute coronary blood flow, microvascular resistance and coronary flow reserve have also been described (Morris et al., 2020b, Marin et al., 2024). Analogous to the invasive metrics described above, this work may extend the applicability of computational modelled physiology to the assessment of microvascular coronary physiology.

The latest European Society of Cardiology guidelines have now endorsed computed physiology (Vrints et al., 2024) with class 1, level of evidence B, recommendation, to assess intermediate lesions. The task force highlights the 'unique advantage' of providing physiological assessment, including the intracoronary pressure distribution along artery, without the need for a pressure wire. The guidelines stop short recommending computed FFR (vFFR) as comparable with invasive FFR but do suggest it is superior to standard angiography-guided revascularisation. These statements are based on the results of the FAVOR III China study which reported reduced MI and ischaemia-driven revascularisation in the QFR-guided arm, compared with standard angiographic guidance (Song et al., 2022).

1.10 Wall shear stress

WSS is another important haemodynamic phenomenon. The frictional stresses that flowing blood impose on the luminal surface of a vessel influence atherosclerotic plaque development and composition (Alexander et al., 2020). These mechanical forces, their magnitude, location, and direction can predict lesion development and plaque rupture (Kwak et al., 2014). The effects of WSS are more important in areas where flow is disturbed by the presence of stents or bypass graft surgery due to the complex flow patterns created (Davies, 2009). Accurately modelling WSS requires accurate internal luminal morphological information. This can be provided by OCT, but not by angiography. Work on WSS was published applying CFD-based analyses including and excluding side vessels. Wellnhofer et al. reported up to 12 Pascals difference in WSS and 78.7% volume flow change in the main vessel between such approaches, emphasising the importance of accounting for bifurcations and significant side-branches in physiological flow modelling (Wellnhofer et al., 2010).

Currently, no single system that fuses CA and OCT to produce 3D reconstructions of targeted arteries and their side-branches and performs CFD analyses in clinically tractable time periods

is available. WSS analyses rely on 3D modelling because it is impossible to measure *in vivo*. Such modelling techniques and work are limited to research settings and are not assessed in routine clinical practice. Tools that can accurately model WSS are likely to help clinicians and the cardiovascular research community to better understand the interaction between WSS and atherosclerotic plaque progression, erosion and rupture, potentially leading to the ability to manipulate these effects and reduce current events in patients with coronary disease. Such work depends on detailed, accurate, 3D, anatomical models that do not currently exist. Ideally, these would incorporate the detailed luminal information provided by OCT and combine this with the 3D centreline data provided by the invasively obtained angiogram. Such tools would be very advantageous in the field of WSS simulation.

1.11 Summary, unmet clinical need and ambition for this thesis

IHD remains the leading cause of death globally. One of the main treatments of IHD is revascularization with PCI. The decision as to whether to perform PCI or not depends on the results of anatomical and physiological tests. When PCI is deemed to be appropriate, these same investigations also guide the optimal strategy, extent of PCI, the requirement for any adjunctive therapies and even adjudicate the success of the result. A wide and diverse range of investigations are available, all with their own strengths and limitations. No single test provides a truly comprehensive assessment. During invasive CA, contemporary international guidelines now endorse adjunctive (i.e. done at the same time as coronary angiography) physiological lesion assessment (1A indication) to determine the appropriateness of PCI, *and* intravascular imaging to guide PCI strategy in bifurcation, long or complex disease (1A indication). Currently, this requires an invasive angiogram, plus two separate adjunctive assessments, with their own separate catheters, extended procedural time and considerable associated cost.

No current method provides physiology and high-resolution anatomical detail in a single test. Such a test would be highly desirable and may improve patient assessment and outcomes whilst reducing procedural time, cost and effort. The ambition of this PhD project was therefore, to develop a prototype model, capable of incorporating and *fusing* imaging data from invasive angiography and OCT, and that can combine this with 3D CFD modelling to provide a truly comprehensive assessment of coronary arterial circulation with unparalleled high-resolution 3D anatomical *and* physiological data all in a single method. Such a model has the potential to advance patient assessment in four novel ways.

- First, it would provide guideline-indicated physiology and anatomical data at reduced time, effort and cost, in a single modality.
- Second, it would, in principle, also resolve some of the limitations of the current techniques when they are used independently. For example, OCT provides very high-resolution luminal anatomical data but can only appreciate the vessel as a perfectly straight tube. Angiography represents the 3D course of coronary arteries but cannot provide detailed luminal anatomy. By fusing the two together, one would anticipate a tool that provides the best of both modalities, without the limitations of either.
- Third, by fusing angiography-derived vessel data with OCT-derived luminal imaging from different branches, it is, in theory, possible to also generate a 3D branching tree that can accurately model detailed bifurcation anatomy. This is not currently possible. Given the 1A indication for bifurcation intervention, this could be highly desirable pre- and post-bifurcation PCI.
- Fourth, computed physiology has been shown to offer additional value and extended applicability assessing microvascular physiology, in the context of ANOCA, also now indicated in international guidelines (1B). If this could also be integrated into such a model, this would only extend applicability further. Modelling of WSS would also be improved because this relies heavily on accurate 3D coronary models and so this would be of potential interest to researchers in this area.

The aim of this PhD project was therefore to develop and validate an image analysis protocol that fuses CA and OCT to accurately reconstruct coronary anatomy, including bifurcations and branching trees, all within a predictive CFD-based model of coronary physiology that can predict clinically relevant patient-specific hemodynamics.

Chapter Two:

Thesis Aims, Hypothesis, Objectives and Outline

2.1 Thesis aims

The clinical motivation and potential benefits of the work in this thesis are outlined in Chapter one. The overarching aim was to develop a prototype image analysis protocol that fuses complementary CA and OCT data to accurately reconstruct branched 3D coronary anatomy within a CFD model that can be used to simulate and predict clinically relevant hemodynamic metrics (Figure 2.1). The aim was, therefore, ambitious. Accordingly, the aim was not to produce a fully optimised and validated 'finished product'. Even within the commercial sector, this would take a research and development team several years to complete. Rather, the aim was to develop a prototype platform with preliminary validation against existing models and clinical data.

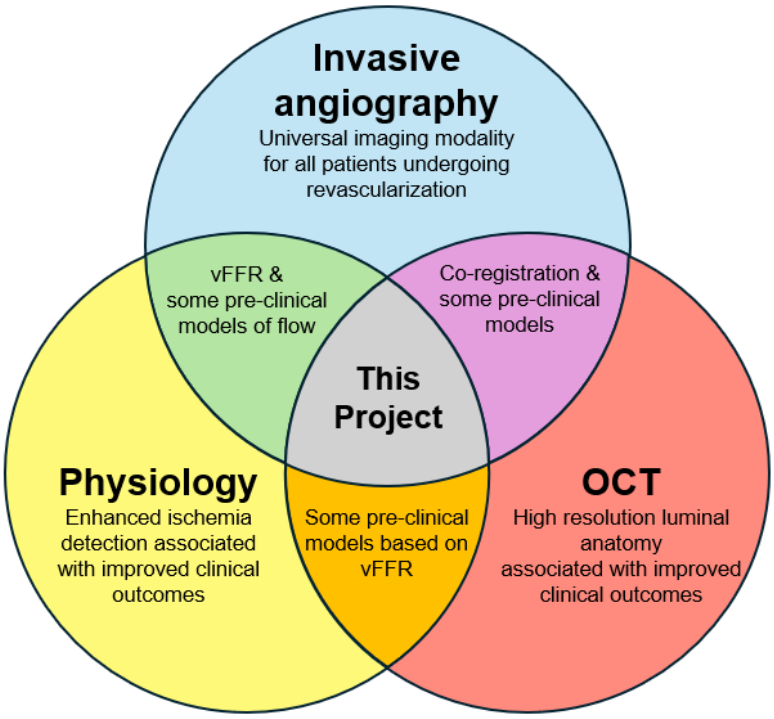

Figure 2.1. A Venn diagram that illustrates the benefits of coronary intravascular imaging, invasive angiographic imaging and physiological assessment, how they have been integrated and fused thus far, and how the current project attempts to bring the benefits of all these methods together in a single platform.

2.2 Hypothesis

Complementary CA and OCT data can be fused together to produce representative, 3D, geometric, in silico coronary models suitable for physiological CFD analysis.

2.3 Thesis outline and objectives

As presented in Chapter one, coronary arterial 3D reconstruction is described in the literature. However, relatively few models have entered clinical practice and those that have are predominantly simple, single lumen models, from a single imaging modality. Some methods have explored combining different imaging modalities and some have attempted to fuse CA and OCT data. Each method has approached this problem differently and each has relied on certain assumptions. In this thesis, I build on these methods, aim to minimise assumptions, and develop novel methods and approaches to solving this complex imaging problem, not least, in capturing the bifurcation region accurately. To accomplish the above aims, a number of technical challenges must be overcome. These challenges represent the objectives of this thesis as summarised in this thesis outline.

Chapter three outlines the process of vessel segmentation from CA, from image acquisition and choice to the 3D modelling of single branches and presents the existing segmentation tool and how its output generates the needed data for the novel workflow, with an in-depth description of its underlying mathematical procedures. Chapter three also discusses torsion compensation in the context of Frenet frames representation of the 3D CA-derived vessel centrelines, which is essential when it comes to OCT lumen orientation and positioning onto CA centrelines

Chapter four presents the process of 2D OCT lumen segmentation and the type and quality of data needed to perform reconstructions, with a list of requirements that must be met so the data is usable by the OCT segmentation software. It presents the OCT-based optimisation protocol for lumen orientation on a straight vessel centreline. The methodology that robustly fuses OCT and CA information longitudinally and finds the correspondence between the anatomical information from OCT and CA is presented. Chapter four also discusses potential of the interpretation of OCT data in terms of disease prognosis/diagnosis, with a focus on lumen ellipticity.

Chapter five analyses, in detail, the nature of the data extracted using OCT. It discusses inherent challenges due to the nature of OCT acquisition, and their impact on clinical diagnosis and modelling and compares CA and OCT anatomical data. Chapter five also presents a novel methodology that uses lumen ellipticity to identify stenosed regions of vessels.

Chapter six demonstrates the methodology that robustly joins the centrelines of a main vessel and one or more of its side branches whilst maintaining the integrity of the bifurcation, to produce a branched, 3D, arterial centreline model. Chapter six also shows the fusion of the luminal (vessel surface) edges of a main branch and side branch whilst maintaining the integrity of the bifurcation anatomy and the surface mesh, to produce a branched, 3D, arterial surface mesh.

Chapter seven applies CFD simulation techniques to the developed single and branching tree coronary models and derive the vessel outlet resistance. It also presents the CFD results modelled from combined angiography and OCT. It includes comparisons with pressure wire data obtained in the catheterization laboratory and from angiography-only reconstructions.

Chapter eight analyses the developed process and results when compared to relevant work in the literature, and the assumptions and their impact on results to bring awareness to limitations of any of the processes described. It revisits research objectives and draws conclusions according to the results, verification and analyses while reflecting on project hypothesis based on the testing and analysis. Chapter eight also includes the challenges and uncertainties of the results and work, concluding with a list of suggestions for future work if this project is continued.

Chapter Three:

Reconstruction of Single Coronary Branches from Angiography

3.1 CA for 3D coronary reconstruction

In this chapter, single vessel reconstruction from CA will be described and explored. Single vessel modelling is based on the software developed by The Mathematical Modelling in Medicine Group at The University of Sheffield, called VIRTUheart (Solanki et al., 2021, Morris et al., 2013). The fundamentals of image acquisition, projection angle choice and image segmentation will be discussed. Novel methods presented build on the existing VIRTUheart suite segmentation tool which is also discussed in this chapter. Three significant novel developments to the VIRTUheart segmentation tool are presented here, namely, using the Frenet Frame to describe the vessel centreline and compensate for torsion, combining single vessel centrelines to create branching centreline models ready for 3D bifurcation reconstruction, and the back-projection of the CA-derived lumens onto the original angiograms. The former is essential since OCT-derived lumens are irregular thus, the orientation of the normal vectors influences the orientation of the OCT lumens, hence, the shape of the vessel. The latter is for clinical use and decision making, whereby clinicians will be able to locate specific regions in the context of the CA (i.e. co-registration). All in all, this the work in this chapter prepares the CA-derived anatomical information for the integration of the OCT lumens.

Traditionally, 3D coronary reconstruction has been derived from 2D projected (silhouette) images acquired by x-ray-based CA. Although these reconstructions, at the time, were a significant step forward in the coronary imaging and reconstruction field, they relied on methods that significantly limit the accuracy of the resultant 3D geometry. For a coronary artery to be imaged by CA, the arteries must be filled with radio-opaque contrast medium. This contrast marks the unobstructed path that blood takes proximally to distally in the artery. If the coronary artery is regarded as a series of consecutive cross-sections, in healthy areas of the artery, the radio-opaque contrast medium is expected to fill the full cross-section up to the arterial wall. This would show up on the angiogram as a darker grey colour, marking where blood flow is present. On the other hand, if the artery is diseased, with plaque obstructing blood flow, the radio opaque contrast medium will not be able to fill the whole cross-section, only the areas not blocked by disease. Therefore, on the angiograms, this diseased section of the artery will appear as a smaller dark grey section, marking obstructed blood flow.

The quality of the anatomical information obtained from CA depends on the quality of the angiogram and the choice of projection it was taken from. Factors that affect image quality include:

- Appropriate projection angles for the vessel being imaged, including the proximal, stenotic and distal segments and magnification of vessels (Tafti and Byerly, 2025),
- Image resolution, determined by the imaging system hardware
- Radiation exposure (kV settings; low, medium or high), kept as low as reasonably achievable which may facilitate 2D image interpretation but not necessarily 3D reconstruction (Lyu et al., 2020).
- Opacification of the artery (how well the artery is filled with contrast),
- Arterial foreshortening: impossible to reduce this to zero for a length of coronary artery (Green et al., 2005a, Pederzani et al., 2022)
- Motion, including patient, cardiac pulsatility and breathing (Zir et al., 1976a, Galbraith et al., 1978b, Yamamoto et al., 2009).

The vessels of the coronary circulation are wrapped around the heart, so are curved in some areas, tortuous in others, and a combination of the two in many instances. Choosing an 'appropriate' projection that captures the anatomy of a specific coronary artery but minimises all of the above limitations, can be challenging. There will always be an aspect of the 3D anatomy that is not fully represented in the 2D image. The coronary vessels are curved and tortuous, therefore, the impact on the apparent length, also known as foreshortening, and on the apparent shape is significant, and even more so when it comes to computational fluid dynamic techniques. Imaging a curved section of the artery perpendicular to the plane of curvature may cause the curved section to appear straight and much shorter than its real length, which is a misrepresentation of the anatomy and can have a deleterious clinical impact if the angiogram is being used for PCI planning. This must be understood and accounted for in any 3D reconstruction method. It is also important to note that current techniques derive 3D anatomy from paired CA projections and so the best that can be achieved is a circular or elliptical, with assumptions, reconstructions. Thus, any eccentricity in the artery of plaque will be eliminated in the reconstruction. Given that no coronary artery is stenosed in a perfectly concentric fashion, all CA-derived reconstructions (which all produce axisymmetric reconstructions) will be inaccurate to some extent.

3.2 Modelling of single branches from CA

3.2.1 CA image acquisition

In the coming sections, the theory behind the development of the segmentation procedure using paired angiogram images to extract the 3D centreline and grey-scale vessel radii is described. Segmentation relies on a pair of angiographic image projections, acquired at least 25, but preferably thirty degrees apart. During acquisition, the patient lies supine on the table in the catheterization laboratory and the C-arm is rotated in two axes (cranial to caudal and left to right) to view the arteries from the anterior aspect from any number of straight or oblique angles, as shown in Figure 3.1. The projections are chosen by the radiographer and the clinician, depending on the vessel to be imaged and individual patient anatomy.

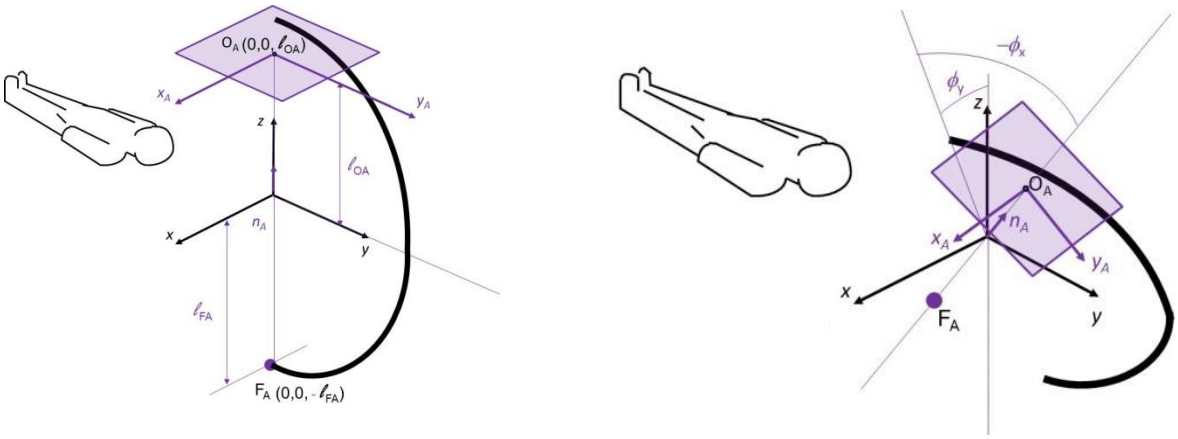

Figure 3.1. The image acquisition procedure. Patient is on the table in the catheterisation lab, and the C-arm, holding the x-ray source and detector units is rotated both right to left and top to bottom, to acquire images from two distinct views.

3.2.2 Projecting the 3D centreline

After image acquisition, the angiogram (Digital Imaging and Communications in Medicine) DICOM data are uploaded into the VIRTUheart software which then uses epipolar geometry to relate the anatomical data between both projections (Frison, 2018b). A 3D object, like the coronary artery, that is being examined from different angles and is being projected onto different projection planes, according to the rotation of the C-arm, which holds an x-ray source on one end and a detector plane on the other, will naturally look slightly different in each

projection. It is in this instance that epipolar geometry, also known as ‘stereo vision’, is useful, as it relates the 2D information in each projection to the original 3D object.

The 3D arterial centreline looks like that shown in Figure 3.2. It is made of a series of 3D points, and has a normal, tangent and binormal vector at every point that fully describes the centreline.

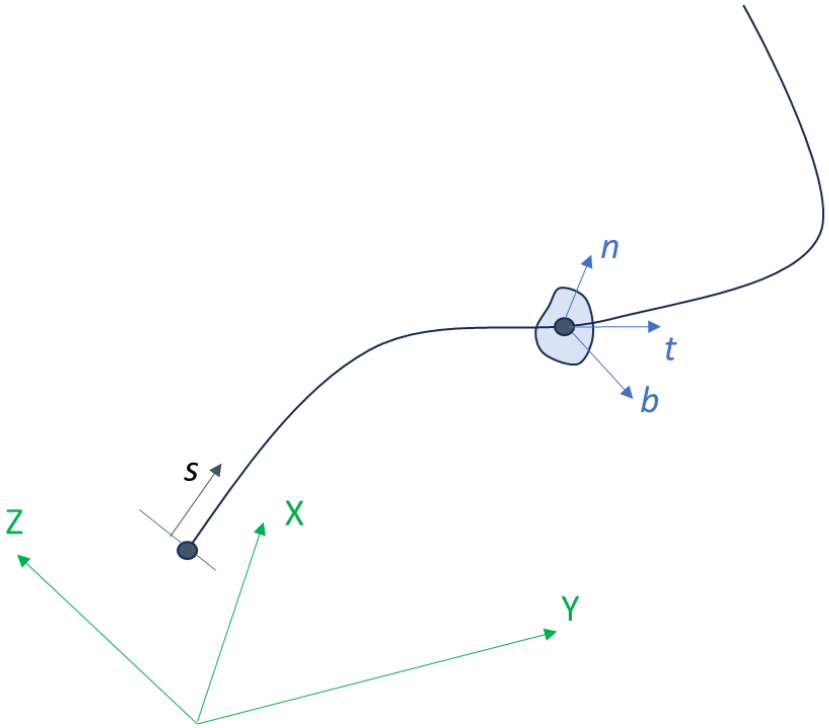

Figure 3.2. The 3D centreline of a coronary artery. It is fully described by a set of 3D points (X, Y, Z), and a set of normal (n), tangent (t) and binormal (b) vectors at every point. s is the cumulative distance (s) along the centreline.

The discrete representation of the centreline is defined by the sequence of points $\{x; y; z\}_G$ where G indicates that these are global co-ordinates, using the convention illustrated in Figure 3.1. The projection is along a line from the source through each point onto the projection plane. To compute the projection requires the co-ordinates in a co-ordinate system in which the local z axis passes through the source and is orthogonal to the projection plane. These co-ordinates are computed using a rotation matrix R_{GA} that is determined by the two degrees of freedom of the C-arm (rotation about x and about y). The angles of rotation of the C-arm describe the rotation matrices in Equation 3.1-3.3.

$$R_y = \begin{bmatrix} \cos\phi_y & 0 & \sin\phi_y \\ 0 & 1 & 0 \\ -\sin\phi_y & 0 & \cos\phi_y \end{bmatrix}$$

Equation 3.1. Rotation matrix describing the LAO/RAO rotation.

$$R_x = \begin{bmatrix} 1 & 0 & 0 \\ 0 & \cos\phi_x & -\sin\phi_x \\ 0 & \sin\phi_x & \cos\phi_x \end{bmatrix}$$

Equation 3.2. Rotation matrix describing the cranial/caudal rotation.

$$[R]_{GA} = [R_y][R_x]$$

Equation 3.3. Rotation matrix from the global co-ordinate system to the local co-ordinate system of frame A.

R_y is the LAO/RAO rotation matrix due to rotations of ϕ_y magnitude and R_x is the Cranial/Caudal rotation matrix due to rotations of ϕ_x magnitude, $[R]_{GA}$ is the rotation matrix from global co-ordinates to co-ordinates in frame A.

The points on the centreline and the tangent, normal and binormal vectors can be projected into angiographic image planes. For any point in 3D, the co-ordinates in the frame defined by the rotation angles of the C-arm are computed (Equation 3.4):

$$\begin{Bmatrix} x_A \\ y_A \\ z_A \end{Bmatrix} = [R]_{GA} \begin{Bmatrix} x_G \\ y_G \\ z_G \end{Bmatrix}$$

Equation 3.4. Computing the 3D coordinates of a point in the local frame A from the global frame.

where x_G, y_G and z_G are the 3D coordinates of a point in the global coordinate system, and x_A, y_A and z_A are the 3D coordinates in the local coordinate system of frame A.

The 2D co-ordinates of the projection of the points into the image plane are (Equation 3.5):

$$\begin{Bmatrix} x_{AP} \\ y_{AP} \end{Bmatrix} = \frac{LSD}{LF + z_A} \begin{Bmatrix} x_A \\ y_A \end{Bmatrix}$$

Equation 3.5. Computing the projected 2D coordinates of a point in the local frame A.

where x_{AP} and y_{AP} are the 2D coordinates of the point in the projection A, LSD is the distance from course to detector, and LF is the distance from patient to source.

In this way, the points that make up the 3D centreline of the coronary artery are mapped from 3D to 2D and vice versa.

3.2.3 Representing the centreline using the Frenet frame

Now that the 3D points that make up the centreline are characterised, it is time to describe the backbone of the 3D reconstruction, that is the centreline. This section provides a deeper look into how the normal, tangent and binormal vectors, which fully describe a 3D centreline are computed. The Frenet formulae, which describe the derivatives of the normal, tangents and binormals of a 3D curve, in terms of each other, are an addition to the current version of the VIRTUheart Suite and have been used previously to describe curved coronary vessel centrelines (Fallavollita and Cheriet, 2008, Csippa et al., 2021, Wang et al., 2024). This is because radius values obtained from angiography allow the construction of uniform circular contours, the orientation of which are not dependent on the tangent, normal and binormals as the irregular contours derived from OCT are. The classical Frenet-Serret formulas determine the unit tangent, normal and binormal vectors at any point on the curve (Frenet, 1852). The tangent vector is defined as $T_s = \left\{\frac{dx}{ds}\right\}$, where ds is a segment of the total length S of the curve and dx is an infinitesimal distance on the curve, and has unit length, $|T_s| = \left|\frac{dx}{ds}\right| = \frac{1}{ds}|dx| = 1$, and is therefore also the unit tangent vector:

$$\hat{T} = \left\{\frac{dx}{ds}\right\}$$

The remaining relationships between the Frenet vectors and the curvature (κ) and torsion (τ) of the curve are given, in matrix notation, by Equation 3.6:

$$\begin{Bmatrix} \frac{d\hat{T}}{ds} \\ \frac{d\hat{N}}{ds} \\ \frac{d\hat{B}}{ds} \end{Bmatrix} = \begin{bmatrix} 0 & \kappa & 0 \\ -\kappa & 0 & \tau \\ 0 & -\tau & 0 \end{bmatrix} \begin{Bmatrix} \hat{T} \\ \hat{N} \\ \hat{B} \end{Bmatrix}$$

Equation 3.6. The Frenet vectors (tangent, normal and binormal)

Using the discrete representation of the centreline and if the j^{th} point on the centreline has co-ordinates $\{ X(j); Y(j); Z(j)\}$ and taking a first order forward-difference approximation, a vector pointing along the local tangent vector at point *j* is:

$$T(j) = \begin{Bmatrix} X(j+1) - X(j) \\ Y(j+1) - Y(j) \\ Z(j+1) - Z(j) \end{Bmatrix}$$

The length of this vector, $ds(j)$, is:

$$ds(j) = \sqrt{\big(X(j+1) - X(j)\big)^2 + \big(Y(j+1) - Y(j)\big)^2 + \big(Z(j+1) - Z(j)\big)^2}$$

and so, the unit normal tangent, $\hat{T}(j)$, is (Equation 3.7):

$$\hat{T}(j) = \frac{1}{ds(j)} \begin{Bmatrix} X(j+1) - X(j) \\ Y(j+1) - Y(j) \\ Z(j+1) - Z(j) \end{Bmatrix}$$

Equation 3.7. The tangent vector

Then from the first equation of the Frenet-Serret formula, again using a first order forward-difference representation (Equation 3.8):

$$\frac{d\hat{T}}{ds}(j) = \kappa(j) \cdot \hat{N}(j)$$

or

$$\hat{N}(j) = \frac{1}{\kappa(j)} \frac{d\hat{T}}{ds} = \frac{1}{\kappa(j)} \cdot \frac{1}{ds(j)} \{\hat{T}(j+1) - \hat{T}(j)\}$$

Equation 3.8. The normal vector

$\kappa(j)$, the curvature at point *j*, is computed so that $\hat{N}(j)$ is a unit vector

Note that this expression will always yield an $\widehat{N}$ vector that points towards the centre of curvature, and so for a planar curve there will be a flipping of the normal (through 180 degrees) at a point of inflection, and thus a large apparent torsion at the point of inflection even though the curve is planar.

Then the binormal vector is the cross-product of the tangent vector with the normal vector (Equation 3.9):

$$\hat{B}(j) = \hat{T}(j) \times \hat{N}(j)$$

Equation 3.9. The binormal vector

The torsion, $\tau(j)$, is the rate of rotation of the binormal vector about the tangent vector. The angle between $\hat{B}(j+1)$ and $\hat{B}(j)$ is determined from the cross product and the torsion is the determined by dividing this angle by the length of this section of the curve (Equation 3.10).

$$\tau(j) = \frac{sin^{-1}\left(\hat{B}(j) \times \hat{B}(j+1)\right)}{ds}$$

Equation 3.10. Torsion

Note that the use of the cross product rather than the scalar product identifies the sign of the rotation. Rotation angles of greater than ninety degrees are identified by the sign of the scalar product. The angle of rotation of the tangent vector, α, can be computed from the scalar product of the tangent vector at the given point on the curve with the tangent vector at the previous point, see Figure 3.3 and Equation 3.11.

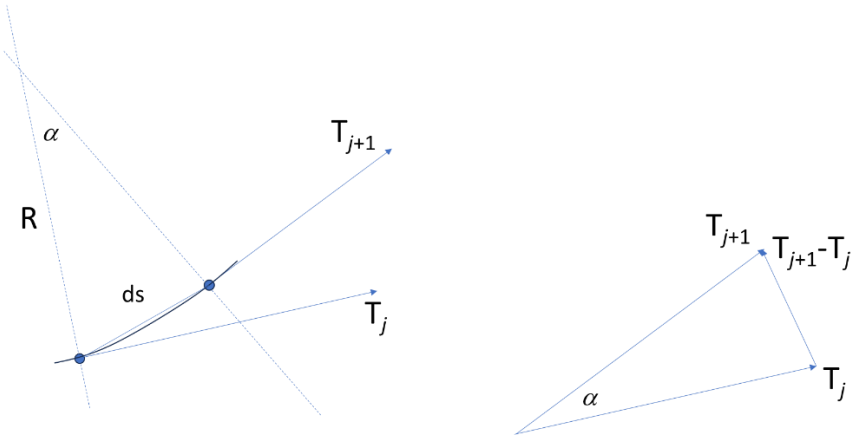

Figure 3.3. Rotation of the tangent vector. T_{i+1} and T_j are the tangent vectors at the point on the curve, and the point before it, respectively. R is the radius of the circle formed by the two points and α is the angle of rotation.

$$\alpha(j) = cos^{-1}\left(\hat{T}(j) \cdot \hat{T}(j-1)\right)$$

Equation 3.11. The angle of rotation of the tangent vector

Over every increment ds along the centreline, the cross section rotates about the binormal axis (the curvature is in the TN plane). The rotation by an angle α about the $\hat{B}$ axis is described by the general rotation matrix:

$$Rot3D = \begin{bmatrix} cos\alpha + \hat{B}_x{}^2(1-cos\alpha) & \hat{B}_x\hat{B}_y(1-cos\alpha) - \hat{B}_z sin\alpha & \hat{B}_x\hat{B}_z(1-cos\alpha) + \hat{B}_y sin\alpha \\ \hat{B}_x\hat{B}_y(1-cos\alpha) + \hat{B}_z sin\alpha & cos\alpha + \hat{B}_y{}^2(1-cos\alpha) & \hat{B}_y\hat{B}_z(1-cos\alpha) - \hat{B}_x sin\alpha \\ \hat{B}_x\hat{B}_z(1-cos\alpha) - \hat{B}_y sin\alpha & \hat{B}_y\hat{B}_z(1-cos\alpha) + \hat{B}_x sin\alpha & cos\alpha + \hat{B}_z{}^2(1-cos\alpha) \end{bmatrix}$$

Figure 3.4 demonstrates the impact of Frenet frame for torsion compensation on contour positioning. The blue contours are those positioned using the normal, binormals and tangents pre torsion compensation, and the red are those post. The red contours show a more vessel-appropriate fit, especially in areas of increased tortuosity and curvature.

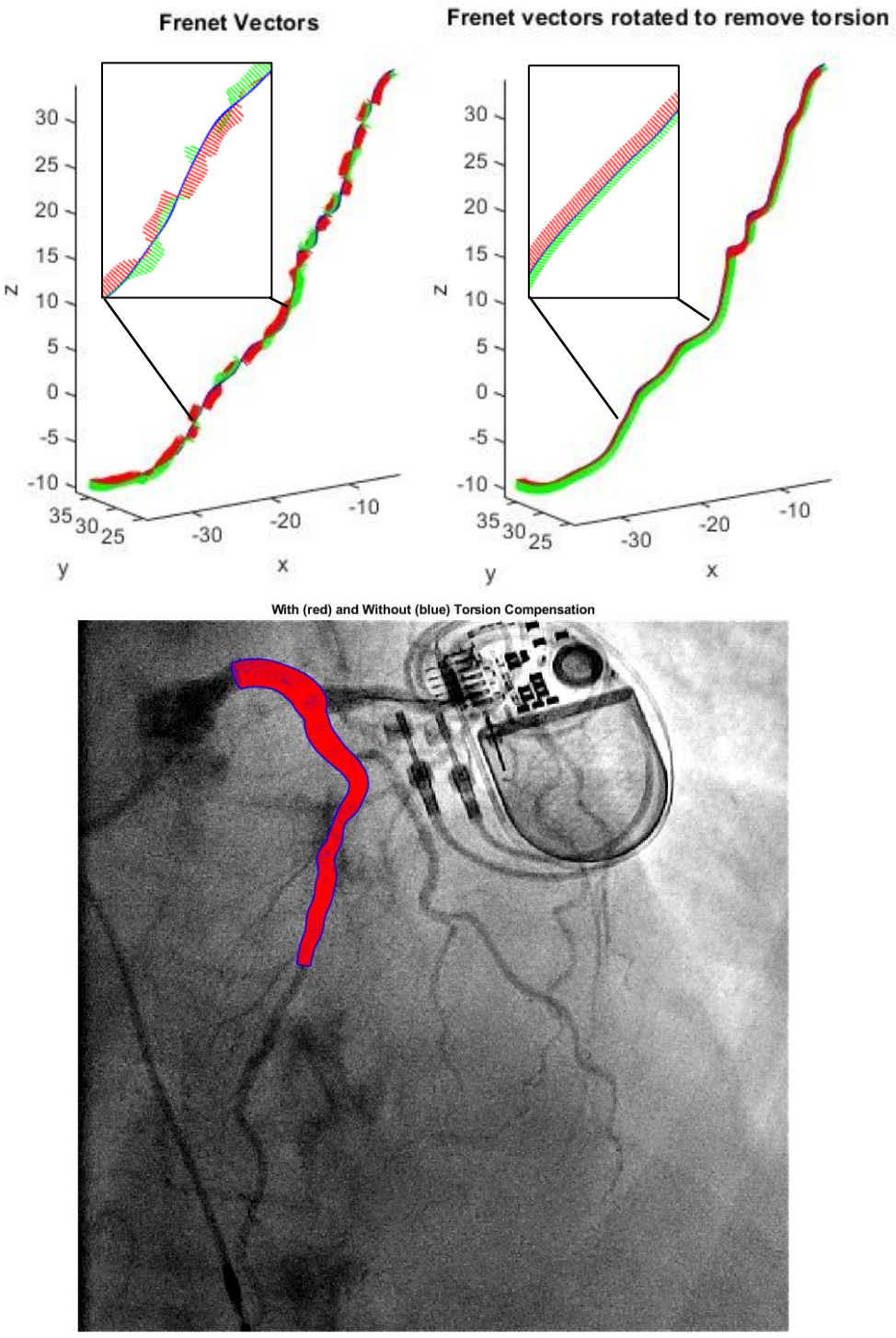

Figure 3.4. (top) Centreline with tangent, normal and binormal vectors for a typical artery before (left) and after (right) using the Frenet frame to compensate for torsion. The figure on the top right exhibits more consistency of its vectors. (bottom) CA-derived vessel contours projected back onto angiogram for illustration of the segmented section. This can be a clinically useful tool, especially when the angiogram image is lacking sufficient resolution.

3.3 Processing the angiograms

The angiograms are 2D silhouette images that are in grey scale. The only way to determine the radius of the vessel at every centreline point, is to interrogate this grey scale map. From the angiogram shown in Figure 3.4, it can be said that between what is considered as 'vessel' and what is 'background' there is a steep, sudden change in the grey scale value of the pixels that make up this area of the angiogram. The VIRTUheart segmentation tool follows the following procedure for segmentation (Solanki et al., 2021, Frison, 2018b):

1. Performs image processing operations to sharpen the image,
2. Computes the 'vesselness' of each pixel (the likelihood that it is a pixel within a vessel). This is based on the Hessian matrix at each pixel. The filter used is based on that published by Jerman (Jerman et al., 2015).
3. Binarizes the image using a threshold on the vesselness,
4. Skeletonises the image so that it becomes a map of vessel centrelines,
5. Extracts the shortest path along the vessel centreline between two user-selected points,
6. Computes the distance transform at points on the centreline using the binarized image (obtained in 3) to identify the projected radius corresponding to each centreline point. The distance transform is a measure, usually applied to binary images, of the distance of a point or pixel to a chosen boundary. This is usually produced in the form of a matrix or image, that contains distance values, instead of intensity values. In the VIRTUheart Suite, the chosen boundary is the vessel edge, and the projected radius is computed as the distance from this edge to the centreline point.
7. Expresses the 2D centreline as

   $\{x\}_A = f(t)$ and $\{x\}_B = f(u)$

   on the two projections. This produces a continuous representation of the centreline, that is used in step 9 below,

8. Uses the camera angles and C-arm geometry to project each centreline point in projection A onto projection B (each point in A becomes an epipolar line in B),

9. Computes the intersection of the epipolar line in B with the centreline in B,
10. Computes the 3D co-ordinates of each point from the 2D co-ordinates in each projection,
11. Repeats steps 8 to 10 projecting points on B onto A, and
12. Assembles the 3D centreline and construct a circular-section lumen by averaging the radii from projections A and B, compensating for the magnification factor.

When OCT anatomical data is available, step 12 replaces the circular lumens with OCT cross-sections.

3.4 Process for single vessel reconstruction

Although CA is a useful imaging modality when informing about the curvature of the vessel in 3D, its images lack luminal detail relative to intravascular techniques. Accordingly, a modeller's best estimation with regards to the shape of the coronary lumens using data only from CA is that the lumens are circular. Although, in principle, multiple projections might be taken in the clinic, in general it is often difficult to find even two in which vessels of interest are clearly visible. The process for computing the 3D centreline therefore uses the minimum two projections. The cross-section lies in a plane normal to the 3D centreline at each point, but even an ellipse has three degrees of freedom (the major diameter, the minor diameter and the angle of orientation) and so it is not possible, from two projections, to identify a unique ellipse that is consistent with two projections. The simplest compromise is to assume that the vessel has a circular cross-section that is the average of those from the two projections. With OCT, of course, this is not the case as the lumens are images from inside the vessel. In this stage, the Frenet-compensated frame for the 3D vessel centreline representation was coded and implemented ready for both the CA-derived circular lumens and the OCT lumens.

Circular lumens are created using the radii obtained from the segmentation. Every circle is made up of 48 points which are drawn by creating a point every $2*\pi/48$ of angle at the specific radius at desired centreline point (Figure 3.5), from the origin of the co-ordinate system, then shifted to the specific centreline point as shown in Equation 3.12.

$$\text{circle point} = \text{radius(s)} * \cos(\theta) * \text{B} + \sin(\theta) * \text{N} + \begin{Bmatrix} x_O \\ y_O \\ z_O \end{Bmatrix}_G$$

Equation 3.12. Defining the points that make up the circles representing the angiogram-derived vessel wall.

where radius(s) is the radius of the vessel at point s and angle θ.

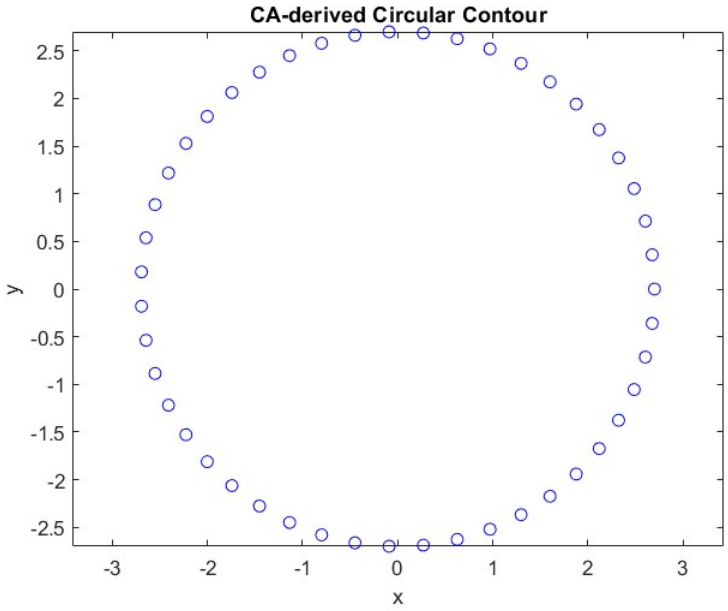

Figure 3.5. Illustration of the definition of the idealised circles that define the lumens, according to CA.

When the circles are created and appropriately positioned on the centreline, a surface mesh is constructed as a final step to the reconstruction protocol, prior to CFD. This surface mesh is made up of forward (green) and backward (orange) triangulations that connect consecutive circles, as shown in Figure 3.6. The full triangulations, which are defined such that the surface normal vectors are consistently orientated, in this case pointing outwards, are shown in Figure 3.7.

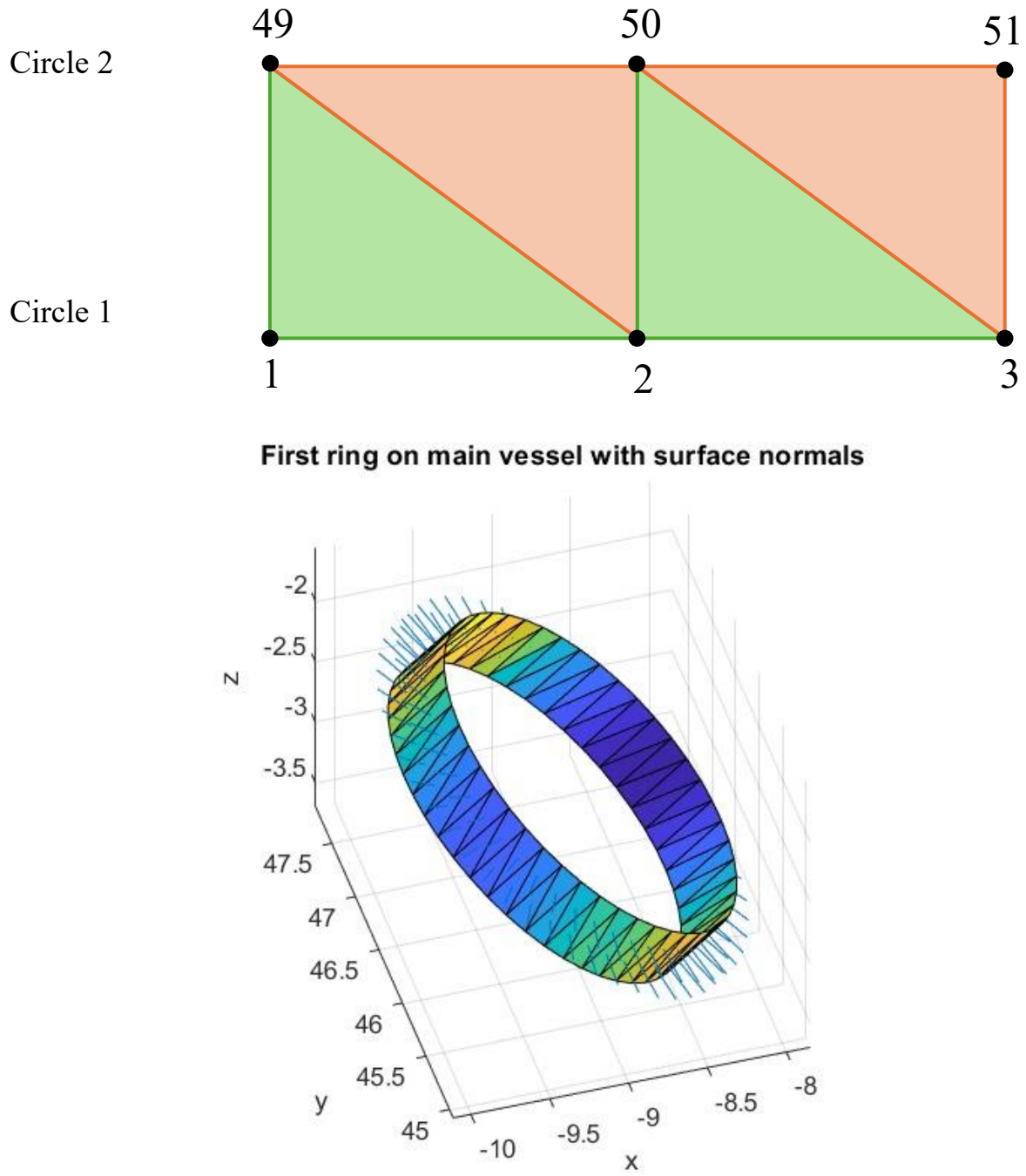

Figure 3.6. (Top) An illustration of the forward (green) and backward (orange) triangulations joining consecutive circles that make up the surface mesh and (Bottom) The first ring joining the first two circles on the main vessel with the directions of their normal vectors.

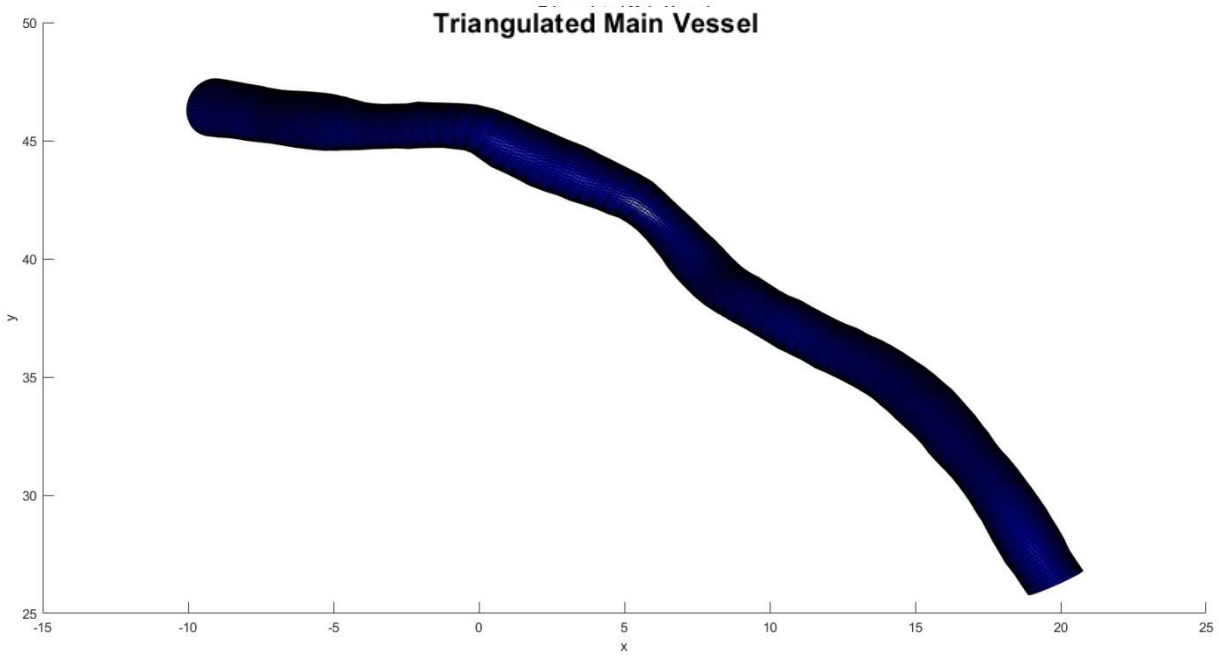

Figure 3.7. Triangulated surface of the main vessel.

3.5 Summary

The work done in this chapter demonstrates:

1. How the existing VIRTUheart segmentation tool extracts the 3D points that make up the CA centreline and the radii from the greyscale angiograms, which are used to create circles that represent the vessel wall at the centreline points,
2. How the 3D vessel centrelines are compensated for torsion using the implemented Frenet frame method, which is an essential step prior to OCT integration/fusion for appropriate lumen orientation,
3. The developed meshing protocol, whereby the cross-sectional luminal circles are connected using triangles which form the luminal vessel surface, i.e. the 3D reconstruction of the coronary vessel.

3.6 Clinical data in this thesis

The ultimate aim of the work in this thesis was to perform a primary, proof-of-concept validation of the developed reconstruction method (Chapter seven). This required clinical data collection. The same clinical data were used in the coming chapters, to help at various stages of reconstruction method development. For that reason, a description of the clinical data follows in Tables 3.1 and 3.2 which outline the patient-specific and vessel-specific data relating to the twenty cases reconstructed using the protocol presented in this chapter, respectively. Clinical cases were from patients with stable coronary syndrome, undergoing elective invasive coronary angiography with a view to PCI. The inclusion criteria for this study were:

- Age >18 years,
- Any coronary lesion suitable for pressure wire analysis and OCT imaging. For bifurcation lesions: amenable to a provisional main vessel treatment strategy with main vessel diameter of 2.5 mm and a side branch diameter of 2 mm based on operator visual estimation,
- Any patient with stable angina, silent ischaemia, unstable angina or NSTEMI (Non-ST-elevation myocardial infarction) and
- Informed consent.

The exclusion criteria were:

- Cardiogenic shock,
- LVEF (Left ventricular ejection fraction) <30%,
- STEMI (ST-elevation myocardial infarction) (as unable to give informed consent prior to procedure) eGFR (estimated glomerular filtration rate) <30,
- Severe asthma contra-indicating the use of adenosine,
- High degree AV block on 12 lead ECG precluding the use of adenosine,
- Pregnancy,
- Inability to consent and
- LMS coronary bifurcation lesions.

The data were collected from:

The Norfolk and Norwich University Hospitals, Norwich, UK. Principal investigator was Dr Simon Eccleshall and co-investigator was Dr Natasha Corbalis. Data collection started in August 2023 and is ongoing, with full ethical approval (West Midlands - Solihull REC, 23/WM/0129, IRAS of 325142).

Northern General Hospital, Cardiothoracic Centre, Sheffield Teaching Hospitals NHS Foundation Trust, Sheffield, UK. Principal investigator Professor Julian Gunn and co-investigator Dr Paul Morris. Data collected from July 2024-December 2024 with full ethical approval (South Yorkshire REC 16/NX/0897, IRAS 208985).

All angiograms were examined with the support of Dr Daniel Taylor and Dr Paul Morris, who have provided valuable clinical judgement. Dr Daniel Taylor also contributed to the segmentation of the CA-images and the processing of the CA-derived single lumen reconstructions.

Case	Age	Sex	Comorbidities	Medication	Indication	Hospital
1	72	M	Smoker, previous myocardial infarction, previous PCI	Aspirin, ticagrelor, atorvastatin, ramipril, bisoprolol	Staged revascularisation for stable coronary disease after previous ACS	NNUH
2,3	72	M	Previous myocardial infarction, previous PCI	Aspirin, ticagrelor, atorvastatin, ramipril	Staged revascularisation for stable coronary disease after previous ACS	NNUH
4,5	61	M	Previous myocardial infarction, previous PCI, dyslipidaemia	Aspirin, ticagrelor, atorvastatin, ramipril, bisoprolol	Staged revascularisation for stable coronary disease after previous ACS	NNUH
6,7	74	M	Malignancy, previous cardiovascular event, ex-smoker, previous myocardial infarction, previous PCI	Aspirin, ticagrelor, atorvastatin, ramipril, bisoprolol	Staged revascularisation for stable coronary disease after previous ACS	NNUH
8,9	53	M	Hypertension, family history of CAD	Aspirin, clopidogrel, atorvastatin	Stable angina	NNUH
10,11	62	M	Ex-smoker, previous myocardial infarction, previous PCI, hypertension	Aspirin, ticagrelor, atorvastatin, ramipril, bisoprolol	Staged revascularisation for stable coronary	NNUH

					disease after previous ACS	
12,13	70	M	Ex-smoker, previous myocardial infarction, previous PCI, dyslipidaemia	Aspirin, ticagrelor, atorvastatin, bisoprolol	Staged revascularisation for stable coronary disease after previous ACS	NNUH
14,15	61	M	Diabetes, smoker, previous myocardial infarction, previous PCI, hypertension, dyslipidaemia	Aspirin, clopidogrel, atorvastatin, bisoprolol	Stable angina	NNUH
16,17	53	M	Smoker, previous myocardial infarction, previous PCI	Aspirin, ticagrelor, atorvastatin, ramipril, bisoprolol	Staged revascularisation for stable coronary disease after previous ACS	NNUH
18	66	M	Ex-smoker	Aspirin, ticagrelor, ramipril and lansoprazole	Staged revascularisation for stable coronary disease after previous ACS	NGH
19	72	M	Hypertension, dyslipidaemia, chronic obstructive pulmonary disease, mild LV systolic dysfunction	Aspirin, atorvastatin	Staged revascularisation for stable coronary	NGH

					disease after previous ACS	
20	75	F	Hypertension, dyslipidaemia, chronic obstructive pulmonary disease, mild LV systolic dysfunction, pacemaker for complete heart block, and stage II chronic kidney disease.	Aspirin, atorvastatin, ramipril, prasugrel, bisoprolol	Staged revascularisation for stable coronary disease after previous ACS	NGH

Table 3.1. Outline of the patient-specific details of the twenty cases studied in this thesis. The cases were imaged in Sheffield's Northern General Hospital and in the Norfolk and Norwich University Hospitals.

Case	Vessels	Proximal Pressure	Distal Pressure	FFR	Clinically Significant Stenosis (according to clinical guidelines)?	Medina Classification (for bifurcations)
1	LAD	87	63	0.72	Yes	-
2	LAD	72	59	0.82	No	111
3	Diagonal	77	62	0.81	No	
4	LAD	92	68	0.74	Yes	010
5	Diagonal	89	69	0.78	Yes	
6	LAD	72	61	0.85	No	010
7	Diagonal	79	72	0.91	No	
8	LAD	64	52	0.82	No	010
9	Diagonal	82	70	0.93	No	
10	LAD	115	73	0.65	Yes	110
11	Diagonal	110	82	0.75	Yes	
12	LAD	108	68	0.64	Yes	110
13	Diagonal	82	65	0.79	Yes	
14	LAD	66	33	0.49	Yes	010
15	Diagonal	73	68	0.94	No	
16	LCX	90	85	0.95	No	010
17	OM	90	86	0.96	No	
18	LAD	92	81	0.87	No	-
19	LAD	79	65	0.82	No	-
20	LAD	112	93	0.92	No	-

Table 3.2. Outline of the vessel-specific details of the twenty cases studied in this thesis. Eight cases had an FFR >0.80, thus indicating a need to be stented.

Chapter Four:

3-D Reconstruction of Single Lumen Coronary Vessels Using Coronary Optical Coherence Tomography

4.1 OCT imaging of the coronary lumen

The focus in this chapter is on modelling single coronary branches from OCT, how the images are acquired and the nature of the anatomical data obtained. The challenges described in Chapter three, namely the impact of projection angle choice, foreshortening and eccentric stenoses are not applicable to OCT, but OCT is associated with its own challenges and limitations.

OCT, being an intravascular imaging technique, produces contours that represent the luminal vessel wall. These contours clearly show stenosed cross-sections and whether the stenosis is eccentric or concentric. In the ideal scenario, the OCT catheter holding the lens is pulled distally to proximally from inside the vessel, with the lens at the centre of the cross-section, perfectly in the plane of the cross-section being imaged. However, the OCT catheter is left to move freely inside the vessel, which causes the lens to get closer to specific sections of the wall and then move away to other sections. This is especially evident in curved sections whereby the catheter, due to conservation of inertia, may come into contact with the vessel wall. This has little to no impact on the extracted contour. However, it is not always the case that the lens is in a plane parallel to the plane of the cross-section being imaged, i.e. not exactly perpendicular to the centre line. This may result in the imaged cross-section to appear larger in area than it originally is. This is more significant in sections of the vessel where it is very curved or tortuous, and the pullback speed of the catheter is faster than the recovery of the catheter orientation.

Contrary to CA, where imaging the distal artery can be challenging due to a relative absence of contrast density which makes it difficult to discern the luminal border edge from background tissues, OCT struggles from various artefacts as listed by (Araki et al., 2022). They mention two non-stent related artefacts relevant to this work: guidewire shadowing and suboptimal blood pool displacement, which leads to ‘swirl’ artefact. After completing this work, a third can be added which is catheter imaging (the OCT run including images from the catheter itself). First, guidewire shadowing occurs due to the OCT light rays being blocked by the guidewire carrying the OCT camera resulting in an incomplete contour. Studies have approached this artefact in different ways, such as by using convoluted neural networks to detect guidewire shadows and complete the contour (Haft-Javaherian et al., 2024). In this work, the contours used are those as segmented by Abbott's Ultreon™ OCT proprietary software. Second, and

depending on where the operator chooses to start the pullback, the lens often continues its motorised pullback into the guiding catheter (Figure 4.1A). In the protocol presented here, such frames are disregarded because they do not yield any coronary anatomical information. The third challenge that OCT may face when imaging the proximal vessel is 'swirl' artefact (Figure 4.1B). This occurs at the very proximal position, immediately next to the catheter tip, because the contrast agent mixes in a swirling fashion with blood that is flowing around the outside of the catheter into the artery. OCT relies on the blood pool being fully displaced from the artery, but this is impossible at the catheter tip. In the protocol presented in this thesis, any frames where this results in an inability to confidently discern the luminal contour are also disregarded.

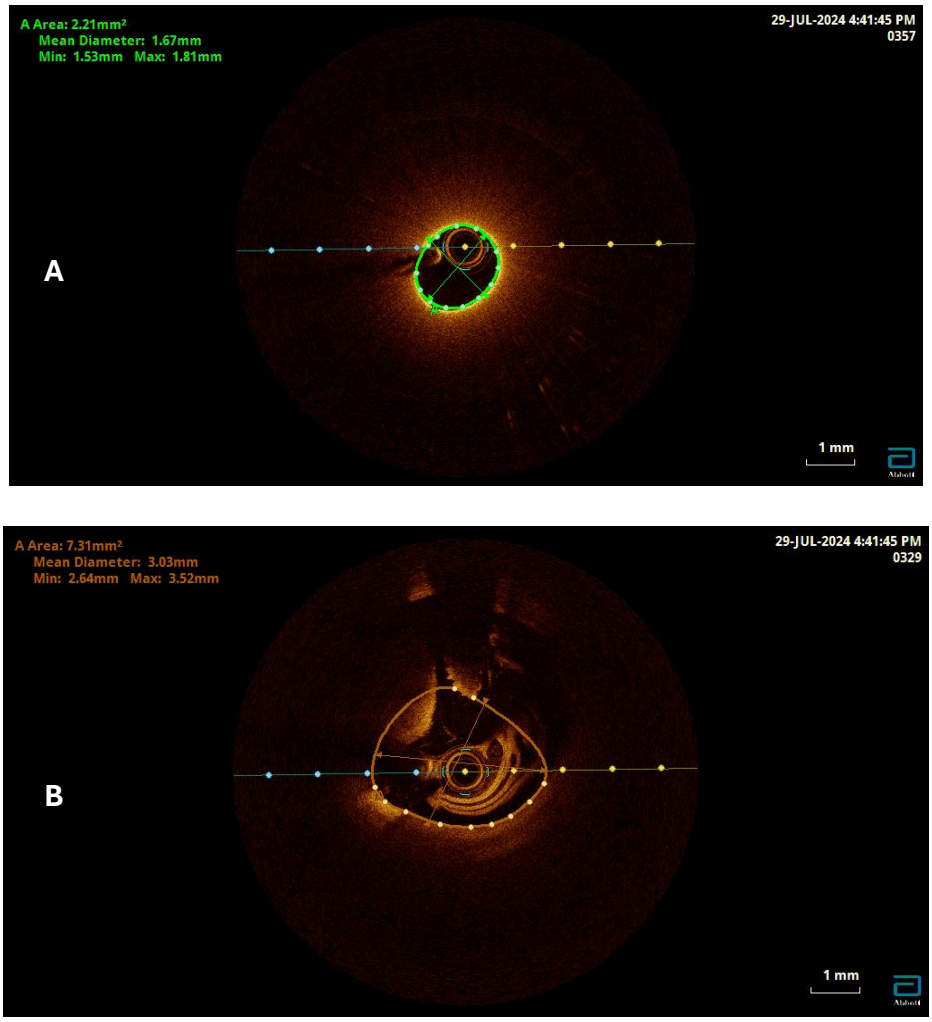

Figure 4.1. (A) OCT frame acquired from within the catheter. This, and similar frames, do not contain meaningful anatomical information from the vessel and are thus disregarded from this work. Similarly for frames such as (B) which exhibit the 'swirl' artefact due to incomplete blood displacement at the catheter tip.

A primary aim of this thesis is to fuse CA with OCT information to produce an optimal reconstruction of the coronary vessel. OCT captures the cross-section of the vessel in detail but knows nothing about the 3D shape of the vessel centreline. The latter can be reconstructed from CA (Chapter three) but there is insufficient information to do better than assume circular cross-sections. Figure 4.2 (left) illustrates the centreline in 3D and Figure 4.2 (right) illustrates a cross section on the centreline. Data from the angiogram is coloured blue and data from the OCT is coloured red. The 3D centreline is reconstructed from the angiogram using a method based on projection of epipolar lines between pairs of images. At each point on the centreline there is a local tangent vector, and the orientation of the cross section is defined by a normal and a binormal vector that are defined using a Frenet frame convention defined in Chapter three. The OCT images are centred at the camera origin. As the guidewire on which the camera is mounted is pulled along the vessel, it is often in practice close to the vessel wall, and so the OCT axes are centred close to the vessel wall, as illustrated in Figure 4.2 (right). Their orientation is determined by the rail guiding the camera, and is not, in general, the same as the Frenet vectors. Figure 4.2 (left) shows the CA-centreline in red, and line followed by the OCT centroid in blue. These are not generally the same, but the expected deviation is small. The maximum possible error, because the OCT centroid is confined in that it must lie within the vessel lumen, is approximately the radius of the vessel, and, in practice, the OCT centroid and the centreline determined by the CA projection will be much closer than that. For the reconstructions in this thesis, it is assumed that the centrelines are the same. Accordingly, the tangent vectors are the same and therefore the OCT cross-sections are exactly perpendicular to the CA-centreline.

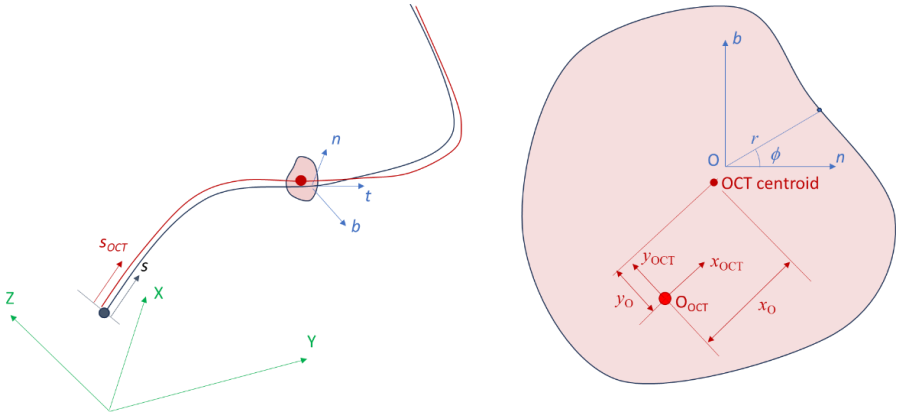

Figure 4.2. (left) The red CA-centreline (segmented) and blue OCT-centreline (joins cross-sectional centroids). (right) An OCT cross-section on the centreline.

There are two remaining challenges in the fusion of the CA and OCT data:

1) Determining where the individual OCT frames belong, longitudinally, on the CA-centreline.
2) Determining the relative orientation of the Frenet normal and binormal vectors defined by the CA-centreline and the x and y axes of the OCT images. This is important especially when WSS and similar haemodynamic parameters are simulated around bifurcations. This is also relevant in the context of treatment decision and strategy guidance (PCI and CABG), which are also dependent on geometry and detailed regional anatomy.

4.2 Longitudinal alignment of CA and OCT data

Regarding the longitudinal position of the OCT frames on the CA-centrelines, ideally, the OCT run and the CA-segmented section of the vessel are the same. The ideal 'automated' software would include:

1) Using the angiograms that show the start and end points of the OCT catheter's run
2) Automatic extraction of the start and endpoints for the CA segmentation of the vessel centreline
3) Stacking of the OCT frames, equidistantly on the CA-centreline using the known OCT frame-to-frame distance.

Theoretically, this would be the most efficient method for CA-OCT longitudinal alignment. Realistically, however, this is prone to errors for three main reasons:

1) The nature of CA being a 2D imaging modality for 3D structures:
   If a section of the vessel is foreshortened in the 2D angiogram, then the frames from the OCT might not correspond to the location on the angiogram. This can occur anywhere in the vessel.
2) Epipolar line issues when CA-segmenting proximal vessel sections:
   OCT runs start distally in the vessel and span all the way to the proximal end into the catheter. For CA-segmentation, segmentation software faces issues with epipolar lines in the proximal ends of the vessels, like in the LMS, when the vessel is perpendicular to the chosen view, making segmentations of these ends challenging.
3) Imaging the catheter and the 'swirl' artefact: As described previously.

Therefore, in addition to the frames on the OCT run that correspond to the catheter and the swirl artefact, which are disregarded, there are still some frames from the proximal sections that do not have a corresponding CA-centreline section to be positioned on. It is the modeller's decision how to deal with such frames. The first option is to disregard such frames and limit the 3D model to the frames that correspond to the centreline. This is viable as the focus of the modelling in this case is simulating flow around the bifurcation. However, this entails loss of potential valuable anatomical data obtained from OCT. The second option is to assume that the centreline proximally to the centreline start point, is a straight vessel section in the direction of the tangent vector at the current start point of the CA-centreline. Although this is not the exact anatomical shape, it preserves the OCT data proximally and uses it in combination with the available and extractable CA data. The first option is adopted in this work. This is a significant step forward from the current OCT-based coronary models, which are all perfectly straight vessels, with no appreciation of curvature and tortuosity which the angiograms can provide.

In this work, the following methodology for longitudinal alignment was adopted:

1) Catheter and 'swirl' OCT frames disregarded.
2) Segmented CA and OCT diameters plotted against vessel length for visual comparison (Figure 4.3 – left).
3) The diameter plots shifted to align as best as possible (Figure 4.3 – middle).

4) Sections of the vessel without data from both imaging modalities disregarded (Figure 4.3 – right).

The alignment, shift and discarding steps are further explored next.

To assess whether the acquired CA and OCT data correspond to the same sections of the vessel the diameters were compared. The vessel effective diameters were:

1) Extracted from the OCT cross-sections, by computing the area of each cross-section using the shoelace formula for area (Equation 4.1) then computing the effective diameter (Equation 4.2). The effective diameters from CA and OCT were plotted against vessel length as shown in Figure 4.2 (left) for cases 1, 2 and 3 for demonstration.

$$Area = 0.5 * \sum_{i=1}^{N} (x_i y_{i+1} - x_{i+1} y_i)$$

Equation 4.1. Computing the area of an OCT cross-section using the Shoelace formula. N is the number of points that make up each OCT cross-section, and x and y are the coordinates of each point.

$$Effective\ diameter = 2 * \sqrt{\frac{Area}{pi}}$$

Equation 4.2. Computing the effective diameter of an OCT cross-section from its area

2) Aligned by visually examining the plots and shifting the OCT curve with respect to the CA curve to achieve maximum correspondence (Equation 4.3). This is shown in Figure 2 (middle).

$$x_{OCT\_shifted} = x + shift$$

Equation 4.3. Shifting the OCT effective diameter curve a distance 'shift' to achieve maximum correspondence with the CA diameter curve.

3) Non-corresponding sections were discarded, by finding the larger of the two minimum x values from CA and OCT and the minimum of the two maximums (Equations 4.4, 4.5). This is demonstrated in Figure 4.3 (right).

$$x_{min} = \max\left(\min\left(x_{OCT\_shifted}\right), \min(x_{CA})\right)$$

$$x_{max} = \min\left(\max\left(x_{OCT\_shifted}\right), \max(x_{CA})\right)$$

Equations 4.4 and 4.5. Finding the x limits of the overlapping sections of the OCT and CA diameter curves.

Acquiring this data and discarding the sections that lack correspondence allows us to explore how differently CA and OCT capture the vessel diameters in healthy and diseased sections of the vessel. It can also allow us to quantify any systematic differences that exist between both modalities. This is explored in Chapter five.

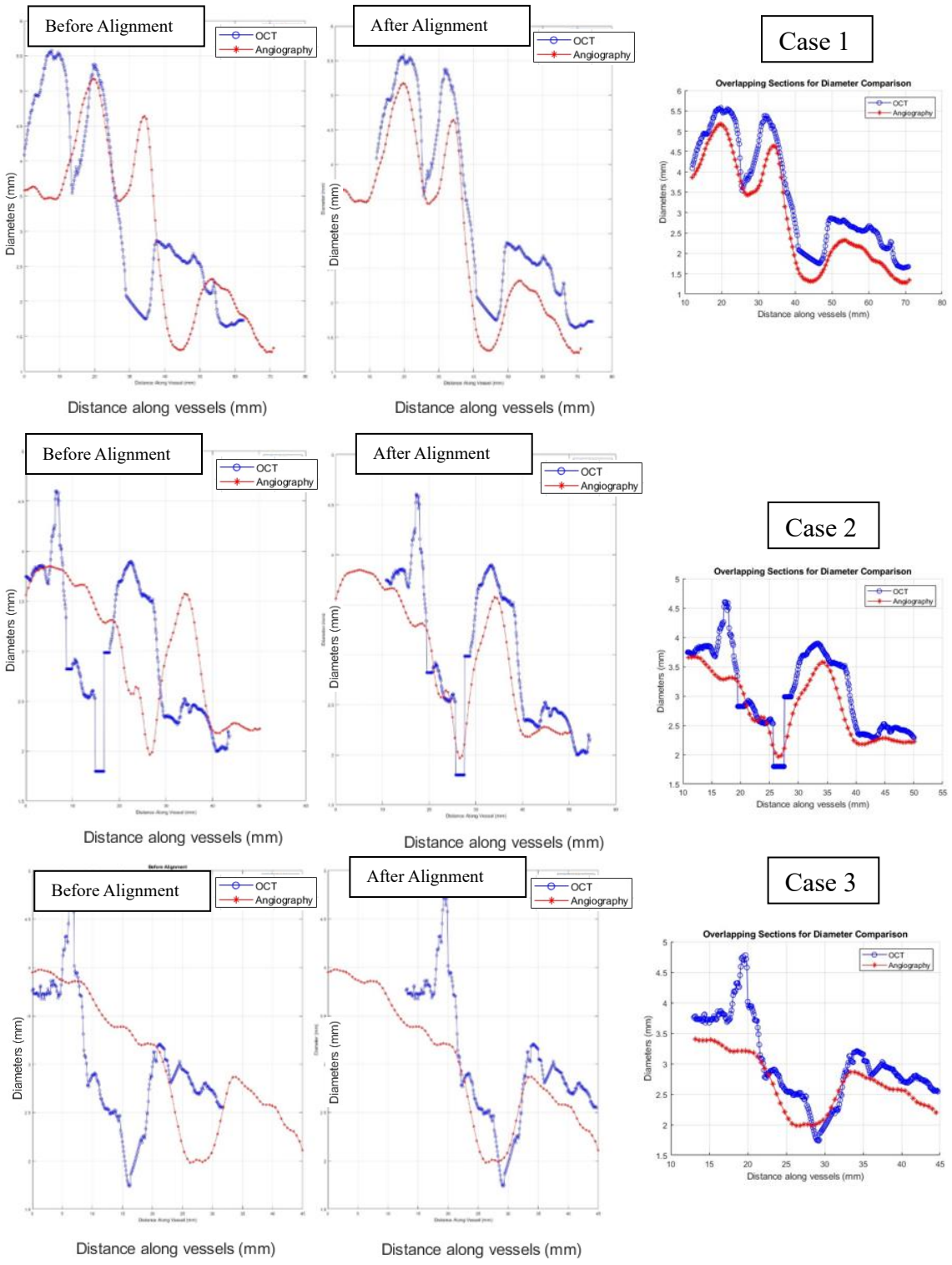

Figure 4.3. This is an illustration, of cases 1-3, whereby the diameter data from CA and OCT were acquired, aligned and then examined for correspondence. The non-corresponding sections for each were discarded to produce the last image in every series. The corresponding set of diameters were used to quantify any systematic differences between the image acquisition of the two imaging modalities.

4.3 OCT lumen orientation optimisation

As discussed in the preceding section, a method is required to orientate the OCT axes onto the Frenet normal and binormal vectors to ensure that the OCT sections are appropriately orientated in three dimensions in the vessel reconstructions. The tangent vector at every point is known from the CA reconstruction and the shape of the cross-section is known from the OCT reconstruction. At every cross-section there is a single degree of freedom, θ, that describes the orientation of the OCT x-axis relative to the Frenet normal. The centreline is represented by a series of discrete points and the vector $\{\theta\}$ describes the rotation at every point. A general process has been developed to find the optimal $\{\theta\}$ vector to minimise a declared cost-function. Assume that a cost function can be defined that is a function of $\{\theta\}$.

$$cost\ function = f(\{\theta\})$$

Assuming that the cost function is defined so that a small value represents a good solution, the optimal solution, θ_{opt}, is when the cost function is minimised. The optimal solution, $\{\theta_{opt}\}$, is found using Matlab's *fsolve* function (Equation 4.6):

$$\{\theta_{opt}\} = \{\theta\}\ that\ minimises\ f(\{\theta\})$$

Equation 4.6. A cost function with an optimal solution θ_{opt}.

In the following sections, cost functions associated with three methods for determining the orientation of the cross-sections are developed and discussed. The first assumes that the area overlap between successive frames is maximised. The second is to minimise the difference between the projected diameter of the OCT cross-section onto any CA image and the CA diameter. The third is a smoothness constraint that prevents rapid change of the orientation between cross-sections. Note that the first and third methods only determine the relative rotation of cross-sections. Any absolute rotation can be added to solution vector as a constant

offset without changing the cost-function. The second method does give an absolute orientation within an angular range.

A composite cost function can be defined by taking the weighted sum of individual cost functions. This is a general process that can be applied to aggregate any series of cost functions. For the three cost functions developed and implemented in this thesis, the composite cost function is (Equation 4.7):

$$\begin{aligned} &Cost\ function \\ &\quad = (weight1 * area\ overlap\ optimisation) \\ &\quad + (weight2 * angio\ optimisation) + (weight3 * smoothing) \end{aligned}$$

Equation 4.7. The OCT lumen orientation composite cost function that includes a term for each: area-overlap optimisation, angio-optimisation and smoothing. Each term has a weighting factor to scale its impact on the overall optimisation.

A clear advantage of formulating the cost function in this way is that the relative emphasis on each of the individual cost functions can be changed simply by altering the weights. The solutions with single cost functions can be generated just by setting the other weights to zero.

4.3.1 Area-overlap optimisation

Researchers have approached the OCT lumen orientation optimisation challenge in different ways (Wu et al., 2020, Ellwein et al., 2011, Bourantas et al., 2013, Zhu et al., 2025). Some have decided that the key is linking the orientation of consecutive cross-sections relative to each other. One such way is to assume an initial orientation for the first cross-section, determine its area, and then rotate the consecutive cross-section in so that the area overlap between every two consecutive cross-sections is maximum. When this is done and the orientation of the second cross-section is determined, a similar procedure is done between cross-sections number two and three, and so on. This assumes that between consecutive frames, the luminal area is not expected to change drastically. Even in the presence of a stenosis, and due to the frame rate

and the speed of the automatic pullback, the decrease in area is gradual and is spread over several frames.

The cost function for the area-overlap method is:

$$cost\ function_{area\ overlap} = Area_1 + Area_{2-rotated} - 2 * Area_{overlap}(\theta)$$

Using the Shoelace formula to compute signed areas for 2D shapes made of N points is:

$$Area = 0.5 * \sum_{i=1}^{N} (x_i, y_{i+1}) \times (x_{i+1}, y_i)$$

Accordingly, the cost function becomes as shown in Equation 4.8. Figure 4.4 shows an example of a first frame (red) and the original (purple) and rotated (green) second frame to minimise non-overlapping area.

$$Cost\ Function_{area\ overlap} =$$

$$abs\left(0.5 * \sum_{i=1}^{N} (x_{i1}, y_{i1+1}) \times (x_{i1+1}, y_{i1})\right) + abs\left(0.5 * \sum_{i=1}^{N} (x_{i2}, y_{i2+1}) \times (x_{i2+1}, y_{i2})\right)$$

$$-abs\left(\sum_{i=1}^{N} (x_{i1}, y_{i1+1}) \times (x_{i1+1}, y_{i1}) - (x_{i2}, y_{i2+1})(x_{i2+1}, y_{i2})\right)$$

Equation 4.8. Area-overlap cost function

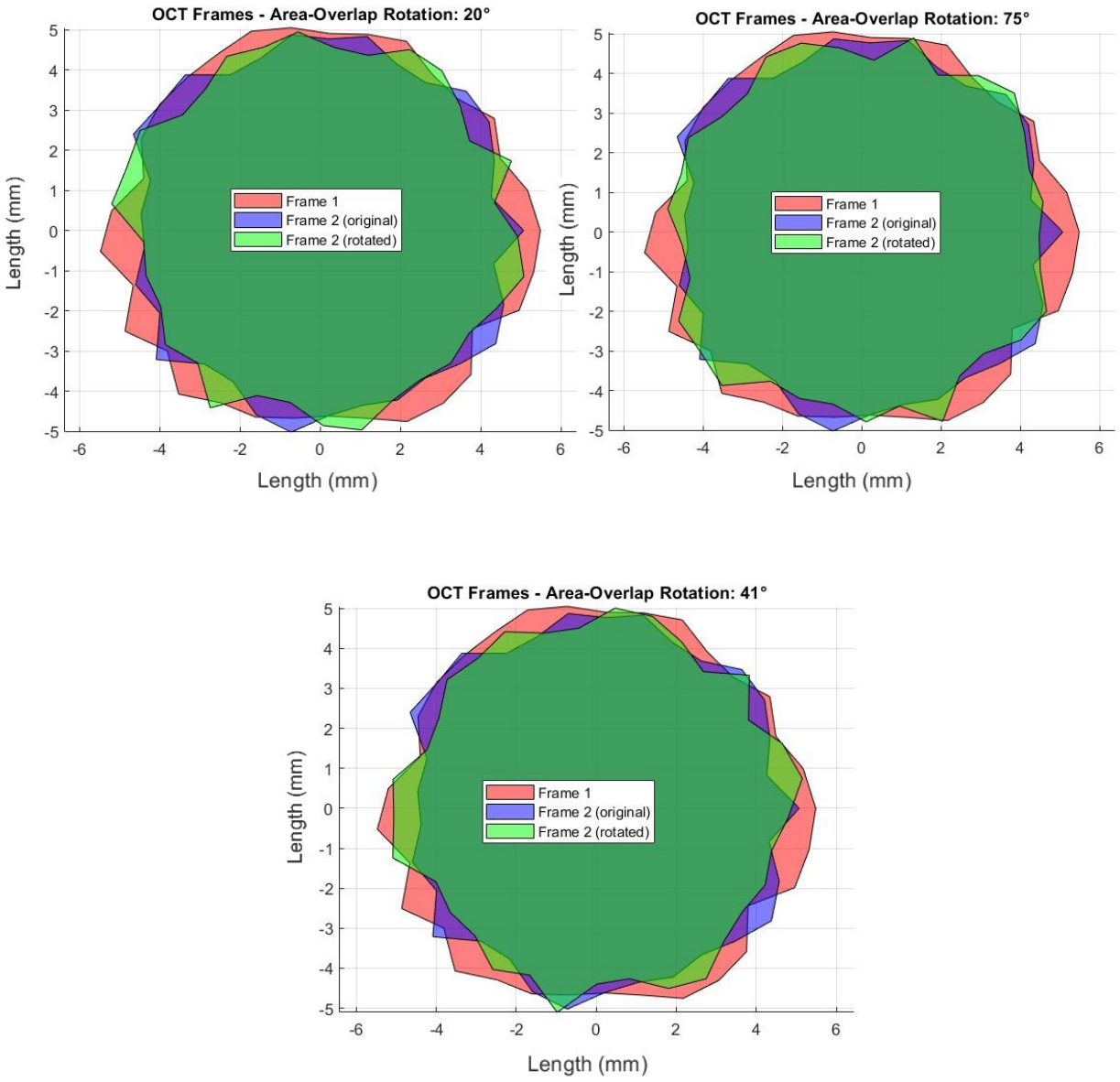

Figure 4.4. Three OCT frames; the reference frame is in red. The goal is to rotate the second frame (purple = unrotated, green = rotated) through several angles to find the rotation angle to produces the minimum non-overlapping area between both frames.

Although the area-overlap methodology has been the basis for several published OCT-based studies, it is dependent on the initial assumed orientation of the first cross-section. This is a significant factor especially in the more curved and tortuous sections of the vessel where the orientation of the frame with respect to the radius of curvature will impact whether the vessel is wider or shallower in the different directions in 3D, thus potentially impacting future CFD simulation results.

It is possible that for some lumens, one lumen will be completely 'contained' in its preceding lumen, meaning that it is much smaller in size that it is completely engulfed inside it, as shown in Figure 4.5. Therefore, no matter the rotation angle, the overlapping area will remain equal to the engulfed contour area. The *fsolve* function based on minimising non-overlapping area will not be able to find a solution for such a case. Accordingly, an additional layer was added in the developed protocol to find the cases where the area of a lumen and the overlapping area between this lumen and its preceding lumen are equal using Equation 4.9.

$$\text{Consecutive Area Difference} = \mathrm{A}_{\mathrm{lumen}} - \mathrm{A}_{\mathrm{intersection}}$$

Equation 4.9. Finding the difference between the area of a lumen and the difference between that and the overlapping area with its preceding lumen.

In the cases that satisfy this criterion, the rotation angle is obtained through linear interpolation between the rotation angle one lumen prior to the lumen in question and a lumen two frames away from that in question. This combination was chosen because the goal is to relate a frame to a next best consecutive frame downstream of the artery. The lumens that exhibit this criterion are usually those at extreme stenoses or at bifurcations. Two OCT lumens that exhibit this criterion are shown in Figure 4.5 in green and blue. Linear interpolation was performed to obtain a value of the appropriate rotation angle for this lumen since, as seen in Figure 4.5 (top) and as expected, the overlap difference is zero. The new rotation angle is approximately 1.13° and is shown in Figure 4.5 (bottom).

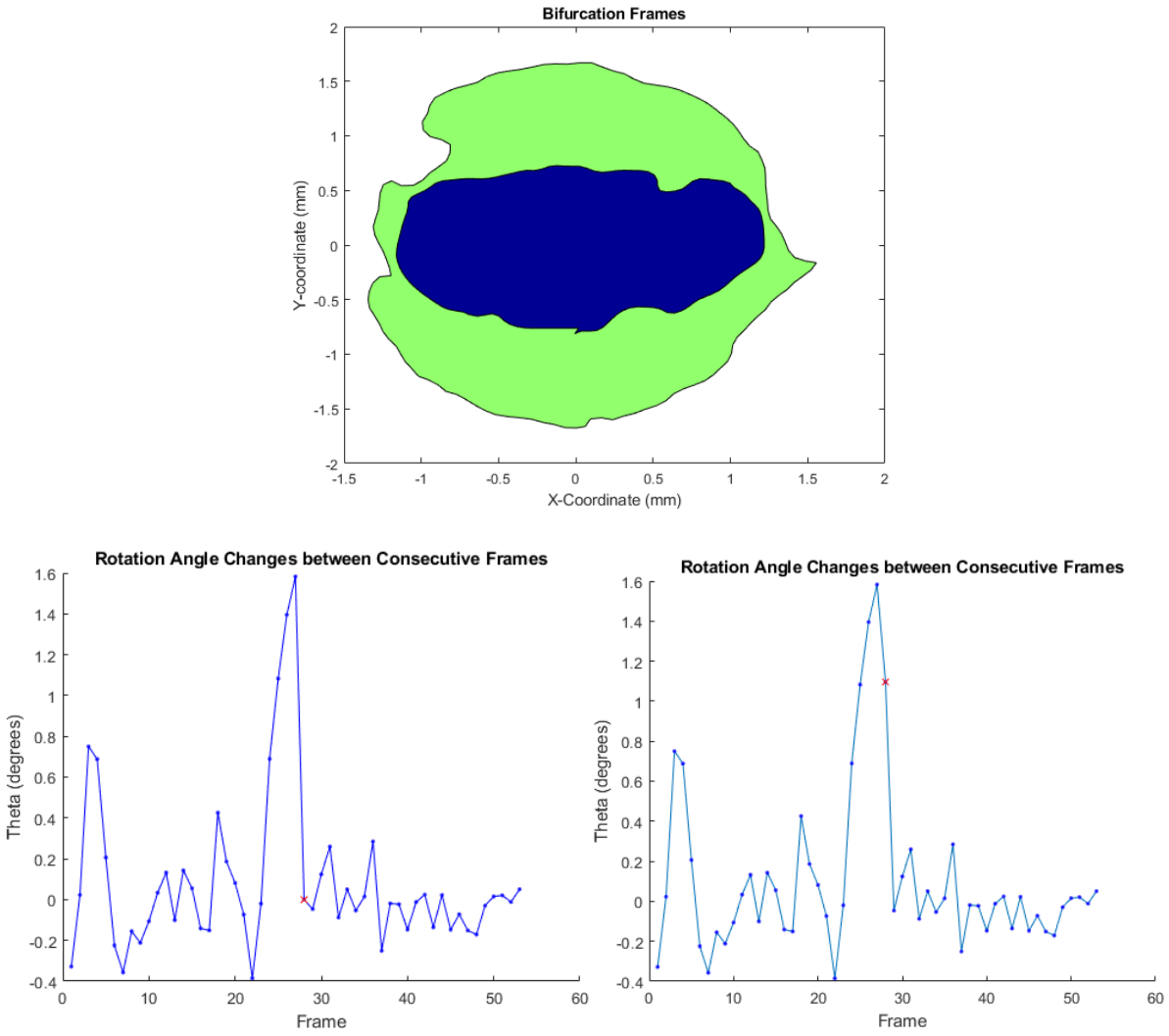

Figure 4.5. Difference between lumen area and overlapping area for every lumen and its preceding lumen, before (top) and after (bottom) linear interpolation was performed for frame 27, which has an overlapping difference of zero.

4.3.2 Angio-optimisation

This section describes the novel methods developed to optimise the appropriate rotation of the OCT cross-sections, which is dependent on the greyscale distribution of the angiogram and is be referred to as 'the angio-optimisation method' throughout this thesis. The developed method is as follows:

1) In terms of ϕ, the radius at any point is:

$$r(\phi) = r(\psi - \theta_0)$$

Where θ_0 is the initial angle of the OCT x-axis and ψ is the angle between the vector from the centroid of the cross-section and the cross-sectional point and the OCT x-axis.

For any candidate orientation, θ_j , of the OCT axis relative to the Frenet normal at the j^{th} point on the centreline, the 3D co-ordinates of the points on the OCT cross-section are:

$$\begin{Bmatrix} x_{G_{r,\phi}} \\ y_{G_{r,\phi}} \\ z_{G_{r,\phi}} \end{Bmatrix} = \begin{Bmatrix} x_{G_0} + n_X r cos\phi + b_X r sin\phi \\ y_{G_0} + n_Y r cos\phi + b_Y r sin\phi \\ z_{G_0} + b_Z r sin\phi \end{Bmatrix}$$

2) For any cross-section, every point on the surface of the lumen can be projected onto the projection plane (A). The projected co-ordinates of the points on the cross-section are $\left\{x_{A_{P_{r,\theta_j}}}; y_{A_{P_{r,\theta_j}}}\right\}$ and the projected centroid coordinates are $\left\{x_{A_{P_O}}; y_{A_{P_O}}\right\}$:

$$\begin{Bmatrix} x_{A_{r,\phi}} \\ y_{A_{r,\phi}} \\ z_{A_{r,\phi}} \end{Bmatrix} = [R]_{GA} \begin{Bmatrix} x_{G_{r,\phi}} \\ y_{G_{r,\phi}} \\ z_{G_{r,\phi}} \end{Bmatrix}$$

$$\begin{Bmatrix} x_{A_{P_{r,\phi}}} \\ y_{A_{P_{r,\phi}}} \end{Bmatrix} = \frac{LSD}{LF + z_{A_{r,\phi}}} \begin{Bmatrix} x_{A_{r,\phi}} \\ y_{A_{r,\phi}} \end{Bmatrix}$$

3) For any point on the projected OCT section, the unit projected tangent and normal vectors in the projection plane are:

$$t_{A_P} = \left\{\xi_{A_{P_T}}; \eta_{A_{P_T}}\right\} \text{ and } n_{A_P} = \left\{-\eta_{A_{P_T}}; \xi_{A_{P_T}}\right\}$$

And the local radius of each point on the cross-section of the surface of the lumen in the projection plane is the dot product of the vector from the projected centroid with the unit normal (Equation 4.10):

$$r_{A_O}{}^{+} = \max\left(\begin{Bmatrix} x_{A_P r,\phi} - x_{A_P O} \\ y_{A_P r,\phi} - y_{A_P O} \end{Bmatrix} \cdot \begin{Bmatrix} -\eta_{A_P T} \\ \xi_{A_P T} \end{Bmatrix}\right)$$

$$r_{A_O}{}^{-} = \min\left(\begin{Bmatrix} x_{A_P r,\phi} - x_{A_P O} \\ y_{A_P r,\phi} - y_{A_P O} \end{Bmatrix} \cdot \begin{Bmatrix} -\eta_{A_P T} \\ \xi_{A_P T} \end{Bmatrix}\right)$$

Equation 4.10. Positive and negative extreme point distances (radii) from the centroid of the OCT cross-section.

4) Compute the difference between the diameters of the segmented angiographic projections and the projected OCT segmentations on each of the two projections. Each of these differences is an element of the cost-vector corresponding to the rotation of the axes of the OCT section at that point on the centreline (Equation 4.11).

$$Cost\ Function_{angio-optimisation} = \left(r_{A_O}{}^{+} - r_{A_O}{}^{+}{}_{angio}\right)^2 + \left(r_{A_O}{}^{-} - r_{A_O}{}^{-}{}_{angio}\right)^2$$

Equation 4.11. Angio-optimisation cost function

The four steps described above are illustrated in Figure 4.6. Panel A shows the 3D points of the OCT cross-section on the relevant centreline point, with the Frenet normal, tangent and binormal vectors, and the original 2D x and y axes. This cross-section is then projected onto the first angiogram in (B). The angiogram is zoomed in for illustrative purposes, with the vessel boundary marked in yellow. In (C) the normal to the CA-centreline is marked in black and the extreme points on the OCT frame along this line are marked in red. These OCT extreme points are then compared to their CA counterparts, shown in yellow. Their distances from the centreline point are the 'radii' and the radius error are computed as shown in Equations 4.10 and 4.11. The angio-optimisation cost function (Equation 4.11) aims to minimise these errors by minimising the sum of the positive and negative extreme errors.

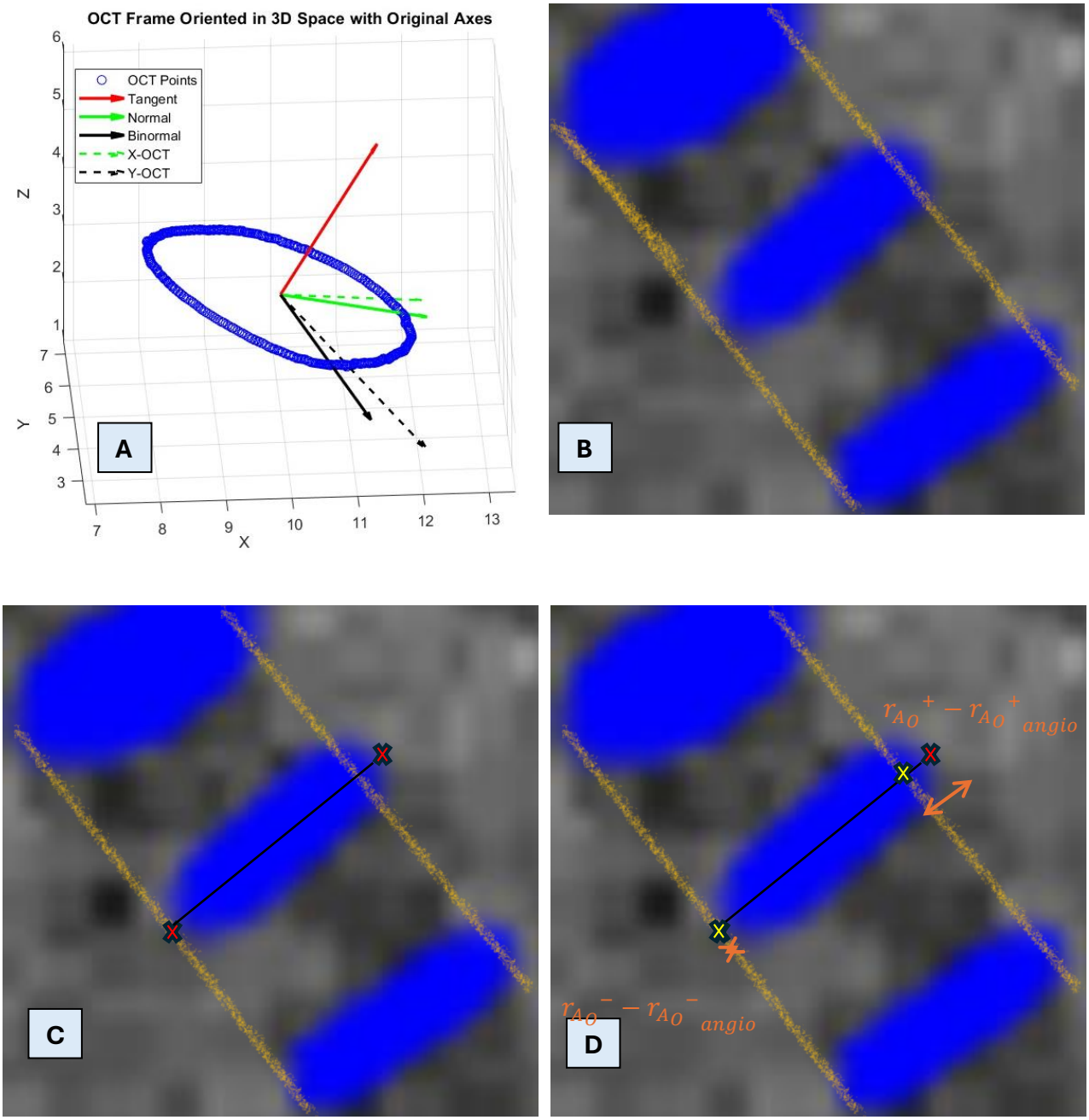

Figure 4.6. The angio-optimisation method. (A) Shows the OCT-cross section in 3D with the Frenet normal, tangent and binormal vectors as well as the OCT x and y-axis. (B) Shows the projected OCT frame on the relevant angiogram (zoomed in), with the vessel edges as seen on the angiogram marked in yellow. (C) Shows the extreme OCT points along the centreline normal vector which (D) are compared to the extreme points as identified from the greyscale of the angiogram, which then allows the computation of the error in radius for the positive and negative extremes. The error values are what is minimised in the cost function for this orientation optimisation method.

The above process has been implemented to map the perimeter of each OCT cross-section onto the angiographic projections to optimise the orientation of the OCT cross-sections.

In chapter five, a detailed comparison of CA and OCT diameters is conducted. It has been previously found that CA tends to underestimate the diameter of the vessel, especially in the proximal segments (Kim et al., 2016, Kubo et al., 2013, Chamié et al., 2021). One of the reasons this is happening might be the incomplete filling of the vessel with radio-opaque contrast media thus appearing smaller that it is. It is important to appreciate that extracting the vessel radius from CA is purely greyscale dependent and the angiogram pixel size is typically 0.3 mm, which is a significant proportion of the vessel diameter. The edge of the vessel is blurred by the limits of resolution. OCT, however, has very large contrast between what is vessel wall and what is the blood flow path and has much higher resolutions.

The combination of angio-optimisation and area-overlap optimisation, without smoothing, was explored for the flagship case (Figure 4.7). There is a rapid variation of theta along the length of the vessel, and this is implausible given the guidance of the camera system on the guidewire. This shows the importance of implementation of the smoothing constraint.

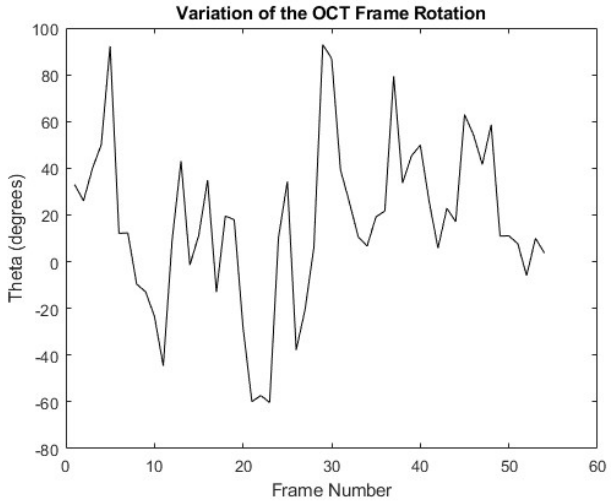

Figure 4.7. The change in the value of optimisation angle of orientation using the area-overlap and angio-optimisation for the first 53 frames of the OCT run.

4.3.3 Smoothing

The area-overlap and angio-optimisation cost functions each compute the optimal orientation of each section in isolation. The actual orientation of the camera system is determined by the orientation of the guidewire on which it is mounted and, although this will vary as the guidewire moves along the vessel, in practice it will not vary rapidly. This is recognised by adding a cost function that imposes smoothness (Equation 4.12). This function penalises high curvature of the theta function.

$$(Cost\ Function_{smoothness})_j = -\theta_{j-1} + 2\theta_j - \theta_{j+1}$$

Equation 4.12. Smoothing cost function

The main strength of the composite cost function (Equation 4.7) is that by adjusting the weights of the different terms, the optimisation method can be adjusted for different cases, depending on the quality of data. For instance, if the CA and OCT radii are comparable, then a larger weighting can be imposed on the angio-optimisation term etc. This feature allows the user to tailor the optimisation to the context of the case at hand. In the future, further testing on the optimal weights for each optimisation term can be performed for mass reconstruction of cases with decreased manual input.

4.4 Lumen area and asymmetry to identify stenoses

With OCT, the intraluminal detail provides us with a wealth of anatomical measurements that can be used to identify areas of potential disease. For instance, a drop in *lumen area*, whether sudden or gradual usually either corresponds to a stenosis or a bifurcation. *Lumen circularity* can be used to assess how healthy a vessel is. A circular cross-section is assumed to be healthier, except if plaque has developed uniformly along the circumference of the cross-section. Two measures of circularity are proposed in this thesis. The first is based on the second moments of area of the cross-sections, borrowing the process from structural mechanics. The second moment of area identifies the bending characteristics of a beam of a given cross-section, but for this application its merit is that it identifies asymmetry in the cross-section. The second is based on the Fourier decomposition of the radius of the vessel in cylindrical co-ordinates. This

can also identify asymmetry by examining the relative magnitudes of the harmonic terms relative to the mean radius but in this thesis the focus is on the term in the Fourier series that identifies vessel ellipticity.

4.4.1 The area test

The vessel being analysed here is the pre-PCI LAD of the flagship case as it exhibits a combination of stenotic and bifurcation characteristics in its area plot. For Figure 4.8, the area of every tenth frame of the 540-frame run is plotted. It can be said that there is an overall decrease in frame area proximally to distally, which is natural since most vessels in the circulatory system experience tapering and have smaller distal areas for more efficient nutrient exchange. Also, the blood in the distal sections of the coronaries is expected to be less pulsatile, thus allowing for the vessel wall to be smaller and less thick.

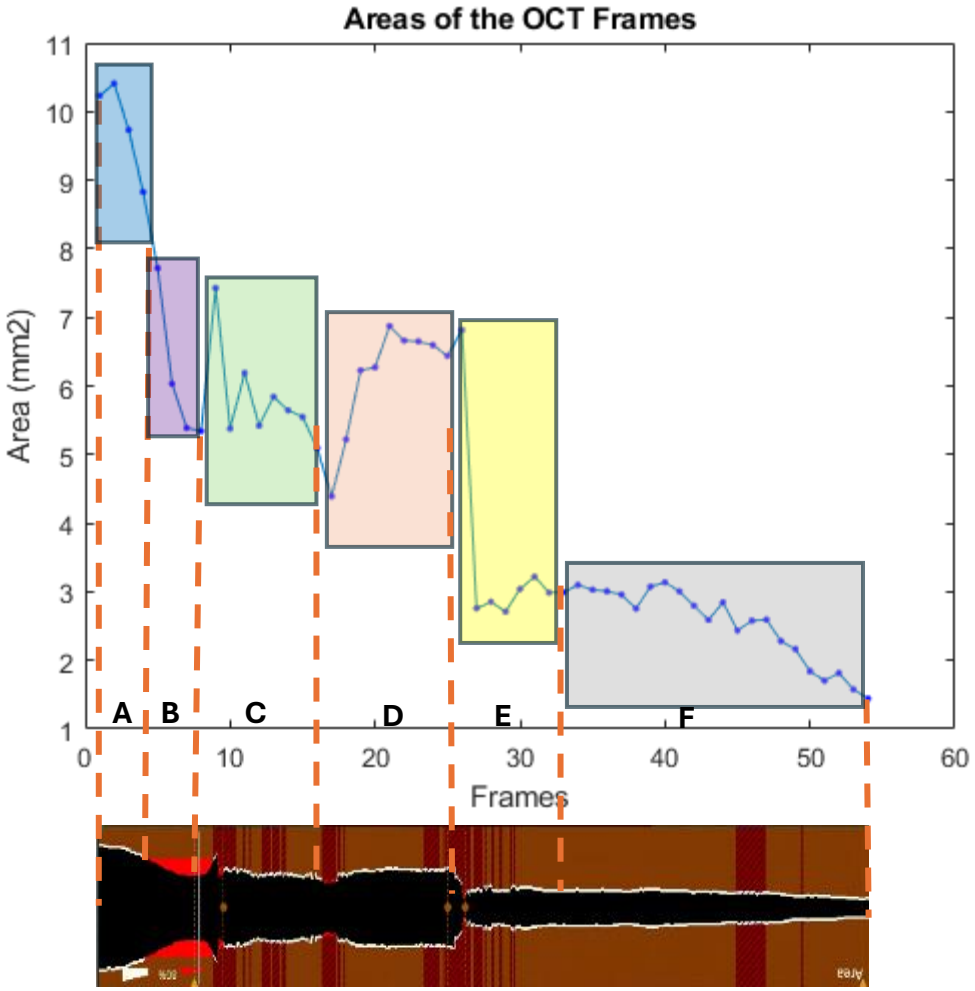

Figure 4.8. Area of OCT cross-sections with respect to the longitudinal OCT pullback. (A) Start of diffuse stenosis, characterised by sharp area decrease. (B) Sharper area decrease, continuation of stenotic region. (C) Recovery and start of second stenotic region. (D) Recovery and stable area region pre-bifrucation. (E) Bifurcation: Transition from main vessel to side branch and start of post-bifurcation stenotic region. (F) Healthy tapering region.

Section A shows a sharp area decrease from approximately 10.3 mm^2 to 8 mm^2 for less than five frames. An even sharper area decrease is shown in section B, thus indicating the possibility of a diffuse stenosis being present over all frames in both sections A and B. Due to OCT being an intraluminal imaging modality, the user can tell how far along the section of the coronary branch that was imaged by OCT a specific frame is. However, the user does not have enough information to know where in the full tree this branch is located or even where the specific section that was imaged is along the branch. Accordingly, from just the information provided in the bottom (longitudinal) image of Figure 4.8, it is impossible to tell whether the imaged

section is at the start of a branch, post a previous bifurcation, or in the middle of an already existing branch, etc. This is an example as to why coupling intraluminal modalities, such as OCT, with the more general picture modalities, such as ICA, is beneficial. With section C, it seems as though the vessel recovers from a previous stenosis and then suffers from another one that is less steep. Recovery in this section, however, appears to be quite steep, steeper than the second recovery phase at the beginning of section D. This can be due to several reasons: 1) Since each represents the changes that happened for its previous ten frames, what seems sudden, can be gradual over ten frames. If this is true, then this means that over ten frames, which is approximately 1.4 mm, the area has increased from 5.3 mm^2 to 7.5 mm^2, which is significant. This change would have been due to poor quality segmentation; however, this area change is obvious in the longitudinal image of the vessel, showing an evident change in lumen diameter. This drastic change directly feeds the Abbott software's algorithm, which detects such changes, and uses a backwards protocol to predict how long the stenosis is and how big the vessel is expected to be had the stenosis been absent. The backwards protocol finds the recovery radius and draws a straight line backwards from this point to the point where the straight line meets the vessel body. This corresponds to the highlighted red area in the longitudinal image. However, this protocol can be quite crude, since it can be prone to misinterpretation in the presence of artefact and longer, diffuse stenoses. Accordingly, it may be that analysing both the area changes and the I_I/I_{II} ratio, assessing circularity, in conjunction would allow the development of a protocol for categorising the different sections of the targeted vessel as either 'bifurcation', 'stenosis' or 'healthy', rather than just relying on the observed vessel radius from the OCT run. Section D starts with a recovery phase after the diffuse stenotic region and then enters a stability phase pre-bifurcation. Vessel area changes fluctuate within 0.1 mm and 0.2 mm, and then suddenly drops from a 'mother vessel' area of 7 mm^2 to 'daughter vessel' area of 2.7 mm^2. The vessel area increases again gradually, indicating the possibility that a third, post-bifurcation stenotic region might be present. Bifurcation stenoses are a common phenomenon and require careful planning and awareness of the impact of stenting on blood flow and the interaction between the branches pre- PCI. Combining area and circularity measurements to assess the state of vessel lumens to identify areas of stenosis renders itself useful in the area of bifurcation PCI, since, to the bare eye, the radius change post-bifurcation shown in the longitudinal image might be too insignificant to raise any alarms. Section F appears to be a healthy distal tapering section from 3 mm^2 to the end of the vessel at 1.4 mm^2 over 210 frames, which is equivalent to 29.2 mm.

4.4.2 Asymmetry tests

A key objective of imaging, and the consequent 3D modelling, of patient anatomy is to identify areas of disease and quantify its severity, to facilitate clinical decision-making. This can be done in different ways and in different stages, either at the imaging stage, by the clinicians, after reconstruction, or after 3D modelling and CFD, when fluid slow simulations can indicate the presence of disease using measures such as the vFFR. When a blood vessel is non-diseased, its shape tends to be more axisymmetric, i.e. more circular. As coronary disease develops, the plaque tends to be on one side of the vessel wall (eccentric plaque), resulting in an asymmetric shape, resulting in irregularly shaped lumens (DeVos et al., 2024, Murasato et al., 2022, Beier et al., 2016, Mintz and Guagliumi, 2017). Characterising and quantifying this irregularity can support the diagnosis of diseased vessels, and the more accurate and efficient the quantification process is, the more readily will it be used in the clinical context. This can be done by interrogating the shape of the OCT contours, in different ways, as is explored in this section.

4.4.2.1 Second moment of area

The second moment of area is a measure of a distribution of a shape around an axis. It is a main concept in structural mechanics and has several applications in various fields such as construction engineering and material sciences, with regards to choosing appropriate shapes and materials for buildings, parts etc. according to the needed function. It also describes how resistant a shape is to deformation about a specific axis. I_{xx}, I_{yy} and I_{xy} are the measures of the second moment of area of a 2D shape in the xy plane, as shown in Equations 4.13-4.15. If the shape being analysed is regular, i.e. triangle, the dA term can be expressed as the actual area of the shape and the limits of agreement can be assigned accordingly. In the case of an OCT cross-section, the shape is irregular, therefore, it is discretized into smaller, more regular shapes and the integrals of each are summed. If the chosen axes pass through the centroid of the shape and the shape is symmetrical, I_{xy} will equal zero.

$$Ixx = \int y^2 dA, \quad Iyy = \int x^2 dA, \quad Ixy = \int x\, y\, dA$$

Equations 4.13-4.15. The three components of the second moment of area of a 2D shape about the x and y axes.

If an irregular cross-section is divided into n triangles, and the second moment of area of the whole shape is being calculated about its principal axes (the axes about which the product of inertia is zero and pass through the centroid), the following steps are undertaken:

1. Compute the area of each triangle (A_i)
2. Compute the centroid of each triangle (x_i,y_i)
3. Compute Ixx_{ic}, Iyy_{ic} and Ixy_{ic} about each triangle's centroid
4. Compute the centroid of the whole irregular shape (X_s,Y_s)
5. Use the parallel axis theorem to shift the moment of inertia to the global centroidal axis:

$$Ixx_i = Ixx_{ic} + A_i\,(y_i - Y_s)$$
$$Iyy_i = Iyy_{ic} + A_i\,(x_i - X_s)$$
$$Ixy_i = Ixy_{ic} + A_i\,(x_i - X_s)(y_i - Y_s)$$

6. Sum Ixx_i, Iyy_i, and Ixy_i for all triangles to get the global moments of inertia about the axes that pass through the shape's centroid

$$Ixx = \sum_{i=1}^{n} Ixx_i$$
$$Iyy = \sum_{i=1}^{n} Iyy_i$$
$$Ixy = \sum_{i=1}^{n} Ixy_i$$

One way to assess asymmetry is by borrowing this concept from structural mechanics and computing the second moment of area about the principal axes of each lumen, I_I and I_{II}, are computed, as shown in Equation 4.16, then the ratio between them is obtained. A ratio of 1 indicates that the second moment of area about both principal axes are equal, indicating a fully symmetrical shape. For lumens that have a ratio close to 1, such as that in the second frame in Figure 4.9, are expected to be more symmetrical than those with a ratio further from 1, such as that in the 29th frame.

7. Compute the principal moments of area:

$$I_{I,II} = \frac{I_{xx} + I_{yy}}{2} \pm \sqrt{\left(\frac{I_{xx} - I_{yy}}{2}\right)^2 + I_{xy}^2}$$

Equation 4.16. Moment of area about the principal axes of a 2D shape

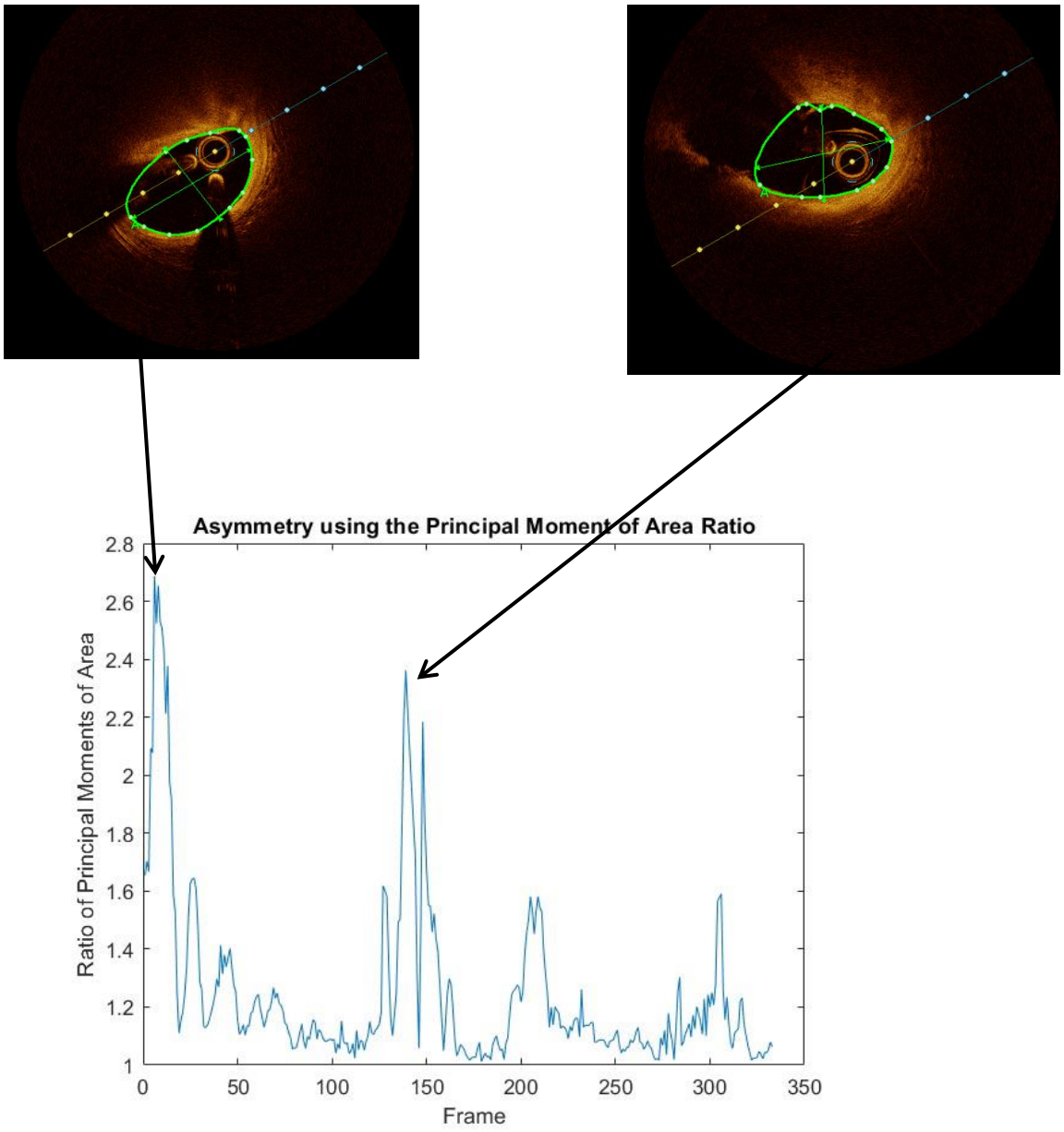

Figure 4.9. Graph showing the ratio of the moment of area about the principal axes for each of the 333 frames. Two frames are chosen to demonstrate ellipticity as shown, which are those with the larger ratio values.

4.4.2.2 Fourier expansion

Another way to assess asymmetry is to examine the coefficients in a Fourier series decomposition of the vessel radius (representing the cross-section geometry in polar co-ordinates. On a particular cross-section in OCT co-ordinates, corrected for the shift of origin to the centroid, the mean radius and the Fourier coefficients can be determined by the Fourier decomposition of $r(\theta)$ (Equation 4.17). θ this the angle that describes the set of points that make up the shape. It is the angular variable.

$$r(\theta) = r_0 + \sum_{i=1}^{N} \left(a_n cos(n\theta) + b_n sin(n\theta)\right)$$

Equation 4.17. The Fourier decomposition equation

The Fourier decomposition describes a shape as a combination of sine and cosine functions. The decomposition consists of different terms, called harmonic modes, whereby each describes a specific geometric feature of the shape. For example, the first term, the 0-theta term (the first bar in Figure 4.10), describes the average radius of the shape. The second term, the 1-theta term (the second bar in Figure 4.10), describes the lateral shift of the shape. The third term, the 2-theta term (the third bar in Figure 4.10), can describe the ellipticity of the shape, which can be very useful to identify non-circular cross-sections of the vessel.

In this section the focus is on the 2-theta term from the Fourier decomposition, and its description of the ellipticity of the vessel. In a healthy vessel, elliptical frames are usually present closer to bifurcation. In a stenosed vessel, elliptical frames can indicate the presence of disease. Figure 4.10 shows the Fourier expansion of to OCT frames, one elliptical and one not.

The 2theta term is more pronounced in the elliptical term expansion. Therefore, an examination of the 2theta term of the Fourier expansion of OCT cross-sections can be used to identify non-circularity, thus disease or bifurcations.

Additionally, an alternative to applying the area-overlap protocol to all frames and rotating each frame individually, the following can be done:

1) The more elliptical frames can be extracted using the 2theta component,

2) The area-overlap optimisation protocol can be applied on these cross-sections to extract the appropriate rotation angle,
3) Linear interpolation of the value of rotation angle to obtain a rotation angle for the remaining OCT frames and rotating them accordingly.

This method has merit because elliptical frames are more effective in finding an orientation that is based on actual anatomical features. Circular frames on circular frames with comparable sizes can result in the area-overlap optimisation protocol being sensitive to segmentation errors.

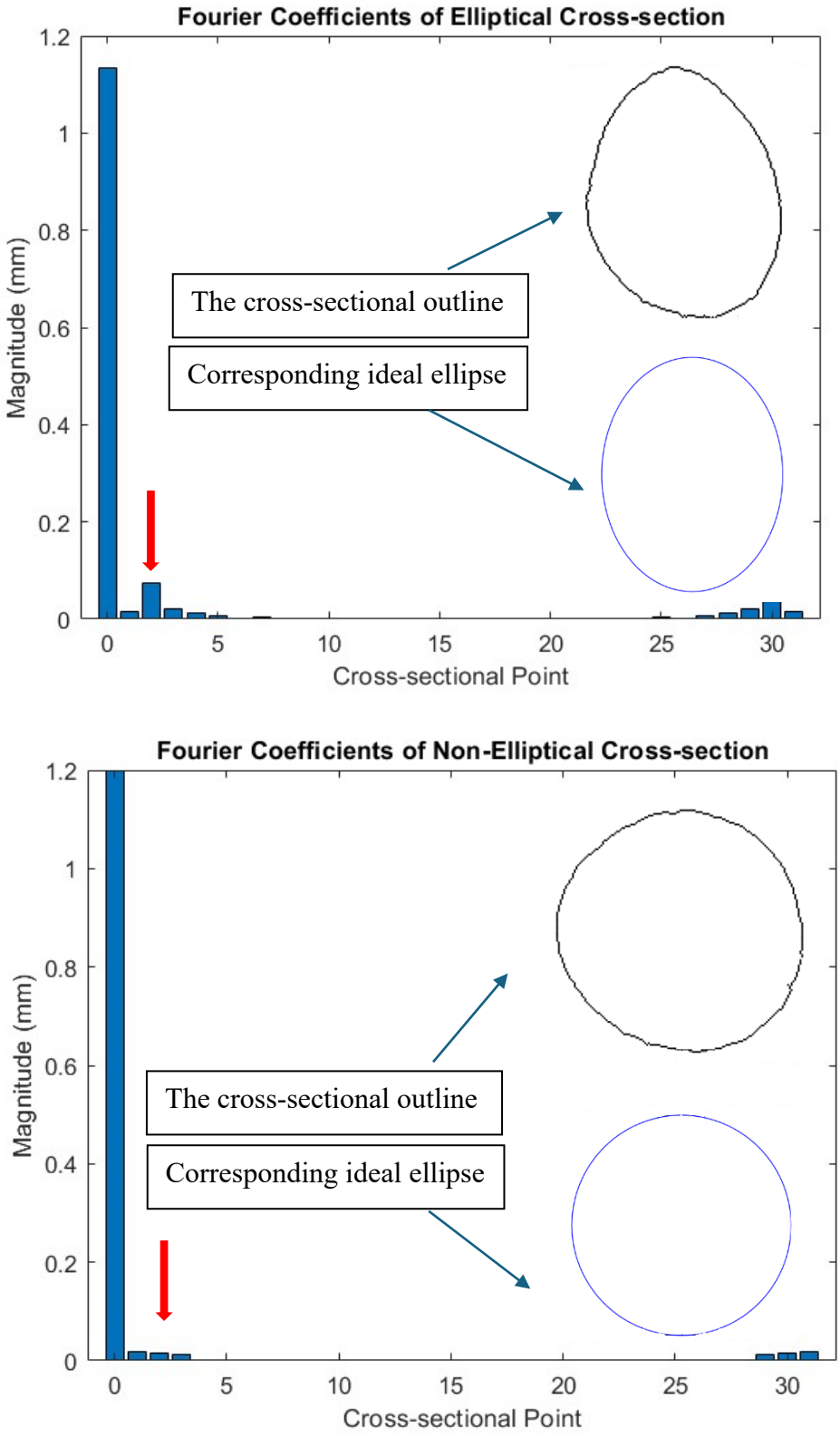

Figure 4.10. The Fourier expansion of an elliptical and non-elliptical frame. The 2theta term (red) is more pronounced for the elliptical frame and can be used to identify non-circularity.

Using the Fourier decomposition and obtaining the ratio between the 2-theta and the 0-theta term (Figure 4.11) the most elliptical frames can be identified.

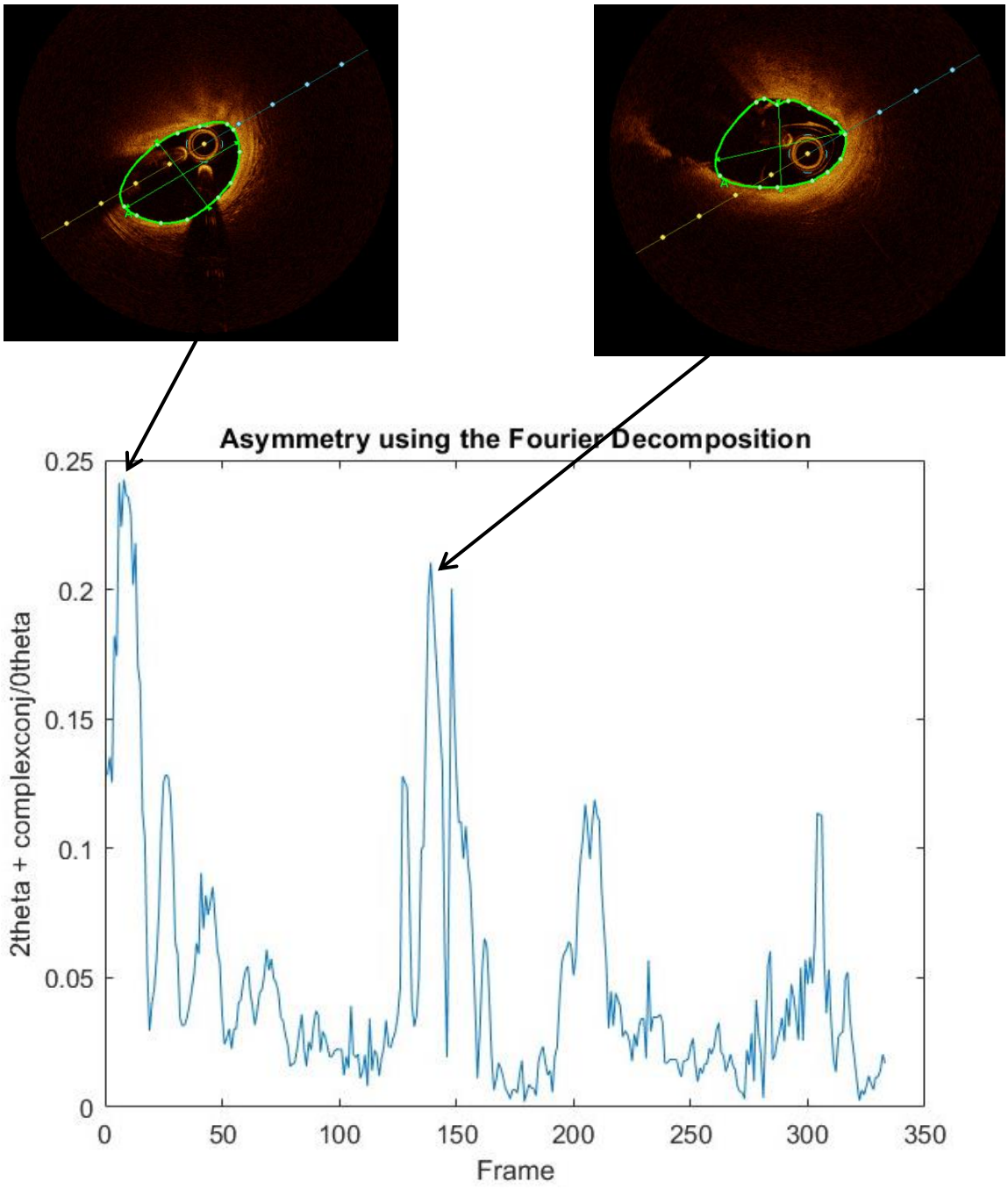

Figure 4.11. A graph of the ratio between the 2-theta and 0-theta coefficients of the Fourier decomposition of each frame. The graph shows two clear peaks that refer to elliptical frames. The frames are also included in the figure.

Of course, the two methods, using the ratio of the principal moments of area and the ratio of the 2-theta and 0-theta terms address distinct properties of the cross-sections, they both identify elliptical frames, which supports the hypothesis that in coronary vessels at bifurcations and at stenoses, the deviation from circularity is elliptical.

4.5 Reflection and summary

This chapter has presented the general methodology for the fusion of anatomical data from the two imaging modalities, CA and OCT. This fusion methodology included both longitudinal alignment and cross-section orientation optimisation. The longitudinal alignment included careful examination of the data obtained from both modalities: Whether they carry meaningful anatomical data from the vessel (non-catheter images), whether they are polluted due to the imaging process (swirl artefact) and whether the sections of the vessel have corresponding data from both modalities. Data not satisfying these criteria were excluded, resulting in a waste of imaging potential. This is further explored in Chapter five. Regarding cross-section orientation optimisation, three optimisation methods were developed, area-overlap and smoothing, which are relative methods, and angio-optimisation, which is a global orientation method. With area-overlap, consecutive cross-sections can be rotated to achieve maximum overlapping area, as the rotational change between consecutive OCT frame acquisitions is not expected to be drastic. The smoothness cost function imposes necessary constraints on the smoothness of the orientation changes along the length of the vessel. Area-overlap optimisation can either be applied on all consecutive cross-sections, and be dampened by smoothing, or it can be applied to select elliptical frames in the OCT run to extract rotation angles that are interpolated to obtain rotation values for the remaining frames. This is because elliptical frames can better inform on orientation compared to the more symmetrical circular frames. The main disadvantage of area-overlap optimisation is its dependence on the orientation of the first (reference) frame, hence being a ‘relative’ optimisation technique. In the future, this can be avoided. Since the frames closer to the bifurcation are usually more elliptical, and it is expected that the major axis of the bifurcation frame is along the normal to the centreline in its plane of curvature, then the appropriate rotation angle of the bifurcation frame can be obtained as the angle which aligns the major axis of the elliptical cross-section with the centreline normal. This rotational angle can be then used as an overhead to the individual frame area-overlap rotational angles, thus advancing this optimisation technique from ‘relative’ to ‘global’.

The third optimisation technique is the angio-optimisation, which uses the CA-greyscale to rotate OCT frames so that the error between the projected OCT-radius and CA-radius is minimised. This can be done using information from both CA-projections to increase accuracy. Although theoretically sound, this optimisation technique is highly dependent on how comparable the radius information from CA and OCT are. Unfortunately, the radius data are not always comparable, especially in sections very proximally in the vessel (further explored in Chapter five), thus compromising the effectiveness of this optimisation technique.

Accordingly, the main result of this chapter is the composite cost function, with weighted terms for all three optimisation methods. It is flexible and can be tailored to cases, depending on which optimisation method is most suitable.

This chapter also discussed the ability to identify key characteristics of the vessel, including bifurcations and lesions, using area tests and asymmetry measures, such as second moment of area and Fourier expansion. This has been illustrated on a case in this chapter.

For this work, twenty patient coronary vessels were reconstructed using the mechanisms described in this chapter, with 100% reconstruction success rate. All reconstructions were performed in under three minutes. The list of reconstructed cases is in Table 1 in Chapter three.

Chapter five further explores OCT data, and its comparison to CA. It also quantifies, in the context of twenty patient-specific cases the differences between both modalities, and the challenges, as well as advantages, associated with the fusion process.

Chapter Five:

Fusion of OCT and Angiography Data for Coronary Modelling

5.1 Overview of fusion

CA and OCT are complementary in nature. If they could be fused together, the anatomical data provided by CA and OCT have the potential to reconstruct and simulate the coronary tree in a more complete manner. Traditionally, coronary 3D models were dependent on the silhouette images that CA provides. Although these reconstructions, at the time, were a significant step forward in the field, they were associated with limitations, as described in Chapter three. When combining two powerful coronary imaging modalities, it is essential that the strengths of both are identified and capitalized on while limiting the shortcomings of each. Determining how the data fits together is also of equal importance.

In context of using both CA and OCT for 3D coronary modelling, the more accurate term is 'fusion'. This is because the data obtained from each modality will be more than just simply combined. They will be intertwined, basing mathematical measurements of CA-derived parameters of anatomical features, such as the vessel centreline, to position OCT-derived vessel lumens, but in an orientation that relates to the original CA projections, etc. Developing a novel method to fuse complementary CA and OCT data fusion, as well compare these data, is the focus of this chapter. Dr Daniel Taylor has contributed to the statistical analysis of the comparison between CA and OCT, which is included in this chapter. The statistical analysis in this chapter was mainly performed as follows:

2) Numerical accuracy testing: Using Bland Altmann bias and limits of agreement
3) Correlation analysis: Due to the small sample size, the data is not parametric. Therefore, a non-parametric test (Man-Whitney U test) was used to assess the difference between groups. The p-value and Spearman's correlation coefficient (r) were computed.

5.2 Outline of the main differences between OCT and CA

For a coronary artery to be imaged using CA, the arteries must be filled with radio-opaque contrast medium. This contrast medium marks the unobstructed path that blood takes proximally to distally in the artery. If we think of the artery as a set of consecutive cross-sections, in healthy areas of the artery, the radio-opaque contrast medium is expected to fill the full cross-section up to the arterial wall. This shows up on the angiogram as a darker grey colour, marking where there is blood flow. On the other hand, if the artery is diseased in a specific cross-section, with plaque obstructing blood flow, the radio opaque contrast medium will not

be able to fill the whole cross-section, only the areas not blocked by disease. Therefore, on the angiograms, this diseased section of the artery will appear as a narrowing, with less contrast (paler).

The heart is a complex 3D organ, with the epicardial coronary arteries coursing along the epicardial surface. CA is a 2D imaging modality. Naturally, therefore, CA represents a significant reduction in anatomical information. Extracting the shape of a structure from a single orientation, or view, can be challenging. Some views can make the vessel appear shorter. The divergent x-rays can also make the arteries closer to the source (like the LCX) appear bigger than they really are (John Lampignano, 2017). However, the coronary vessels are both curved and tortuous, therefore, the impact on the apparent length, also known as foreshortening, and on the apparent shape is significant, and even more so when it comes to computational fluid dynamic techniques. Imaging a curved section of the artery parallel to the plane of curvature may cause the curved section to appear straight and shorter than its real length, which is a misrepresentation of the anatomy. Treatment choice and computational modelling results are thus related to the choice of view/projection angles. This is especially important in the cases where stenotic plaque is eccentric stenosis and not concentric. The direct impact this would have on the angiogram is that the radio-opaque contrast medium will be more present and visible in specific views, and not all, resulting in this section of the artery appearing narrower in some views compared to others. This is a clinical challenge, where one view of the artery indicates the presence of disease and the other does not.

The challenges described above, namely the impact of projection angle choice, foreshortening and eccentric stenosis are not applicable to OCT. OCT being an intravascular imaging technique produces contours that represent the vessel wall. These contours, which follow the vessel wall, clearly show stenosed cross-sections, whether the stenosis is eccentric or not. In the ideal scenario, the OCT catheter with the camera is pulled distally to proximally from inside the vessel, with the camera at the centre of the cross-section, in the plane with the cross-section being imaged. However, the OCT catheter is left to move freely inside the vessel, which causes the camera to get closer to specific sections of the wall and then move away to other sections. This is especially evident in curved sections whereby the catheter, due to conservation of inertia, is expected to come into contact with the vessel wall and then readjust. This has little to no impact on the extracted contour. However, it is not always the case that the camera is completely in the plane of the cross-section. This may cause the resulting cross-section to appear larger in area than it originally is. This is more significant in sections of the vessel where

it is very curved or tortuous, and the pullback speed of the catheter is faster than the recovery of the catheter orientation.

5.3 Discarded anatomical data

When assessing the quality of data from an OCT run or from CA for fusion, two parameters must be considered

- First, what percent of the anatomical data has corresponding sections from both imaging modalities? In other words, is there enough data from both modalities, that correspond to the same section of the vessel, for reconstruction from fused CA-OCT to occur? This was explored in Chapter four, whereby the CA and OCT diameters were shifted for maximal alignment and the non-corresponding sections were discarded (See Chapter four, section 2).
- Second, are there any additional reasons why any sections of the anatomical data that satisfy the first criterion cannot be incorporated into the fusion process?

The second question is explored in this section.

In this study, coronary arteries from twenty patients with coronary artery disease were reconstructed, as outlined in Chapter three, section 2.5, from fused CA-OCT and a pattern was found regarding the usefulness of the anatomical data. It was found that for all cases, sections of data were discarded. This was for the following reasons:

- CA data from the very proximal segments of the vessel (such as the LMS) usually had parallel epipolar lines in the paired images. This limited the methods described in Chapter three which rely on perpendicular epipolar lines. Some CA data from the very proximal sections had to be excluded in some cases.
- CA data from the very distal segments of the vessel were occasionally too pale (lacking contrast) compared to the proximal sections, and this made it challenging to discern the luminal edge from the background. The distal CA data therefore had to be excluded in some cases.
- In some cases, acquired OCT frames extended proximally, beyond the arterial ostium, into the guiding catheter and these had to be discarded.
- Some acquired OCT frames included ‘swirl artefact’. This occurs where there has been insufficient clearance of blood from the imaged field. Typically, it occurs around the

catheter tip where contrast is infused into the coronary arteries through the guiding catheter. As described previously, blood (cellular) obscures the light waves emanating from the OCT lens and so such frames are discarded.

Table 5.1 shows the number of discarded frames per run for each of the twenty cases, and the length of vessel this corresponds to. Figure 5.1 illustrates the trend between cases, showing that on average, 21.44% of the OCT data is discarded either because it is from the catheter or due to the swirl artefact.

Case	Frames	Length (mm)	Percentage (%)	Case	Frames	Length (mm)	Percentage (%)
1	61	12.2	16.3	11	99	9.9	18
2	100	10	18.2	12	75	7.5	13.6
3	222	22.2	40.4	13	181	18.1	32.9
4	45	9	12	14	27	2.7	4.9
5	41	8.2	10.9	15	245	24.5	44.5
6	32	3.2	5.8	16	221	22.1	40.2
7	108	10.8	19.6	17	214	21.4	38.9
8	57	5.7	10.4	18	60	6	10.9
9	61	6.1	11.1	19	108	21.6	28.8
10	206	20.6	37.5	20	52	10.4	13.9

Table 5.1. This table shows, for all twenty coronary vessel cases, the number of frames that were discarded either because they are cross-sections of the catheter, or because they are polluted by the swirl artefact. This is translated into the length of vessel it corresponds to and put into context to quantify how much of the vessel (percentage of total length) this represents.

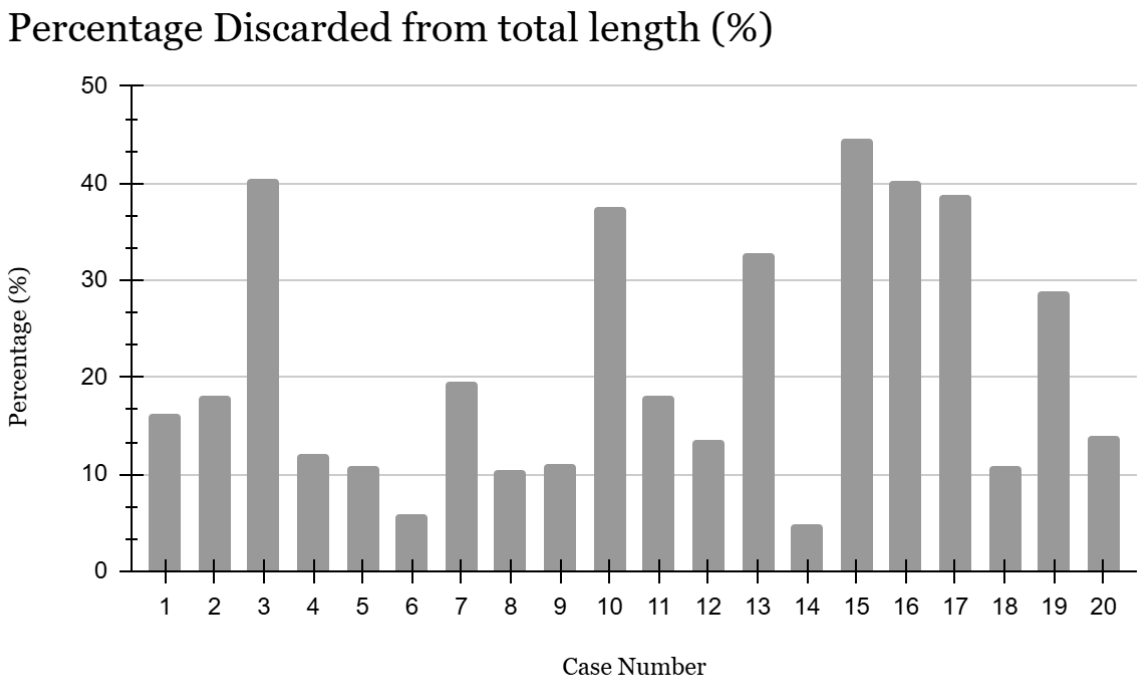

Figure 5.1. This is a visualisation of the data presented in Table 5.1, showing the mean value for the percentage of equivalent OCT vessel length that is discarded either due to imaging the catheter or to the swirl artefact.

With a further look into the discarded data from the LAD (15.66 ± 9.7 mm) and diagonal vessels (25.34 ± 13.84 mm), that data does not suggest a significant difference between the discarded data percentages for each (P 0.10, t-score -1.75), ruling out a trend for one of these vessel types experiencing more swirl during OCT imaging than the other. If on average, 21.44% of all OCT runs are discarded solely due to catheter/swirl artefact, this is an indication that much data is wasted. However, the region of interest, the bifurcation region, is captured fully, therefore reducing the impact of the discarded frames on the current workflow.

5.4 Comparison of the imaged CA and OCT diameters

For the remainder of the frames, CA-derived diameter data were interpolated and matched to OCT results according to normalised vessel length (i.e., for every OCT measurement, a corresponding CA-derived diameter was yielded at the same location of OCT measurement). The CA maximum diameters were found to be significantly different ($P < 0.01$), while the respective minimums were found to be not significantly different ($P > 0.01$) using an independent variable t-test. This is an indication that when imaging smaller diameters, both imaging modalities report similar diameters, which might suggest that there is better agreement between the modalities in the distal segments of the vessels when compared to their proximal counterparts.

With a further look into which segments of the vessel have the highest diameter agreement between CA and OCT, the diameters were divided into three sections:

1) Pre-bifurcation (Frames 1 → '*trouser*' – 11),
2) Bifurcation and (Frames '*trouser*' – 10 → '*trouser*' + 10)
3) Post-bifurcation (Frames '*trouser*' + 11 → end).

The norm of the vector of differences between the CA and OCT diameters for each segment was computed (Equation 5.1) and is shown in Table 5.2.

$$norm\ of\ diameter\ differences = norm\left(\begin{Bmatrix} diam_{CA\,(1)} \\ diam_{CA\,(2)} \\ \vdots \end{Bmatrix} - \begin{Bmatrix} diam_{OCT\,(1)} \\ diam_{OCT\,(2)} \\ \vdots \end{Bmatrix}\right)$$

Equation 5.1. Computing the norm of the difference vector between CA and OCT diameters.

The pre- and post-bifurcation mean values and standard deviations were 7.53 ± 3.73 mm and 5.19 ± 2.7 mm, respectively. The pre-bifurcation mean was greater, thus suggesting greater disagreement in the proximal segments. The difference norms from the pre-bifurcation segment were significantly different from the bifurcation segment ($P < 0.001$, U-statistic = 326.0), while the post bifurcation and bifurcation segments showed non-significant differences ($P > 0.05$, U-statistic = 133.5).

All in all, it can be concluded that from the data above, the diameters from CA and OCT are more in agreement when imaging smaller vessel sections (possibly more distally) when compared to proximal sections. With a closer look at the sections of the bifurcation, the diameter values from CA and OCT have deviated from each other more in the pre-bifurcation segments, compared to the bifurcation and post-bifurcation segments, further supporting the conclusion that the larger the diameter is, the worse the CA-OCT agreement.

	Difference norm (Pre-Bifurcation)	Difference norm (Bifurcation)	Difference norm (Post-Bifurcation)
1	7.66	4.07	5.99
2	5.64	2.39	5.70
3	7.22	2.26	3.26
4	4.54	6.57	2.69
5	5.34	4.17	4.27
6	10.93	1.13	8.80
7	6.60	5.75	7.40
8	19.17	5.81	9.69
9	3.70	1.72	3.03
10	5.47	7.62	11.89
11	10.32	4.03	2.92
12	6.93	0.82	1.72
13	5.56	2.23	3.08
14	5.98	1.58	3.26
15	5.54	2.79	4.81
16	8.94	8.71	6.98
17	6.07	7.45	6.14
18	14.29	3.83	5.98
19	4.33	2.60	3.15
20	6.34	1.85	2.97

Table 5.2. The values of the norm of the vector of differences between the CA and OCT diameters for each segment (pre-bifurcation, bifurcation and post-bifurcation).

As an additional way to assess diameter agreement is through investigating correlation using Spearman's correlation coefficient (r). Mean values were compared with the paired t-test and Wilcoxan signed-rank test as appropriate. Agreement between CA and OCT-derived diameter data was assessed with Bland Altman plots. Simple linear regression modelling was used to investigate for interaction between agreement with vessel size and position. To aid data visualisation, the dataset was binned by grouping every twenty consecutive data points (Figure 5.3). The following analyses were conducted with R studio version 2024.04.2+764.

A total of 6,620 matched diameter data points were generated from the twenty arteries. There was a modest relationship between CA and OCT derived diameters (r 0.68, $p<0.0001$). Mean CA-derived diameter (2.75 ± 0.67 mm) was significantly lower than mean OCT-derived diameter (2.99 ± 0.74 mm, $t = 33.9$, $p<0.0001$). Across all cases, CA-derived diameter underestimated OCT derived diameter by 0.23mm (95% LOA -0.13 to 0.59). There was a strong linear interaction between mean diameter and agreement, with CA underestimating OCT by a larger amount for larger diameter arteries ($p_{interaction}<0.0001$) (Figure 5.2). There was also a linear interaction between agreement and normalised length, with CA underestimating OCT by a larger amount in more proximal arteries ($p_{interaction}<0.0001$) (Figure 5.3).

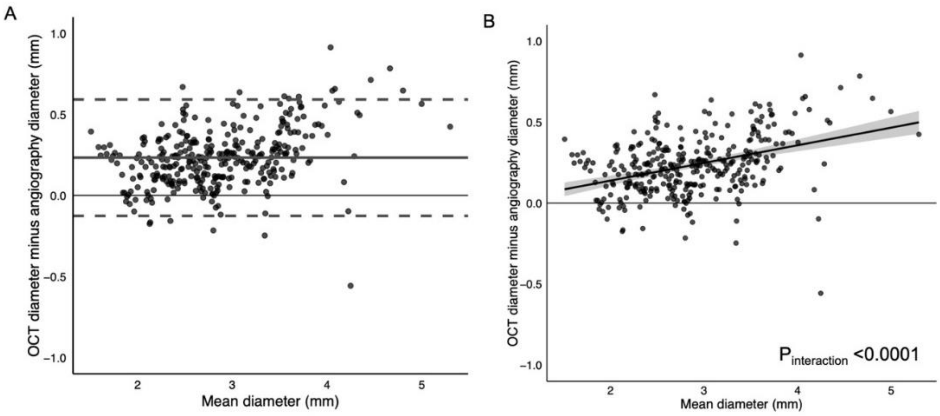

Figure 5.2. Agreement as a function of vessel size. Both figures display binned data. Panel A: Bland Altman plot: The overall positive bias means that OCT measures the arterial diameter larger than CA; mean bias = 0.23 mm (95% LOA -0.13 to 0.59). Panel B: Simple linear regression analysis demonstrating how this effect is more pronounced in regions of artery with larger diameter.

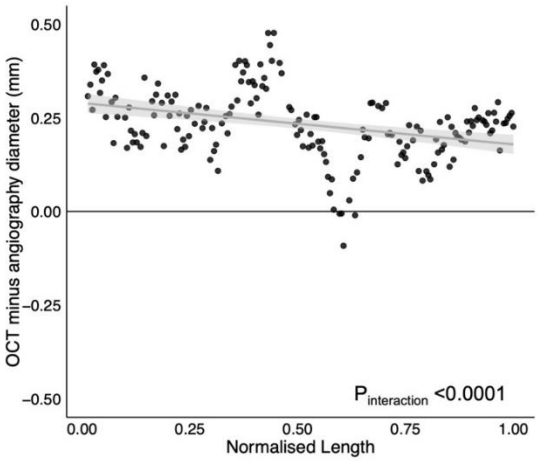

Figure 5.3. Agreement as a function of vessel length. At more proximal positions in the artery, there is a greater underestimation of diameter by angiography compared with OCT ($P_{interaction}$<0.0001)

All in all, the data from the twenty cases analysed in this thesis suggests that for larger sections of the vessel, including the proximal segments, the discrepancy between the reported diameters for corresponding sections of the vessel from OCT and CA is higher than for smaller diameter sections. In general, the discrepancy between OCT and CA when reporting diameters is approximately 0.23 mm, which is similar to the findings of other studies (Antonsen et al., 2015).

5.5 Vessel ellipticity and its potential for clinical use

Due to the distinct nature of OCT compared to CA, namely it being an intravascular imaging technique, certain aspects of the anatomy that were never captured with CA are now possible to be captured and analysed, providing an insight into the state of the vessel being imaged. One such aspect is vessel ellipticity. As discussed in Chapter four, ellipticity is a measure of non-circularity, and is the ratio between the 2theta and zero-theta terms as presented in Chapter four. A perfectly circular contour is expected to have zero ellipticity, however, due to the nature of the vessels, consistent branching of the vessel, disease, or even the effect of the OCT catheter and pressure wires on the vessel wall, the contours are never perfectly circular; a degree of ellipticity always exists.

$$Ellipticity = \frac{|second\ harmonic|}{|fundamental\ frequency|}$$

Equation 5.2. Computing the ellipticity of the OCT cross-sections as the ratio between the magnitude of the second harmonic and the fundamental frequency of the Fourier decomposition of the vector of radii.

Table 5.3 shows the norm and the maximum ellipticity for all twenty cases. Maximum ellipticity varies from 0.19-0.43. The corresponding frames for the maximum and minimum maximum ellipticity are shown in Figure 5.4. An interesting next step can be to investigate the impact of the bifurcation angle on the ellipticity of the bifurcation contours, and whether this translates into predisposition for disease in the bifurcation region or not.

Case	Ellipticity norm	Ellipticity max	Case	Ellipticity norm	Ellipticity max
1	1.73	0.34	11	2.6	0.24
2	1.76	0.2	12	2.32	0.35
3	2.07	0.26	13	1.82	0.22
4	1.14	0.19	14	2.86	0.23
5	1.27	0.24	15	2.06	0.33
6	2.44	0.34	16	1.88	0.29
7	2.32	0.31	17	1.88	0.21
8	3.55	0.39	18	1.83	0.22
9	2.69	0.34	19	1.49	0.27
10	2.32	0.43	20	1.66	0.27

Table 5.3. The values of the norm of the ellipticity vector for all twenty cases, as well as the maximum ellipticity value for each case.

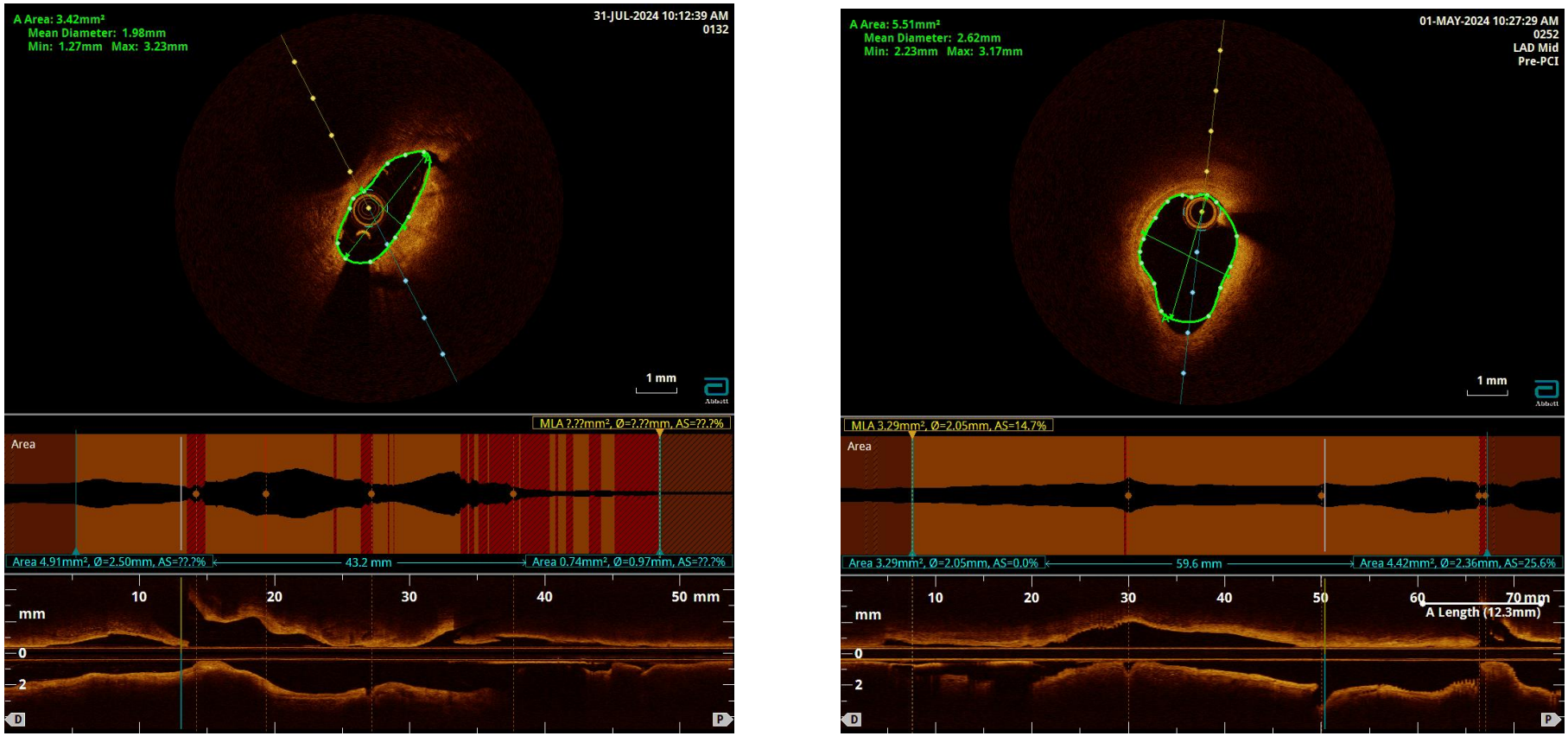

Figure 5.4. The cross-sections having the maximum (Case 10) and minimum maximum (Case 4) ellipticity values across all twenty cases. The cross-section from Case 10 appears to be stenosed at the bifurcation, contrary to that from Case 4 (healthy bifurcation), thus it is expected that the combination of bifurcation and stenosis will produce the largest value of ellipticity.

In this section, the hypothesis tested was that more elliptical sections of the vessel indicate either presence of bifurcation or stenosis. Figures 5.5-5.7 show the ellipticity measures for all frames in cases 1, 4 and 6, respectively, with the frame with the global maximum peak ellipticity for each case. These cases were chosen since, as shown in Table 5.4, they included a healthy case with a bifurcation, a healthy case with multiple bifurcations and a stenosed case with a bifurcation, thus inclusive of the anatomical phenomena being discussed in this section. Table 5.4 shows all twenty cases, the identified peaks, whether the peaks indicate bifurcation or stenosis, and in the case that the peak is a bifurcation, how far away is it from the 'trouser' frame, where the vessels are branching off. For example, for case 1, there was one main ellipticity peak. This peak, as outlined in Table 5.3, was at a bifurcation, exactly where the vessels are branching off. For case 4, there were three main peaks. All were indicative of bifurcations in the vessel, all within 2 frames (0.4 mm) from where the 'trouser' frame is. Similarly for case 6, three main peaks were identified, however, two were indicative of bifurcations and one was a stenosed region, all within 28 frames (2.8 mm) from the 'trouser' frame.

As shown in Table 5.4, computing ellipticity and identifying its peak values for full OCT runs was reliable when identifying bifurcations and stenoses. All peaks either indicated bifurcations or stenoses, with no false alarms. It would be interesting to expand this work to a larger scale with more cases to determine the cases where this way of identifying bifurcations and stenoses might fail.

The right-most column of Table 5.4 shows how different the predicted ellipticity bifurcation frame was from the 'trouser' frame. The maximum discrepancy was thirty frames (3 mm). Accordingly, if a clinician wanted to identify the 'trouser' frame for stent implanting, for instance, this work has shown that ellipticity can predict the location of the 'trouser' frame within an error of 3 mm. This measure was not possible before with CA and has the potential to save time in the clinic and serve as a decision support tool, especially in complicated areas needing stenting such as bifurcations.

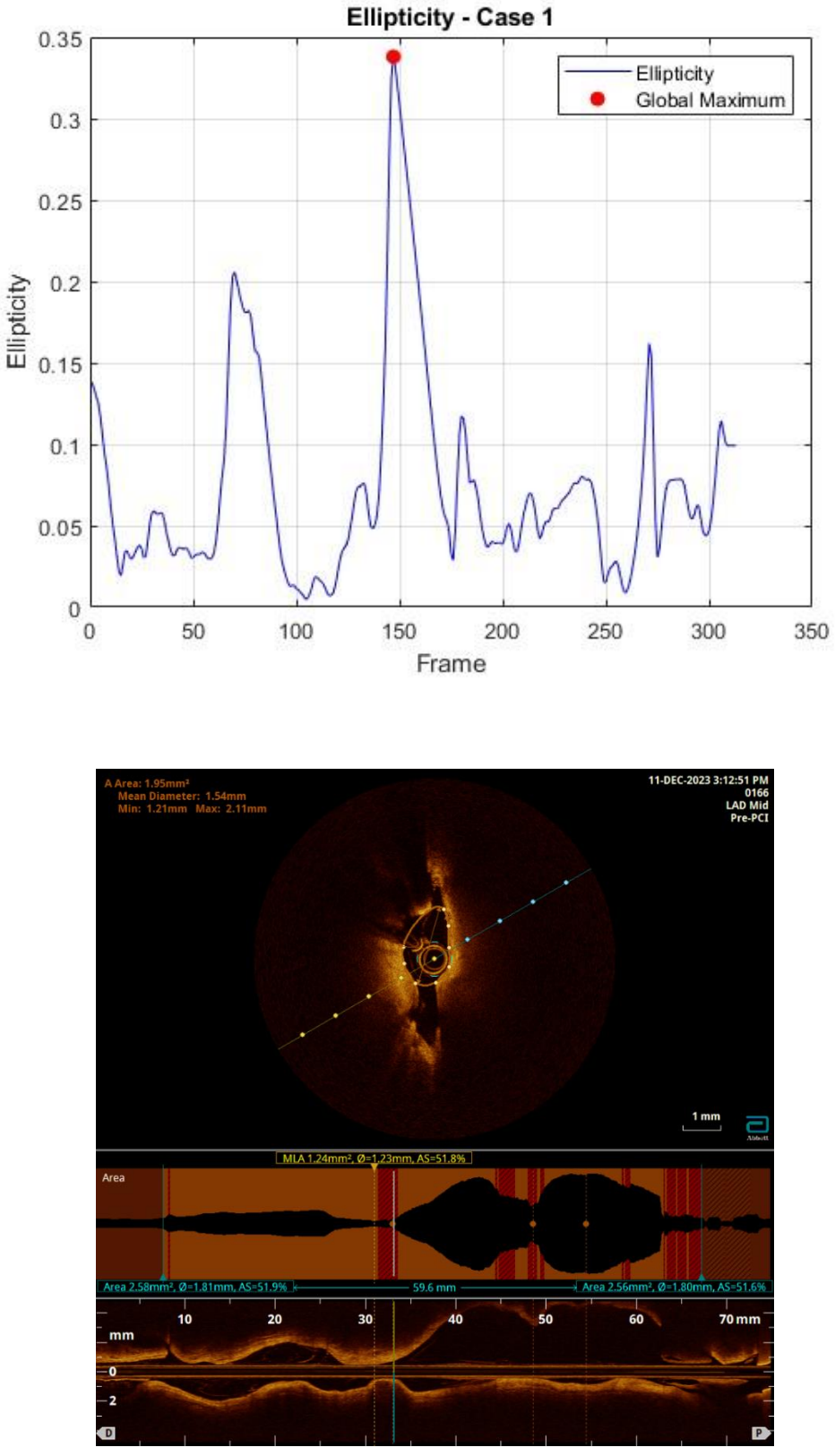

Figure 5.5. (top) The ellipticity for all frames in case 1 (bottom) frame with the global maximum peak ellipticity.

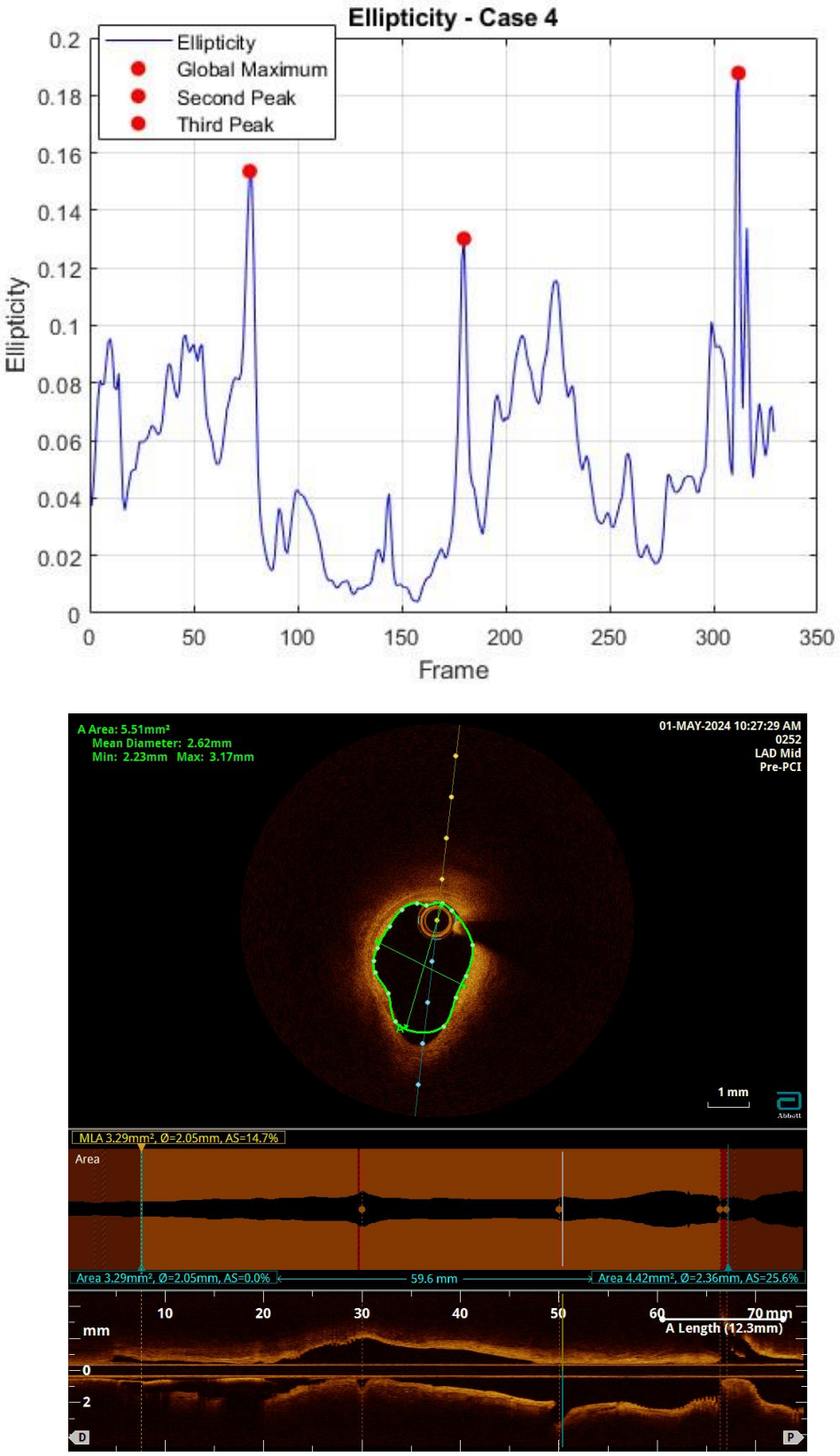

Figure 5.6. (top) The ellipticity for all frames in case 4 (bottom) frame with the global maximum peak ellipticity.

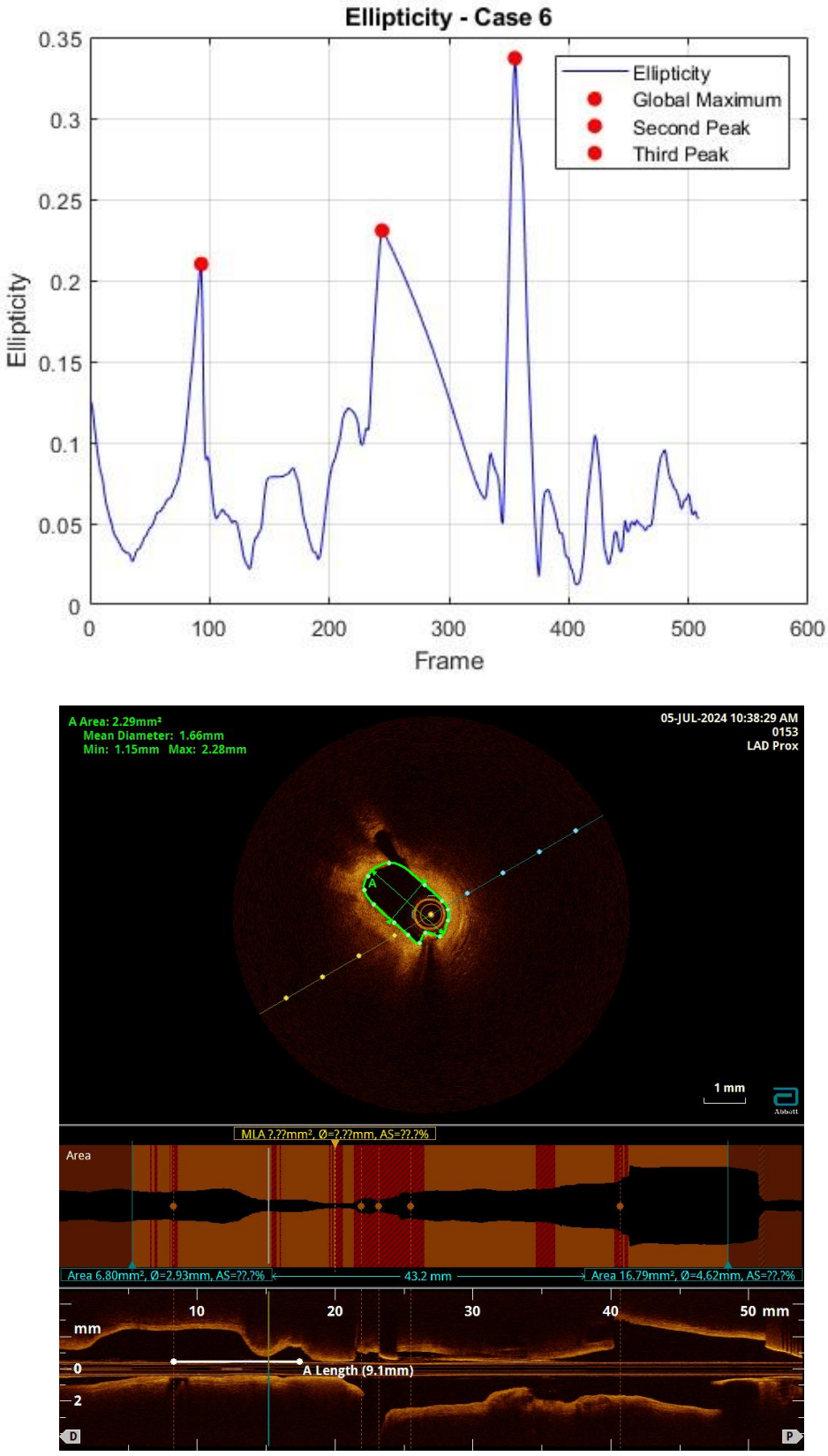

Figure 5.7. (top) The ellipticity for all frames in case 6 (bottom) frame with the global maximum peak ellipticity.

Case	Peak Type	How many frames away from the 'trouser' frame?
1	Bifurcation	0
2	Bifurcation	13
	Stenosis + Bifurcation	30
3	Bifurcation	1
	Stenosis	-
	Bifurcation	4
4	Bifurcation	2
	Bifurcation	2
	Bifurcation	0
5	Stenosis	-
	Bifurcation	2
6	Bifurcation	6
	Bifurcation	28
	Stenosis	-
7	Bifurcation	7
	Bifurcation	3
8	Bifurcation	5
	Stenosis	-
	Stenosis	-
	Stenosis	-
9	Bifurcation	3
10	Bifurcation	7
11	Stenosis	12
	Bifurcation	-
12	Bifurcation	12

13	Stenosis	8
	Bifurcation	-
14	Bifurcation	17
	Stenosis + Bifurcation	18
	Bifurcation	11
	Bifurcation	13
	Stenosis	-
15	Bifurcation	0
	Stenosis	-
16	Bifurcation	0
17	Bifurcation	10
18	Stenosis + Bifurcation	1
19	Bifurcation	1
20	Bifurcation	2

Table 5.4. The identified peaks for all twenty cases, whether the peaks indicate bifurcation or stenosis, and in the case that the peak is a bifurcation, how far away is it from the 'trouser' frame, where the vessels are branching off.

It is important to note that the contours as extracted from Abbott's OCT machine, and thus, the ellipticity measurements of the contours, are highly dependent on Abbott's software for contour edge detection. For most contours, the edge detection software performs well, however, for more tricky contours, such as those at the bifurcation, the edge detection can miss the true edges of the vessel, as shown in Figure 5.8, thus impacting the ellipticity measurements. Usually, when the Abbott software is not confident in a specific contour, it presents it in an orange colour, for it to be rechecked by the user. In this thesis, the orange contours are discarded, and interpolation occurs between the closest green contours pre and post the orange contour to replace it. This is done since the frame-to-frame distance is small, 0.1-0.2 mm, thus drastic changes are not expected between consecutive frames.

With the forementioned challenges with contour extraction, Table 5.3 still shows reliability in ellipticity measures to identify areas of bifurcation/stenosis. The potential main issue with identifying stenoses using ellipticity is in the cases where plaque is uniformly distributed around the vessel wall, not affecting circularity very much. However, plaque usually builds up gradually in a vessel, so there is not one frame that can be identified, such as the 'trouser' frame to indicate stenoses. Fortunately, it has been previously reported that most coronary stenoses are eccentric (Yamagishi et al., 2000). Anyway, for the minority of cases where the stenoses are concentric, the best way might be to investigate vessel diameter changes and not ellipticity.

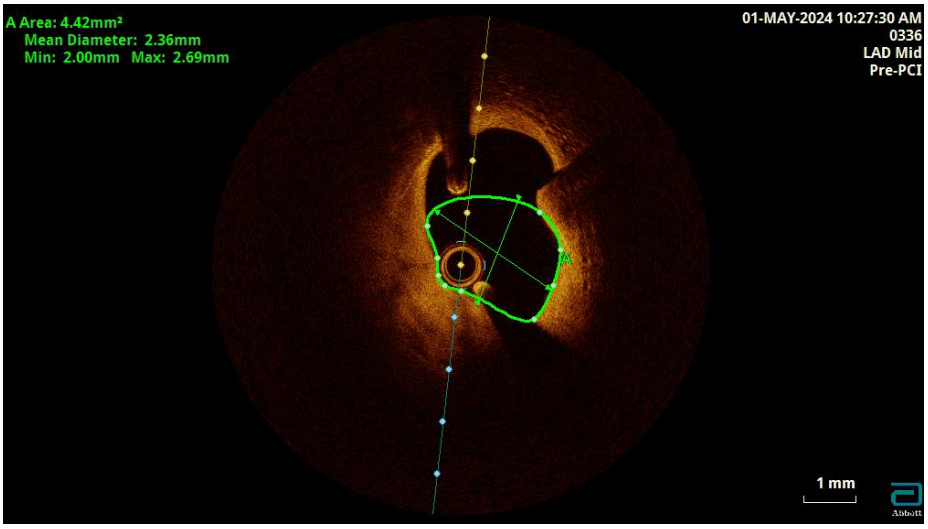

Figure 5.8. Example of a frame from the Abbott OCT machine, where the edge detection algorithm misses the true edge of the vessel yet is still shown in green.

5.6 The fusion protocol and summary

As described in Chapters three and five, anatomical data from CA and OCT are complementary. Table 5.5 describes how the data was acquired, extracted and fused, in order.

Acquired Data	Conditions
Two OCT pullbacks from both branches	- Long enough common stem section to allow segmentation of a pre-bifurcation section.
Two paired angiographic images > 30° apart	- Obtained from two distinct projections that are more than thirty degrees apart and that open the bifurcation in question as much as possible. - Angiograms show the start and end of the OCT pullback (visibly show the catheter retracted from the distal to the proximal end) to guide the fusion of the CA centreline with the OCT pullback. - ECG-gating is needed to know when the heart is in its end-diastolic phase, and the vessels are in maximum dilation for segmentation.
Extracted Data	**Processing**
Angiographic centreline of each vessel	- 3D normal vectors to the bifurcated centreline model at every centreline point obtained. - Fitted through the bifurcation protocol presented in Chapter six to produce a branched centreline model.
OCT-derived lumen contours	- Contours rotated according to the 3D normal vectors to obtain their appropriate orientation with respect to the angio-centreline branched model.
Processing and Final Product	
OCT-derived lumen contours appropriately orientated and appropriately positioned on the angiographic centreline.	

Table 5.5. Description of how OCT and CA data were fused for modelling, starting from data acquisition and data processing to the final 3D product.

For single vessel modelling from both CA and OCT, the longitudinal position of the OCT frames on the CA-centreline and the orientation of the frames with respect to each other and with respect to the centreline are essential. Both aspects were discussed in Chapter four, starting with the extraction of the diameter data from CA and OCT and the alignment and discarding of the non-corresponding sections, followed by the description of the three different methods for OCT cross-section orientation: Area-overlap optimisation, angio-optimisation and smoothing. A composite cost function that includes a term for each method with a weighting factor, that minimises:

1) The total non-overlapping area between consecutive cross-sections,
2) The error between the projected OCT radius and the CA-radius
3) The rotational change between consecutive cross-sections

was also presented.

In conclusion, this chapter has thoroughly examined the anatomical data from OCT and identified areas where the data is not useful for fused reconstruction and discarded such areas. These included areas where the catheter was imaged, or the swirl artefact interfered with the segmented vessel contours. The data diameters from CA and OCT were also compared, aligned and the sections of the vessels with no corresponding anatomical data from both modalities were discarded. This allowed a further examination of the differences between the data derived from CA and OCT, which showed a systematically smaller diameter extracted from CA when compared to OCT, with better agreement between the values from the two modalities in areas with smaller stenoses, whether from the bifurcation regions or from the post-bifrucation ends of the vessels. Accordingly, the fusion process of the polished OCT and CA data was presented, whereby the OCT frames are appropriately positioned onto the CA centreline, and 3D, fused, single vessel reconstructions of the coronaries were produced. The reconstructions of cases 6,7 and 14 are shown in Figure 5.9, overlayed on their equivalent CA-only reconstructions. It is important to note that the OCT reconstructions shown in Figure 5.9 are all before any additional surface smoothing was performed. All CA and CA-OCT reconstructions for the twenty cases are shown in Appendix 1, alongside their chosen CA images.

This marks the completion of CA-OCT fusion. The same protocol is followed to fuse data for branching vessel modelling, which is discussed further in Chapter six.

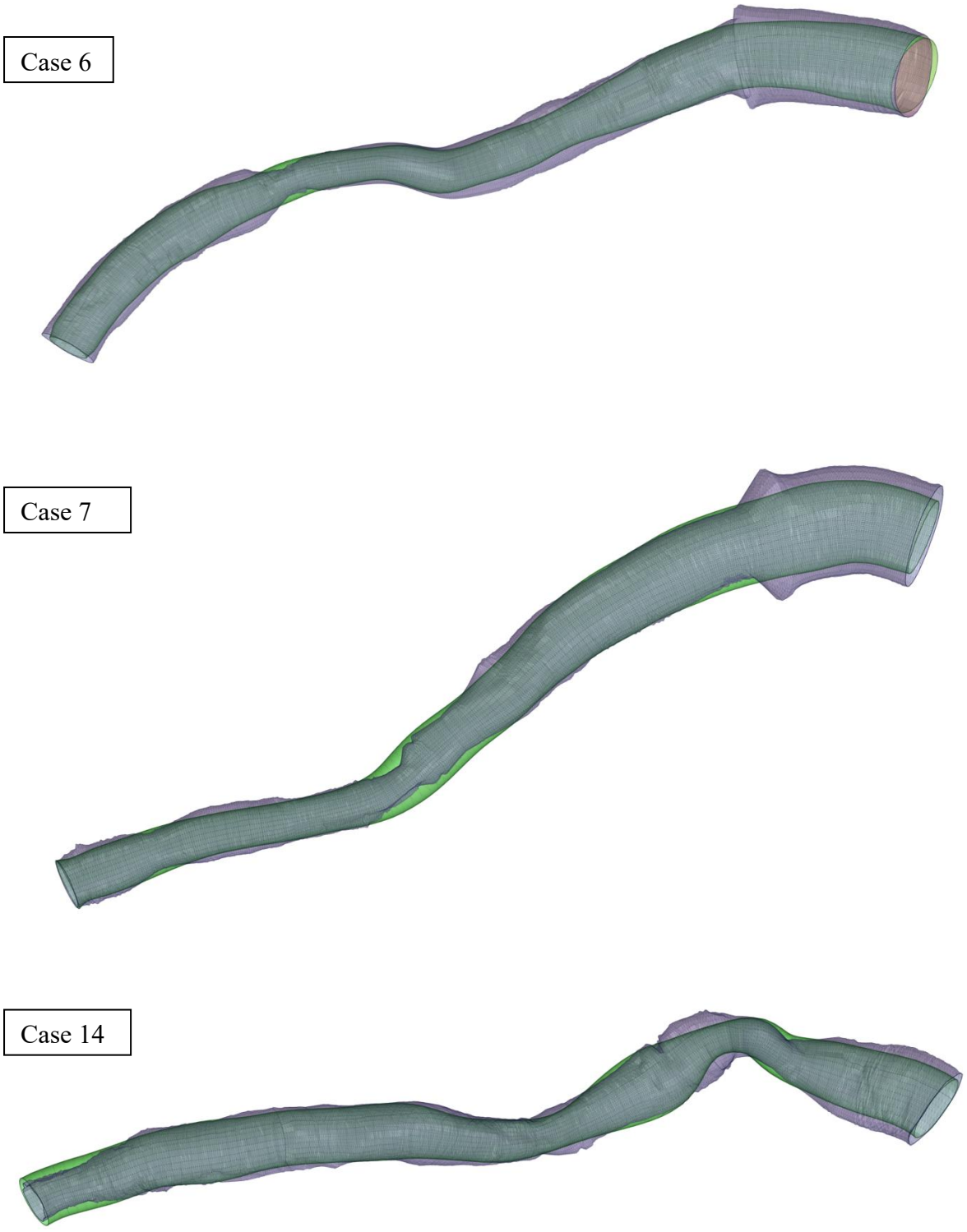

Figure 5.9. 3D reconstructions of coronary vessels from cases 6, 7 and 14. The reconstructions are presented here before any additional smoothing has been performed on the surface prior to CFD. (OCT = purple. CA = green).

Chapter Six:

Development of a Method for Reconstructing 3-D Coronary Arterial Bifurcation Anatomy

6.1 Overview of the bifurcation reconstruction protocol

In this chapter, I describe the development of a novel methodology for 3D coronary bifurcation reconstruction. It is demonstrated on vessels segmented from CA only, however, the same protocol is followed when modelling branches of vessels from CA and OCT, after the data is fused as shown in Chapter five.

6.2 Segmentation of individual branches

The first step to the reconstruction bifurcating vessels is to segment the individual vessels that make the branches. Since bifurcations involve a main vessel and a side branch, the paired CA images that are selected for segmentation must both show the main vessel and its side branch in sufficient detail for reconstruction of both branches.

For simplicity, the work described in this thesis focused on acquiring main and side branch data from the same pair of angiographic images. The use of independent pairs of angiograms that each optimise imaging for each of the separate vessels may be more accurate, but if this approach were adopted, patient movement, cardiac motion and breathing all contribute to a misalignment of the reconstructed vessels, and this would require complex correction along with increased user input. This was deemed an unnecessary complication, especially given that final goal was a tool that only extracted centreline data from CA, with the luminal surface being derived from the fused OCT data. Yes, certain angiographic views are preferred for specific vessels, however, in this work we were able to specifically choose cases where the same two views were sufficient for the segmentation of both vessels, which is what other studies have found to be plausible (Green et al., 2005a). However, for the bifurcation code to be more widely applied in the clinic, it would benefit from a development that renders it flexible to accept main vessels and side branches to be segmented from the same pair, from distinct pairs, or one same and just one distinct pair. The pair used for demonstration is the flagship case LAD-Diagonal pair and is presented in Figure 6.1, using the two views LAO 0.24 CRA 35 and LAO 42 CRA 32.47. As previously stated, this is a NGH case, that was specifically chosen for demonstration because it exhibits a combination of stenotic and bifurcation regions, which challenged the mathematics of the protocol being presented here.

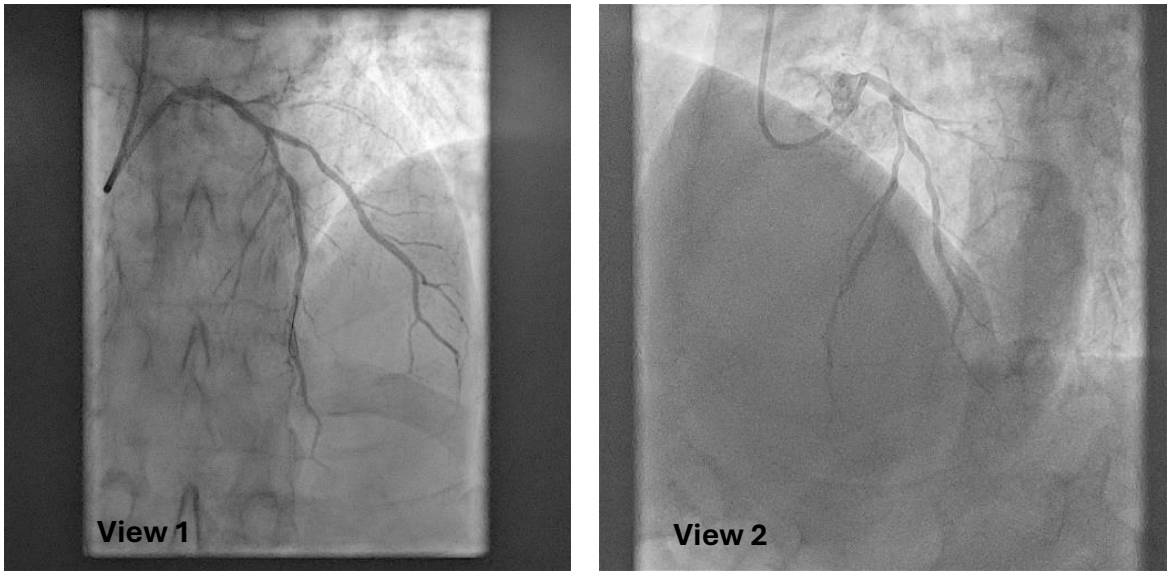

Figure 6.1. The two CA views chosen for the flagship case (LAD-Diagonal): LAO 0.24 CRA 35 and LAO 42 CRA 32.47. this is a NGH case, that was specifically chosen for demonstration because it exhibits a combination of stenotic and bifurcation regions, which challenged the mathematics of the protocol being presented here

The main and side branch being segmented using the segmentation tool means that their 3D centrelines as well as their radius information at every point on the 3D centreline are extracted. This is used as the main input to the bifurcation tool. The 3D centrelines of the main and side branch are expected to overlap in the proximal, common stem section, pre-bifurcation, since this is the shared anatomical feature between them. However, the centrelines, as shown in the example in Figure 6.2, are close to each other but do not perfectly overlap where expected. This is most likely due to specific parts of the segmentation procedure that are done manually and are thus prone to small errors that can propagate. For example, at the earliest stage of CA segmentation, the user must input manually the desired proximal and distal points, for the vessel to be segmented between the two designated points. Since the segmentation procedure must be done twice for a bifurcation case, once for each vessel, it is very unlikely that the user choses the exact proximal point twice. Additionally, the segmentation tool interpolates automatically the centreline, between the operator-selected points, to create the full centreline, meaning that for the common stem sections of the centrelines to be completely overlapping, they must contain the same points. For this case, the difference between the proximal points for both vessels is 0.966 mm and the pixel size is 0.4012 mm x 0.4012 mm which is

approximately 2.4 pixels. The solution to this problem lies in finding the bifurcation points on each vessel and using one as an anchor point, which is described in the next section.

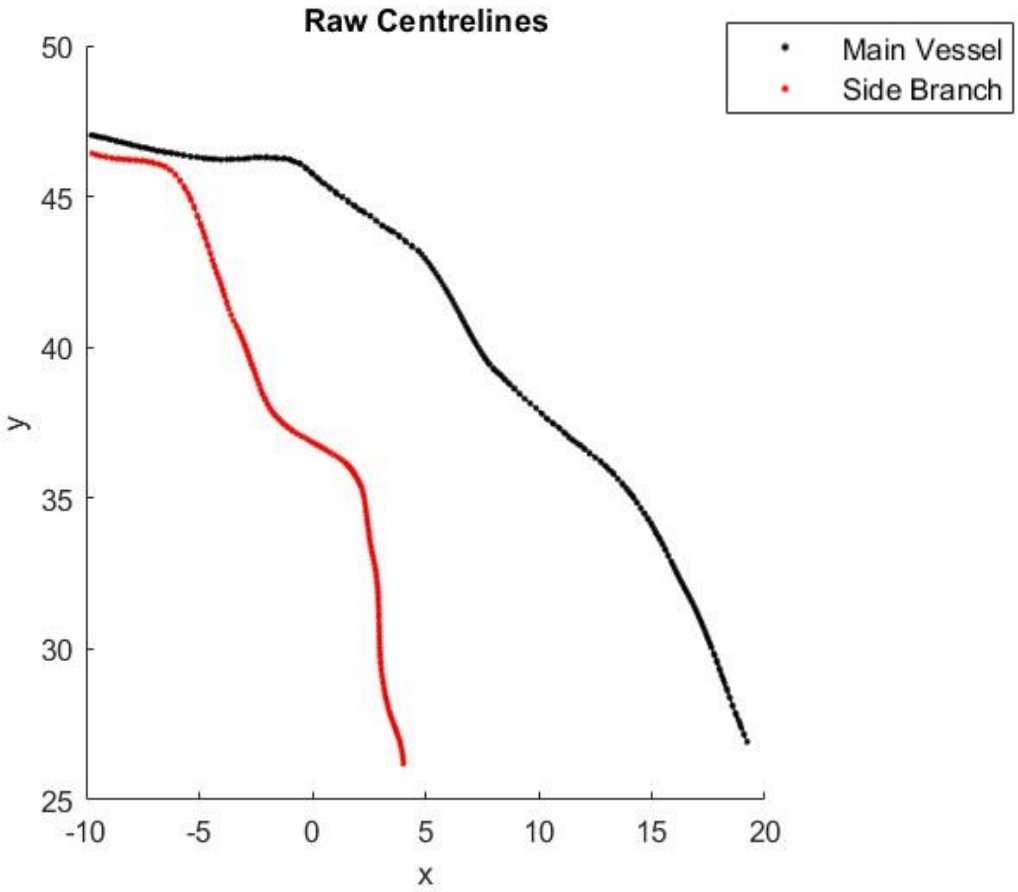

Figure 6.2. The raw 3D centrelines of the main and side vessels as extracted from the segmentation tool. As seen, the proximal common stem section does not overlap in both vessels.

6.3 Identification of the bifurcation point and creation of the common stem

To align and join the centrelines within the common stem accurately, the bifurcation point must be identified. The bifurcation point was defined as the point after which the centrelines of both vessels diverge. The procedure for achieving this required the user to select a point on each of the paired CA images that represents an identical anatomical point. This was called the 'co-

registration point'. Since bifurcation points are reliable anatomical landmarks that can be seen in both images, this was chosen as the co-registration point. The segmentation tool retained the co-registration point, by giving this point a z = 0 coordinate, which made it simple to identify the bifurcation points, when the raw centrelines were extracted (Frison, 2018b). A simple 3D shift was then applied to the points that made up the main vessel centreline so that both bifurcation points coincided (Equation 6.1). This bifurcation point was then projected onto both angiographic projections (Figure 6.3).

$$\begin{Bmatrix} x_{shift} \\ y_{shift} \\ z_{shift} \end{Bmatrix} = \begin{Bmatrix} x_{SB\_bifurcation} \\ y_{SB\_bifurcation} \\ z_{SB\_bifurcation} \end{Bmatrix} - \begin{Bmatrix} x_{MV\_bifurcation} \\ y_{MV\_bifurcation} \\ z_{MV\_bifurcation} \end{Bmatrix}$$

$$\begin{Bmatrix} x_{MV\_shifted} \\ y_{MV\_shifted} \\ z_{MV\_shifted} \end{Bmatrix} = \begin{Bmatrix} x_{shift} \\ y_{shift} \\ z_{shift} \end{Bmatrix} + \begin{Bmatrix} x_{MV} \\ y_{MV} \\ z_{MV} \end{Bmatrix}$$

Equation 6.1. Shift of the main vessel so the bifurcation points on both the main vessel and side branch coincide.

For this case, the vessel centrelines did not tend to fluctuate about the z = 0 line, which might not be the case with other vessels. Accordingly, prior to the vessel joining, the bifurcation code prompted the user to examine the z-distribution of the vessels to appreciate the fluctuation around the z = 0 line and decide whether there is minimal fluctuation, and the z = 0 points can be identified automatically, or manual intervention from the user is needed to identify the desired point due to fluctuation. Once this was done, the centreline section prior to the bifurcation point, on the main vessel, which corresponds to the common stem was replaced by the corresponding section on the side branch centreline to produce the combined centreline model.

To illustrate the resulting bifurcating centrelines, the segmented centrelines and bifurcation points were projected back onto the original angiograms, as shown in Figure3 and the ideal circles were positioned perpendicular to the centreline, as described in Chapter three (Figure 6.4).

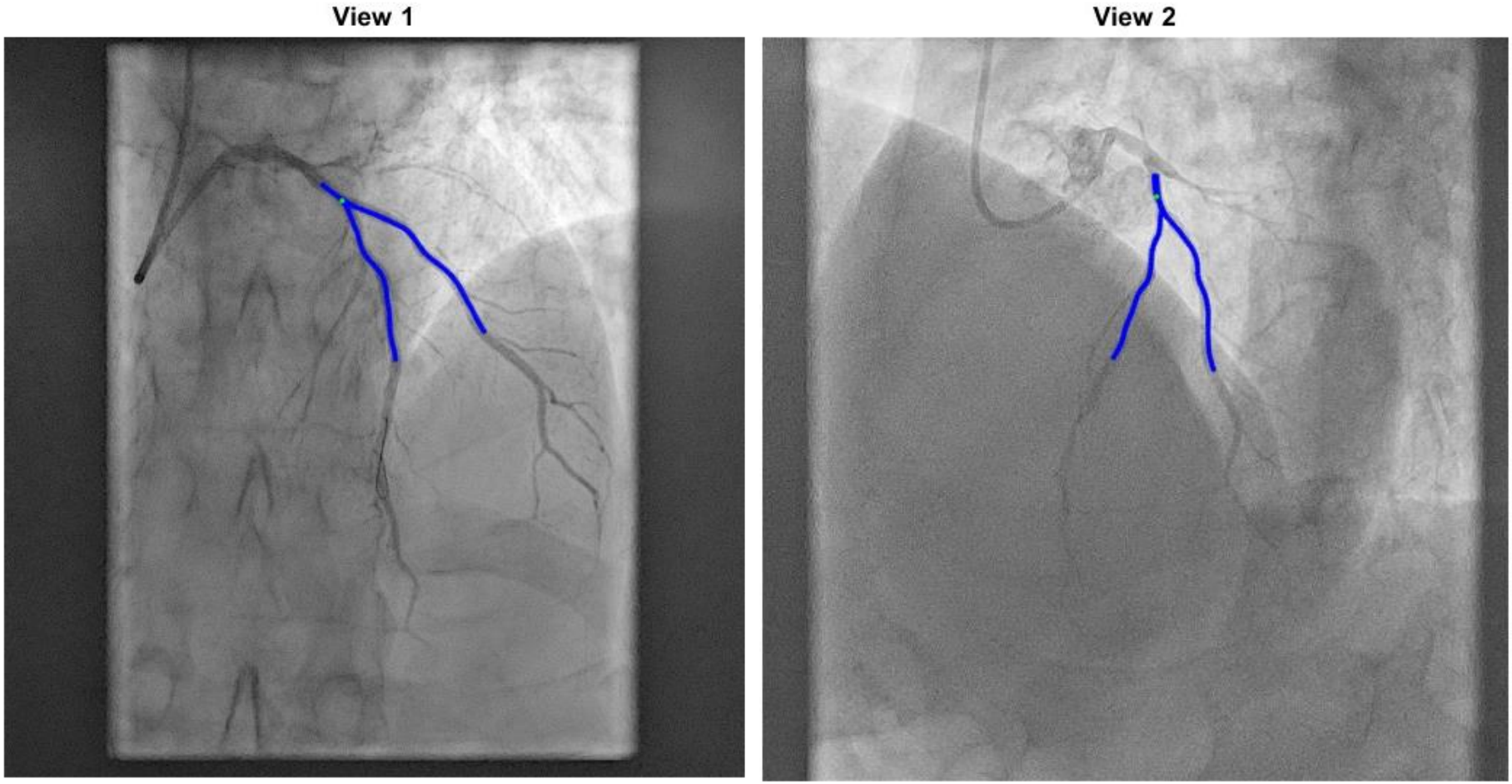

Figure 6.3. The joined centrelines (blue) and bifurcation points (green) when projected back on the two angiographic views.

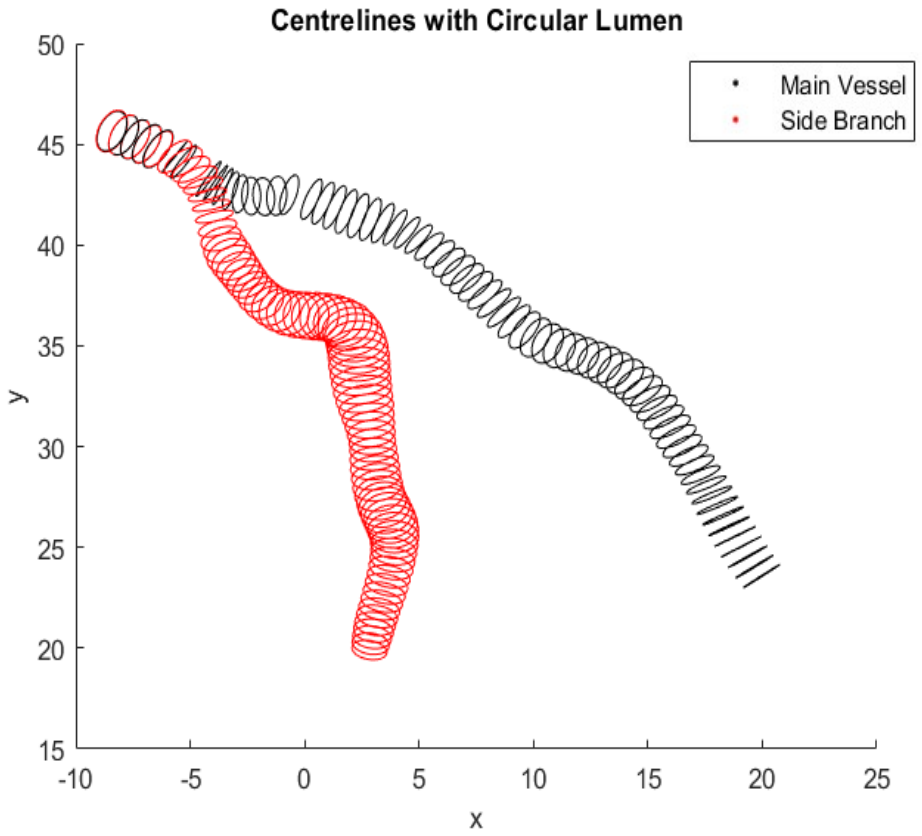

Figure 6.4. The centrelines joined at the common stem, showing the ideal circles with CA-derived radii positioned along the lengths of both centrelines.

6.4 Patching of the branches

Bifurcation anatomy is complex, and it is practically impossible to observe the complex 3D anatomy from a single pair of angiogram images. Not only does the angiographic method reduce the complex 3D shape to a simplified (averaged) axisymmetric reconstruction, but it is impossible to view the anatomy immediately adjacent to the bifurcation in two views because the anatomy will always be shadowed by the vessel in at least one view. Of course, this is exactly why OCT fusion will be superior to angiographic methods, because it does not require assumptions and is not derived from x-ray silhouettes like CA.

Researchers have tried, in different ways, to model what the bifurcation looks like using CA, while making several assumptions. Most modellers have decided to trace the edges of the vessels in the bifurcation region and use these data to define the reconstructed bifurcation anatomy (Wu et al., 2020, Auricchio et al., 2014). Others have relied on assumptions regarding and idealised bifurcation anatomy and used this to attach the proximal and distal segments of

the vessels (Medrano-Gracia et al., 2016a). The former assumes the shape of the bifurcation can be extracted using 'edge detection' either manually, automatically, or semi-automatically and the second disregards the uniqueness of patient-specific bifurcations and imposes a standard shape based on an atlas. The method developed in this work, incorporates aspects of both methodologies.

With a deeper examination of the point at which the vessels diverge, the bifurcation point, it is important to be aware that:

1. Foreshortening and/or vessel overlap at the bifurcation area might have occurred. Foreshortening can be identified by zooming in on the projected cross-sections. With no foreshortening each cross-section is a straight line. The more foreshortened the vessel is, the more circular the projected cross-section. Overlap makes it very challenging to identify the true bifurcation point where the vessel completely divides. Additionally, one cannot reconstruct the major axis, minor axis and orientation of an ellipse from two angiographic projections, and there is absolutely minimal information in the edges to try to reconstruct a 3D bifurcation.
2. The way the common stem was created is by forcing a similar, yet different, common stem on the main vessel, as shown in Equation 1.

Therefore, unrealistic tight curvatures may be generated in the centrelines that would interfere with the extracted radii causing circle overlap at these tight curvatures. This phenomenon can also occur if the vessel under investigation is tortuous, and sections of it are not well-represented in the angiograms. The procedure described below can also be applied in such sections. The patching procedure targets this area of tightness at the bifurcation point by interpolating using Hermite Cubic patches between a point proximal and a point distal to the bifurcation point, as shown in Figure 6.5, to produce a smoother curvature that mitigates issues of overlap. This procedure does smooth out lesions that are right at the bifurcation. Therefore, if a lesion is precisely at the bifurcation region, then the single vessel analyses, or perhaps the 3-vessel 0D analyses, are likely to be superior to the current full 3D analysis. The final patched models are shown in Figure 6.6.

Interpolation using Hermite Cubic splines was chosen mainly because it is continuous and maintains the continuity of its derivatives at the points of interpolation (Gessat et al., 2011). They can be used to define curves whose shape is unknown prior to the interpolation. B-splines, however, are useful when there is a specific path that must be followed, defined by the knots.

This is helpful when curves are pre-defined. However, in the case of the patching presented in this project, initially the patch shape is undefined, only the start and end points and gradients are known, and an efficient procedure is needed to save precious time in the clinic, making the Hermite Cubic Spline the most suitable choice (Frison, 2018b, Marcinnó et al., 2025). The form of the spline is presented in Equation 6.2.

$$p(t) = (2t^3 - 3t^2 + 1) * p_0 + (t^3 - 2t^2 + t) * m_0 + (-2t^3 + 3t^2) * p_1 + (t^3 - t^2) * m_1$$

Equation 6.2. The Hermite Cubic Spline

Where p_0 is the starting point (the proximal point of the patch), p_1 is the ending point (the distal point of the patch), m_0 is the gradient at the starting point and m_1 is the gradient at the ending point.

Currently, the patching spanned from the point Bifurcation Point – 2 on the common stem and finishes at Bifurcation Point + 5 on each of the daughter vessels and created sixteen points on each side of the patch. This was chosen because a more gradient change is expected post-bifurcation point, so the allocation of patching pre and post bifurcation point were decided accordingly. It might be interesting to experiment with longer or shorter patches from just a single point pre-bifurcation and a single point post-bifurcation until up to double the radius, both proximally and distally to quantify the effect on the final shape of the bifurcation. However, as long as the patch is not erasing vital shapes of the vessel, given the very small distances between the points on the centreline, it is not expected that this choice will impact the bifurcation region geometry significantly.

The vessel radii at the patch were linearly interpolated taking the original points and radii as the vectors of coordinates and the new set of points of the patch as the query points. Linear interpolation was chosen as it can very simply represent the mild decrease in radius in the short distance spanned by the patch, as it goes from proximal to distal, which is what was expected anatomically. Linear interpolation has been used by researchers for similar purposes, to model vessel radius, and to model sequestered flux through the vessel wall in the coronary circulation.

This spans over a short length, pre and post bifurcation point, and it overcomes the challenge of curvature discontinuity of the vessel post bifurcation, which is illustrated in Figure 6.7,

where instances where the radius of vessel curvature is smaller than the radius of the vessel (and overlapping radii) occurred.

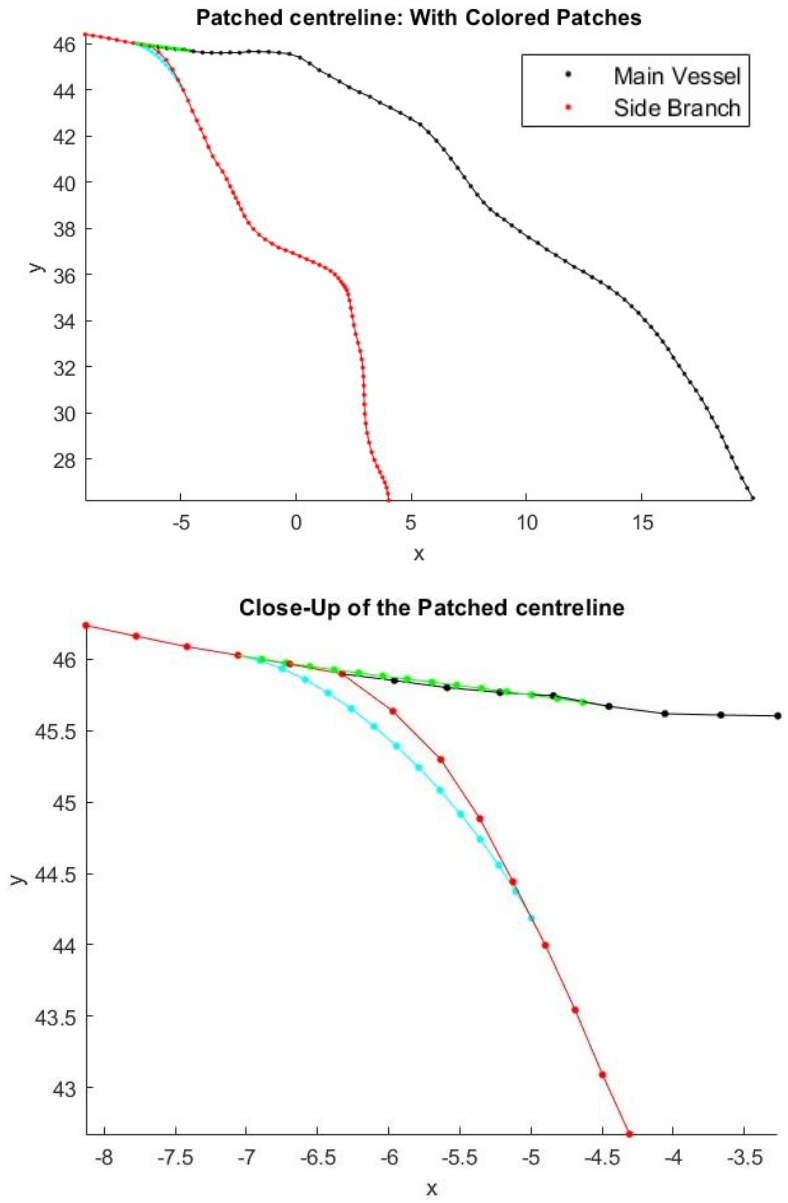

Figure 6.5. The targeted area of tightness at the bifurcation point, replaced by interpolating using Hermite Cubic patches between a point proximal and a point distal to the bifurcation point, to produce a smoother curvature that mitigates issues of overlap. (top) full model, (bottom) close-up of bifurcation area.

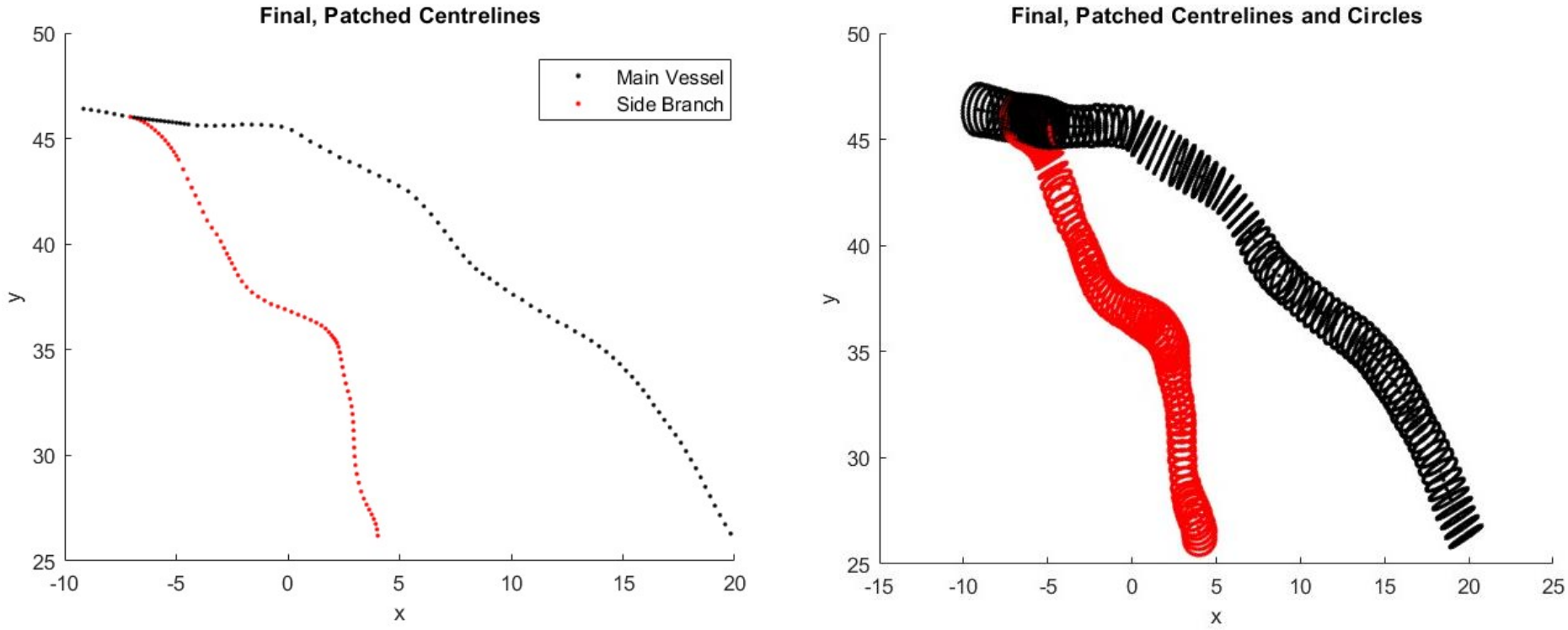

Figure 6.6. The final patched centrelines of both vessels (left) and the centrelines with the idealised circles representing the vessel wall on the centreline points (right).

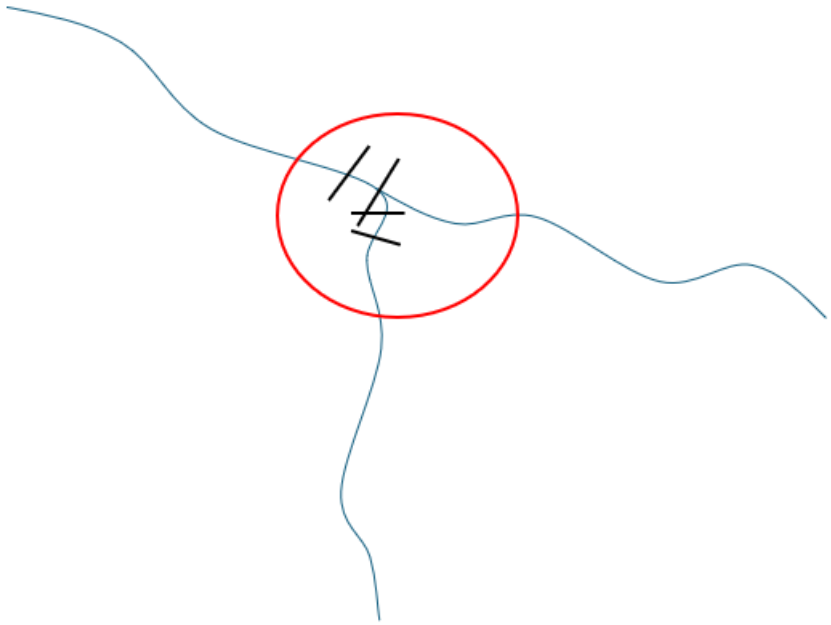

Figure 6.7. An illustration of a bifurcation exhibiting post-bifurcation curvature discontinuity, demonstrating radii (the short black segments) overlapping in areas where the radius of curvature is smaller than the radius of the vessel.

The side branch meshed surface was created as described (Figure 6.8). The triangulated surfaces of both vessels were combined to produce the full, branching surface model, shown in Figure 6.9.

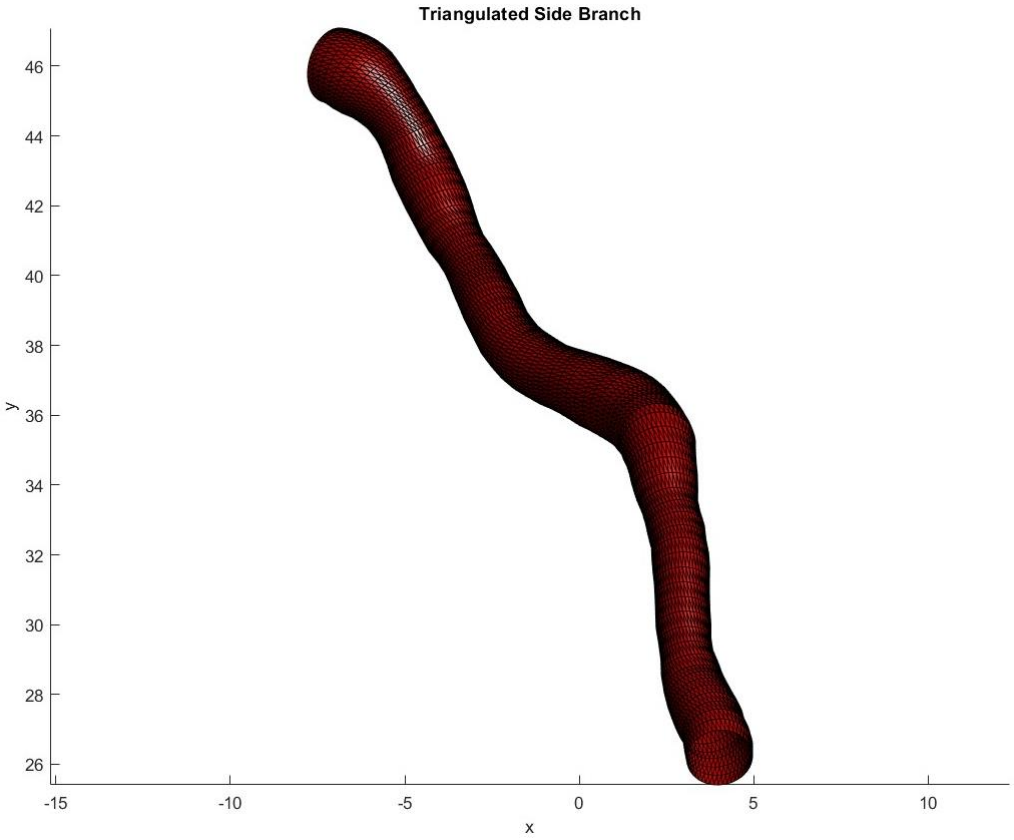

Figure 6.8. Triangulated surface of the side branch.

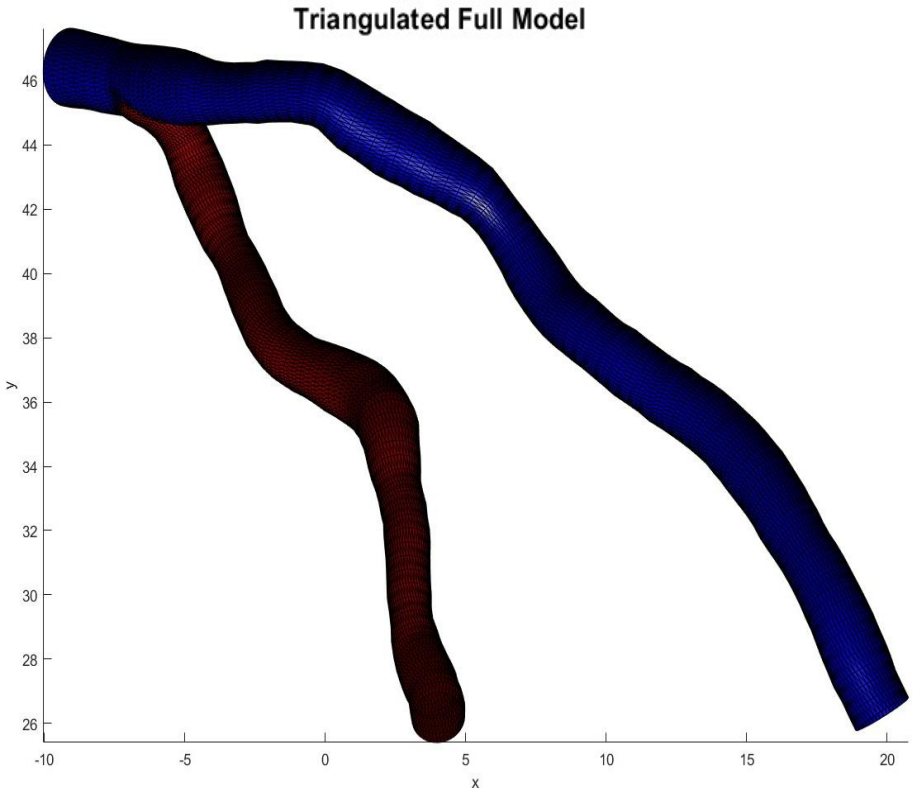

Figure 6.9. The full model with surface triangulations (main vessel in blue and side branch in red).

6.5 Identifying internal points

After the surface triangulations were created, the model was ready for the overlapping issue of the triangulations in the region of the bifurcation to be dealt with. To do that, all the nodes that are internal to the model were identified, and the triangles that had at least one of their nodes being internal were identified and deleted from the surface triangulation to produce cut surfaces. The procedure followed here was majorly inspired by that presented in (Lo, 1995, Segura and Feito, 1998, Jiménez et al., 2010).

The nodes, which are the points on the idealised circles that make up the triangulations, were categorised as internal, on the surface or external. Figure 6.10 is a summary of the steps involved to determine which points are internal to the bifurcated model and thus will be deleted, and the coordinates of the points of intersection. The first step was to isolate the points that are in the patched region. This was essential for time efficiency, ensuring that only the points that might be involved in the intersection were targeted instead of searching the full vessels. One vessel was then regarded as a set of edges and the other was regarded as surfaces. The task was to identify if a line segment intersects a triangular surface. This was done by checking two criteria:

1. If the two endpoints of the line segment are on opposite sides of the plane containing the triangular surface.
2. If the point of intersection of the plane and the line segment lies inside the triangular surface.

If both these criteria are met, then the line segment intersects the triangular surface at the identified point of intersection.

Assume DE is a segment on vessel 1, triangle ABC is a triangle connecting three of the points on vessel 2, θ_1 is the angle between AD and the normal vector (N) and θ_2 is the angle between AE and N. The dot product of AE and N is computed and must be satisfied. For Criterion 1 to be met, Equation 6.3 must be satisfied.

$$dot(AD, N) * dot(AE, N) \leq 0$$

Equation 6.3. Checking for Criterion 1: Do the endpoints of the segment lie on opposite sides of the plane containing the triangular surface?

To identify the segments that meet this criterion, the three possible scenarios were laid out (Figure 6.11).

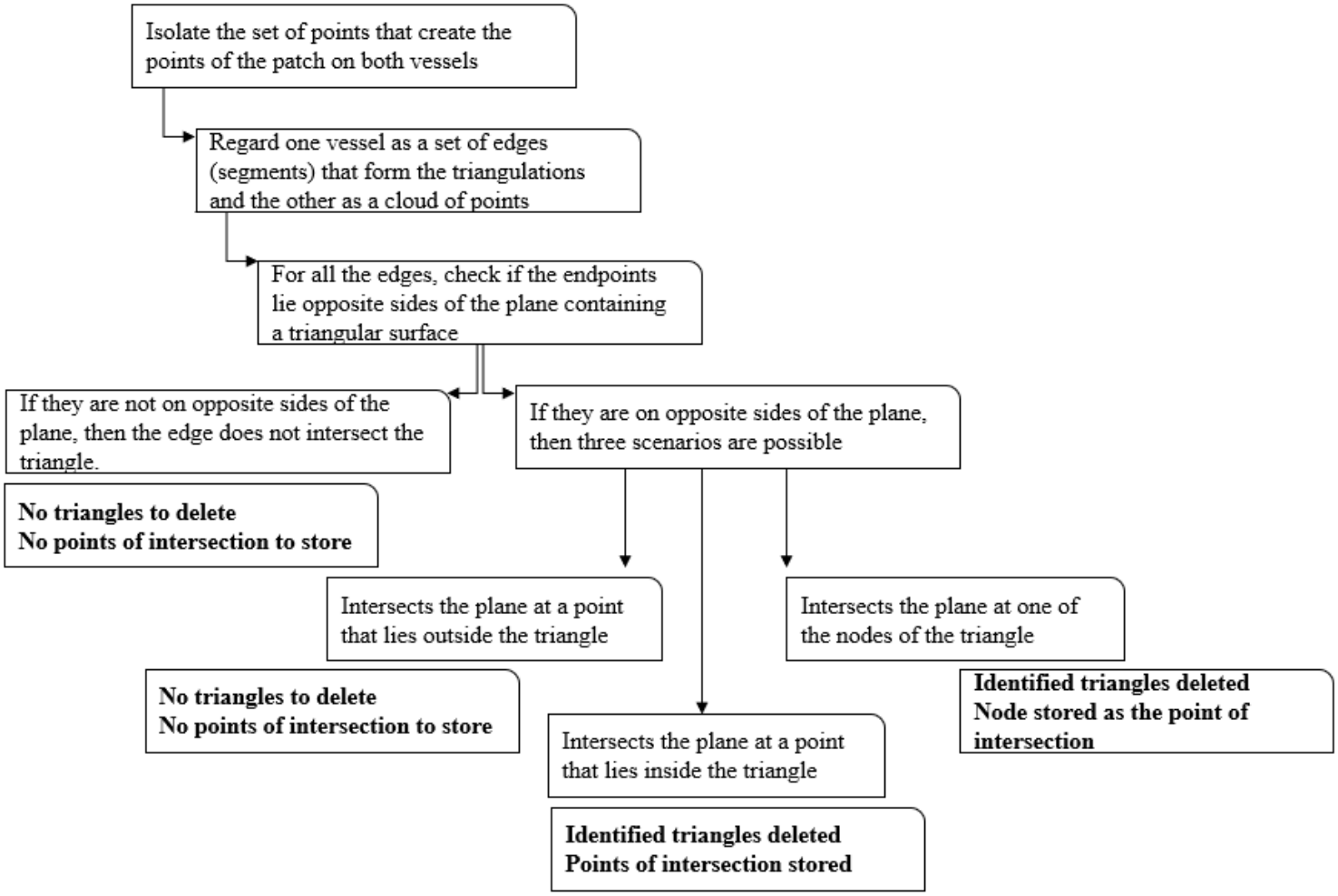

Figure 6.10. The procedure involved in identifying internal nodes and thus triangles and deleting them. The points of intersection of the edges on one vessel and the triangles of the other are stored for use in stitching the vessel together at a later step.

Scenario 1. If D and E are on opposite sides of the plane containing triangle ABC.

- θ_1 is acute and θ_2 is obtuse, thus the multiplication of the dot products will be negative.
- An intersection might be present; criterion 2 must be checked.

Scenario 2. If one point (E) is on the surface of the triangle.

- θ_1 is acute and θ_2 is a right angle, thus the multiplication of the dot products will be zero.
- Point E is stored as the intersection point. No triangles deleted.

Scenario 3. If D and E are on the same side of the plane containing triangle ABC.

- θ_1 is acute and θ_2 is acute, thus the multiplication of the dot products will be positive.
- No intersection between the segment DE and the triangle ABC.
- No points of intersection stores and no triangles deleted.

For the segments that satisfied Scenario 1, Criterion 2 is checked using Equation 6.4.

$$dot(cross(AB, AP), N) \leq 0 \; and \; dot(cross(BC, BP), N) \leq 0 \; and \; dot(cross(CA, CP), N) \leq 0$$

Equation 6.4. Checking for Criterion 2: Does the point of intersection of the line segment and the plane lie inside the triangular surface?

Three scenarios exist for this as outlined in Figure 6.12:

Scenario 1. The point of intersection is internal to the triangular surface.

- Point of intersection stored and triangle deleted.

Scenario 2. The point of intersection is coincident with one of the nodes of the triangular surface.

- Point of intersection stored and triangle deleted.

Scenario 3. The point of intersection lies outside the triangular surface.

- Criterion 2 not satisfied.
- No points of intersection stored, and no triangles deleted.

Scenario 1: D and E are on opposite sides of the plane containing triangle ABC

θ1 is acute = cosine is positive

θ2 is obtuse = cosine is negative

Scenario 2: E is on triangle ABC

θ1 is acute = cosine is positive

θ2 is right = cosine is zero

Scenario 3: D and E are on the same side of the plane containing triangle ABC

θ1 is acute = cosine is positive

θ2 is acute = cosine is positive

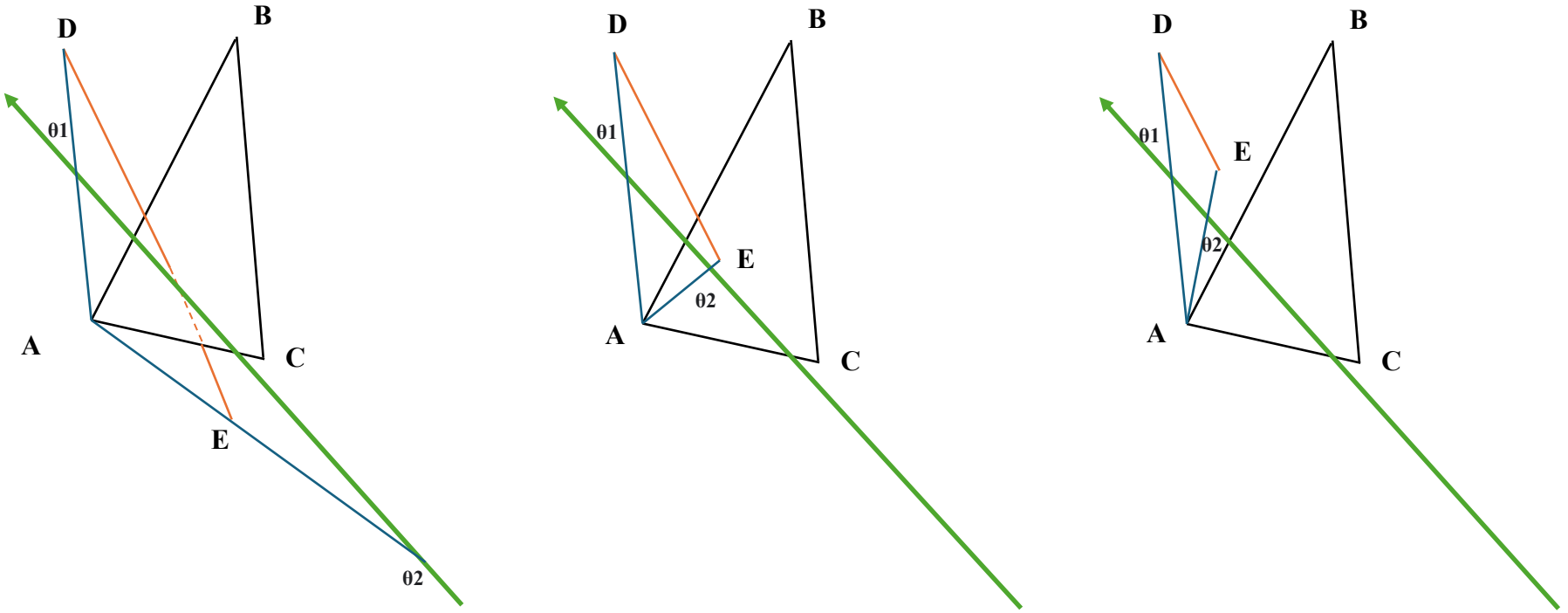

Figure 6.11. The three scenarios for criterion 1. Scenario1 is when the two endpoints of the line segment DE are on opposite sides of the plane containing triangle ABC. Scenario 2 is when one of the endpoints of segment DE are on the plane containing triangle ABC. Scenario 3 is when both endpoints are on the same side of the plane containing triangle ABC.

Scenario 1: P is distinct from either A, B, or C

AB x AP = N ==== N.N = 0

BC x BP = N ==== N.N = 0

CA x CP = N ==== N.N = 0

Scenario 2: P coincides with either A, B, or C

AB x AP = 0 ==== N.N = 0

BC x BP = 0 ==== N.N = 0

CA x CP = N ==== N.N = 0

Scenario 3: P lies outside triangle ABC

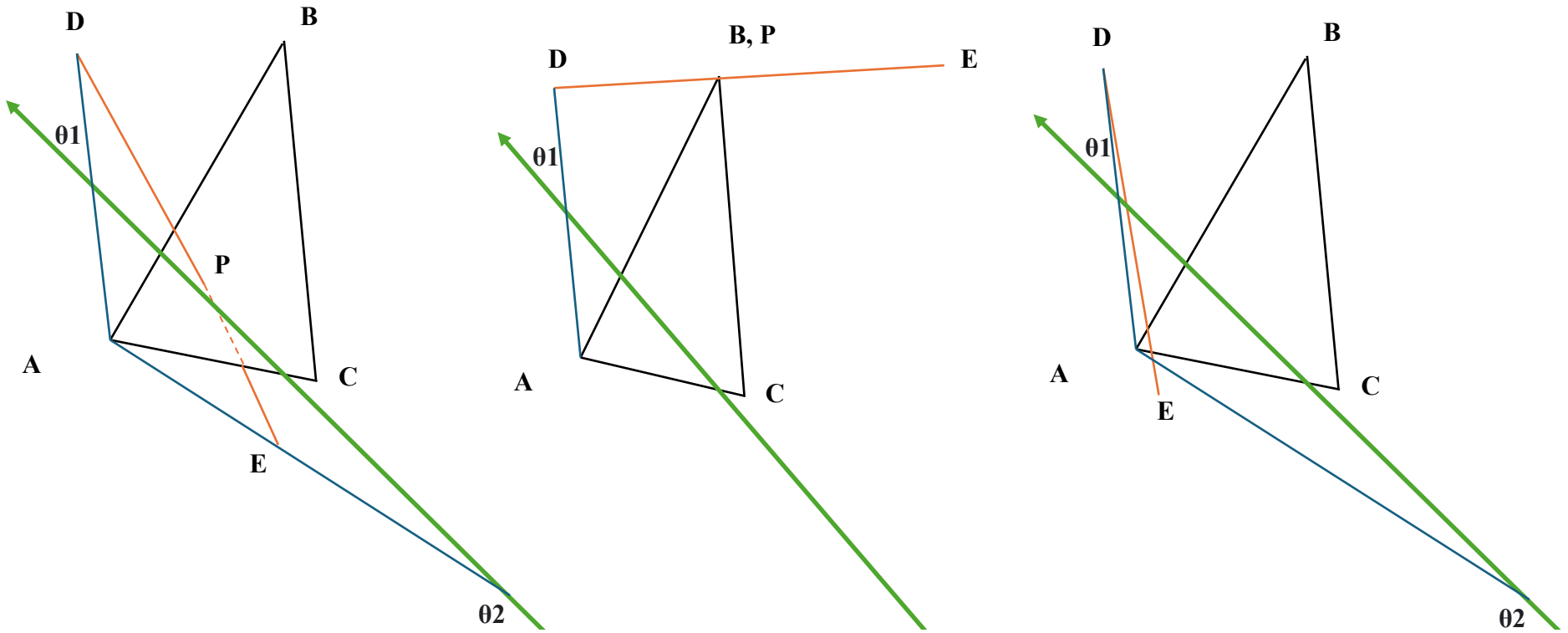

Figure 6.12. The scenarios that can occur if the endpoints of a line segment are on opposite sides of a plane containing a triangular surface.

Once the points of intersection were identified and the triangles that were either fully or partially internal to the bifurcated geometry deleted, as identified by the blue sections in Figure 6.13 and the geometry was divided into a cut surface of the main vessel, a cut surface of the side branch and a curve that joined all the stored intersection points (Figures 6.14 and 6.15).

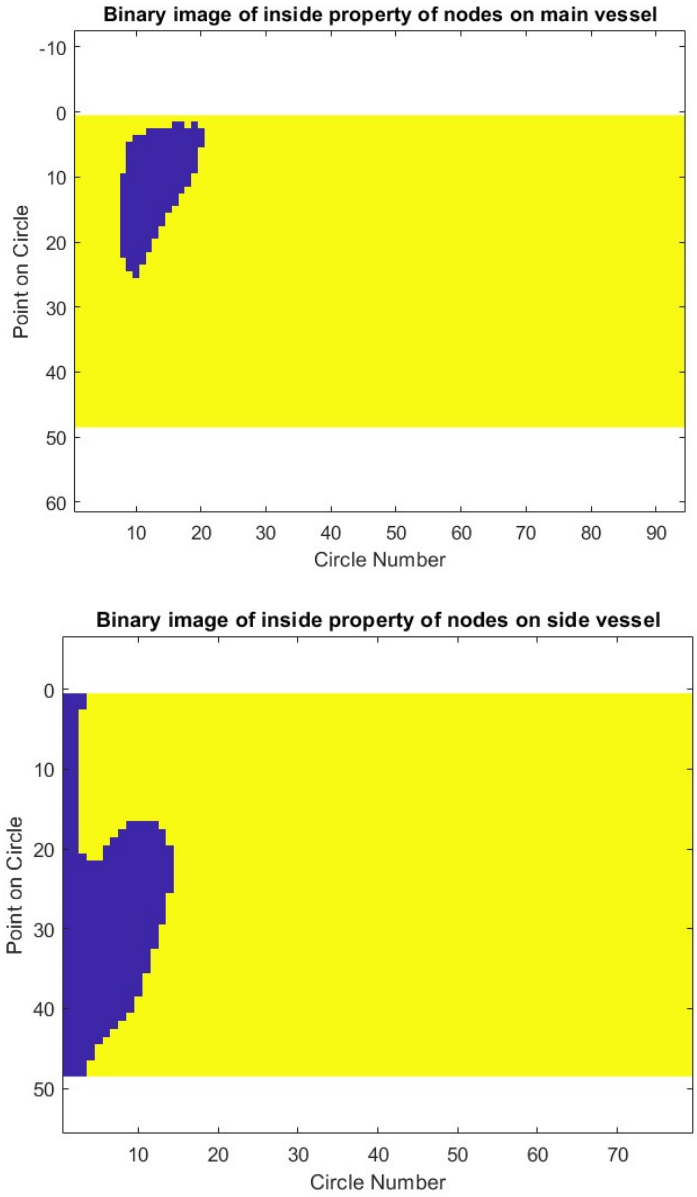

Figure 6.13. Contour plots of both vessels showing, in blue the points of the main vessel that were inside the side branch (top) and the points of the side branch that were inside the main vessel (bottom) and the points in yellow that were not inside a specific vessel. In this case, the side branch starts off fully inside the main branch, hence the points starting off all blue.

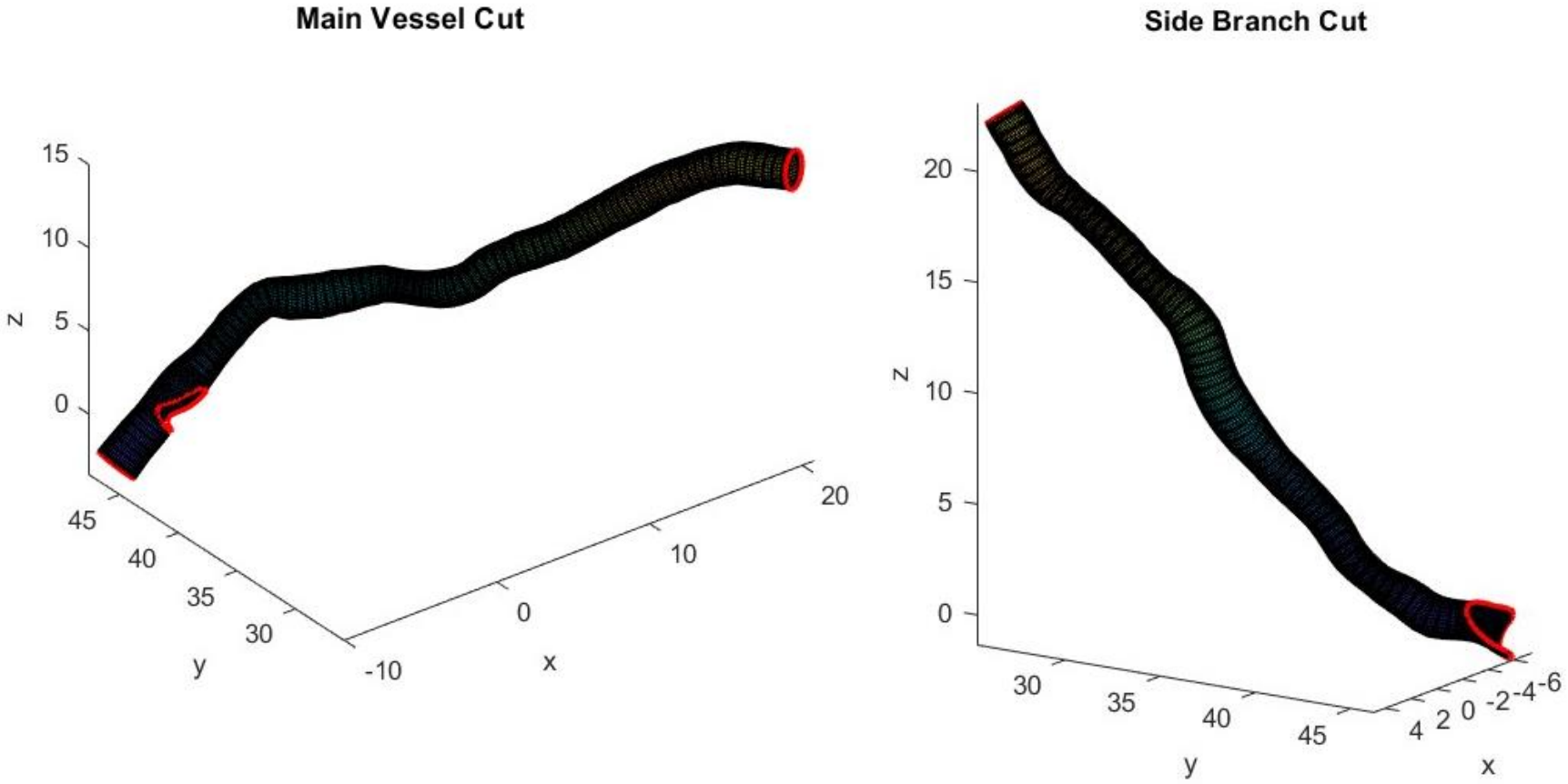

Figure 6.14. (Left) Main vessel surface after overlapping sections with the side branch in the bifurcation region were deleted and (Right) Side branch surface after the overlapping sections with the main vessel in the bifurcation region were deleted.

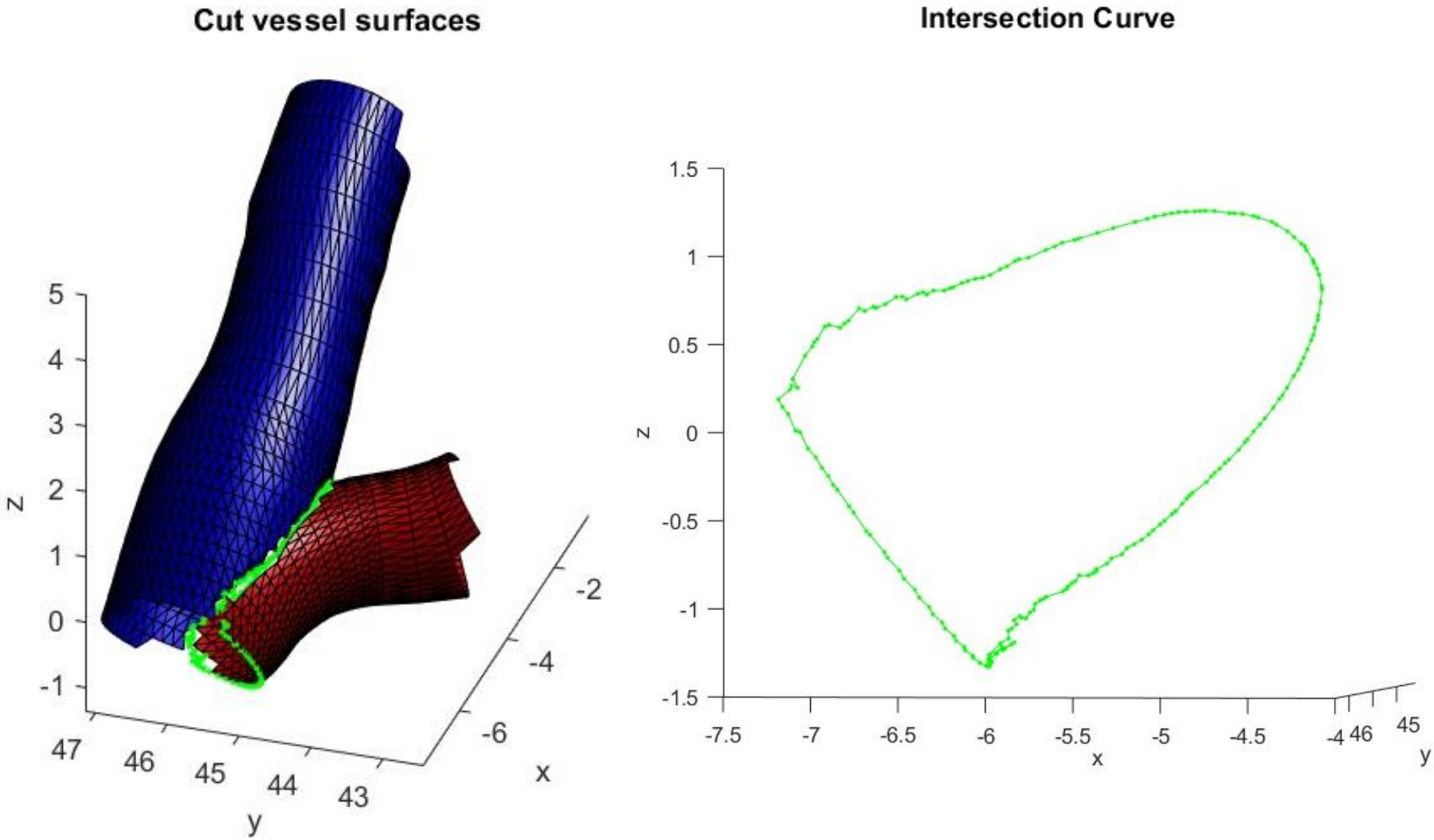

Figure 6.15. (Left) A close-up of the cut surfaces of the main vessel (blue) and side branch (red) in the bifurcation region, and the intersection curve (green), at which both vessels were stitched (next step).

6.6 Stitching the vessels at the intersection curve

From this point on, the free edge of the main vessel at the bifurcation region resulting after the deletion of the internal triangles will be referred to as ‘the main vessel cut’ and that of the side branch will be referred to as the ‘side branch cut’. To stich the vessels at the intersection curve:

1. The intersection curve, which was the curve formed by joining all the points that form the perimeter of intersection of the main and side vessels, was decimated. This was because some of the points on the curve were very close to each other, which can occur in cases such as when the triangulations result in a triangle with two edges intersecting the interior of another at an area close to one of its vertices (narrowest area) (Figure 6.16).

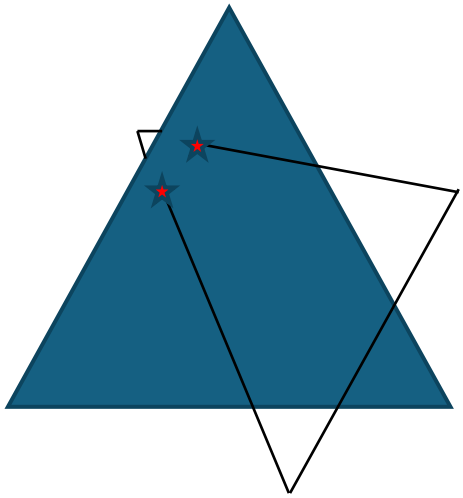

Figure 6.16. An example of a case where two intersection points can be exceptionally close to each other. In this case, the black edges of the triangle are intersecting the interior of the blue triangle at the points marked in red. Since, these points happen to be in the region close to a vertex of the triangle containing the black edges, the points are exceptionally close to each other and are targeted by the decimation procedure to refine the intersection curve.

2. The closest points to the main vessel cut on the intersection curve were computed and replaced the original main vessel cut curves. The same procedure occurred between the side branch cut and this new curve, stitching both vessels together smoothly. In this step, a decision was made to replace the points, which pulled the specific node of a triangle to the new location. This was because the distances between the original cut point and

that it would be replaced with were very small, making replacement a plausible idea. This method of 'moving' nodes, or choosing alternative ones was used by (de Oliveira Miranda et al., 2015). Alternatively, a threshold value can be chosen and all the cut points less than this value away from their closest counterparts on the intersection curve be replaced by them, while the rest be replaced by the mean of both points. The resulting stitched vessels are shown in Figure 6.17.

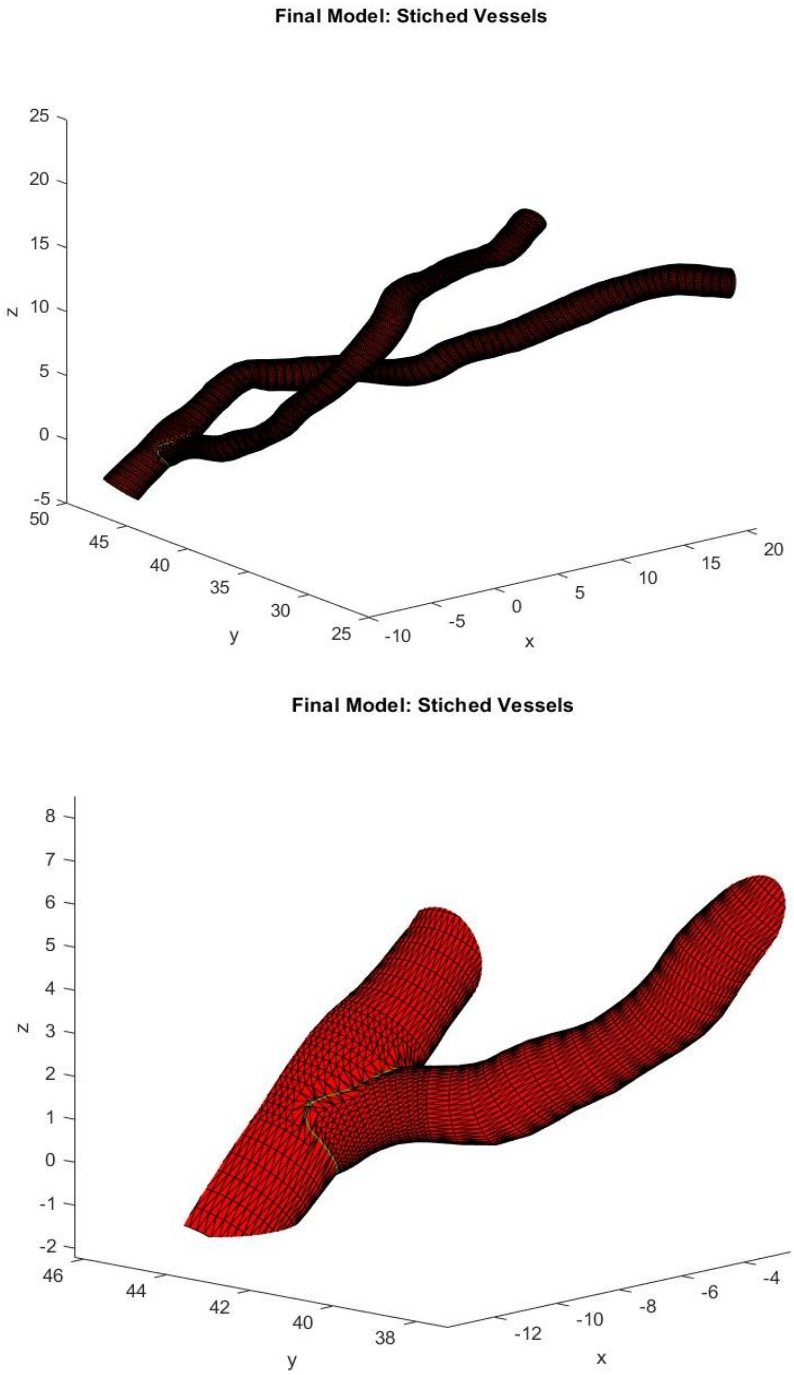

Figure 6.17. The final and stitched branched model.

It is important to note here that in some cases, more than one point on the main vessel (or side branch) cut can be close to the same point on the intersection curve. Meaning that some of the points on the intersection curve will be left unconnected, leaving holes in the stitched area of the surface mesh, as shown in Figure 6.18.

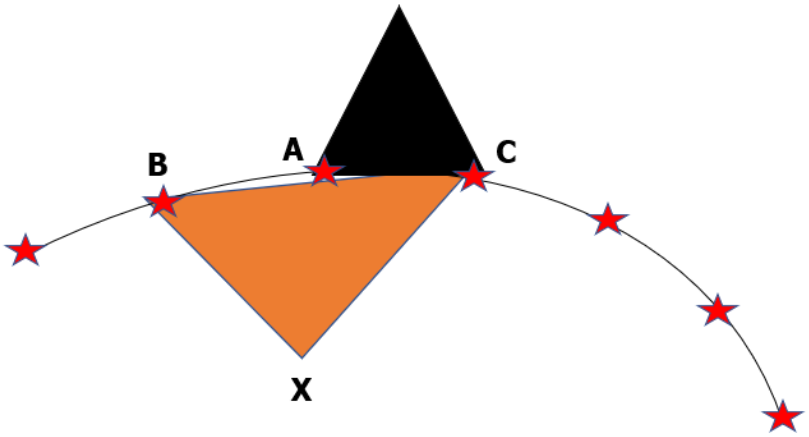

Figure 6.18. An illustration of the case where a hole can be formed in the stitched area of the triangulated surface. The black triangle belongs to the main vessel, the orange triangle belongs to the side branch, and the curve of red stars represents the intersection curve. This case occurs when a point (A in this case) is 'skipped' by a vessel (the side branch in this case) because it is not the closest point to any of the points on this vessel. This results in the point not being connected to any of the surface triangulations, leaving a hole in the final model.

In this work, there are two stages which deal with this issue separately. Having both in place is redundant so the second was favoured. However, both are presented here:

1. Finding the two closest points to point A on the intersection curve (B and C). The common aspect between points B and C is the triangle they share on the side branch surface (in orange). Triangle BCX is identified and replaced with two triangles, BXA and AXC, thus closing the hole as shown in Figure 6.19.
2. Seal the holes is using ANSYS Fluent's wrapping feature which takes in a geometry (the produced stereolithography (.stl) file) and wraps it with a surface mesh that is then the basis for the meshing of the internal volume (the fluid domain).

This surface mesh was exported from MATLAB as a .stl file and imported into Fluent for the volume mesh to be created (Figure 6.20) and the simulations to be performed.

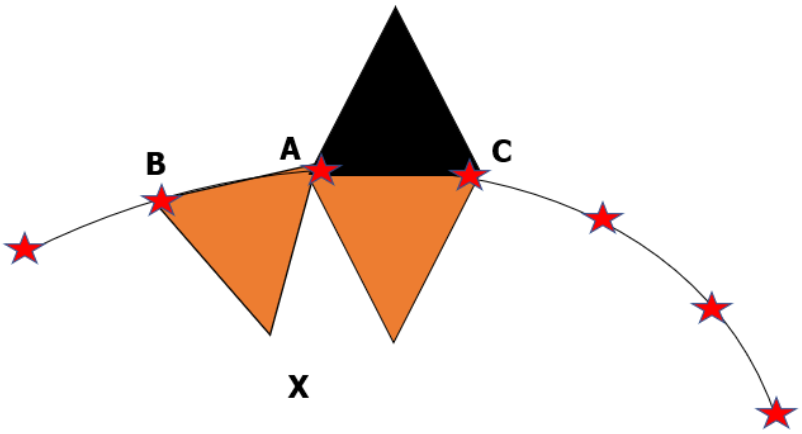

Figure 6.19. Sealing the holes by dividing the triangle that skips a point on the intersection curve in two, so it joins at every point.

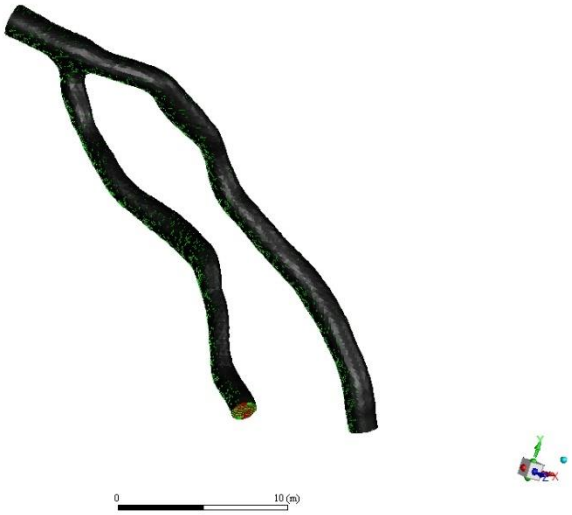

Figure 6.20. (Top) Volume mesh of the fluid domain and (Bottom) An example of a CFD simulation with pressure boundary conditions performed on this bifurcating model.

6.7 Summary

The bifurcation reconstruction protocol was demonstrated in this chapter using circular lumens with CA-derived radii. The same protocol was followed when reconstructing bifurcations using fused CA and OCT:

1) CA-centrelines were obtained from the segmentation (Chapter three)
2) CA and OCT data were aligned, and the lumens were positioned appropriately (Chapter four)
3) OCT lumens were patched and stitched (Chapter 6) just like the circular lumens are, in the CA-based bifurcation reconstruction presented in this chapter.

The main achievement is the construction of a continuous and coherent triangular surface mesh that describes the whole of the bifurcating vessel, including the region of the bifurcation and serves as the starting point for construction of a volume mesh for CFD solution.

A total of eight bifurcated geometries were constructed using this protocol, as presented in Table 6.1. The CFD results are presented in Chapter seven.

Case	Origin	Vessels	Originated from which single cases?
1	NNUH	LAD	12
	NNUH	Diagonal	13
2	NNUH	LAD	4
	NNUH	Diagonal	5
3	NNUH	LAD	6
	NNUH	Diagonal	7
4	NNUH	LAD	8
	NNUH	Diagonal	9
5	NNUH	LAD	10
	NNUH	Diagonal	11
6	NNUH	LAD	2
	NNUH	Diagonal	3
7	NNUH	LAD	14
	NNUH	Diagonal	15
8	NNUH	LCX	16
	NNUH	OM	17

Table 6.1. Outline of the patient cases that were modelled as branching vessels, each main vessel and its corresponding side branch, in this thesis. The eight cases were imaged in the Norfolk and Norwich University Hospital.

The difficulties encountered were mainly the surface mesh becoming tangled when the cross-sections changed too rapidly in the bifurcation region. This occurred in six out of the eight total cases, usually the cases with a stenosed bifurcation. This was solved by using Fluent's wrapping function to re-organise the triangulated surface in this reason, especially since the tangled triangles have small minimum angles and large aspect ratios (>1) which are indicators of poor quality for meshing. Equation 6.5 shows how the aspect ratio of a triangle is calculated:

$$Aspect\ Ratio = \frac{Longest\ Side}{Shortest\ Side}$$

Equation 6.5. The aspect ratio of a triangle

Another way to avoid potential difficulties in the meshing process is to use fewer OCT cross-sections, so that any discontinuities are automatically smoothed. Figure 6.21 exhibits three branching reconstructions from fused CA-OCT, with stenosed bifurcations after they have benefitted from the wrapping function for smoother surface meshing. Smoothing is essential, especially when modelling the coronaries from OCT this type of reconstruction involves 2D image stacking to represent a 3D structure, like CT imaging, which is expected to have sharp ridges between the images. All eight branching vessel cases reconstructed from fused CA-OCT are presented in Appendix 2. Chapter seven presents the CFD results using both, the single vessel and bifurcation cases.

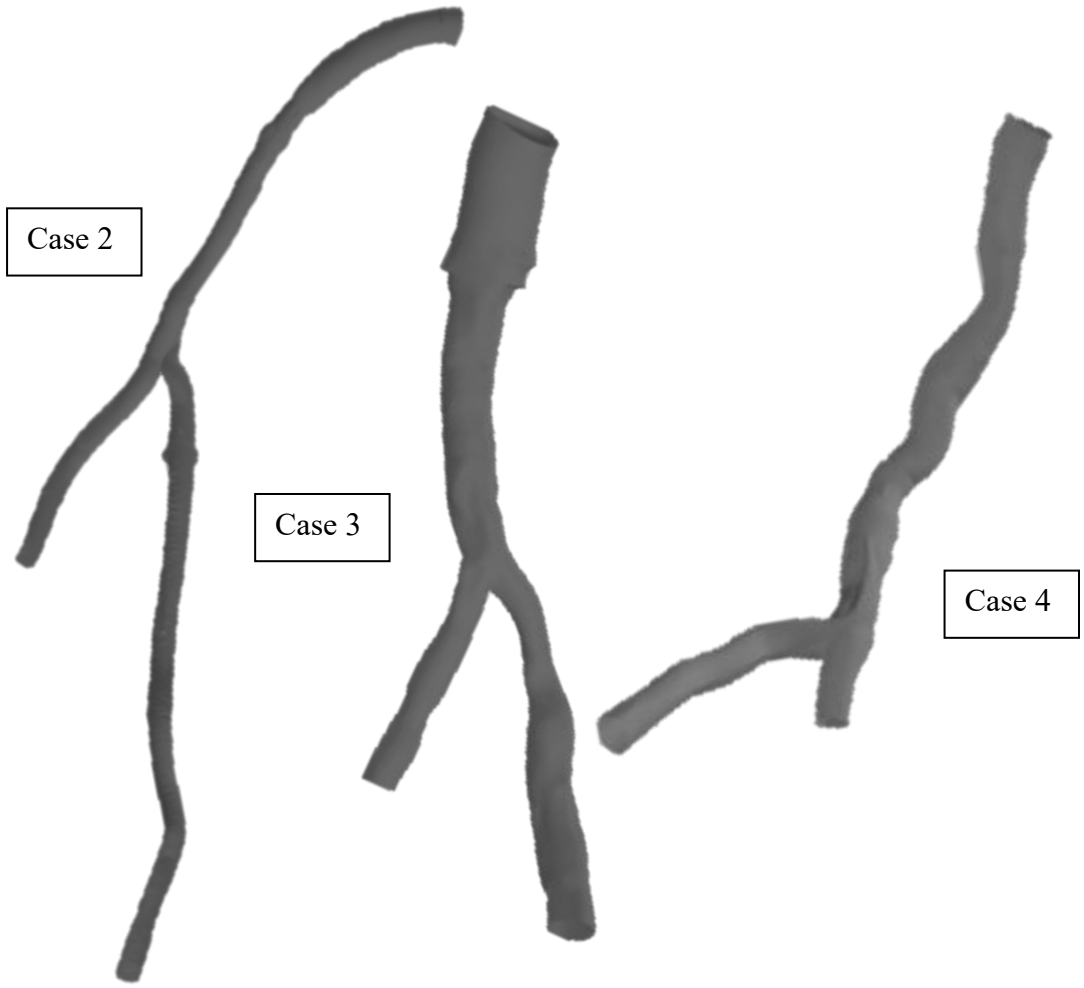

Figure 6.21. Bifurcation Cases 2-4, which are cases that have exhibited entanglements of the surface mesh at the bifurcation region and have been subjected to Fluent's wrapping and smoothing function.

Chapter Seven:

Executing and Validating the Novel Fusion Method Using Clinical Data

7.1 Outline of the coronary data used in this study

In the previous chapters, I have described the development of a novel prototype method that fuses complementary CA and OCT data to reconstruct the 3D anatomy of human coronary arteries. I have also presented anatomical data comparing the novel fusion method against the currently used CA-only method. In this chapter, I have deployed the model on real clinical data and present a primary, proof-of-concept validation. Patient and vessel characteristics of all included cases are outlined in Chapter 3, tables 1 and 2. Twenty single vessels were reconstructed in silico in this study (See Appendix 1), from twelve different patients, including eleven LADs, seven diagonals, one LCX and one OM, all cases were either pre-PCI or assessed and deemed appropriate for PCI deferral. No post-PCI cases were considered. The clinically measured FFRs ranged from 0.49 to 0.96 with an average of 0.81. In this work, a 'grey zone' is identified as the set of vFFR values that are between 0.78 and 0.83. These are the vFFR values which are close enough to the threshold for intervention, and in addition to the simulated vFFR, benefit from an invasive measurement of the FFR too. The clinical data available to this study from the NNUH cohort supported the reconstruction, and comparison with invasive physiological data, of eight bifurcations (see Appendix 2).

Regarding segmentation, the following criteria were followed for branching model reconstruction:

1) The same pair of angiogram images were used to segment both vessels of the branch,
2) The OCT catheter, as visible on the angiogram films, was used as guidance, where possible, for the proximal and distal points for the CA-segmentation and
3) The OCT runs when extracted from the Abbott machines, were extracted with a 10mm field of view (to avoid larger OCT cross-sections being cut-off from the viewing panel, impacting segmentation).

The three primary goals of this chapter are to compare:

1) Flow and coronary microvascular resistance values (CMVR) from the novel fusion (Q_{Fused} and $CMVR_{Fused}$) and CA-only methods ($Q_{CA\text{-}only}$ and $CMVR_{CA\text{-}only}$),
2) Single branch vFFR from the novel fusion method ($vFFR_{Fused}$) against vFFR computed with (a) the existing CA-only method ($vFFR_{CA\text{-}only}$) and (b) against the invasive FFR, measured with the pressure.

3) Single branch vFFR with (a) branching vessel vFFRs ($vFFR_{branching}$) and (b) clinical FFR.

The statistical analyses performed in this chapter are divided into three types:

4) Diagnostic accuracy tests: Including comparing the concordance/discordance number of cases for each type of simulation with the FFR and computing the sensitivity, specificity, negative and positive predictive values (NPV and PPV) and the accuracy,
5) Numerical accuracy tests: Including computing the Bland Altmann limits of agreement and bias, and giving each method an overall scoring, and
6) Correlation analysis: Due to the small sample size, the data is not parametric. Therefore, a non-parametric test (Man-Whitney U test) was used to assess the difference between groups. The P value, r (Spearman's correlation coefficient) and R-squared value were computed.

7.2 Simulated volumetric coronary blood flow rate for single vessels

As discussed in Chapter one, CFD simulations were conducted all using Fluent 2024R2. The volumetric flow rate was computed, by performing CFD simulations with the boundary conditions shown in Table 7.1. The aim of these CFD simulations was to simulate haemodynamic parameters and compare them with their hyperaemic clinically measured counterparts, so blood was modelled as an incompressible, Newtonian fluid with density (ρ) 1056g/m^3 and viscosity (μ) 0.0035 Pa.s, which was also the case with previous studies (Malota et al., 2018, Su et al., 2014). For the wall condition, the vessel walls were modelled as rigid walls, since any perturbation in the walls due to the blood flow is usually averaged out throughout the cardiac cycle, thus having negligible effect on the results of the CFD simulations (Zeng et al., 2008).

Boundary	Condition	Where was the condition obtained from?
Inlet	Uniform pressure inlet	Clinically measured (pressure wires). Average cardiac cycle pressure at the inlet.
Wall	Stationary, no slip wall	Angiogram images are taken at end-diastole.
Outlet	Uniform pressure outlet	Clinically measured (pressure wires). Average cardiac cycle pressure at the outlet.

Table 7.1. The boundary conditions for the pressure-pressure simulations used to compute the volumetric flow rate for each of the twenty single vessel models.

All twenty single vessel cases were run using pressure-inlet and pressure-outlet boundary conditions, to compute the volumetric flow rate (Q). The reconstructions, angiogram images and pressure contours for all twenty CA-only reconstructions and fused reconstructions are provided in Appendix 1. The pressures were derived from those measured directly during the invasive catheterisation procedure. Because pressure can be measured directly and reliably, this means that no assumptions had to be made about the boundary conditions. The pressure wire data measured in the catheterisation lab was presented in Chapter three, table 3.2. The Q_{Fused} and $Q_{CA\text{-}only}$ for all twenty cases are shown in Table 7.2. No comparison can be made against

invasively measured volumetric flow rate because this was not measured at NGH or NNUH, mainly because there are no routinely available methods for measuring this.

A primary limitation of this analysis process of the volumetric flow rate is that it does not account for flow losses along the single lumen that are associated with branching vessels. This means that the flow in proximal sections of the vessel will certainly be less than it should be. However, previous studies have shown that, despite this limitation, vFFR is a blunt measurement and produces a good approximation of FFR. In the VIRTU-1 trial, Morris et al reported a strong correlation between measured and simulated FFR (r 0.84) (Morris et al., 2013).

The Q_{Fused} and $Q_{CA\text{-}only}$ values are plotted in the scatter plot in Figure 7.1 to check for correlation. Ideally, if both imaging modalities produce the same reconstructions of the anatomy, the reported volumetric flow values should be the same. However, since the modalities capture different aspects of the anatomy, it is expected that the agreement between the volumetric flow rates will deviate from being linear with a slope of one. In this case there was a statistically significant correlation between the methods (R^2 0.69, t-score 0.16, $P < 0.00001$).

Case	Q_{Fused} (ml/s)	$Q_{CA\text{-}only}$ (ml/s)	Case	Q_{Fused} (ml/s)	$Q_{CA\text{-}only}$ (ml/s)
1	2.49	1.47	**11**	5.86	5.32
2	2.78	4.92	**12**	4.13	5.53
3	3.03	3.48	**13**	3.08	3.37
4	2.71	1.71	**14**	3.82	3.67
5	3.42	3.21	**15**	1.94	2.42
6	2.86	2.19	**16**	2.3	1.14
7	1.69	2.13	**17**	1.96	1.00
8	2.23	1.36	**18**	2.42	1.11
9	2.11	1.92	**19**	2.36	2.91
10	5.43	6.91	**20**	2.7	2.12

Table 7.2. The simulated volumetric flow rates for all twenty cases. The volumetric flow rate was simulated using 3D coronary reconstructions from fused OCT-CA and from CA-only.

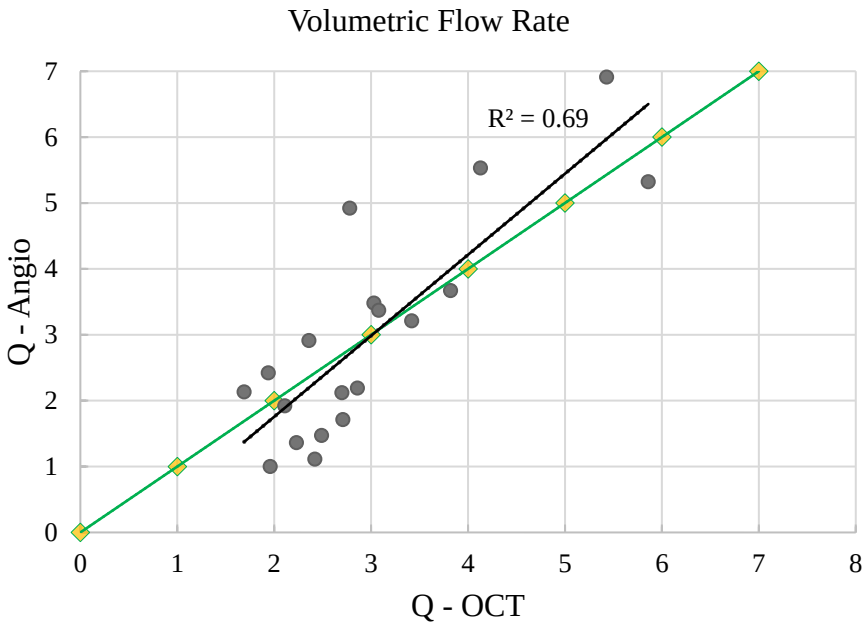

Figure 7.1. A scatter plot showing the agreement between the volumetric flow rate as obtained in silico, using the novel fusion method versus the CA-only method, with the line of best fit. The ideal $R^2 = 1$ line is also plotted as a reminder that ideally, both lines of best fit should be the same.

7.3 Computing the distal resistance of the vessel

With the outlet volumetric flow simulated, the CMVR can be computed. The resistances in a single coronary branch are modelled in series, analogous to an electric circuit with two in-series resistances, as shown in Figure 7.2. The resistance to flow exerted by the vessel (R_{vessel}) is a quadratic relation involving the blood flow (Q) and two constants a_1 and a_2. CMVR is the ratio between the distal pressure and the volume flow rate, which is the hydraulic equivalent of Ohm's law for electric circuits, shown in Equation 7.1.

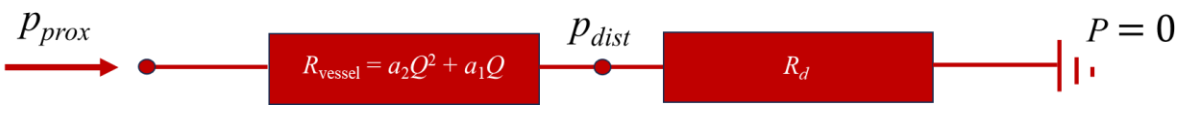

Figure 7.2. Analogy between a single coronary vessel with a characteristic resistance to flow connected with a network of microvasculature and an electric circuit with two in-series resistances.

$$V = IR$$

$$P_{distal} = Q_{distal} * \ CMVR$$

Equation 7.1. The hydraulic equivalent of Ohm's Law in the context of distal coronary microvascular resistance.

V is the voltage difference in the electric circuit (volts), which is analogous to the pressure difference in a blood vessel (Pascals). I (amperes) and Q (m^3/s) are the electrical and blood flows respectively, while the R (ohms) and CMVR (Pa/m^3s^{-1}) are the resistances to electric and blood flows, respectively.

It is assumed that pressure drains to zero (earth). In reality, this is not true because the normal pressure of the right atrium is 0-5 mmHg. However, not only is this not routinely measured, but its overall effect on the calculation is thought to be small, however studies have reported dependence of WSS on the chosen distal pressure especially in diseased vessels (Equbal and Kalita, 2024). The simulation results for $CMVR_{Fused}$ and $CMVR_{CA\text{-}only}$ for all twenty cases are reported in Table 7.3 and plotted in Figure 7.3 to study their agreement. Since it is only a simple mathematical division between the values in Table 7.2 and 7.3, the agreement is expected to be like that shown in Figure 7.1. In this comparison, there was a clinically significant correlation between the methods (R^2 0.59, t-score -1.35, $P < 0.00001$). The average $CMVR_{Fused}$ ($CMVR_{avg\text{-}fused}$) and $CMVR_{CA\text{-}only}$ ($CMVR_{avg\text{-}CA}$) were 3.58 e09 Pa/m^3s^{-1} and 4.14 e09 Pa/m^3s^{-1}, respectively, which is a difference of 0.56 e09 Pa/m^3s^{-1} ($CMVR_{avg\text{-}CA}$ was approximately 16% greater than $CMVR_{avg\text{-}fused}$). These CMVR values are used to compute the vFFR values for all twenty vessels. This to explore how sensitive the computed vFFR values are to the CMVR.

Case	$CMVR_{Fused}$ (Pa/m^3s^{-1}) $x10^9$	$CMVR_{CA\text{-}only}$ (Pa/m^3s^{-1}) $x10^9$	Case	$CMVR_{Fused}$ (Pa/m^3s^{-1}) $x10^9$	$CMVR_{CA\text{-}only}$ (Pa/m^3s^{-1}) $x10^9$
1	3.37	5.71	**11**	1.87	2.05
2	2.83	1.60	**12**	2.20	1.64
3	2.73	2.37	**13**	2.81	2.57
4	3.35	5.29	**14**	1.15	1.20
5	2.69	2.87	**15**	4.67	3.74
6	2.84	3.71	**16**	4.93	9.94
7	5.68	4.50	**17**	5.85	11.45
8	3.11	5.09	**18**	4.46	9.71
9	4.42	4.86	**19**	3.67	2.98
10	1.79	1.41	**20**	4.59	5.84

Table 7.3. The computed distal resistance values for all twenty single vessel cases, computed using the clinically measured distal pressure and the simulated volumetric flow rate for both the novel fusion method and the angiography only methods.

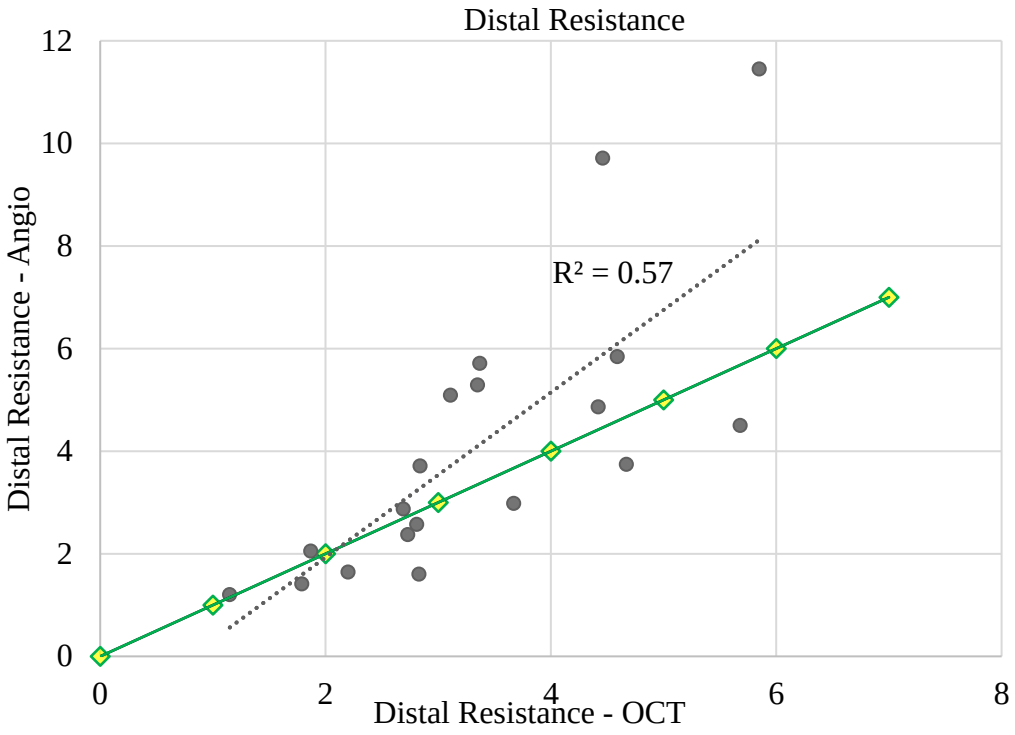

Figure 7.3. A scatter plot showing the agreement between the microvascular resistance as obtained in silico, using the novel fusion method versus the CA-only method, with the line of best fit. The ideal $R^2 = 1$ line is also plotted as a reminder that ideally, both lines of best fit should be the same.

7.4 Computing the vFFR for single vessels

While Q and absolute CMVR are important physiological parameters, their true clinical value in assessing patients and guiding treatment is not yet fully elucidated. Moreover, the simulation of these parameters still requires the deployment of an invasive pressure-wire. By far the most accepted and most frequently used physiological assessment is FFR, and over recent years, vFFR, which is a simulated or calculated value that does not require invasive measurement. In this section I use the novel fusion method to compute vFFR and compare results against (a) the existing CA-only method and (b) against the invasively measured FFR.

To compute the vFFR for all twenty cases two simulations were run in parallel for each case, one with an inlet boundary condition of Q_1 = 3 ml/s and another of Q_2 = 1 ml/s, which are the based on representative hyperaemic and baseline flow values in the major epicardial coronary arteries. These simulations were run with an outlet condition of zero Pascals to compute the pressure drops (Δp_1 and Δp_2) for each case. With the volume flow rates and pressure drops, the coefficients shown in Equations 7.2 and 7.3 can be computed, which can fit into the quadratic Equation 7.4 to compute the distal volumetric flow rate, as previously performed by (Morris et al., 2017). The plot of the pressure drop versus the volumetric flow rate is an upward-facing parabola as shown in Figure 7.4. Figure 7.4 plots in green, the pressure drop at the 1 ml/s and 3 ml/s flow values, and in red, it plots the simulated pressure drop at a flow value between 1 and 3 ml/s. If the simulated volumetric flow rate, shown in Table 7.2, is between 1 and 3 ml/s, then the pressure drop value is expected to be closely modelled by the upward-facing parabola, and the vFFR computed using Equation 7.4 is expected to be a more plausible value. However, for seven cases out of twenty, the simulated volumetric flow value is higher than 3 ml/s, potentially compromising the quality of the vFFR computation. Figure 7.4 shows an example of two cases (7 and 5), one with a simulated Q within 1 and 3 ml/s (left) and one not (right). The flow computed from the clinical pressure-pressure boundary conditions conformed closely to the parabola derived from the 1ml/s and 3ml/s characterisation analyses, except for one case (case 3). For case 3, the volumetric flow rate, which was just higher than 3 ml/s (3.08 ml/s), the extrapolated pressure drop (12 mmHg) was much lower than the clinically measured pressure drop (15 mmHg). For this case there was a deviation of 3 mmHg. This was attributed to the difference between the flow profiles generated by the two boundary conditions. To further investigate this, the pressure drop was simulated in Fluent using a volumetric flow rate of 3.08 ml/s and the value was 12 mmHg. This might be due to the differences associated

with simulating pressure drop using a flow-pressure protocol and the regular pressure-pressure protocol. The distal pressure can be computed by multiplying this volumetric flow rate with the CMVR (as previously described using Ohm's law). The vFFR is then, like the FFR, the ratio between the distal and the proximal pressures, as shown in Equation 7.5.

$$a_1 = \frac{-\Delta p_1 {Q_2}^2 + \Delta p_2 {Q_1}^2}{{Q_1}^2 Q_2 - {Q_2}^2 Q_1}$$

Equation 7.2. The first coefficient in the quadratic equation to compute the vFFR for coronary vessels.

$$a_2 = \frac{\Delta p_1 Q_2 - \Delta p_2 Q_1}{{Q_1}^2 Q_2 - {Q_2}^2 Q_1}$$

Equation 7.3. The second coefficient in the quadratic equation to compute the vFFR for coronary vessels.

$$Q = \frac{-(a_1 + R_{distal}) + \sqrt{(a_1 + R_{distal})^2 + 4 a_2 P_{inlet}}}{2 a_2}$$

Equation 7.4. The distal volumetric flow rate computed using the computed coefficients in Equations 3 and 4.

$$vFFR = \frac{P_{distal}}{P_{inlet}}$$

Equation 7.5. vFFR computation from measured proximal pressure and computed distal pressure.

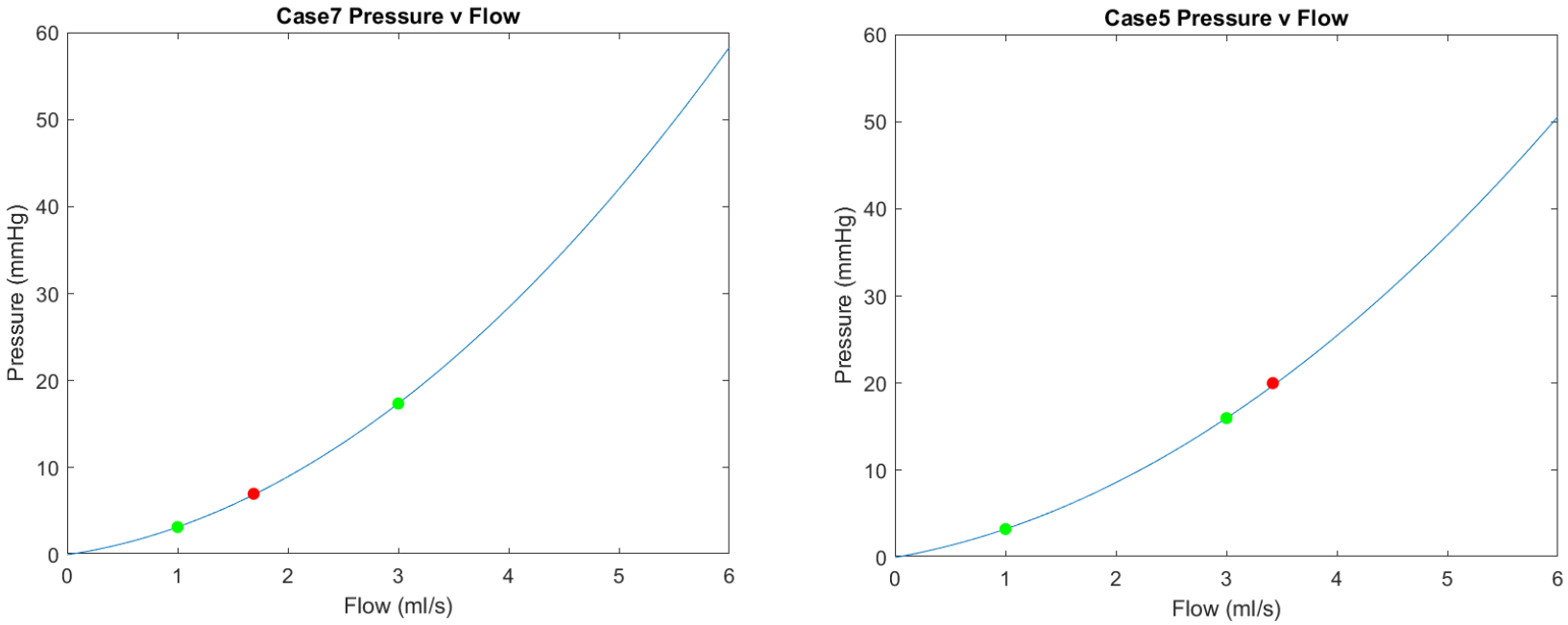

Figure 7.4. Pressure-drop versus volumetric flow rate plots, showing a quadratic relationship. The green points are the pressure drops at the 1 and 3ml/s values, which are the estimated boundaries of the physiological range expected in the coronary arteries. The red point is the actual volumetric flow rate through the vessel and the corresponding simulated pressure drop. (left) Shows a case where the volumetric flow rate through the vessel is within the 1-3 ml/s range, thus having a pressure drop accurately estimated by the quadratic relationship, which is less so in the (right) case where the volumetric flow rate is outside the range and thus the pressure value is extrapolated.

The invasive clinical FFR measurement for each case was compared with the simulated vFFR values derived from both the novel fusion and CA-only methods. For each method, the vFFR was calculated applying both $CMVR_{avg\text{-}fused}$, $CMVR_{avg\text{-}CA}$ as boundary conditions. The results are demonstrated in Table 7.4. The table shows a summary of the FFR versus vFFR for the single vessel twenty cases. Dark green cells indicate FFR ≤ 0.80 and a vFFR ≤ 0.80. Light green cells indicate FFR > 0.80 and vFFR > 0.80. These make up the concordant scenarios. Blue indicates an FFR > 0.80 and a vFFR ≤ 0.80, which is a non-stenting case that was mis-diagnosed to require stenting. Orange is the opposite; it indicates an FFR ≤ 0.80 and a vFFR > 0.80, which means that a vessel that requires stenting was not identified. This is the most serious clinical impact.

		$vFFR_{Fused}$		$vFFR_{CA\text{-}only}$	
Case	**FFR**	**$CMVR_{avg\text{-}fused}$**	**$CMVR_{avg\text{-}CA}$**	**$CMVR_{avg\text{-}fused}$**	**$CMVR_{avg\text{-}CA}$**
1	0.72	0.74	**0.78**	0.58	0.63
2	0.82	0.87	0.89	0.89	0.91
3	0.81	0.89	0.91	0.88	0.90
4	0.74	0.76	**0.79**	0.63	0.67
5	0.78	0.84	0.87	**0.83**	0.85
6	0.84	0.89	0.91	**0.82**	0.85
7	0.91	0.84	0.87	0.87	0.90
8	0.82	0.85	0.87	0.69	0.73
9	0.93	**0.81**	0.84	**0.78**	**0.82**
10	0.65	**0.82**	0.85	0.89	0.91
11	0.75	0.89	0.91	0.89	0.91
12	0.64	0.77	**0.81**	0.85	0.88
13	0.79	0.85	0.88	0.86	0.89
14	0.49	**0.83**	0.86	**0.79**	**0.82**
15	0.94	0.92	0.93	0.92	0.94
16	0.95	0.91	0.93	0.95	0.95
17	0.96	0.91	0.93	0.77	**0.81**
18	0.87	0.84	0.87	0.66	0.70
19	0.82	0.82	0.85	0.85	0.88
20	0.92	0.77	0.81	0.73	0.77
		3/8	2/8	3/8	2/8
		11/12	12/12	7/12	9/12
		5/8	6/8	5/8	6/8
		1/12	0/12	5/12	3/12

vFFR>0.80
vFFR≤0.80

FFR≤0.80 FFR>0.80

Table 7.4. The vFFR using the $CMVR_{avg\text{-}fused}$ and $CMVR_{avg\text{-}CA}$, for both the fused OCT-CA and CA-only geometries. The clinically measured FFR is also included for in the table for comparison. Dark green cells indicate FFR ≤ 0.80 and a vFFR ≤ 0.80. Light green cells indicate FFR > 0.80 and vFFR > 0.80. These make up the concordant scenarios. Blue indicates an FFR > 0.80 and a vFFR ≤ 0.80. Orange indicates an FFR ≤ 0.80 and a vFFR > 0.80. These are the discordant cases. The entries in bold are those that lie inside the grey zone (0.78≤FFR≤0.83).

7.4.1 Diagnostic accuracy

Of clinical relevance is the diagnostic concordance between FFR and vFFR i.e. whether vFFR indicates true positive (≤0.80) or true negative (>0.80). Table 7.5 presents the four combinations of reconstructions with distal resistances and their resulting sensitivity, specificity, negative predictive and positive predictive values (NPV and PPV) and overall accuracy. In Figures 7.5, 7.6 and 7.7, the black lines at 0.80 indicate the threshold for PCI. The points in the top right and bottom left quadrants are concordant, whereas the points in the other quadrants are discordant. $vFFR_{Fused}$ showed the best concordance with the invasive FFR (regardless of which CMVR boundary conditions were applied). $vFFR_{CA\text{-}only}$ was less accurate than $vFFR_{Fused,}$ but for this approach there was an effect from the boundary conditions applied, with the better results being generated when the $CMVR_{avg\text{-}fused}$ boundary conditions were applied (six discordant cases vs ten and six versus nine, respectively). When $vFFR_{Fused}$ was compared with $vFFR_{CA\text{-}only}$, a better concordance was achieved with the $CMVR_{avg\text{-}CA}$ boundary condition than the $CMVR_{avg\text{-}CA}$ boundary condition (three discordant cases versus six).

Although the case numbers in this proof-of-concept validation are low, the $vFFR_{Fused}$ reconstructions with both boundary conditions provided the better diagnostic accuracy against the clinical values, when compared with the $vFFR_{CA\text{-}only}$ reconstructions. Using $CMVR_{avg\text{-}fused}$ as the boundary condition had higher sensitivity and thus may therefore be used to identify cases needing intervention more accurately. Using $CMVR_{avg\text{-}CA}$ was associated with a perfect PPV, with a corresponding NPV of 0.67.

	Sensitivity	**Specificity**	**NPV**	**PPV**	**Accuracy**
$vFFR_{Fused}$ + $CMVR_{avg\text{-}CA}$	0.25	1.0	0.67	1.0	0.70
$vFFR_{Fused}$ + $CMVR_{avg\text{-}fused}$	0.38	0.92	0.69	0.75	0.70
$vFFR_{CA\text{-}only}$ + $CMVR_{avg\text{-}CA}$	0.25	0.75	0.60	0.40	0.55
$vFFR_{CA\text{-}only}$ + $CMVR_{avg\text{-}fused}$	0.38	0.58	0.58	0.38	0.50

Table 7.5. The four combinations of boundary conditions, with their corresponding sensitivity, specificity, negative and positive predictive values (NPV and PPV) and accuracy, for the single vessel reconstructions.

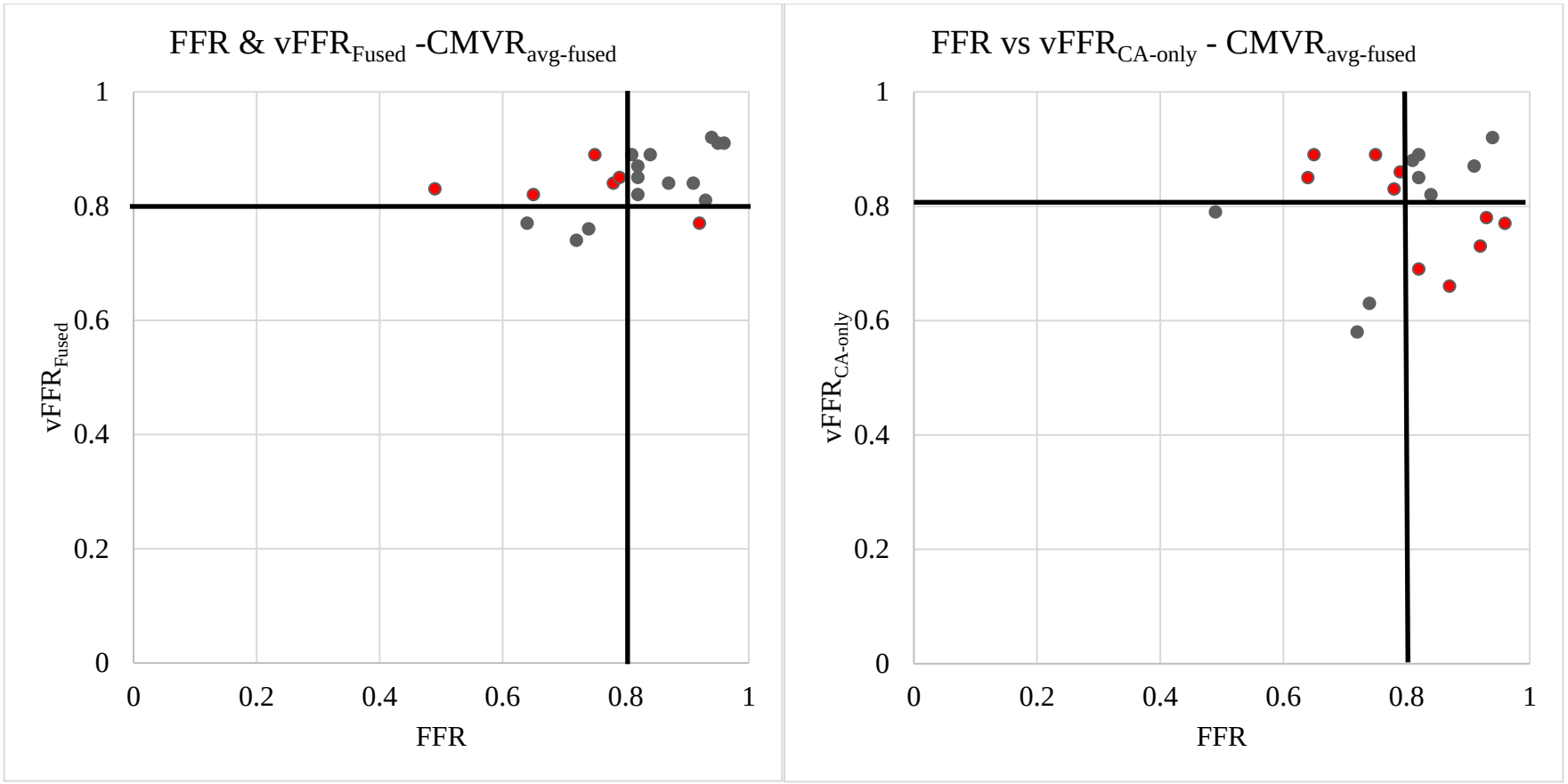

Figure 7.5. Scatter plots of the clinically measured FFR, vFFR$_{Fused}$ and vFFR$_{CA-only}$ using CMVR$_{avg-fused}$, to study their concordance. The black lines at 0.80 mark the critical threshold of stenting. The points in the top right and bottom left quadrants are concordant points, indicating that both the FFR and vFFR values either both indicate the need to stent or not to. The points in the top left and bottom right show discordance between the FFR and vFFR values, whereby one indicates the need to stent and the other does not. vFFR$_{Fused}$ shows better concordance with the FFR than the vFFR$_{CA-only}$ with (six discordant cases vs ten).

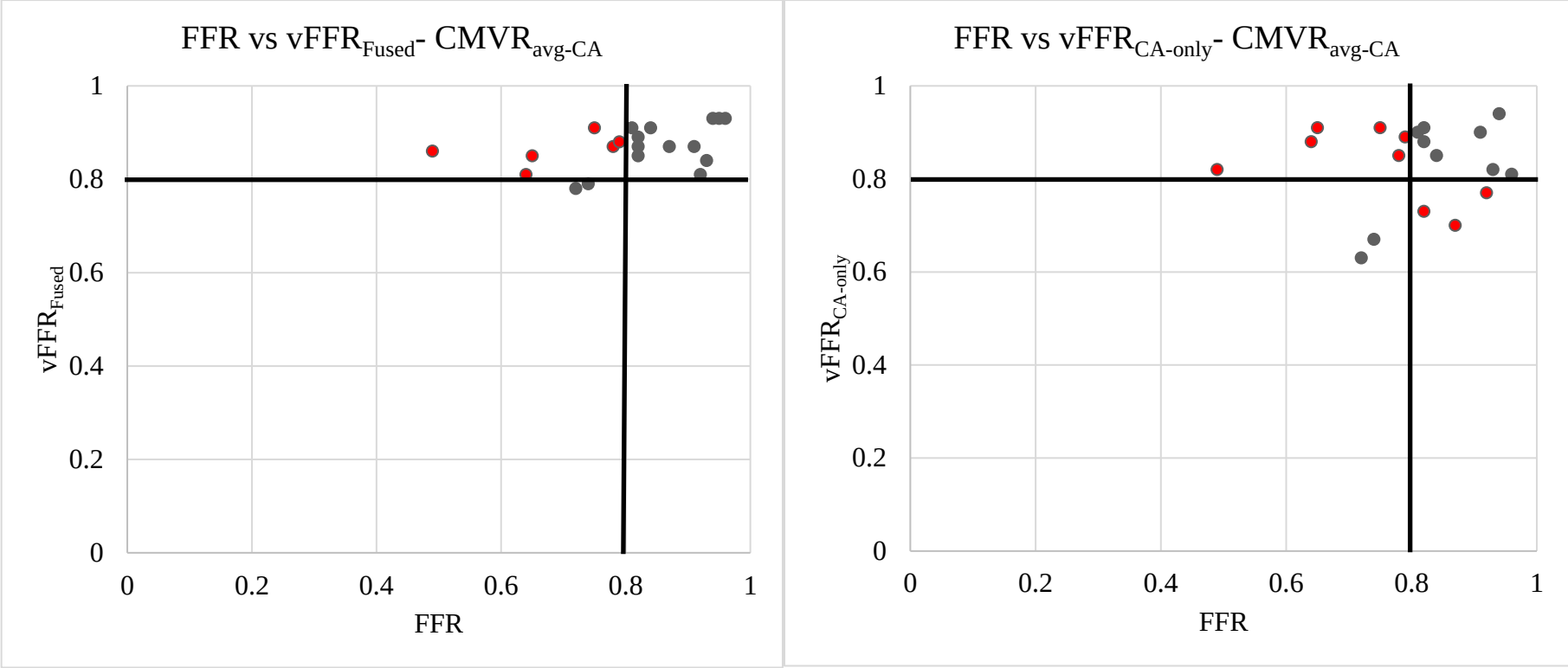

Figure 7.6. Scatter plots of the clinically measured FFR, vFFR$_{Fused}$ and vFFR$_{CA-only}$ using CMVR$_{avg-CA}$, to study their concordance. The black lines at 0.80 mark the critical threshold of stenting. The points in the top right and bottom left quadrants are concordant points, indicating that both the FFR and vFFR values either both indicate the need to stent or not to. The points in the top left and bottom right show discordance between the FFR and vFFR values, whereby one indicates the need to stent and the other does not. vFFR$_{Fused}$ shows better concordance with the FFR than the vFFR$_{CA-only}$ with (six discordant cases vs nine).

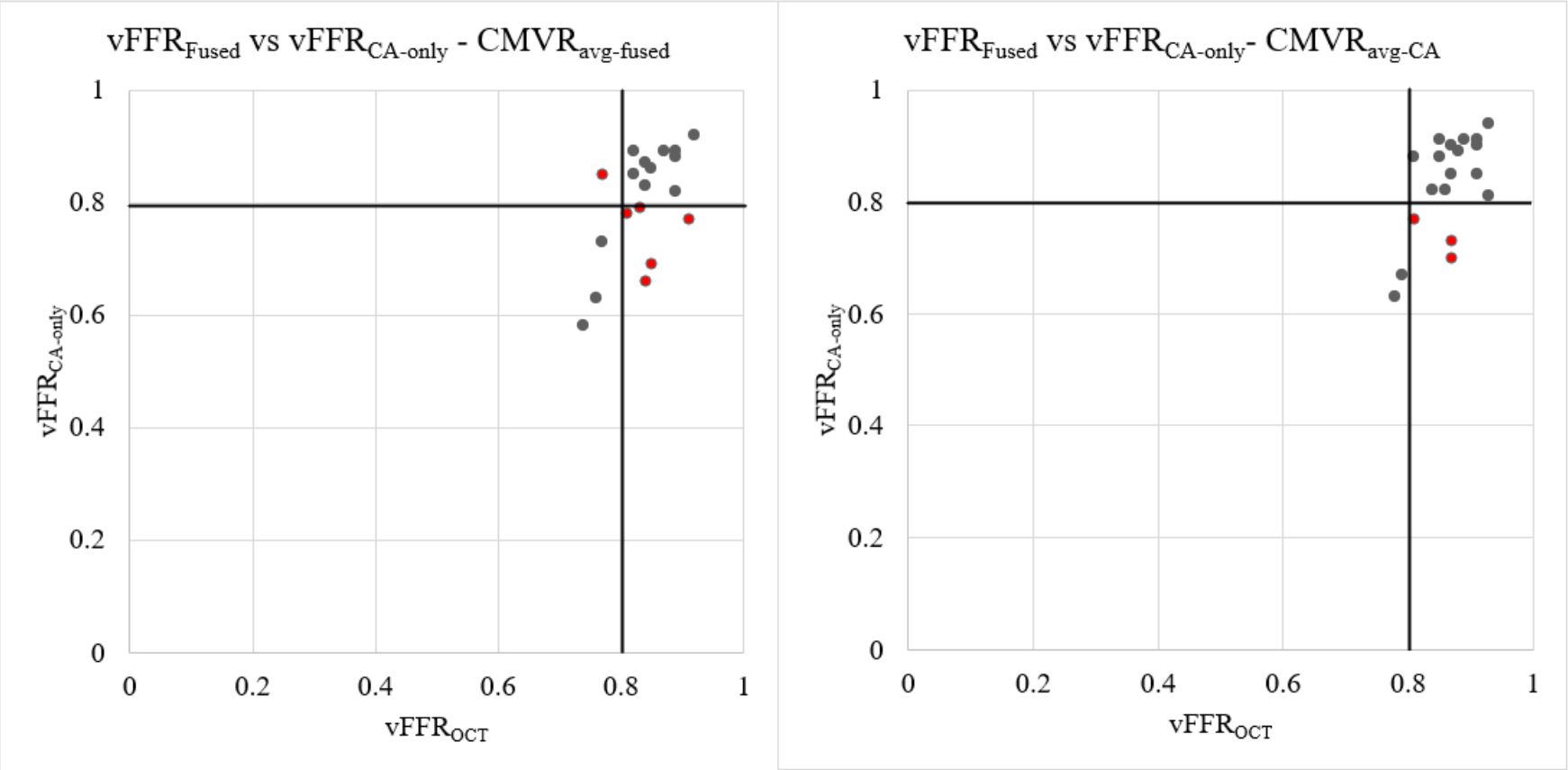

Figure 7.7. Scatter plots of the vFFR from both the fused and CA-only reconstructions using $CMVR_{avg\text{-}fused}$ and $CMVR_{avg\text{-}CA}$, to study their concordance. The black lines at 0.80 mark the critical threshold of stenting. The points in the top right and bottom left quadrants are concordant points, indicating that both the FFR and vFFR values either both indicate the need to stent or not to. The points in the top left and bottom right show discordance between the FFR and vFFR values, whereby one indicates the need to stent and the other does not. $vFFR_{Fused}$ and $FFR_{CA\text{-}only}$ show better concordance with the $CMVR_{avg\text{-}CA}$ boundary condition (three discordant cases vs six).

7.4.2 Numerical accuracy

The best way to assess model accuracy is by Bland-Altman plots and by calculating the associated bias (mean delta) and Bland-Altman limits of agreement (BA-LOA) which reflect the 95% confidence interval of any result, i.e. the BA-LOA indicate the range that one can be 95% confident of the result being in. In short, they represent an 'error range' so that the narrower they are, the more accurate the result. The limits of agreement are only a measure of model accuracy, whereas the diagnostic accuracy (based on dichotomised data; positive or negative only) is a measure of both model accuracy and the cases that just happen to be in those being analysed and studied. Even an excellent model (with very narrow LOA) will generate a very low diagnostic accuracy if the cases are all very close to the FFR ≤ 0.80 threshold and, vice versa, a very poor model (with wide LOA) may appear diagnostically very good if the cases being analyzed are either very low or very high with only very few cases close to the ≤ 0.80 threshold.

The overall bias and BA-LOA for each model and boundary condition combination are presented in Table 7.6. As can be seen in Table 7.6, the model with highest numerical accuracy (narrowest BA-LOA), when compared with invasive FFR was $vFFR_{Fused}$ + $CMVR_{avg\text{-}fused}$ or $CMVR_{avg\text{-}CA}$, followed by $vFFR_{CA\text{-}only}$ + $CMVR_{avg\text{-}CA}$. The differences between these levels of numerical accuracy were statistically non-significant (P >0.05 for all comparisons), which is expected given the low number of cases in this initial, proof-of-concept analysis. When I additionally factored in the overall bias (Equation 7.6), to provide an overall score for each combination (Equation 7.6) the results were similar: The model with highest numerical accuracy (lowest score), when compared with invasive FFR was $vFFR_{Fused}$ + $CMVR_{avg\text{-}fused}$ followed by $CMVR_{avg\text{-}CA}$, followed by $vFFR_{CA\text{-}only}$ + $CMVR_{Fused}$ and $vFFR_{CA\text{-}only}$ + $CMVR_{avg\text{-}CA}$ (the latter two have very similar scoring).

The last two rows show how the vFFR computed from the novel fusion method compares with the current gold standard ($vFFR_{CA\text{-}only}$). As shown, these two rows have the narrowest BA-LOA and the lowest scoring, which is validation for the novel fusion method.

$$Score = |Overall\ Bias| + (Upper\ limit\ of\ agreement - Lower\ limit\ of\ agreement)$$

Equation 7.6. Scoring the Bland-Altmann overall bias and limits of agreement to determine which combination of reconstruction method boundary condition produces vFFR values that agree the most with the FFR. A lower score indicates better agreement.

The corresponding Bland-Altman plots are demonstrated in Figures 7.8-7.10. The Bland-Altmann plots comparing both vFFR values have slightly negative mean difference, indicating a slight overestimation of the vFFR by CA.

	Overall Bias	**BA-LOA**	**Width**	**Score**
FFR vs $vFFR_{Fused}$ + $CMVR_{avg\text{-}CA}$	-0.061	[-0.28 0.15]	0.43	0.49
FFR vs $vFFR_{Fused}$ + $CMVR_{avg\text{-}fused}$	-0.034	[-0.25 0.18]	0.43	0.46
FFR vs $vFFR_{CA\text{-}only}$ + $CMVR_{avg\text{-}CA}$	-0.029	[-0.31 0.25]	0.56	0.59
FFR vs $vFFR_{CA\text{-}only}$ + $CMVR_{avg\text{-}fused}$	0.001	[-0.29 0.29]	0.58	0.58
$vFFR_{Fused}$ vs $vFFR_{CA\text{-}only}$ + $CMVR_{avg\text{-}CA}$	0.032	[-0.11 0.17]	0.28	0.31
$vFFR_{Fused}$ vs $vFFR_{CA\text{-}only}$ + $CMVR_{avg\text{-}fused}$	0.035	[-0.12 0.19]	0.31	0.35

Table 7.6. The overall bias, Bland-Altmann limits of agreement and their width for the six combinations comparing FFR, $vFFR_{Fused}$ and $vFFR_{CA\text{-}only}$ using $CMVR_{avg\text{-}CA}$ and $CMVR_{avg\text{-}fused}$. The last column shows the scoring for the first four combinations to rank their agreement with the clinical FFR.

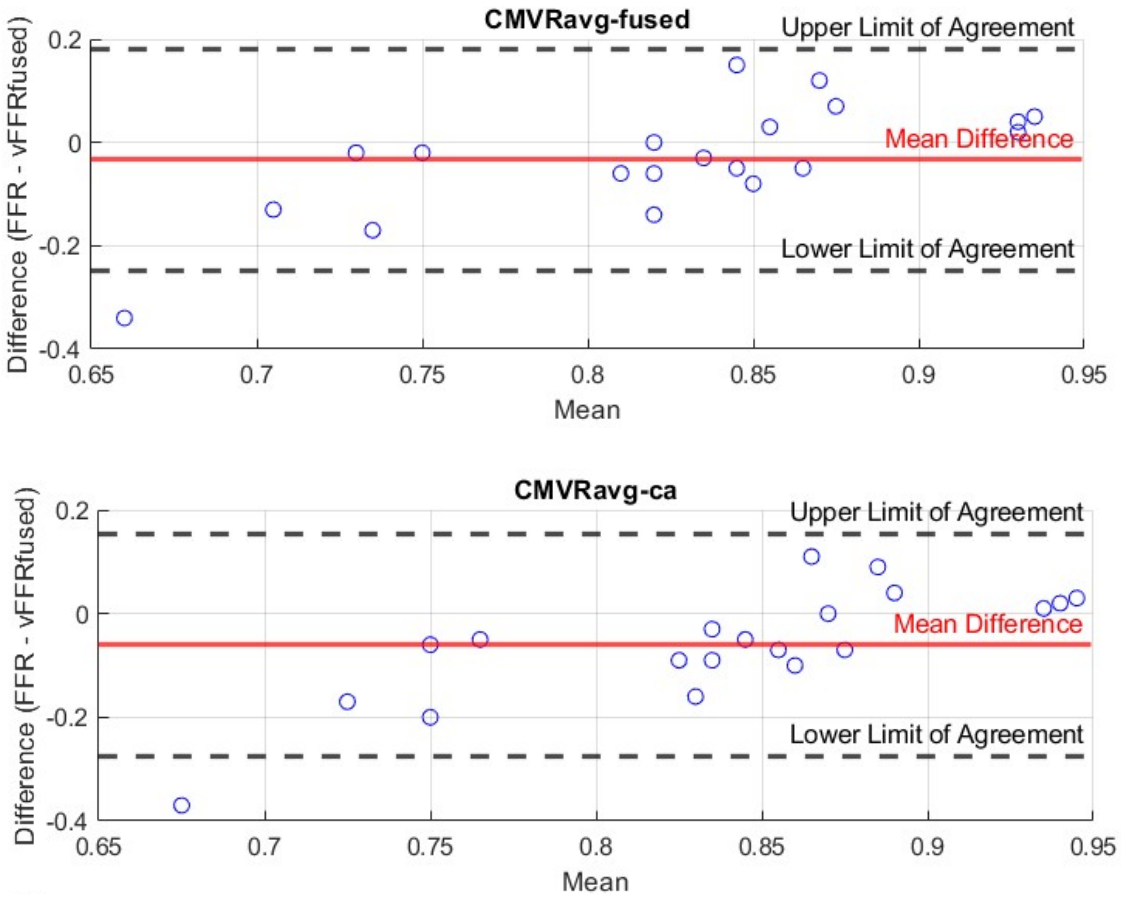

Figure 7.8. Bland Altmann plots of the FFR and $vFFR_{Fused}$ and the limits of agreement using both $CMVR_{avg\text{-}fused}$ and $CMVR_{avg\text{-}CA}$. All the points lie within the 95% limits of agreement.

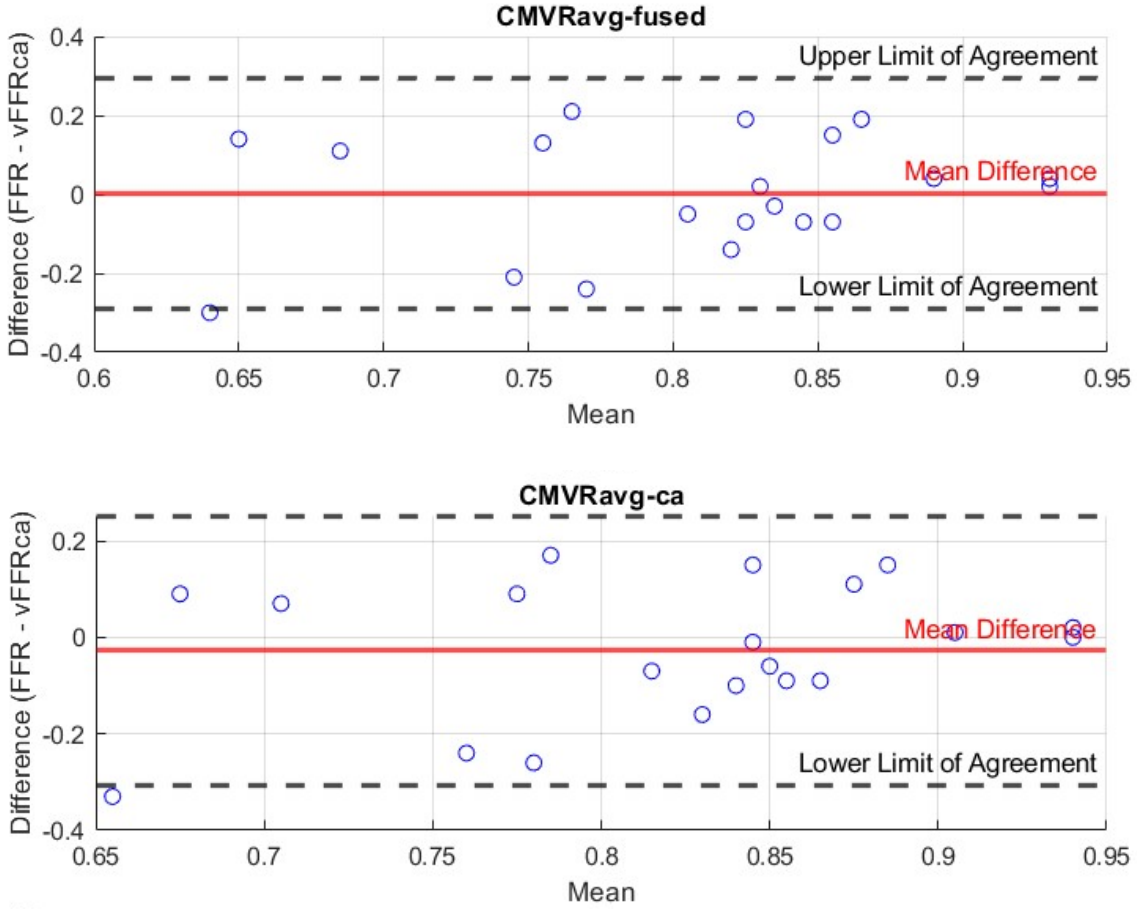

Figure 7.9. Bland Altmann plots of the FFR and $vFFR_{CA\text{-}only}$ and the limits of agreement using both $CMVR_{avg\text{-}fused}$ and $CMVR_{avg\text{-}CA}$. All the points lie within the 95% limits of agreement.

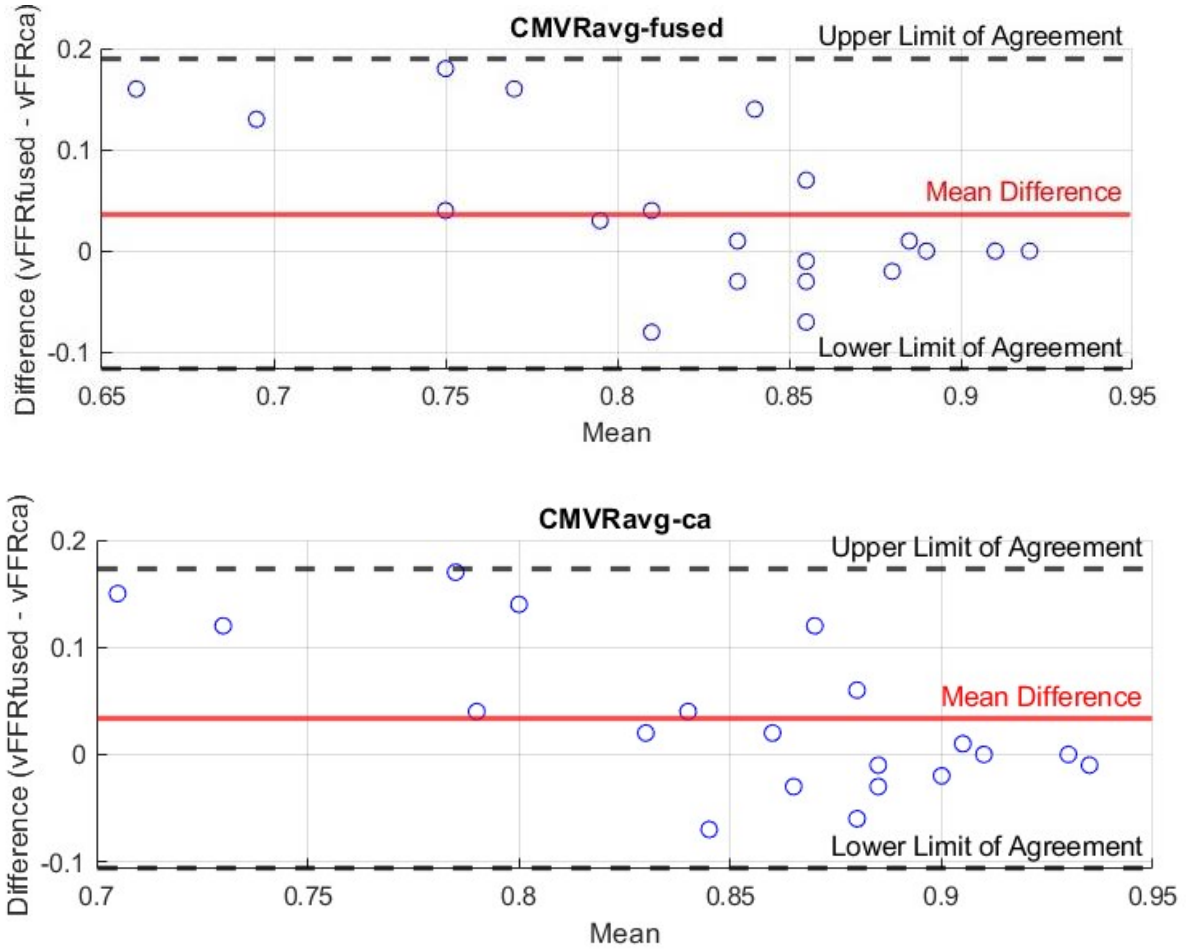

Figure 7.10. Bland Altmann plots of $vFFR_{Fused}$ and $vFFR_{CA\text{-}only}$ and the limits of agreement using both $CMVR_{avg\text{-}fused}$ and $CMVR_{avg\text{-}CA}$. All the points lie within the 95% limits of agreement.

7.4.3 Correlation analysis

In this analysis on just twenty cases, the correlation coefficients between invasive FFR and all modelled vFFR results were statistically non-significant (P>0.05), as is shown in Table 7.7. $vFFR_{Fused}$ (regardless of the distal boundary condition used) demonstrated the closest correlation with the clinical FFR, followed by $vFFR_{CA\text{-}only}$ + $CMVR_{avg\text{-}fused}$ then $vFFR_{CA\text{-}only}$ + $CMVR_{avg\text{-}CA}$. These results are similar to the previous results from the diagnostic and numerical accuracy measurements.

	r	R^2	P	Clinically significant correlation?
FFR vs $vFFR_{Fused}$ + $CMVR_{avg\text{-}CA}$	0.42	0.18	0.065	No
FFR vs $vFFR_{Fused}$ + $CMVR_{avg\text{-}fused}$	0.42	0.18	0.065	No
FFR vs $vFFR_{CA\text{-}only}$ + $CMVR_{avg\text{-}CA}$	0.11	0.013	0.64	No
FFR vs $vFFR_{CA\text{-}only}$ + $CMVR_{avg\text{-}fused}$	0.12	0.014	0.61	No

Table 7.7. The correlation analysis between clinically measured FFR and the single vessel vFFR simulated using both the fused and CA-only reconstructions using $CMVR_{avg\text{-}fused}$ and $CMVR_{avg\text{-}CA}$. All correlations are clinically non-significant.

7.4.4 Single vessel results summary

In summary, in terms of diagnostic accuracy *and* numerical accuracy, the best overall accuracy was with the $vFFR_{Fused}$ method, with the $CMVR_{avg\text{-}fused}$ boundary condition applied, followed by the $vFFR_{Fused}$ method with the $CMVR_{avg\text{-}CA}$ boundary condition applied, followed by the $vFFR_{CA\text{-}only}$ method with the $CMVR_{avg\text{-}fused}$ boundary condition applied. It is important to note that the case numbers are low in this preliminary analysis. It is notable that the agreement between the two experimental techniques (CA- and OCT-derived vFFR) methods was particularly good.

7.5 Computing vFFR for branching vessels

Although it is the current standard of care, calculating vFFR for single, independent branches is not advantageous (Gamage et al., 2022). By considering single lumens in bifurcation cases, one will automatically underestimate proximal (common stem) flow. By incorporating the side branch flow, the proximal flow will increase. Thus, if single branch CFD analysis is applied and there is a lesion in the common stem, the physiological significance of the lesion will be underestimated which, therefore, overestimates the vFFR. The clinical implication is therefore to under treat proximal lesions. Therefore, to improve the accuracy of the model, especially when the clinical region of interest includes a major bifurcation, it would be better to model these effects.

The previous section presented how the vFFR was computed for single vessels. For eight cases out of the twenty, the vessels represented a bifurcation with corresponding main and side vessels. These cases were reconstructed as branches using the novel fusion method. The results are described as $vFFR_{branching}$ for each branch. The branching vessels are modelled as shown in Figure 7.11.

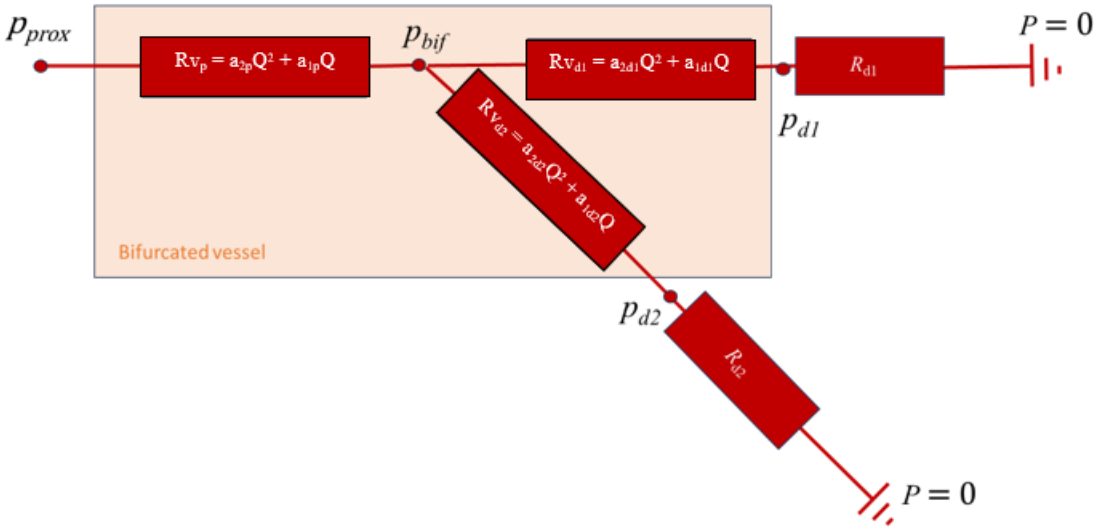

Figure 7.11. The electrical circuit representation of a branching coronary vessel. The vessel is regarded as a three-section circuit, each with a characteristic resistance and the daughter branches being in series to microvascular resistances.

The vessels are divided into three sections:

1. A common proximal section, with inlet pressure of P_{prox} and an outlet at the bifurcation, with pressure of $P_{bif,}$
2. A main vessel with inlet pressure equal to P_{bif}, with a characteristic resistance and microvascular resistance,
3. A side branch with inlet pressure equal to P_{bif}, with a characteristic resistance and microvascular resistance.

Using the Ohm's law analogy produces the four simultaneous equations that are presented in Equation 7.7. a_{1p}, a_{2p} a_{1d1}, a_{1d2} a_{2d1} and a_{2d2} can be computed using Equations 7.2 and 7.3 and Q_{prox}, Q_{dist1} and Q_{dist2} can be computed using Equation 7.4. This allows the computation of the pressure everywhere along the vessel. Equation 7.5 can then be used to compute the $vFFR_{branching}$. The distal resistance was assumed to be the same for both branches for each simulation. The $vFFR_{branching}$ values are presented in Table 7.7, and similarly to Table 7.4, the concordance/discordance is indicated by color-coding. The values are also presented in Figures 7.11-7.13 to study concordance, as done previously. What is interesting to note is that, when comparing Tables 7.4 and 7.7, when branches are modelled and simulated instead of single vessels, the number of orange cells decreased to five cases (from 22), and all vessels with an FFR < 0.80 are identified (dark green). However, there is a slight increase in blue cells (four to eight), which indicates unnecessary stenting which is a waste of time and money.

Table 7.13 shows the volumetric flow rate for each branch for all eight cases, when the branches are modelled as part of a tree. The obtained volumetric flow rate values are compared with those from the single vessel simulations.

$$p_{prox} - p_{bif} = a_{2p}{Q_{prox}}^2 + a_{1p}Q_{prox}$$

$$p_{bif} = a_{2d1}{Q_{dist1}}^2 + a_{1d1}Q_{dist1} + R_{d1}Q_{dist1}$$

$$p_{bif} = a_{2d2}{Q_{dist2}}^2 + a_{1d2}Q_{dist2} + R_{d2}Q_{dist2}$$

$$Q_{prox} = Q_{dist1} + Q_{dist2}$$

Equation 7.7. The four simultaneous equations that allow the computation of pressure and flow everywhere in a branching model.

		$vFFR_{branching\text{-}fused}$		$vFFR_{branching\text{-}CA}$	
Case	**FFR**	**$CMVR_{avg\text{-}fused}$**	**$CMVR_{avg\text{-}CA}$**	**$CMVR_{avg\text{-}fused}$**	**$CMVR_{avg\text{-}CA}$**
1	0.64	0.69	0.65	0.76	**0.80**
	0.79	0.75	0.71	0.77	**0.80**
2	0.74	**0.78**	0.75	0.72	0.76
	0.78	**0.81**	**0.79**	0.72	0.76
3	0.84	0.86	**0.83**	**0.81**	0.84
	0.91	**0.82**	**0.81**	**0.81**	0.84
4	0.82	**0.81**	0.76	0.62	0.66
	0.93	**0.81**	0.76	0.66	0.70
5	0.65	**0.79**	**0.81**	0.66	0.70
	0.75	**0.83**	0.85	0.75	0.79
6	0.82	**0.82**	**0.80**	0.85	0.87
	0.81	0.86	0.84	**0.83**	0.86
7	0.49	**0.79**	0.76	0.69	0.75
	0.94	0.88	0.86	0.71	0.73
8	0.95	0.92	0.91	0.99	0.97
	0.96	0.92	0.91	0.98	0.97

5/7	5/7	7/7	5/7
9/9	6/9	6/9	6/9
2/7	2/7	0/7	0/7
0/9	2/9	3/9	3/9

vFFR>0.80		
vFFR≤0.80		
	FFR≤0.80	FFR>0.80

Table 7.8. The $vFFR_{branching}$ computed using the distal resistance values, $CMVR_{avg\text{-}fused}$ and $CMVR_{avg\text{-}CA}$, for the fused OCT-CA and CA-only geometries. The clinically measured FFR is also included for in the table for comparison. Green cells, as described in the lower panel, indicate FFR ≤ 0.80 and a vFFR ≤ 0.80. Grey cells indicate FFR > 0.80 and vFFR > 0.80. These make up the concordant scenarios. Blue indicates an FFR > 0.80 and a vFFR ≤ 0.80 and orange indicates FFR ≤ 0.80 and a vFFR > 0.80. These are the discordant cases. Entries in bold are within the 'grey zone' for stenting (0.78≤FFR≤0.83).

7.5.1 Diagnostic Accuracy

Similarly to the analysis performed on the single vessel vFFR results in the previous section, the branching vFFR results were examined for their concordance/discordance (Figures 7.12-7.14). $vFFR_{branching\text{-}fused}$ with the $CMVR_{avg\text{-}fused}$ was the most accurate (two discordant cases), followed by the $vFFR_{branching\text{-}fused}$ with both boundary conditions (three discordant cases each), followed by the $vFFR_{branching\text{-}fused}$ with the $CMVR_{avg\text{-}CA}$ boundary conditions (four discordant cases). The best concordance between the two vFFR sets was produced when the $CMVR_{avg\text{-}CA}$ was applied (five discordant cases vs four), although most of the discordant cased were at within the grey-zone.

Table 7.9 presents the four combinations of branching reconstructions with distal resistances and their resulting sensitivity, specificity, negative predictive and positive predictive values (NPV and PPV) and accuracy. Using $vFFR_{branching\text{-}Fused}$ + $CMVR_{avg\text{-}fused}$ produced the highest accuracy and prefect PPV, followed by both $vFFR_{branching\text{-}CA}$ + $CMVR_{avg\text{-}fused}$ and $vFFR_{branching\text{-}CA}$ + $CMVR_{avg\text{-}CA}$.

	Sensitivity	**Specificity**	**NPV**	**PPV**	**Accuracy**
$vFFR_{branching\text{-}Fused}$ + $CMVR_{avg\text{-}CA}$	0.71	0.78	0.78	0.71	0.75
$vFFR_{branching\text{-}Fused}$ + $CMVR_{avg\text{-}fused}$	0.71	1.00	0.82	1.00	0.88
$vFFR_{branching\text{-}CA}$ + $CMVR_{avg\text{-}CA}$	1.00	0.67	1.00	0.70	0.81
$vFFR_{branching\text{-}CA}$ + $CMVR_{avg\text{-}fused}$	1.00	0.67	1.00	0.70	0.81

Table 7.9. The four combinations of boundary conditions, with their corresponding sensitivity, specificity, negative and positive predictive values (NPV and PPV) and accuracy, for the branching vessel reconstructions.

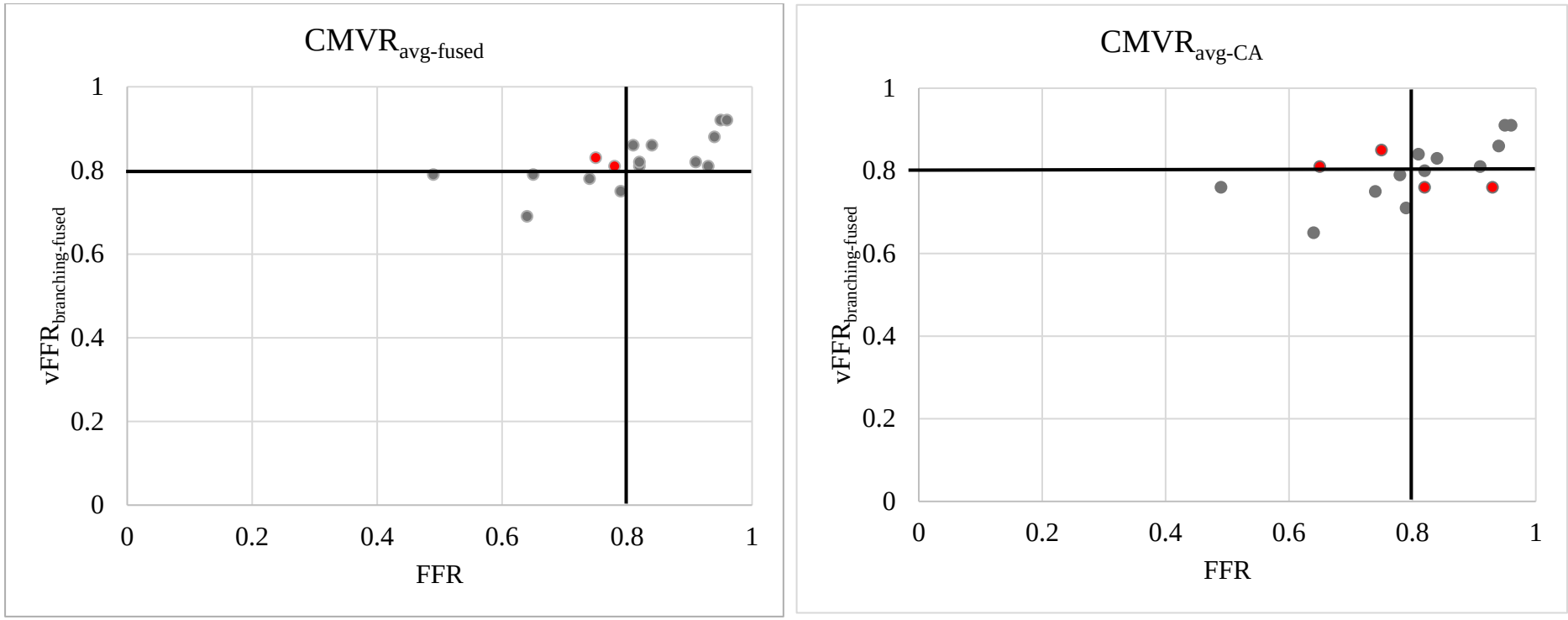

Figure 7.12. Scatter plots of the clinically measured FFR and $vFFR_{branching\text{-}fused}$ using $CMVR_{avg\text{-}fused}$ and $CMVR_{avg\text{-}CA}$ to study their concordance. The orange lines at 0.80 mark the critical threshold of stenting. The points in the top right and bottom left quadrants are concordant points, indicating that both the FFR and vFFR values either both indicate the need to stent or not to. The points in the top left and bottom right show discordance between the FFR and vFFR values, whereby one indicates the need to stent and the other does not. $vFFR_{branching\text{-}fused}$ computed using $CMVR_{avg\text{-}fused}$ produced better concordance with the FFR (two discordant cases vs four).

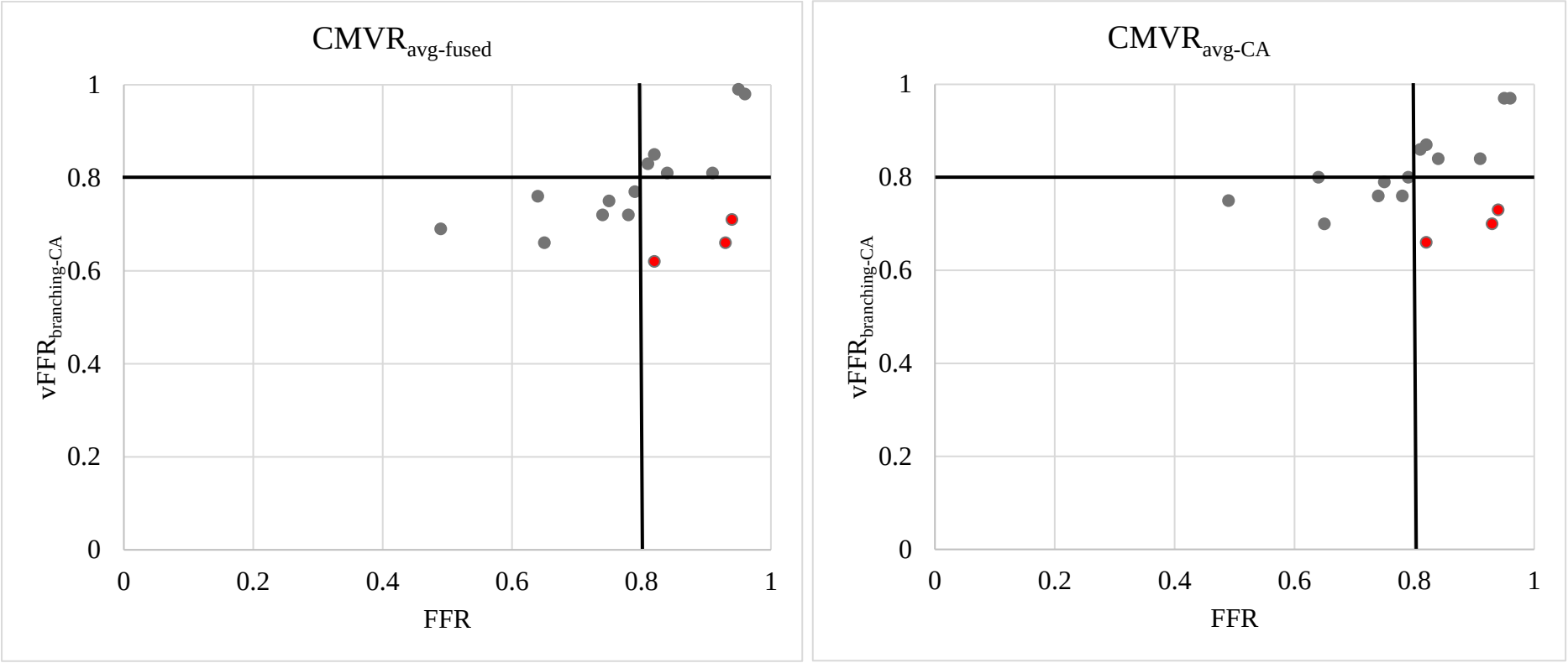

Figure 7.13. Scatter plots of the clinically measured FFR and $vFFR_{branching\text{-}CA}$ using $CMVR_{avg\text{-}fused}$ and $CMVR_{avg\text{-}CA}$ to study their concordance. The orange lines at 0.80 mark the critical threshold of stenting. The points in the top right and bottom left quadrants are concordant points, indicating that both the FFR and vFFR values either both indicate the need to stent or not to. The points in the top left and bottom right show discordance between the FFR and vFFR values, whereby one indicates the need to stent and the other does not. $vFFR_{branching\text{-}CA}$ produced comparable concordance using both boundary conditions (three discordant cases vs three).

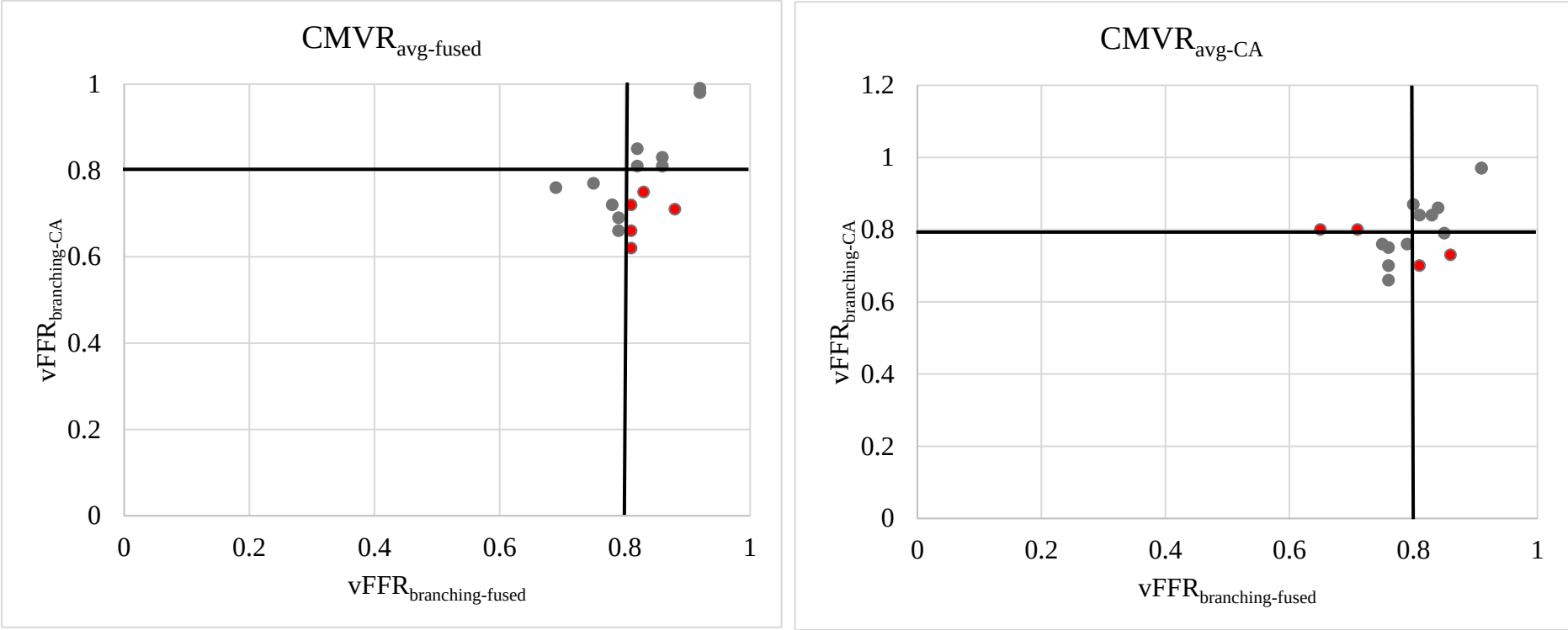

Figure 7.14. Scatter plots of the $vFFR_{branching\text{-}fused}$ and $vFFR_{branching\text{-}CA}$ using $CMVR_{avg\text{-}fused}$ and $CMVR_{avg\text{-}CA}$ to study their concordance. The orange lines at 0.80 mark the critical threshold of stenting. The points in the top right and bottom left quadrants are concordant points, indicating that both the FFR and vFFR values either both indicate the need to stent or not to. The points in the top left and bottom right show discordance between the FFR and vFFR values, whereby one indicates the need to stent and the other does not. The best concordance between the two vFFR sets was produced when the $CMVR_{avg\text{-}CA}$ was applied (five discordant cases vs four), although most of the discordant cases were at the threshold.

7.5.2 Numerical Accuracy

As previously, agreement is assessed using Bland-Altmann plots. To assess agreement, the overall bias and BA-LOA for each model and boundary condition combination are presented in Table 7.10. The model with most agreement with the FFR was $vFFR_{branching\text{-}Fused} + CMVR_{avg\text{-}fused}$, followed by $vFFR_{branching\text{-}Fused} + CMVR_{avg\text{-}CA}$, followed by $vFFR_{branching\text{-}CA} + CMVR_{avg\text{-}CA}$. This was obtained through finding the combination with the narrowest BA-LOA with and through scoring (Equation 7.6). The corresponding Bland-Altman plots are demonstrated in Figures 7.15-7.17.

	Overall Bias	**BA-LOA**	**Width**	**Score**
FFR vs $vFFR_{branching\text{-}Fused} + CMVR_{avg\text{-}CA}$	0.001	[-0.21 0.21]	0.42	0.42
FFR vs $vFFR_{branching\text{-}Fused} + CMVR_{avg\text{-}fused}$	-0.02	[-0.22 0.18]	0.40	0.41
FFR vs $vFFR_{branching\text{-}CA} + CMVR_{avg\text{-}CA}$	0.001	[-0.24 0.25]	0.49	0.49
FFR vs $vFFR_{branching\text{-}CA} + CMVR_{avg\text{-}fused}$	0.031	[-0.21 0.27]	0.48	0.51
$vFFR_{branching\text{-}Fused}$ vs $vFFR_{branching\text{-}CA} + CMVR_{avg\text{-}CA}$	0.00	[-0.15 0.15]	0.30	0.31
$vFFR_{branching\text{-}Fused}$ vs $vFFR_{branching\text{-}CA} + CMVR_{avg\text{-}fused}$	0.051	[-0.12 0.22]	0.34	0.39

Table 7.10. The overall bias, Bland-Altmann limits of agreement and their width for the six combinations comparing FFR, $vFFR_{branching\text{-}Fused}$ and $vFFR_{branching\text{-}CA}$ using $CMVR_{avg\text{-}CA}$ and $CMVR_{avg\text{-}fused}$. The last column shows the scoring for the first four combinations to rank their agreement with the clinical FFR.

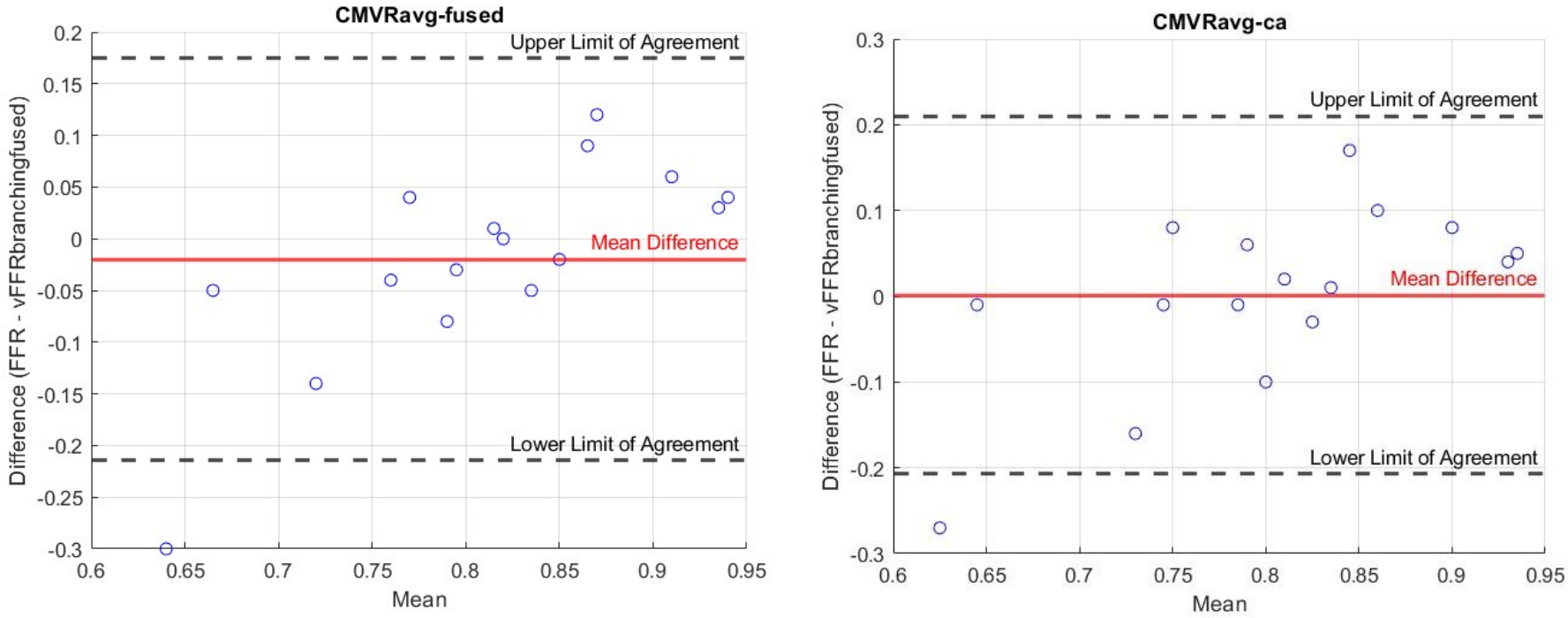

Figure 7.15. Bland Altmann plots of the FFR and $vFFR_{branching\text{-}fused}$ and the limits of agreement using both $CMVR_{avg\text{-}fused}$ and $CMVR_{avg\text{-}CA}$. Most points lie within the 95% limits of agreement.

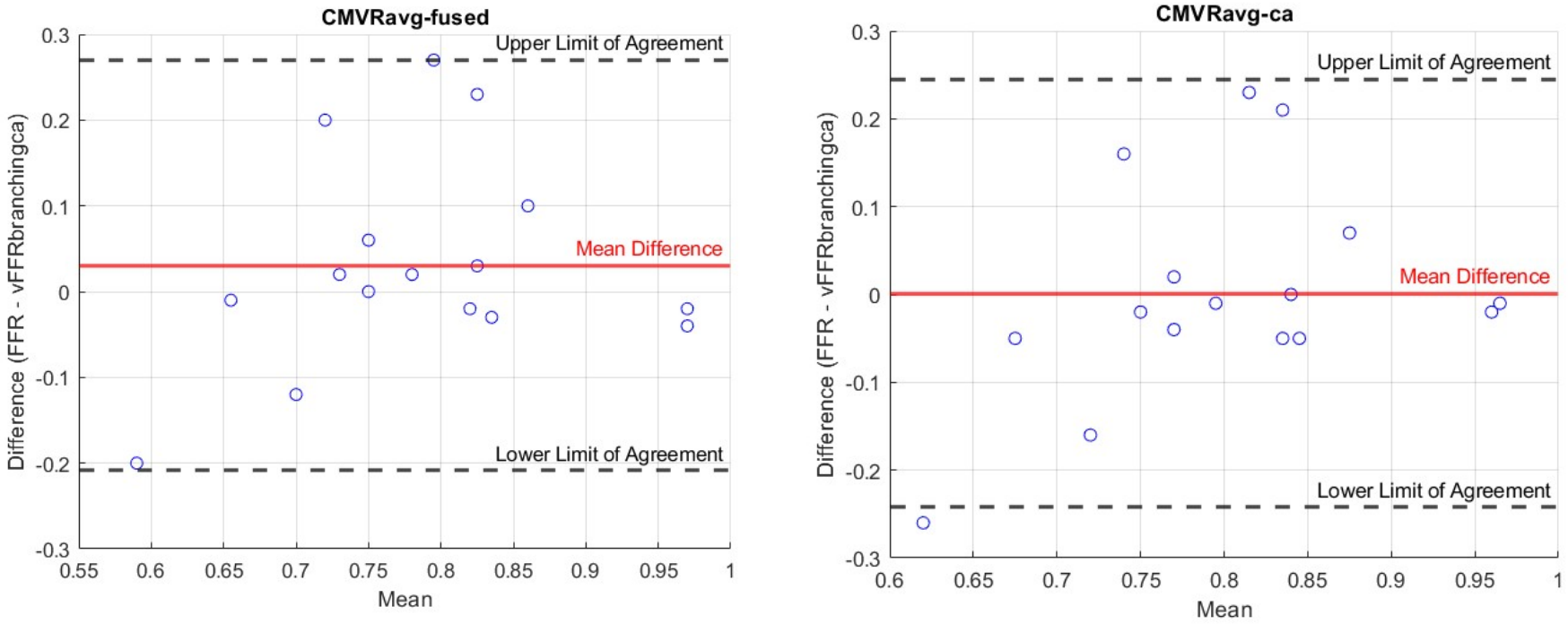

Figure 7.16. Bland Altmann plots of the FFR and $vFFR_{branching\text{-}CA}$ and the limits of agreement using both $CMVR_{avg\text{-}fused}$ and $CMVR_{avg\text{-}CA}$. Most points lie within the 95% limits of agreement.

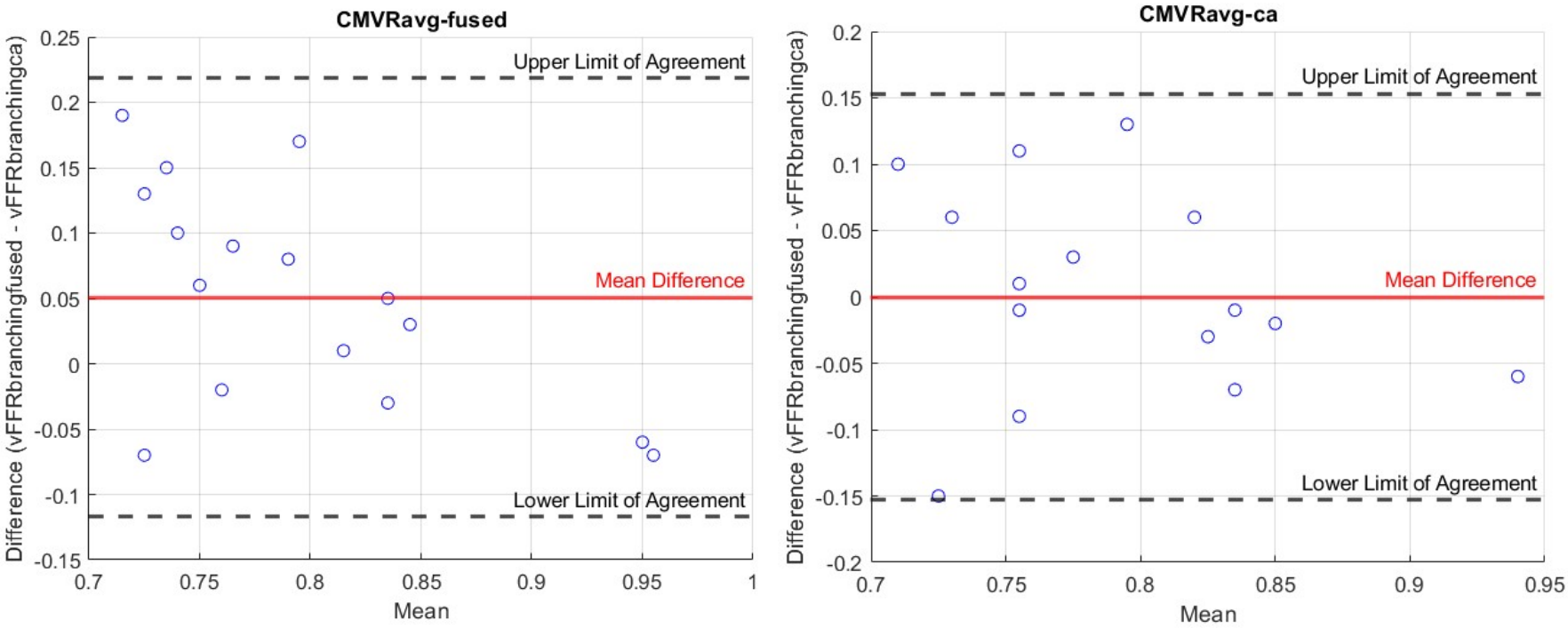

Figure 7.17. Bland Altmann plots of $vFFR_{branching\text{-}Fused}$ and $vFFR_{branching\text{-}CA}$ and the limits of agreement using both $CMVR_{avg\text{-}fused}$ and $CMVR_{avg\text{-}CA}$. All the points lie within the 95% limits of agreement.

7.5.3 Correlation Analysis

Although this analysis on just eight cases, the correlation coefficients between invasive FFR vFFR results were statistically significant for the $vFFR_{branching\text{-}fused}$ reconstructions ($P<0.05$), as is shown in Table 7.11. $vFFR_{branching\text{-}fused}$ (regardless of the distal boundary condition used) demonstrated the closest correlation with the clinical FFR, followed by $vFFR_{branching\text{-}CA}$ + $CMVR_{avg\text{-}CA}$ then $vFFR_{branching\text{-}CA}$ + $CMVR_{avg\text{-}fused}$. These results are similar to the previous results from the diagnostic and numerical accuracy measurements.

	r	**R^2**	**P**	**Clinically significant correlation?**
FFR vs $vFFR_{branching\text{-}fused}$ + $CMVR_{avg\text{-}CA}$	0.68	0.46	0.004	Yes
FFR vs $vFFR_{branching\text{-}fused}$ + $CMVR_{avg\text{-}fused}$	0.57	0.32	0.02	Yes
FFR vs $vFFR_{branching\text{-}CA}$ + $CMVR_{avg\text{-}CA}$	0.47	0.22	0.07	No
FFR vs $vFFR_{branching\text{-}CA}$ + $CMVR_{avg\text{-}fused}$	0.40	0.16	0.081	No

Table 7.11. The correlation analysis between clinically measured FFR and the branching vessel vFFR simulated using both the fused and CA-only reconstructions using $CMVR_{avg\text{-}fused}$ and $CMVR_{avg\text{-}CA}$. Two correlations are clinically significant and two are not.

7.6 Impact of pressure wire on vFFR

The invasively measured FFR for all twenty vessels was performed in the catheterization lab using a catheter and pressure wires. Yan et al. have studied whether the presence of the guide catheter and pressure wires impact the distal pressure measurement and have reported that since the presence of a catheter takes up from the internal volume of the vessel and increases resistance to flow, the pressure drop increases and the volume flow rate drops (Yan et al., 2023). They have reported up to 8 mmHg of distal pressure decrease with a catheter and up to 16.8% decrease in the FFR, which in the cases around the PCI threshold, can alter the treatment decision. If the average (5.8%) FFR decrease were applied to the best performing vFFR from this work, which is $vFFR_{branching\text{-}fused}$, the expected 'true' FFR according to Yan et al. is as shown in Table 7.12. The orange-highlighted cases are those that became discordant with the clinically

measured FFR, and those highlighted in green are those that become concordant. Two cases became concordant versus four which became discordant after applying such compensation. The BA bias and LOA of the FFR and the compensated vFFR are 0.029 [-0.17 0.22], which gives a width of 0.39 and score of 0.42. This shows that the compensated vFFR and the $vFFR_{branching\text{-}fused}$ have similar agreement with the FFR, however, the BA-LOA width are slightly narrower than those from the $vFFR_{branching\text{-}fused}$.

	FFR	**$vFFR_{branching\text{-}fused}$**	**$vFFR_{branching\text{-}fused}$ with 5.8% decrease**	**Difference**	**Change in concordance?**
1	0.64	0.69	0.65	0.04	Concordant
2	0.79	0.75	0.71	0.04	Concordant
3	0.74	0.78	0.73	0.05	Concordant
4	0.78	0.81	0.76	0.05	Became concordant
5	0.84	0.86	0.81	0.05	Concordant
6	0.91	0.82	0.77	0.05	Became discordant
7	0.82	0.81	0.76	0.05	Became discordant
8	0.93	0.81	0.76	0.05	Became discordant
9	0.65	0.79	0.74	0.05	Concordant
10	0.75	0.83	0.78	0.05	Became concordant
11	0.82	0.82	0.77	0.05	Became discordant
12	0.81	0.86	0.81	0.05	Concordant
13	0.49	0.79	0.74	0.05	Concordant
14	0.94	0.88	0.83	0.05	Concordant
15	0.95	0.92	0.87	0.05	Concordant
16	0.96	0.92	0.87	0.05	Concordant

Table 7.12. Clinically measured FFR increased using the percentages computed by Yan et al. which account for the impact of the catheter and pressure wires on the measurement of FFR. The orange-highlighted cases are those that become discordant, and those highlighted in green have become concordant.

7.7 Simulating volumetric flow rate for branching vessels

In this analysis, the volumetric flow rate computed using branching vessels for each branch was compared with its corresponding volumetric flow rate using single vessel models. The correlation between single vessel Q_{fused} and $Q_{branching\text{-}fused}$ was statistically non-significant when both boundary conditions were applied $CMVR_{avg\text{-}fused}$ and $CMVR_{avg\text{-}CA}$ (r 0.45, R^2 0.21, P 0.08 and r 0.48, R^2 0.23, P 0.06). However, for $Q_{CA\text{-}only}$ and $Q_{branching\text{-}CA}$, the results were statistically significant when the $CMVR_{avg\text{-}fused}$ was applied, and non-significant when the $CMVR_{avg\text{-}CA}$ boundary condition was applied (r 0.81, R^2 0.66, P 0.0001 and r 0.22, R^2 0.047, P 0.41). It is expected that the branching vessels will be drawing more flow, however, it is dependent on the assigned distal resistance (which is assumed to be the same for both vessels).

	Q_{fused}	$Q_{branching\text{-}fused}$		$Q_{CA\text{-}only}$	$Q_{branching\text{-}CA}$	
Case		**$CMVR_{avg\text{-}fused}$**	**$CMVR_{avg\text{-}CA}$**		**$CMVR_{avg\text{-}fused}$**	**$CMVR_{avg\text{-}CA}$**
1	4.13	1.85	1.70	5.53	2.69	2.44
	3.08	2.04	1.86	3.37	2.72	2.46
2	2.71	2.54	2.26	1.71	1.93	1.81
	3.42	2.66	2.35	3.21	2.35	2.13
3	2.86	2.38	2.12	2.19	2.23	2.00
	1.69	2.26	2.03	2.13	2.22	2.00
4	2.23	2.10	1.88	1.36	1.68	1.57
	2.11	2.07	1.86	1.92	1.78	1.64
5	5.43	3.43	3.03	6.91	2.78	2.57
	5.86	3.56	3.15	5.32	3.15	2.85
6	2.78	2.82	2.51	4.92	2.35	2.09
	3.03	2.96	2.63	3.48	2.30	2.06
7	3.82	2.00	1.79	3.67	1.90	1.74
	1.94	2.24	1.98	2.42	2.06	1.85
8	2.3	3.05	2.66	1.14	1.91	3.04
	1.96	3.04	2.66	1.00	1.82	2.96

Table 7.13. The $Q_{branching}$ computed using the distal resistance values, $CMVR_{avg\text{-}fused}$ and $CMVR_{avg\text{-}CA}$, for the fused OCT-CA and CA-only geometries. The single vessel Q values are also included for in the table for comparison.

7.8 Branching vessels summary

The case numbers in this proof-of-concept validation were slightly lower than for the single vessel cases. However, the $vFFR_{branching\text{-}fused}$ reconstructions with $CMVR_{avg\text{-}fused}$ provided the better accuracies, followed by $vFFR_{branching\text{-}fused}$ reconstructions with $CMVR_{avg\text{-}CA}$, followed by $vFFR_{branching\text{-}CA}$ reconstructions with $CMVR_{avg\text{-}CA}$.

7.9 Summary

In this chapter, the twenty single vessel models reconstructed using angiography only, and those using the novel fusion method were used to simulate blood flow parameters, such as flow, microvascular resistance and the vFFR. The flow was compared as derived from the CA-only and fused models and the R^2 value was 0.69 ($P<0.00001$), while for the microvascular resistance the R^2 value was 0.57 ($P<0.00001$). The average distal resistances from the CA-only versus the fused models were 3.58e09 versus 4.14e09 Pa/m^3s^{-1}, respectively.

Regarding vFFR, eight combinations of boundary conditions were explored, using the CA-only and fused models, single vessel and branching models and using different distal resistance conditions. All in all, by assessing the scoring for the eight combinations of single and branched lumen reconstructions with $CMVR_{avg\text{-}fused}$ and $CMVR_{avg\text{-}CA}$ boundary conditions, the combinations with the closest agreement with the FFR are ranked as follows:

1) Branching lumen vFFR from novel fusion method with $CMVR_{avg\text{-}fused}$,
2) Branching lumen vFFR from novel fusion method with $CMVR_{avg\text{-}CA}$,
3) Single lumen vFFR from novel fusion method with $CMVR_{avg\text{-}fused}$,
4) Single lumen vFFR from novel fusion method with $CMVR_{avg\text{-}CA}$,
5) Branching lumen vFFR from CA-only with $CMVR_{avg\text{-}CA}$,
6) Branching lumen vFFR from CA-only with $CMVR_{avg\text{-}fused}$,
7) Single lumen vFFR from CA-only with $CMVR_{avg\text{-}fused}$ and
8) Single lumen vFFR from CA-only with $CMVR_{avg\text{-}CA}$.

As can be seen from the rankings, the best agreement was produced using branching lumen reconstructions from fused CA and OCT. The worst agreement between the vFFR and FFR was produced with the single lumen models reconstructed using CA and modelled using the average CA microvascular resistance. This is the current 'gold standard' for vFFR computation. It is worth noting that many discordant cases lie inside the grey zone, which is the zone where it is recommended that an invasive FFR measurement is made. If these cases were considered concordant, then all cases would be concordant with the branching lumen reconstructions from fused CA and OCT. Although the number of cases is too small to tell, it seems that it is worth further exploration of the combinations listed above, since adding OCT data and including branches is suggesting promising improvements to FFR prediction.

Table 7.14 is a summary table, focusing on the sixteen vessels, composing eight bifurcation cases and how the vFFR varied when computed using the different combination of methods. All in all, the differences between the FFR and vFFR for all combinations were not significant ($p>0.05$).

		$vFFR_{Fused}$				$vFFR_{CA\text{-}only}$			
		$CMVR_{avg\text{-}fused}$		$CMVR_{avg\text{-}CA}$		$CMVR_{avg\text{-}fused}$		$CMVR_{avg\text{-}CA}$	
Case	**FFR**	**Single**	**3-vessel**	**Single**	**3-vessel**	**Single**	**3-vessel**	**Single**	**3-vessel**
1	0.64	0.77	0.69	0.81	0.65	0.85	0.85	0.88	0.87
	0.79	0.85	0.75	0.86	0.71	0.86	0.83	0.89	0.86
2	0.74	0.76	0.78	0.79	0.75	0.63	0.72	0.67	0.76
	0.78	0.84	0.81	0.87	0.79	0.83	0.72	0.85	0.76
3	0.84	0.89	0.86	0.91	0.83	0.82	0.81	0.85	0.82
	0.91	0.84	0.82	0.87	0.81	0.87	0.81	0.90	0.82
4	0.82	0.85	0.81	0.87	0.76	0.69	0.62	0.73	0.66
	0.93	0.81	0.81	0.84	0.76	0.78	0.66	0.82	0.70
5	0.65	0.81	0.84	0.85	0.82	0.89	0.66	0.91	0.70
	0.75	0.85	0.87	0.91	0.85	0.89	0.75	0.91	0.79
6	0.82	0.87	0.82	0.89	0.80	0.89	0.76	0.91	0.80
	0.81	0.89	0.86	0.91	0.84	0.88	0.77	0.9	0.80
7	0.49	0.83	0.79	0.86	0.76	0.79	0.69	0.82	0.75
	0.94	0.92	0.88	0.93	0.86	0.92	0.71	0.94	0.73
8	0.95	0.91	0.92	0.93	0.91	0.95	0.99	0.95	0.97
	0.96	0.91	0.92	0.93	0.91	0.77	0.98	0.81	0.97
		2/7	4/7	1/7	5/7	2/7	5/7	1/8	5/7
		9/9	9/9	9/9	6/9	6/9	4/9	8/9	4/9
		5/7	3/7	6/7	2/7	5/7	2/7	6/7	2/7
		0/9	0/9	0/9	2/9	3/9	5/9	1/9	3/9

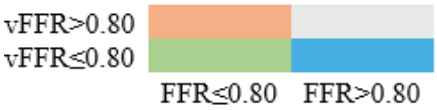

Table 7.14. Compilation of the FFR, single vessel vFFR and branching vFFR for all the cases that were modelled as single and as branching vessels (sixteen cases, constituting eight branching cases). Dark green cells indicate FFR ≤ 0.80 and a vFFR ≤ 0.80. Light green cells indicate FFR > 0.80 and vFFR > 0.80. These make up the concordant scenarios. Blue indicates an FFR > 0.80 and a vFFR ≤ 0.80. Orange indicates an FFR ≤ 0.80 and a vFFR > 0.80. These are the discordant cases.

Table 7.15 includes general comments regarding the eight branching cases, regarding the interpretation of the angiograms, and whether the data from the angiograms and the OCT runs do correspond and are reflected in their corresponding reconstructions. The FFR and vFFR values are also commented on, with regards to whether they reflect the imaging data and how the results have changed using different models with different boundary conditions. This is a 'sanity check' step to further validate the results.

In Chapter eight, the results will be further analysed in the context of the relevant literature, with a delve into future opportunities for development and further refinement of the methods.

	Comments on Branching Cases
1	• Angiogram perhaps indicates a proximal lesion and a distal lesion in the first vessel. This seems to be confirmed by the OCT. • Positive FFR (0.64/0.79) in both vessels, but only marginally so in the second. Negative vFFR (0.77/0.85) for both vessels. 3-vessel vFFRs are positive (0.69/0.75). • The pressure drop across the proximal part of the vessel and the distal part of the first vessel are similar in magnitude. Little pressure drop across the second distal vessel.
2	• Clear stenosis in the OCT reconstruction of the first vessel, just after the bifurcation. Less pronounced narrowing in the proximal vessel. • Positive FFR (0.74/0.78) in both vessels. Positive vFFR (0.76/0.84) in the first vessel but negative in the second. • The 3-vessel result for the first vessel shows a relatively small increase (0.02) in vFFR, but a decrease in the vFFR (0.03) for the second vessel. • The stenosis is difficult to see in the 3D bifurcation. Pressure drops before and after the bifurcation are of similar magnitude.
3	• Angiogram shows a stenosis distal to bifurcation in the first vessel. • Negative FFR (0.89/0.84) and vFFR (0.89/0.84) for both vessels but becomes positive (0.74/0.71) in the 3-vessel analysis. • The changes from the single vessel analyses (0.15/0.13) are large. • The 3D bifurcation exhibits, consistently, a primary lesion distal to the bifurcation in one vessel. Little pressure drop before the bifurcation.
4	• Angiogram appears to show a relatively healthy proximal vessel but possibly diffuse disease in both distal branches, especially so in the first vessel. This appears to be confirmed by the OCT, for which the first vessel is very irregular. • Negative FFR (0.82/0.93) and vFFR (0.85/0.81) in both branches but becomes positive (0.72/0.72) for the 3-vessel analysis. • Both single vessel and 3D bifurcation analyses show that there is little pressure drop before the bifurcation.
5	• Angiogram more difficult to interpret. Perhaps indicates some relatively mild narrowing in the proximal vessel and in the first distal vessel.

	• Positive FFR (0.65/0.75). Negative vFFR (0.82/0.89). Positive 3-vessel vFFR (0.74/0.76) with decrease (0.08/0.10) from the single vessel analysis. • 3D bifurcation confirms mild stenosis just distal to bifurcation in first vessel. Most of the pressure drop occurs before the bifurcation.
6	• Angiogram appears to show significant stenosis immediately proximal to bifurcation, possibly extending into bifurcation. • Negative FFR (0.82/0.81) and vFFR (0.87/0.89) for the single vessel analysis but becomes positive (0.76/0.78) for 3-vessel analysis. • Reduction of ~0.11 might be consistent for proximal stenosis.
7	• Angiogram shows a strong narrowing just distal to the bifurcation in the first vessel. FFR (0.49/0.94) supports this. • It is surprising that this appears not be picked up by vFFR (0.83/0.92). The positive vFFR is picked up (but only just) by the CA segmentation. This is a confounding case. Is the severity of the stenosis being smoothed out because it is close to the bifurcation. • The 3-vessel analysis shows that the vFFRs (0.79/0.88) move towards the threshold for both vessels.
8	• Angiogram perhaps indicates a stenosis just distal to the bifurcation in the second vessel, but this is not confirmed by the OCT. The centreline reconstruction is quite tortuous in this area. • Negative FFR (0.95/0.96) and fusion-based vFFR (0.91/0.91). Positive CA-based vFFR (0.95/0.77) for the second vessel. • The 3D bifurcation based on the OCT cross-sections does not exhibit any strong stenosis.

Table 7.15. General comments regarding the eight branching cases, regarding the interpretation of the angiograms, and whether the data from the angiograms and the OCT runs correspond and are reflected in their corresponding reconstructions. The FFR and vFFR values are also commented on, with regards to whether they reflect the imaging data and how the results have changed using different models with different boundary conditions.

Chapter Eight:

Discussion, Future Work and Conclusions

In this thesis, I have developed a mathematical protocol, that uses angiography and OCT data to model the coronaries, both as single vessels and as branches. Up to my knowledge, no reconstruction protocols of this sort, have produced models that entered clinical practice. The protocols that were successful in entering clinical practice are predominantly simple, single lumen models, from a single imaging modality. I have described the process of vessel segmentation from CA, from image acquisition and choice to the 3D modelling of single branches. I have introduced an additional feature to the existing segmentation tool which is torsion compensation in the context of Frenet frame representation of the 3D CA-derived vessel centrelines, which is essential when it comes to OCT lumen orientation and positioning onto CA centrelines. I have also discussed the process of 2D OCT lumen segmentation and developed an OCT-based optimisation protocol for lumen orientation on a straight vessel centreline. This methodology robustly fuses OCT and CA information longitudinally and finds the correspondence between the anatomical information from OCT and CA. I have analysed, in detail, the nature of the data extracted using OCT and compared it with its corresponding CA data and presented a novel methodology that uses lumen ellipticity to identify stenosed regions of vessels. I have also examined the differences between the arterial luminal diameters as extracted from CA and OCT and reported larger discrepancies in larger diameter lumens. I have developed the methodology that robustly joins the centrelines of a main vessel and one or more of its side branches whilst maintaining the integrity of the bifurcation, to produce a branched, 3D, arterial centreline model. This was accompanied by a method to fuse the luminal (vessel surface) edges of a main branch and side to produce a branched, 3D, arterial surface mesh.

The novel methods mentioned above were demonstrated and validated in Chapter seven, by performing CFD simulations using the developed single and branching tree coronary models to predict the vFFR. The vFFR values from the single and branching models were compared with the clinically measured FFR and the vFFR from the ‘gold standard’ CA-only technique to compare agreement and accuracy. Although the results were statistically non-significant, they do demonstrate a trend towards superiority for the fused modelling over CA-only modelling when compared with the invasive FFR results. Additionally, branched modelling was shown to decrease the number of cases whereby the FFR and vFFR measurements provide contradicting measurements regarding whether to stent or not. Most importantly, it has decreased the number of cases with an FFR that indicated a need for stenting and a vFFR that did not, which are the most clinically critical cases. Sometimes, this was at the expense of stenting cases with an FFR

that did not indicate a need for it. However, for most of such cases, the FFR was in the 'grey zone' (0.78≤ FFR≤0.83), which, anyway, would benefit from clinical measurements in addition to the vFFR measurement.

This chapter will further discuss the results of this work with respect to the literature, areas of potential improvement and clinical application. It also includes the challenges and a list of suggestions for future work if this project is continued.

8.1 Assessing the quality of the clinical data and the CA segmentations

The work in this thesis has produced results that, although non-significant, suggest a trend towards superiority for the combination of CA and OCT data for coronary modelling, to simulate vFFR results that are in better agreement with the clinical FFR. The work has also shown that including branches in the reconstruction and simulation identified all stenosed vessels, that needed stenting (vFFR ≤0.80), which is an important clinical consideration. Both the quality of the clinical data and the underlying mathematical processes and assumptions impact the modelled reconstructions and the resulting CFD.

In this work, clinical data was of three types: angiograms, OCT runs, and physiological (wire-based) measurements of the proximal and distal pressures of the vessels being imaged. In Chapter three, the segmentation protocol from CA was presented and developed. This involved an initial set of requirements for the CA-runs, which included ensuring that they are of appropriate resolution for segmentation of vessel edges and choosing two projections, greater than 30 degrees apart, from which the vessels of interest are optimally imaged. This is a time-consuming step, requiring users with both clinical (anatomical) and technical (segmentation and reconstruction) knowledge, experience and skills to decide on the inclusion/exclusion of specific CA images, in the end-diastolic phase. Studies have introduced deep learning techniques that are able to identify, from a CA run, in the end-diastolic phase, which CA images are the most suitable for segmentation (Liu et al., 2023). This being an automated step has the potential to reduce pre-reconstruction time and effort significantly. Other studies have looked into using AI to analyse angiograms and estimate stenoses (Avram et al., 2023). In the future, a CA-only combined software can benefit from the work by Liu et al., to identify optimal CA images, the work by Avram et al., to identify the patient-specific region of interest, and the

work in this thesis to reconstruct the region of interest, whether it is a single or a branching vessel. This is all regarding the pre-segmentation phase.

During segmentation from CA, the protocol presented in this thesis builds on the VIRTUheart segmentation tool, by additionally compensating for torsion by describing the CA-derived centreline using the Frenet frame. Although this might seem like an unnecessary step for the CA-reconstruction protocol, it is an essential step for OCT data inclusion, due to the irregularity of the contours. The two main limitations regarding segmentation occur proximally, distally and at the bifurcation. Proximally, there is the issue with the epipolar lines of the coronary vessels being parallel thus producing segmentation errors. This usually occurs in the LMS due to the angle it comes off the aorta at. In this thesis, this issue was avoided by segmenting the coronaries just before the LMS bifurcation, which was sufficient since the regions of interest for all twenty cases were more distally in the vessels, and there should be no significant pressure drop across healthy segments of coronary artery. It is important to note that this problem is common to all CA-derived reconstructions. However, if the LMS bifurcation is to be reconstructed using the protocol presented in this thesis, it is expected that this issue will occur more frequently, since the segmentation will start closer to where the LMS branches out of the aorta, preventing accurate segmentation of the LM common stem section. This may involve modifying the segmentation procedure to take in more than two angiographic projections, one of which ensures non-parallel epipolar lines. Distally, there is the issue with insufficient contrast for vessel edge detection, which can benefit from several enhancements techniques presented in the literature, such as the use of morphological operators (Cervantes-Sanchez et al., 2019), vesselness filters (Frangi et al., 1998) etc. At the bifurcation, however, the issue is discerning which parts of the bifurcation region should be included in the single vessel model. The segmentation tool, which operates depending on the greyscale contrast of the images can fail to find the vessel edge as it goes proximally to distally over a bifrucation. The larger the diameters of the vessels at the bifurcation, the larger the bifurcation and the less accurate the greyscale edge detection is. This issue was addressed in this thesis, by assuming a vessel consists of a proximal section, pre-bifurcation, and a distal section, post-bifurcation, and the bifurcation section is a linearly interpolated centreline with interpolated contours between the last proximal contour and the first distal contour. This allows a smooth transition from common stem to daughter branch, avoiding any abnormal sharp angles that can be produced from inaccurate segmentation, and preserves the ‘trouser’ shape of the bifurcation.

The segmentation of the vessels from the same two angiogram images using the Virtu segmentation tool is dependent on the co-registration point chosen by the user at the start of the segmentation process. The segmentation is not as dependent on the choice of start and endpoint since only the sections of the vessel that have corresponding CA and OCT data is used, and the rest is discarded. Therefore, even if the choice of start and endpoints are different between attempts of segmenting the same vessel, the result would be the same. For the work described in this thesis, the co-registration point, for all cases, was chosen to be the point on the centreline, that is equivalent to the carina point on the surface of the vessel. Prior to the segmentation of the twenty cases of this thesis, the segmentation process, with the criterion of the choice of the co-registration point, was performed for practice on additional cases, with the presence of several users. The produced geometries were similar at the bifurcation region, and even with slight changes in where the co-registration point is chosen to be, the interpolation protocol for the bifurcation region neutralises the differences by interpolating pre- and post-bifurcation as described in chapter six. Figure 8.1 illustrates a case that was segmented twice by the same user, resulting in the start, end and co-registration points being slightly different in both attempts. The slight differences in the segmentation are diluted in the geometry, as discussed. However, in the future, it would be interesting to quantify the effect of these differences in segmentation by having multiple users segment the same cases (inter-user variability) and the same user segment the same cases multiple times (intra-user variability), to understand whether this can impact the concordance/discordance especially for cases with the FFR in the critical range.

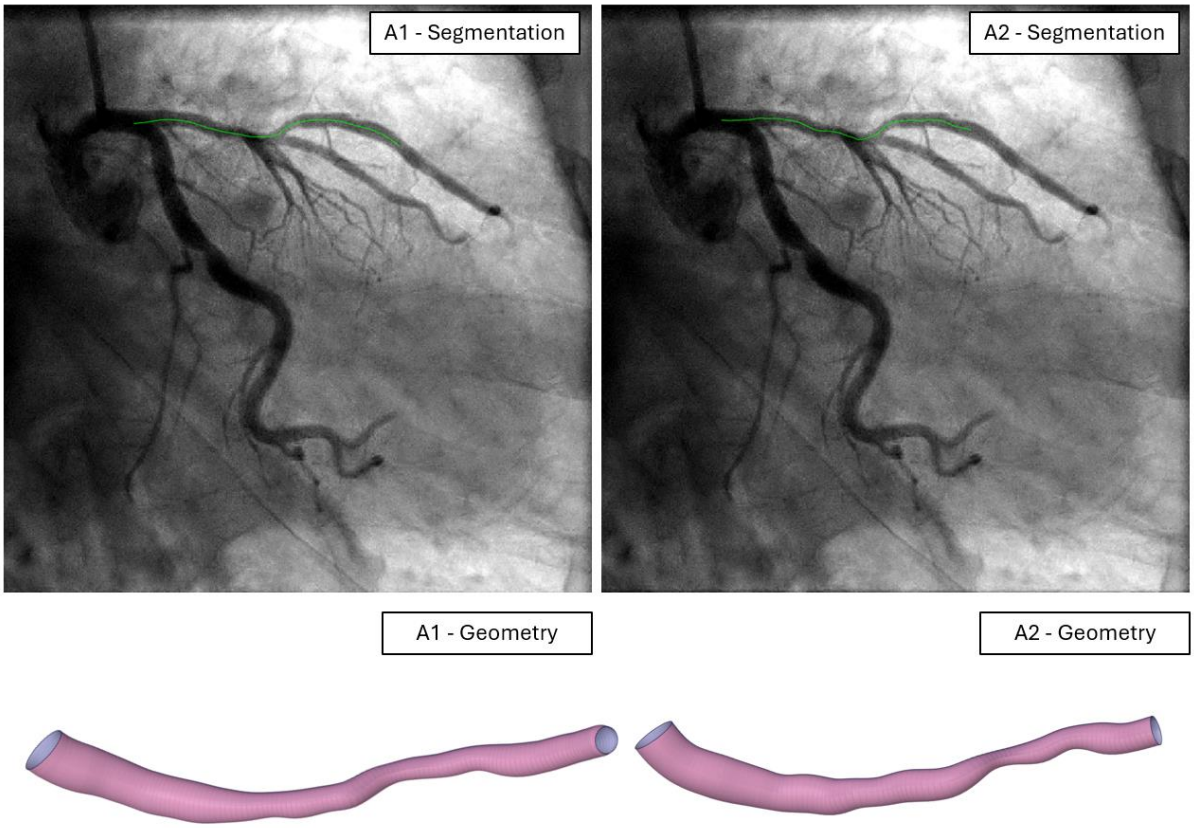

Figure 8.1. LAD vessel segmented twice by the same user. The top images show the segmented centrelines from the two attempts, which were reconstructed using different sets of start, end and co-registration points. The bottom images show the resulting geometries from both attempts.

Additionally, in this work, it was found that the larger the diameter of a vessel is, the greater the discrepancy between the CA and OCT diameter measurements. Although this work has attempted to quantify the systemic differences between measurements from both imaging modalities, this phenomenon calls for larger scale systemic error quantification, using a larger number of cases.

8.2 OCT segmentation

The novel fusion method presented in this thesis combines the CA and OCT data in a way that builds on their respective strengths and produces more realistic the reconstructions than those produces using CA images only. CA, given that it provides a more global view of the coronaries in the context of the heart, is the stronger candidate to be the source where the centreline is

extracted from. OCT is not capable of providing this information since it views the vessel as a single straight-line structure that changes shape as the camera is retracted distally to proximally. However, what it does provide is the shape of the vessel from the inside, which CA does not. This combination of intra and extra vascular images provides information of the coronary vessel with respect to itself and to the rest of the heart. This is what the combination of IVUS and CA also provide, however, OCT has a higher resolution. Both techniques enable different types of plaque to be identified and both are now recommended for use in complex and bifurcation PCI by the European Society of Cardiology (Neumann et al., 2018). In the future, there is no reason why the novel method could be extended to IVUS also, because IVUS provides almost identical imaging information in a very similar fashion to OCT.

The two main aspects of the novel fusion method are: the location of the OCT contours on the CA-derived centreline and their orientation. Regarding the location, it is a challenge to discern, by eye, where a specific contour belongs on the CA-centreline by comparing the longitudinal OCT straight vessel image and the angiogram. This is due to the angiograms being a projection that is (1) subject to foreshortening and (2) a 2D projection of a 3D vessel that, naturally, cannot inform on the anatomical data the chosen projections do not show, thus lacking completeness. The same can be said regarding completeness of the longitudinal OCT image: it does not point out areas of vessel curvature, neither does it show the full 3D shape of the contours. Therefore, in this work, the bifurcation point, which was defined as the carina, on the CA-centreline, and the 'trouser' frame on the OCT run were assumed to be the same and were used as the landmark points. With the OCT frame-to-frame distance and the CA pixel size known, the CA-centreline length was determined and decimated using the frame-to-frame distance for the OCT contours to be placed appropriately. It is also valid to question (1) the carina point on the angiogram, because again, it is chosen visually on the 2D angiogram and can be inaccurate by a few millimetres and (2) the 'trouser' frame, which is usually a set of frames which all indicate the presence of the bifurcation – so which one should be chosen? One other study has used two bifurcations as landmarks and stacked the relevant OCT frames between them (Li et al., 2015). This could have been adopted in this work, however, all twenty vessels were LAD-Diagonal or LCX-OM bifurcations, which means that the other major bifurcation was the LMS bifurcation, which, as mentioned earlier, was more difficult to segment. Other minor bifurcations could have been identified, however, the current VIRTUheart segmentation tool can only accept a single anatomical landmark (a single bifurcation), and so the approach mentioned in Chapter four was used.

Regarding the orientation of the OCT frames, an optimisation cost function was developed, that adopted from Li et al. the idea of maximising the overlapping area between any two consecutive contours (Li et al., 2015), develops an angio-optimisation strategy that ties the shape of the vessel back to the shape on the grey-scale angiogram, and smooths the resulting rotations. A composite cost function includes a term for each method with a weighting factor, that minimises:

4) The total non-overlapping area between consecutive cross-sections,
5) The error between the projected OCT radius and the CA-radius
6) The rotational change between consecutive cross-sections

For the developed area-overlap optimisation method, since it is highly dependent on the consecutive cross-sections having a single distinct orientation that maximises area overlap, it might struggle, for example, away from bifurcations when the vessel is more circular to find the rotation angle, although, arguably, it is considerably less important in these regions, particularly for the CFD simulation. Accordingly, for this work, the area-overlap method was based on non-circular contours where a clear rotation angle was identified that minimised non-overlapping area. Choosing the contours on which the area-overlap optimisation procedure is based is fully manual, thus opening opportunities to automate and cut reconstruction time.

Another way to further optimise the orientation of the OCT contours and can be implemented in the future by using the common stem for branching models. If the vessel being modelled is part of a pair, meaning that it belongs to a branch, and both branches were imaged using CA and OCT, then the shared common stem between the two runs can be used to further rotate the frames for proper orientation, as follows:

1) For both vessels, perform orientation optimisation as described in Chapter four, section three. Since the common stem on both vessels A and B are the same, the common stem from vessel A can be used as reference for further OCT orientation for vessel B.
2) Vessel A is fixed in place and vessel B can be rotated such that its common stem maximally fits the orientation of vessel A's common stem (Equation 8):
3) Once this is done and the frames of the common stem are rotated, the rotation angle of the last frame is then used to rotate the distal section of the vessel starting after the common stem until the last distal frame.

Regarding the angio-optimisation method, as developed in this work, it ties the data from both modalities together and ensures the data appropriately aligns. However, it is highly dependent

on the OCT and CA radii being comparable, which might not always be the case, in all sections of the vessel, especially in the more proximal ends. In Chapter five, the differences between the OCT and CA diameters were explored and the data showed that for larger sections of the vessel, the differences between OCT and CA increase. Accordingly, for this work, although the infrastructure for the angio-optimisation element was created, the optimisation was performed using a weighting factor of zero for this method, due to the differences in diameter. In the future, and since the difference has been quantified for this relatively small cohort of cases, it might be helpful to explore this in many more cases, to re-quantify the differences on a more representative case population and re-compute the scaling factor and use it to implement the angio-optimisation element and explore whether the additional rotations produce a significantly different reconstruction or not.

8.3 The CFD

The main goal of the work in this thesis was to create a full protocol that transforms coronary imaging data into 3D reconstructions that reconstruct the real patient anatomy as accurately as possible. Although the novel fusion method builds on the published angio-derived VIRTUheart process, its underlying mathematical processes required validation. In Chapter seven, the twenty single coronary vessels, each reconstructed twice, once using CA-only and once using the novel fusion method, were used to simulate blood flow using CFD. The CFD simulations were performed for the following reasons:

1. To compare simulated blood flow parameters that cannot be routinely measured in the catheterisation lab and compare with known values (volumetric blood flow and CMVR),
2. To compare simulated blood flow parameters against their clinically measured counterparts (vFFR versus FFR),
3. To determine the combination (reconstruction methodology and boundary conditions) that produces greater agreement with clinically measured (or known) values.

The reconstructions and simulations performed as part of this thesis included:

1. Single vessel from CA only,
2. Single vessel from CA and OCT,
3. Branching models from CA only
4. Branching models from CA and OCT.

This was done to isolate the impact of each addition on its own, for example:

1. 1 versus 2 = Does the addition of OCT anatomical data impact haemodynamic parameters, including the vFFR?
2. 1 versus 3 = Does modelling branches, compared to modelling single vessels, using CA only impact haemodynamic parameters, including the vFFR?
3. 1 versus 4 = Does the combination of OCT and branches with CA improve the computation of vFFR, or does the combination include layers of assumptions that impair the computation?

These were all assessments versus the current gold standard, which is single vessels from CA only.

4. 2 versus 4 = Do the mathematical assumptions associated with using OCT data to model bifurcations impact the computation of the vFFR?

For all CFD simulations, blood was modelled as an incompressible, Newtonian fluid, which was also found to be suitable when simulating flow through the coronaries (Razavi et al., 2011, Chaichana et al., 2012, Carvalho et al., 2020). For the most part, studies have reported that WSS is the main haemodynamic parameter that is not modelled well using Newtonian blood models, which is important especially in stented vessels and those with extreme stenoses (Gaudio et al., 2018, Johnston et al., 2006, Ahadi et al., 2024). In the work in this thesis, all the images used for reconstruction were pre-PCI images (no stents) and WSS was not modelled, which is why a Newtonian blood model was adopted. In the future, and since modelling WSS, especially in the context of bifurcations is important in understanding disease progression etc., it would be interesting to explore how differently Newtonian and non-Newtonian blood models model WSS, and whether there is a more suited non-Newtonian blood model for coronary applications.

With regards to the agreement between vFFR and clinically measured FFR, studies have reported less differences between their simulated and measured values than those reported in this study (Morris et al., 2013, DeVos et al., 2024, Masdjedi et al., 2022). For example, Morris et al and the VIRTU-1 trial reported excellent correlation ($r = 0.84$) (Morris et al., 2013). This is important to note since one of the main comparisons in this thesis is between the CA-derived vFFR and the fusion-derived vFFR and how they compare to the measured FFR. The CA-derived vFFR results presented in this study were produced using the published and validated VIRTUheart protocol used by Morris et al., Pederzani et al. and many others for vFFR

computation (Pederzani et al., 2022). A possible factor that could have caused this is inappropriate CMVR value used for the vessels, due to the location of the stenosed region, with respect to the vessel and to the bifurcation. Again, the CA-derived CMVR value used (4.14 e09 Pa/m^3s^{-1}) has been previously used in all the published VIRTUheart analyses and they have reported better correlation between vFFR and FFR(Morris et al., 2020b, Morris et al., 2016, Morris et al., 2013, Morris et al., 2017, Taylor et al., 2023). Everaars et al. have measured the CMVR in stenosed vessels and reported values that are lower than those computed for this cohort of cases (Everaars et al., 2019). It is a possibility that this rather small cohort of cases exhibit lower/higher CMVR that the usual average, which has impacted the vFFR values. This is another point that that is in favour of continuing this work further to include a larger cohort of patients.

8.4 Clinical Implications

The findings of this work support the use of the three assessments CA, OCT and physiology to diagnose IHD, assess its severity and guide treatment. Although OCT is known to slightly overestimate diameter relative to CA, this work has found that this difference is much more pronounced in the larger diameter vessels than the smaller distal vessels. This is a prototype model that was able to successfully process a single case in less than four hours. With software development and automation, this could be reduced to the order of only a few seconds. With validation on a larger cohort and automation of more steps in this protocol, the processing time is expected to be reduced to clinically tractable timescales, whereby patients are imaged, and the results are presented all in one sitting, avoiding multiple visits to the hospital. Even without CFD (physiological) simulation, the 3D branching modelling may be useful for PCI planning. Another clinical research application will be the ability to perform WSS simulations in greater detail than before and this may have implications for making predictions about atherosclerosis development, response to PCI and even progression from CCS to ACS.

Improvements in the graphical user interface that make it easier for clinicians to access the results of the processing and examine the original images would make clinical translation much smoother and the information clearer and more transparent.

8.5 Conclusions

The work in this thesis contributes novel methodology to the field of coronary modelling and simulations. It builds on the existing angiography-based modelling methods for single branches, by adding OCT anatomical data and branched coronary anatomy to the final reconstructions. This was done by segmenting the angiography and OCT data, combining them by fusing the angiography-derived centreline with the OCT vessel contours, optimising the reconstructions using a composite cost function that obtains appropriate rotation angles that minimise certain non-alignment factors, meshing the resulting surface and simulating haemodynamic parameters. This marks a full protocol from clinical data to blood flow parameters, that can process a single case in less than four hours. Due to the protocol's novelty and patient-to-patient anatomical differences, certain aspects of this protocol are done manually. Automation of such aspects is expected to significantly improve the processing time, and feed back into the clinical setting for further regulation of data acquisition, which can save the time per patient, and clinician subjectivity. The modelling methods presented were validated on twenty patient coronary vessels by simulating vFFR, volumetric flow rate and CMVR and comparing with clinical measurements, where available, and with current gold standard techniques. These comparisons are between this novel, prototype model against a third generation (after numerous improvements) angio-derived method, which is the current gold-standard.

Although this is a relatively small cohort to the usual, the goal of this work was to develop and demonstrate the novel modelling and fusion protocol on several real cases. Nonetheless, it is recommended that the validation of these methods is continued to include a larger cohort, for exposure to more patient differences, more vessel types, more variations of disease, and more data acquisition challenges. This "Version 1.0" prototype may also benefit from optimisation of specific components before full clinical validation in a large cohort. This study also included a single female case, a limitation that can be addressed in future larger cohorts. Although the modelling was targeting coronary arteries, the methods described in this thesis can be applied to other vessels, whether imaged using a single/combination of intra and extra vascular imaging modalities including single/branches, such as the pulmonary, femoral, renal etc. vessels.

Appendix 1: Angiograms, Angio-Reconstructions and Fused Angio-OCT Reconstructions

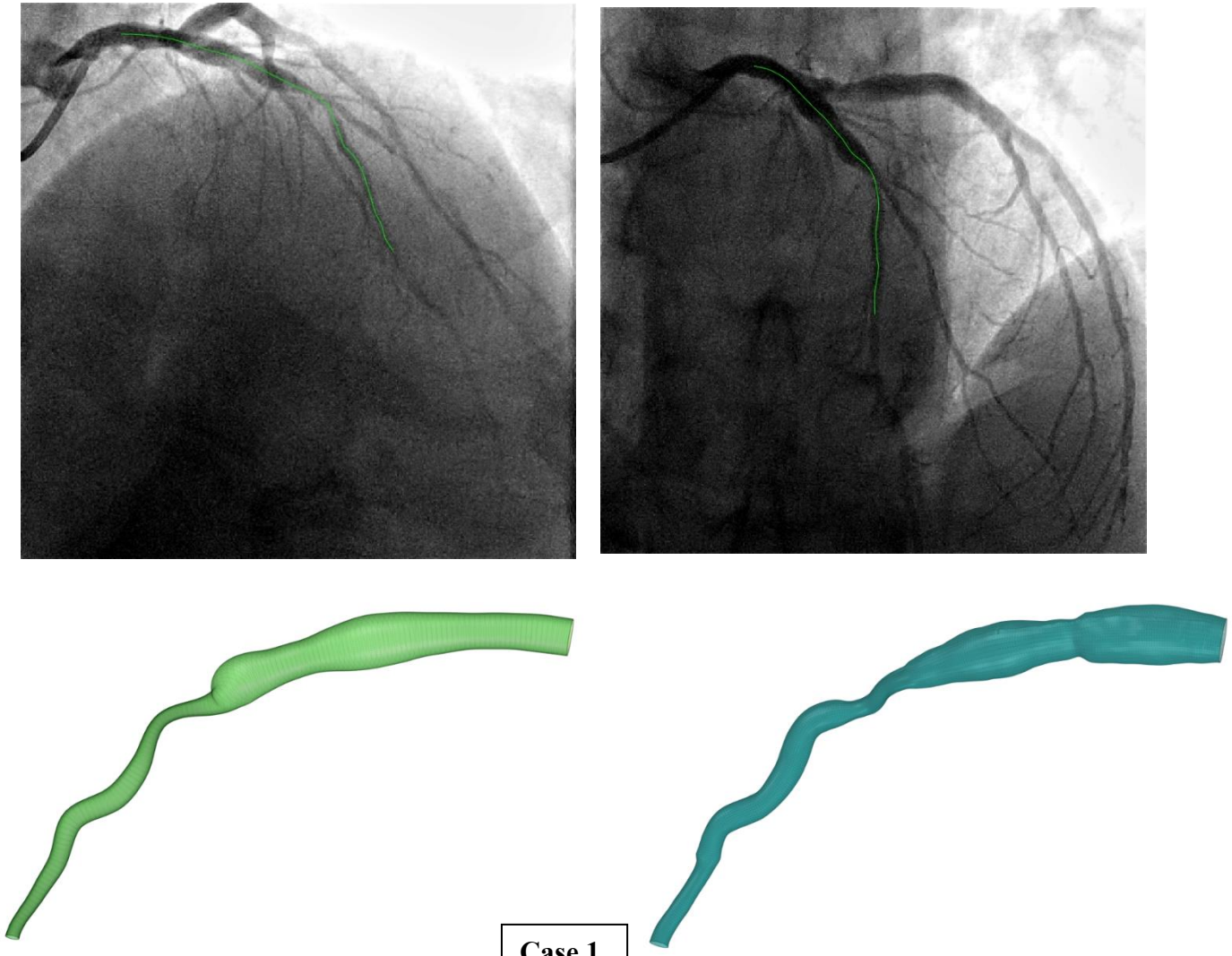

Case 1

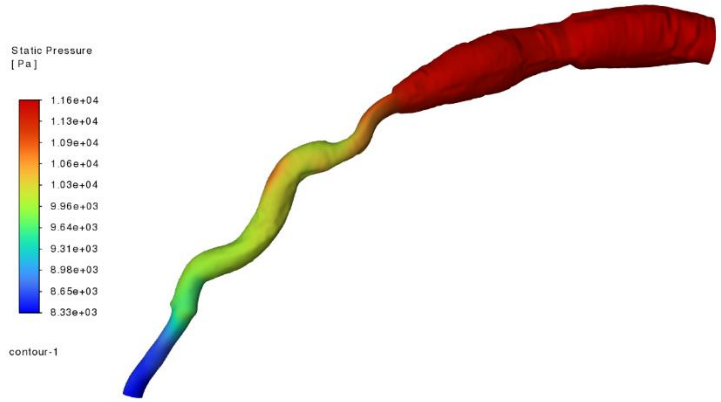

Case 1

Proximal Pressure : 87 mm Hg

Distal Pressure : 63 mm Hg

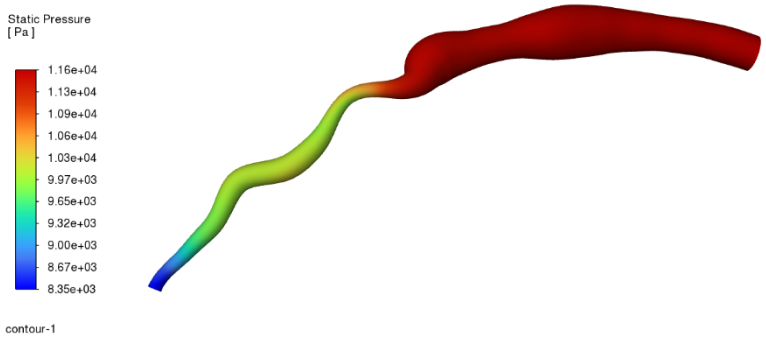

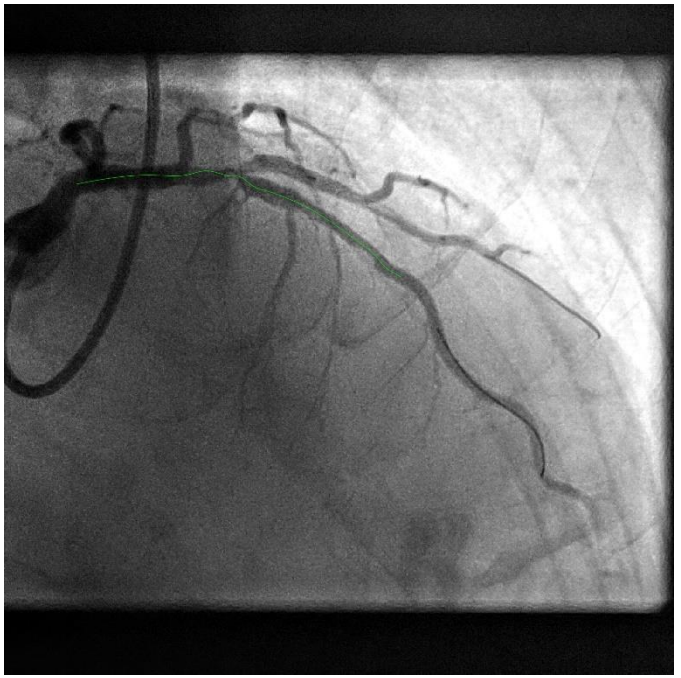

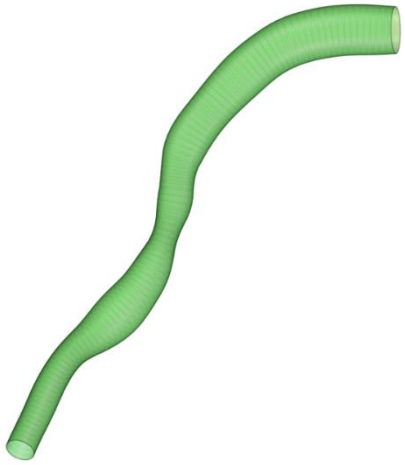

Case 2

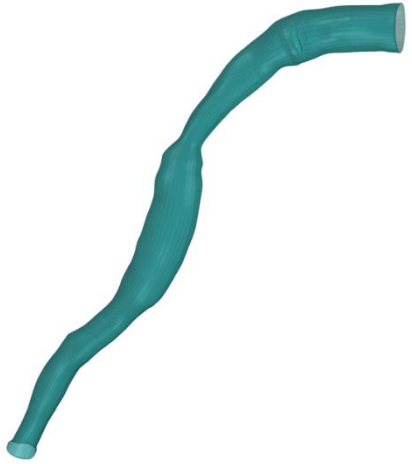

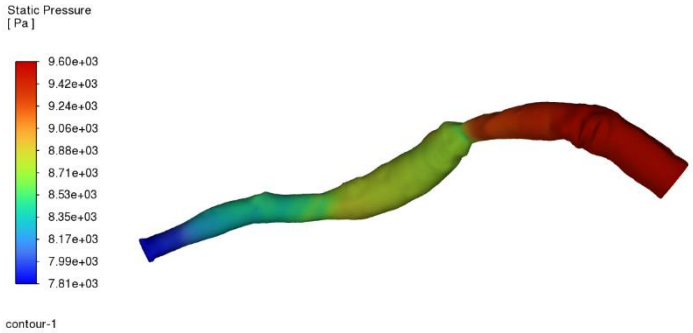

Case 2

Proximal Pressure : 72 mm Hg

Distal Pressure : 59 mm Hg

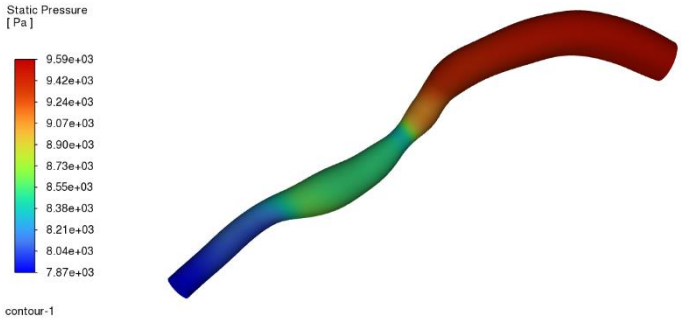

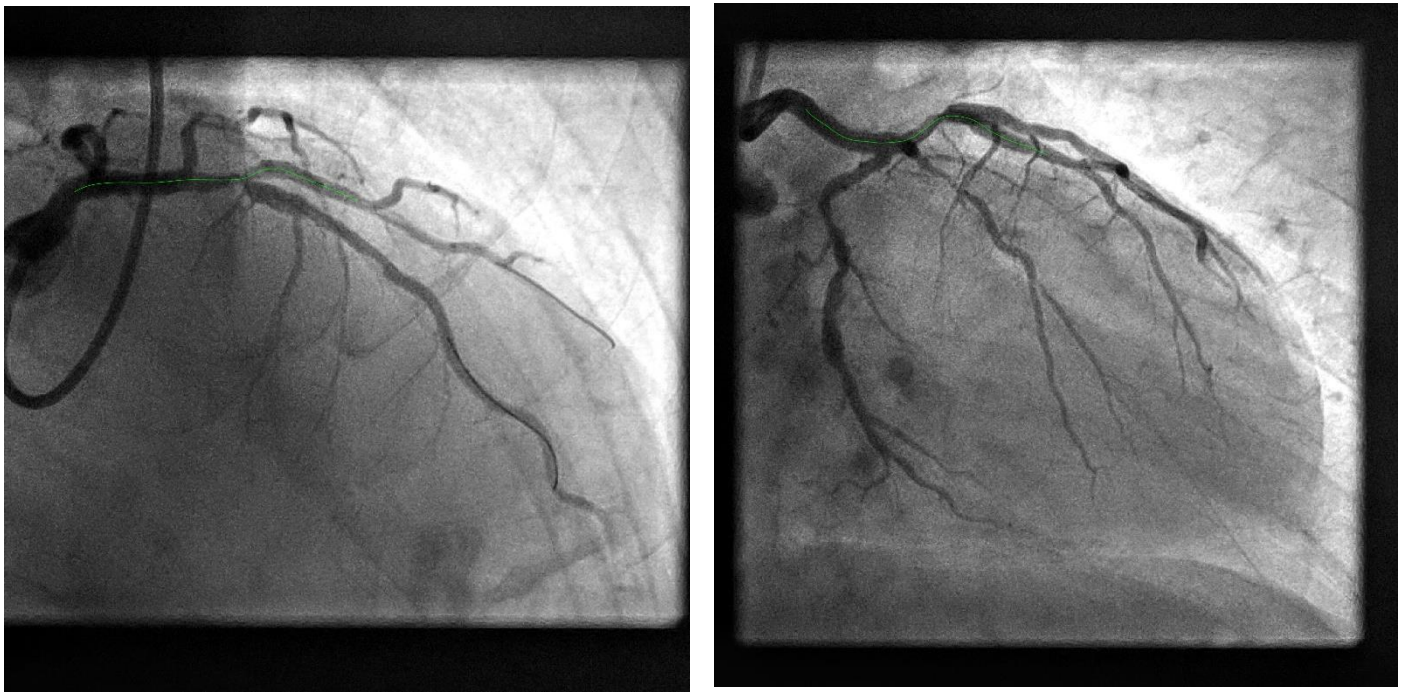

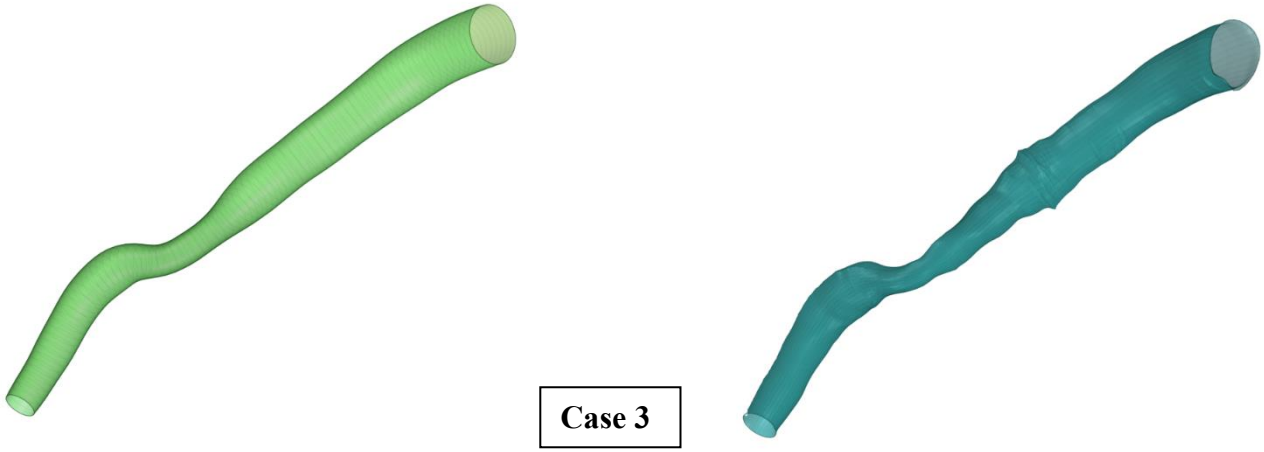

Case 3

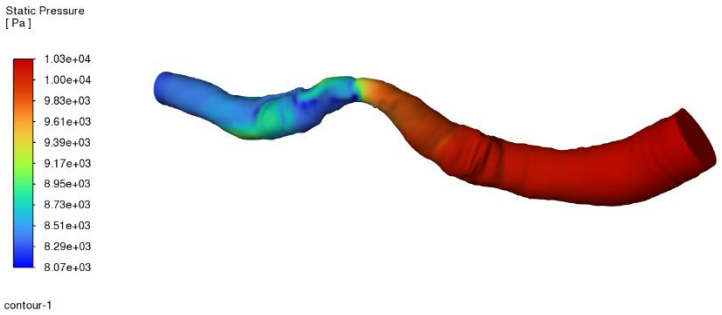

Case 3

Proximal Pressure : 77 mm Hg

Distal Pressure : 62 mm Hg

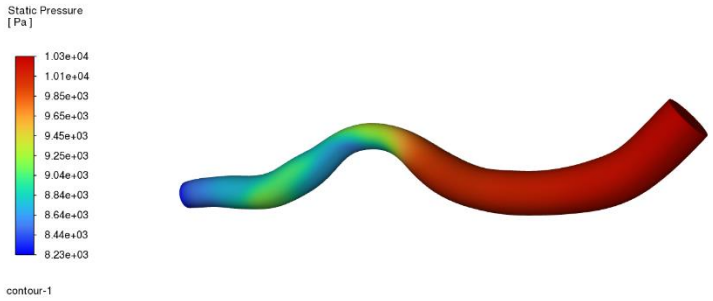

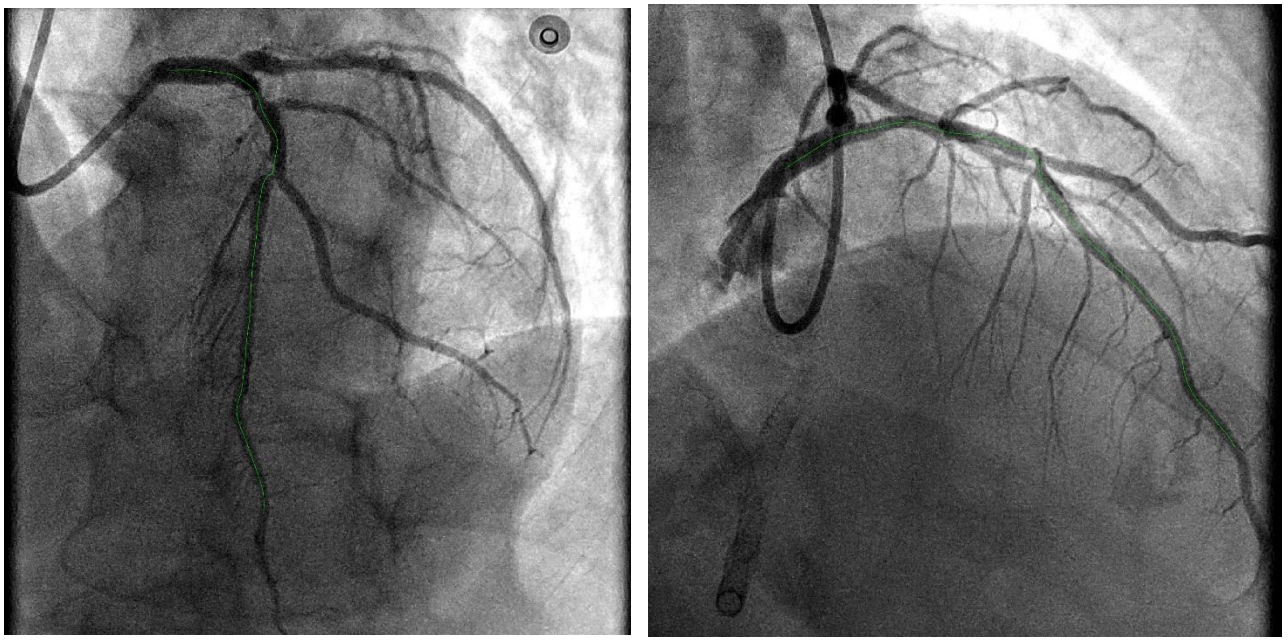

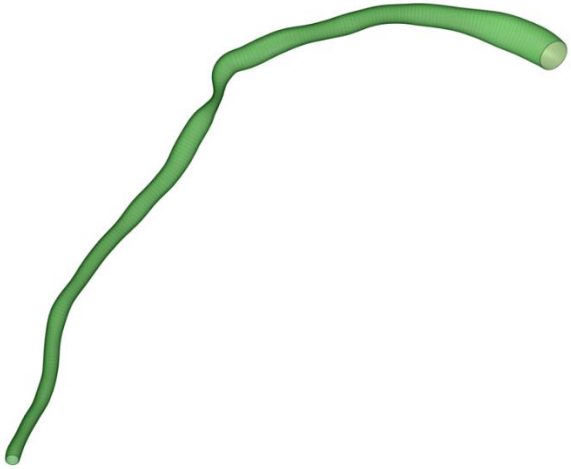

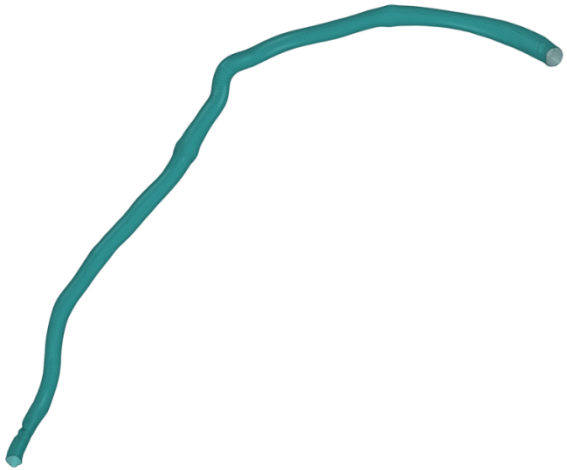

Case 4

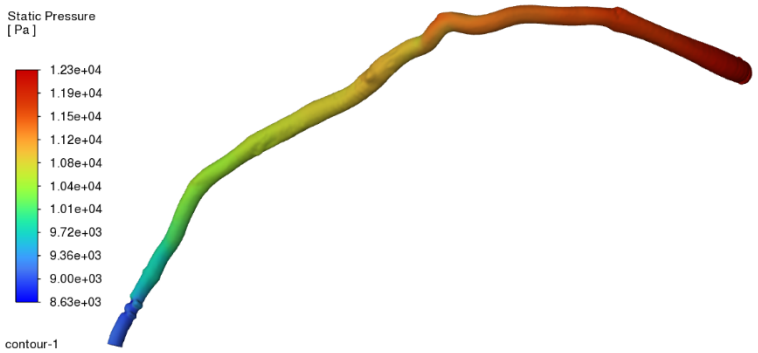

Case 4

Proximal Pressure : 92 mm Hg

Distal Pressure : 68 mm Hg

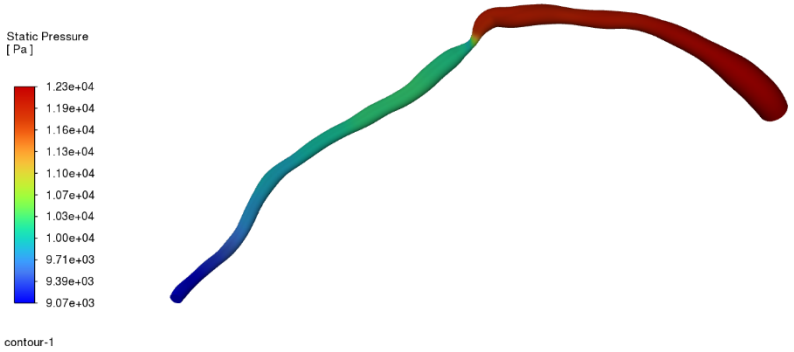

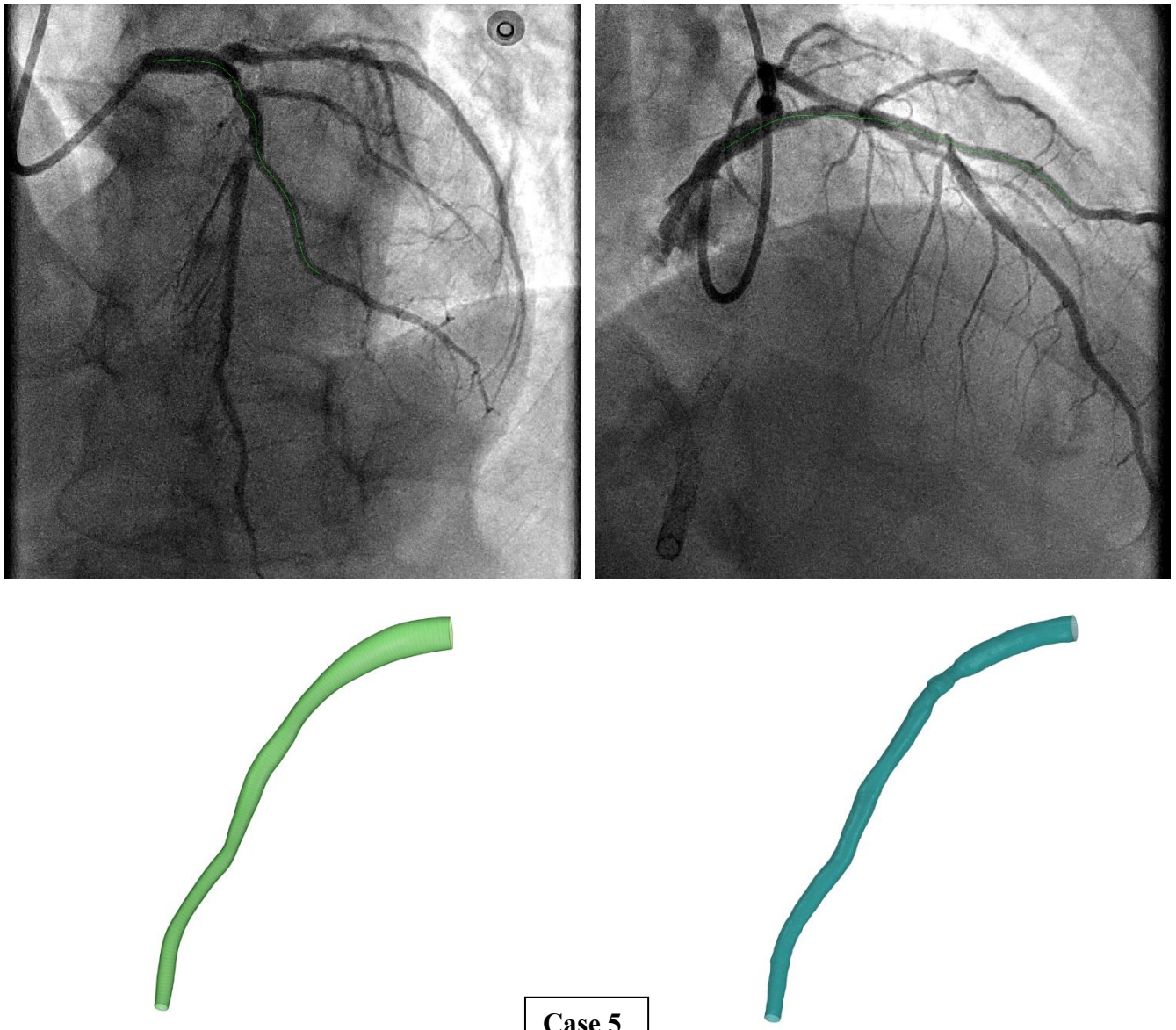

Case 5

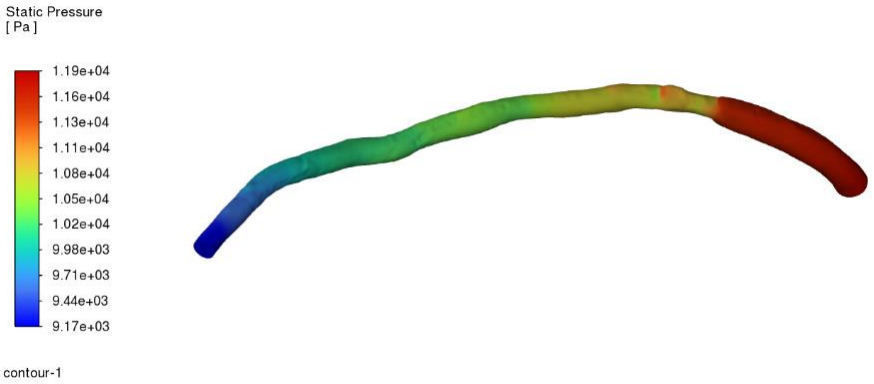

Case 5

Proximal Pressure : 89 mm Hg

Distal Pressure : 69 mm Hg

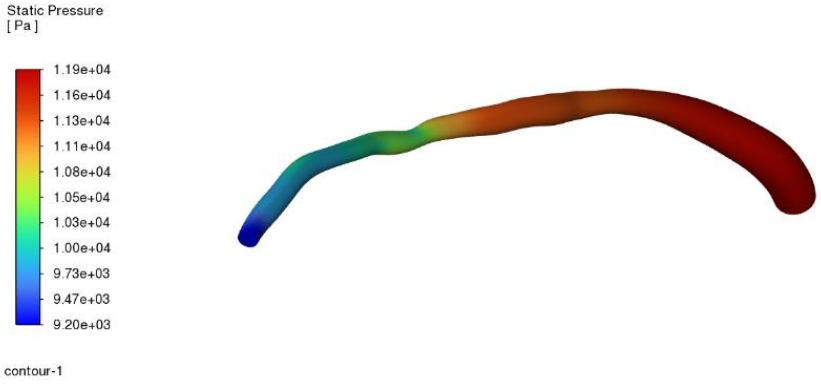

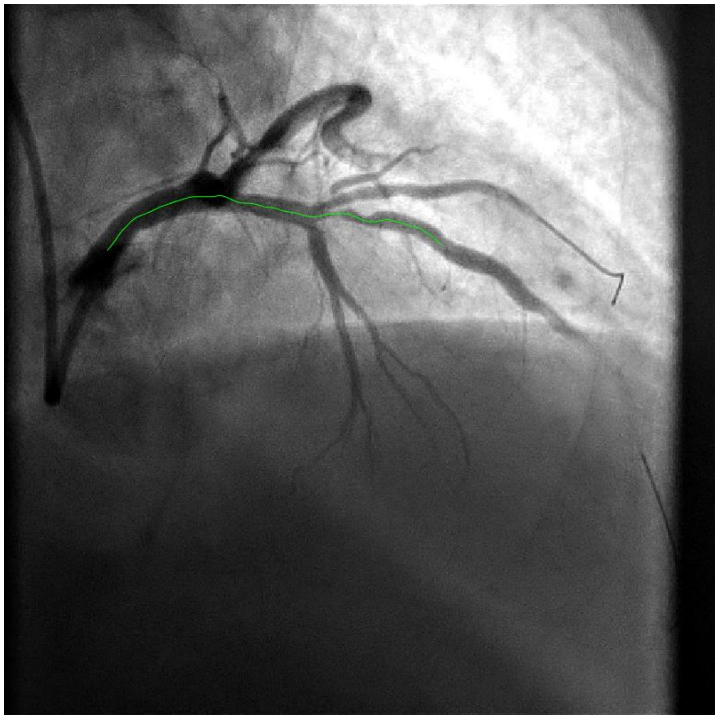

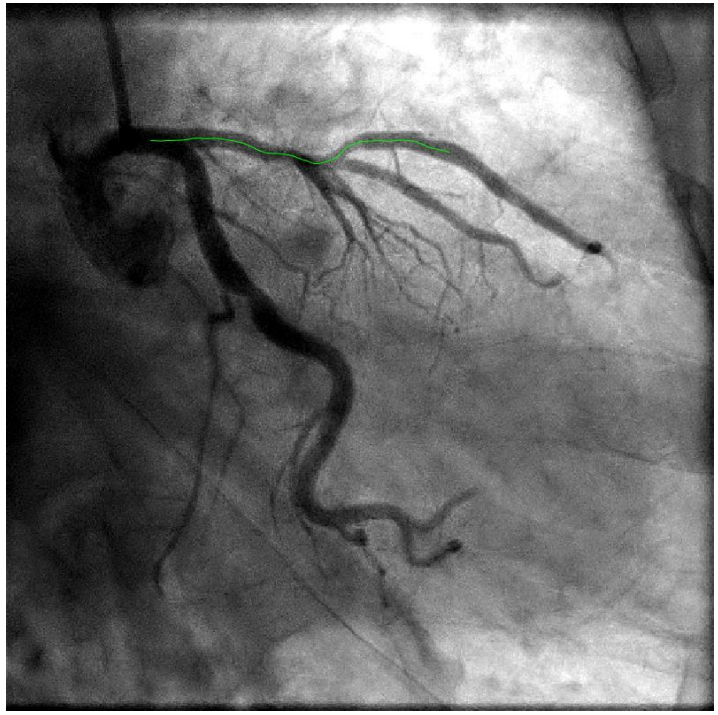

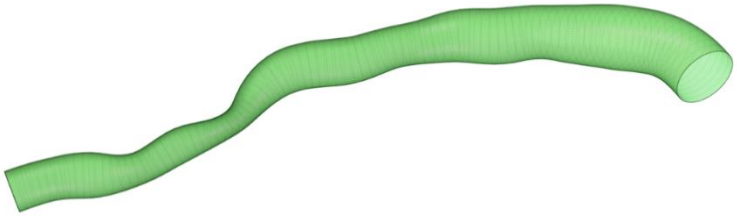

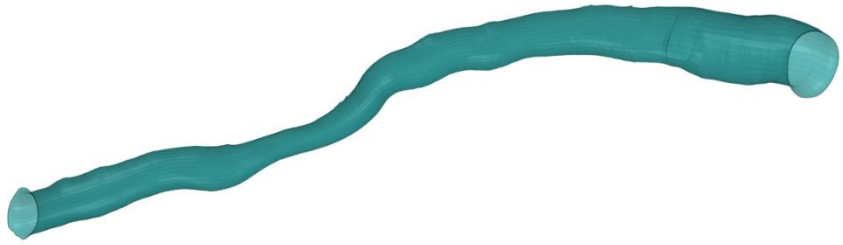

Case 6

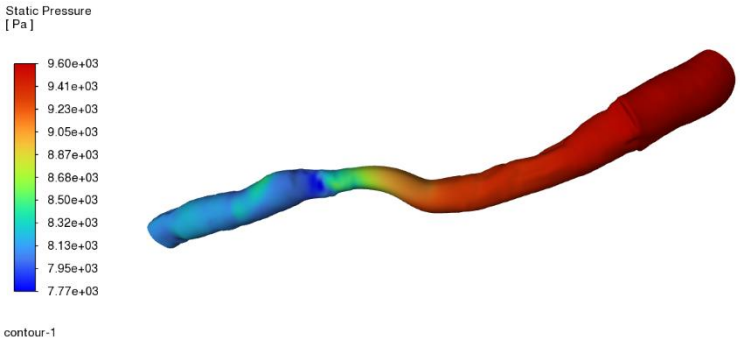

Case 6

Proximal Pressure : 72 mm Hg

Distal Pressure : 61 mm Hg

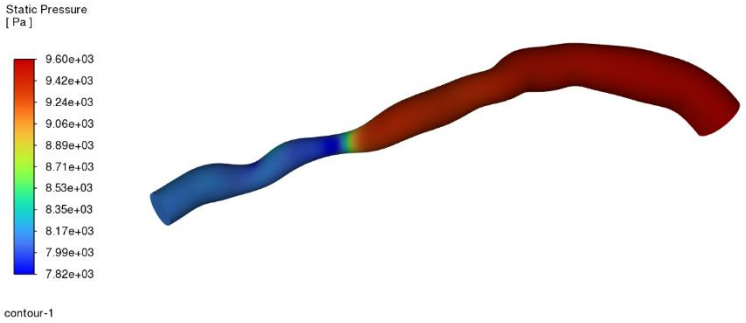

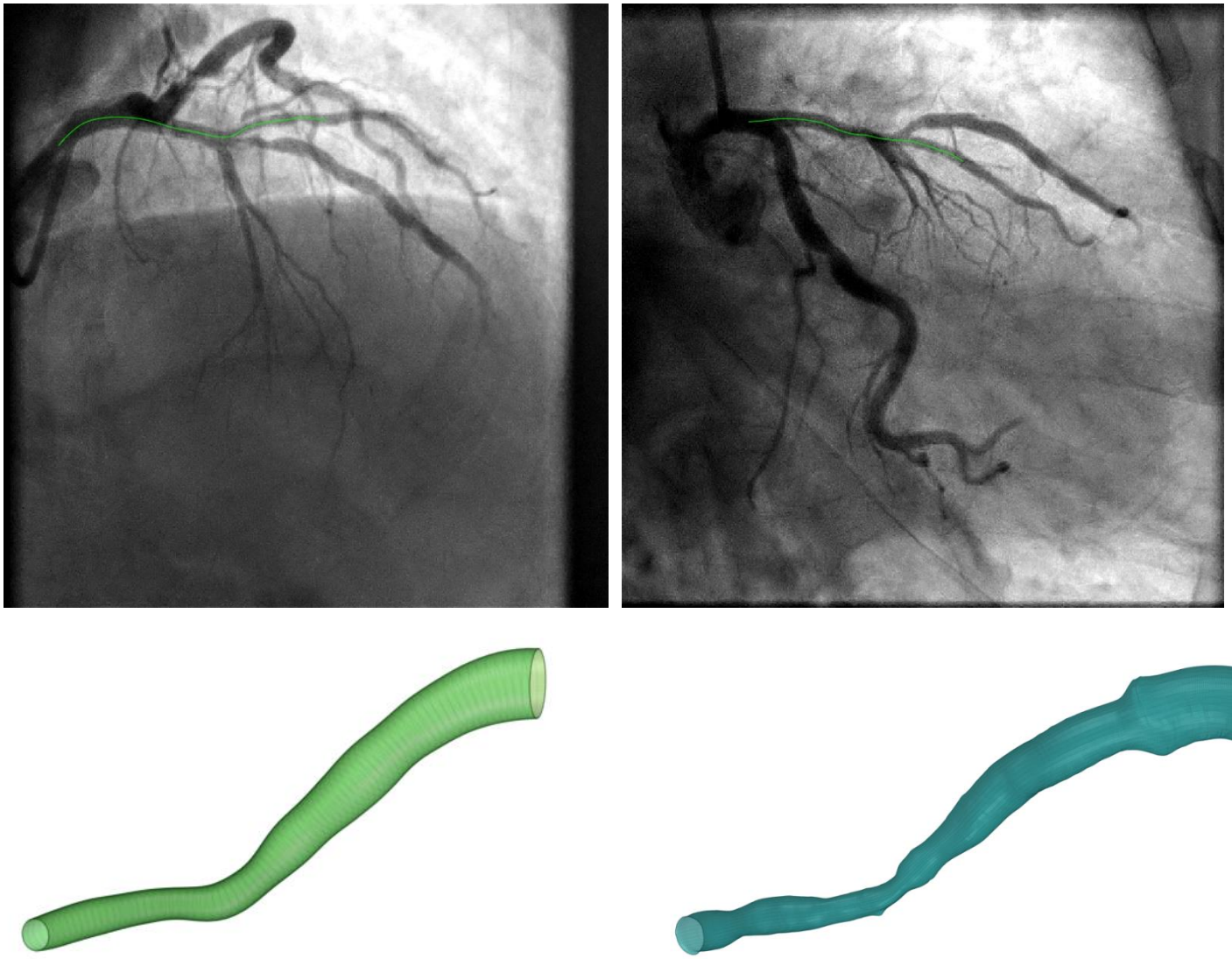

Case 7

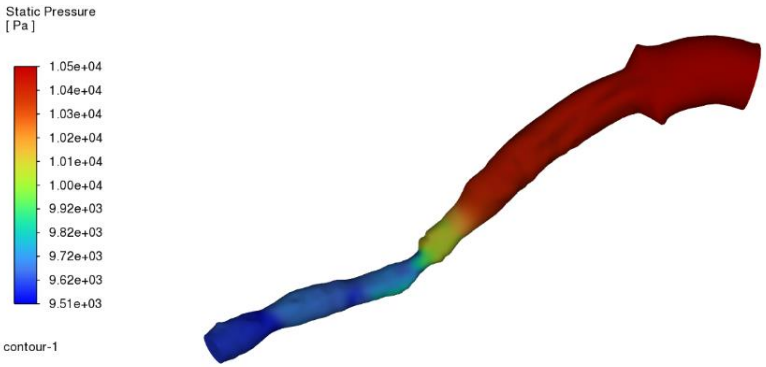

Case 7

Proximal Pressure : 79 mm Hg

Distal Pressure : 72 mm Hg

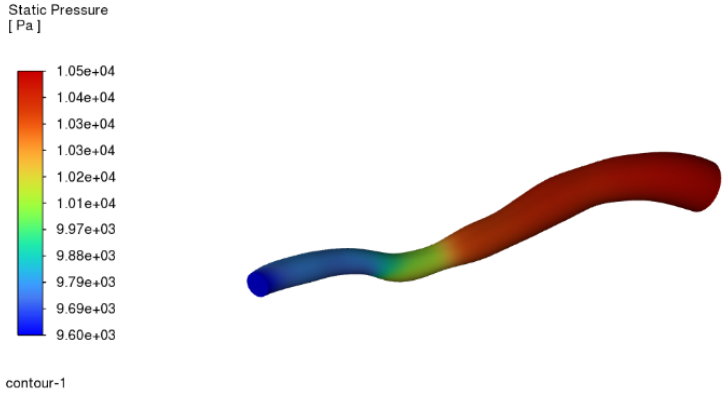

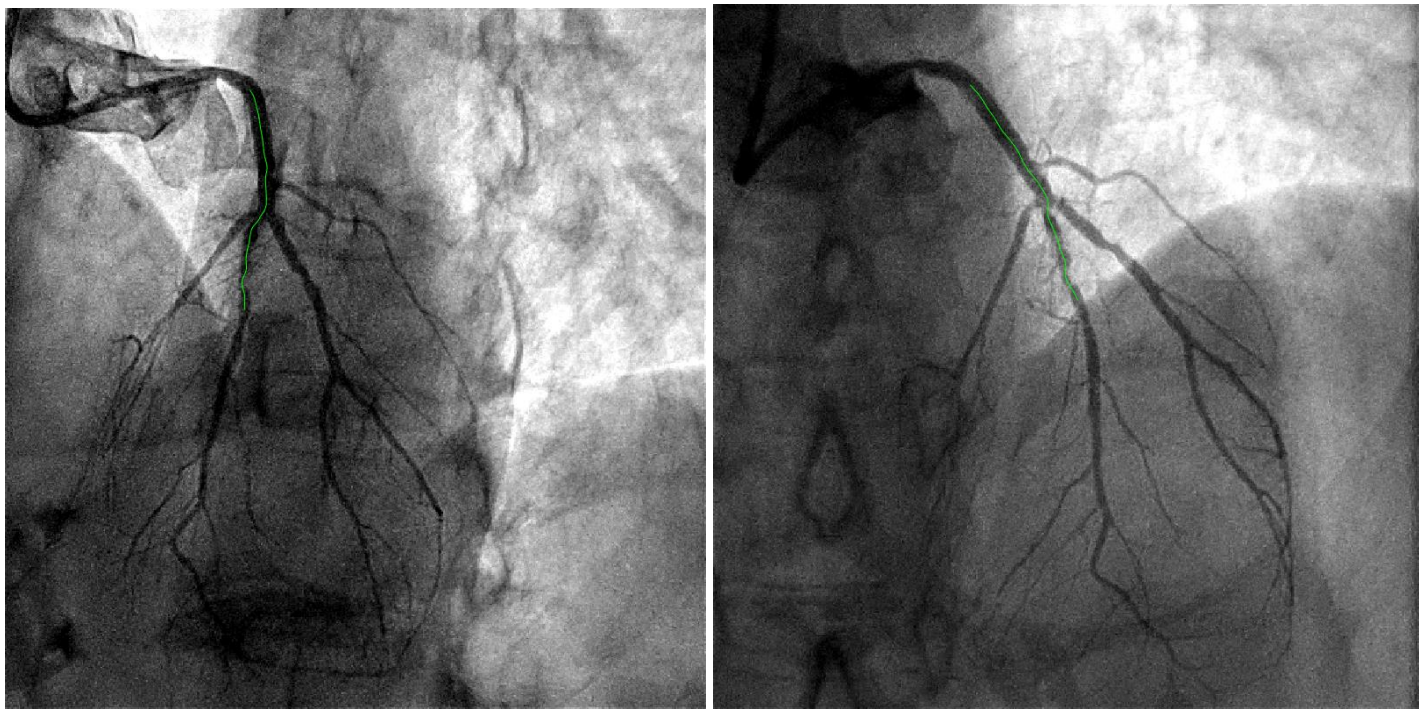

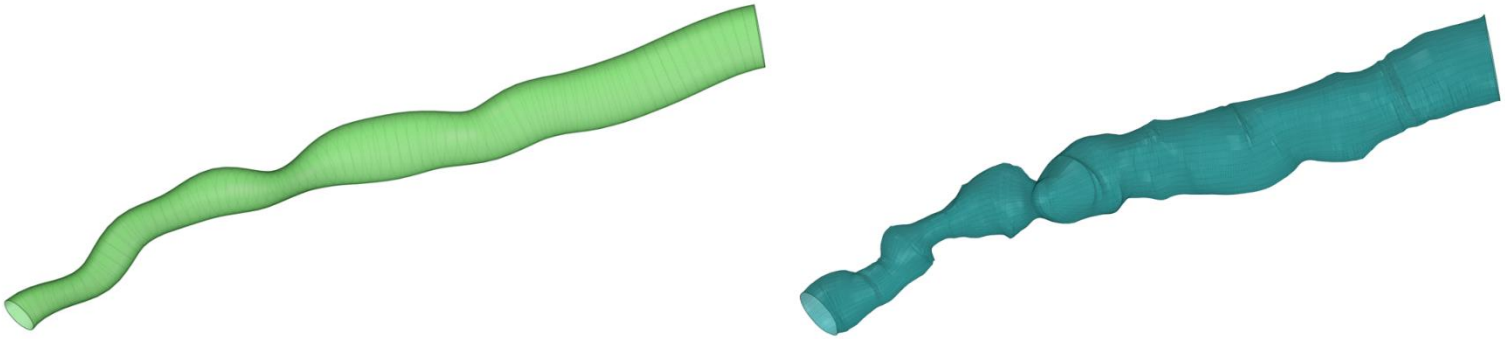

Case 8

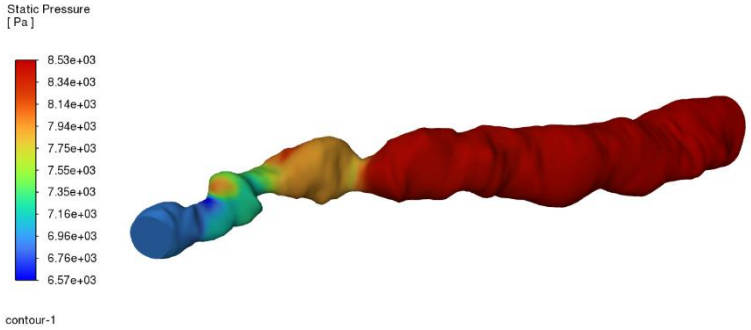

Case 8

Proximal Pressure : 64 mm Hg

Distal Pressure : 52 mm Hg

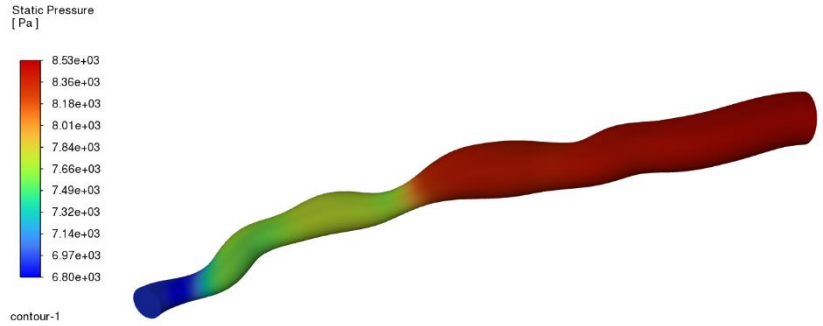

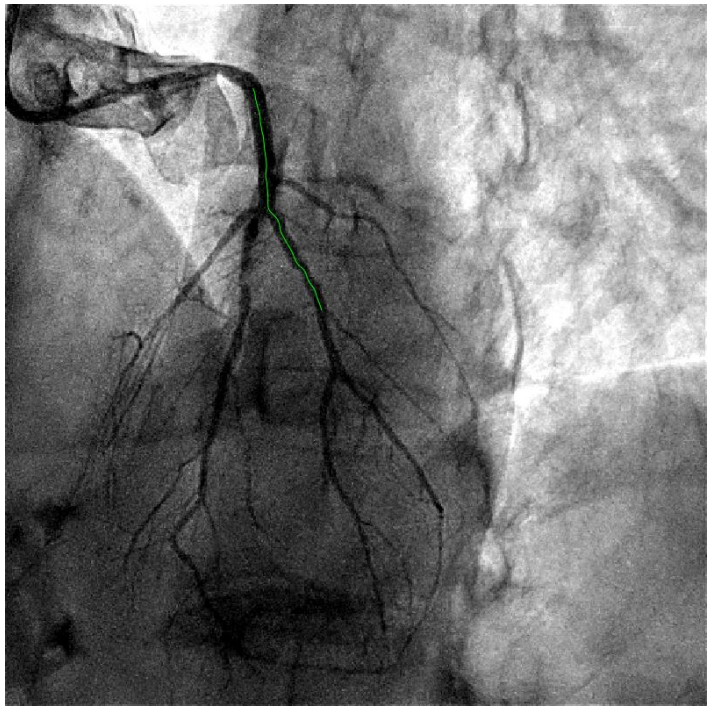

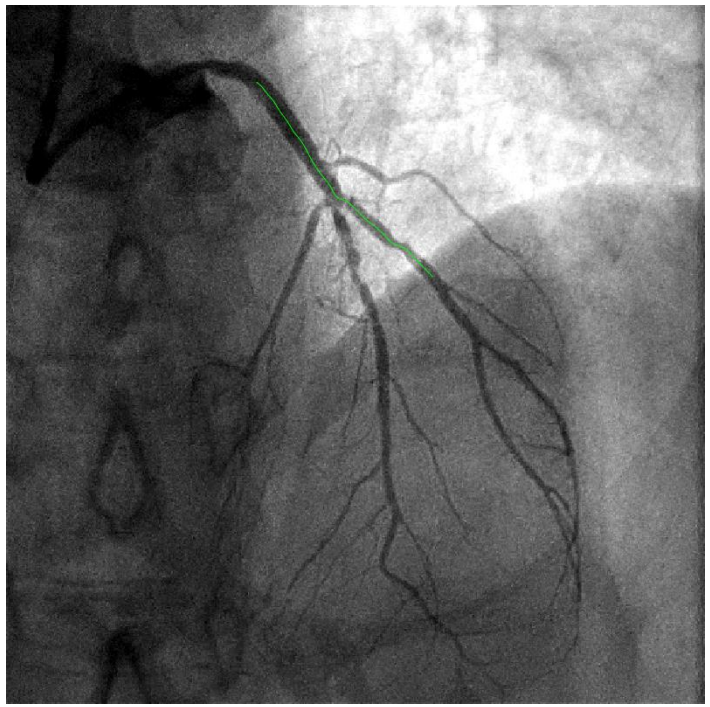

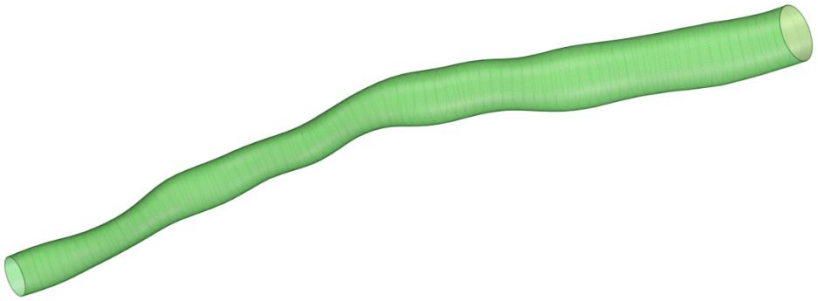

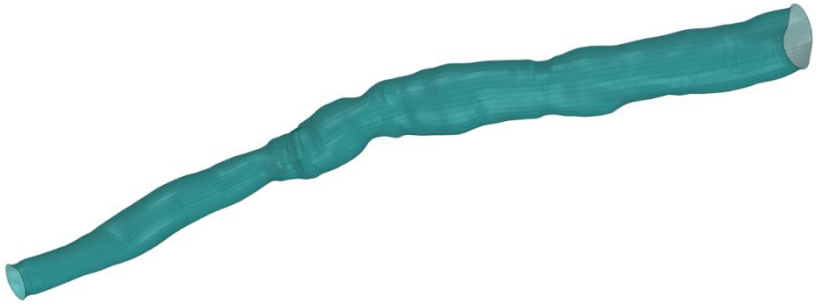

Case 9

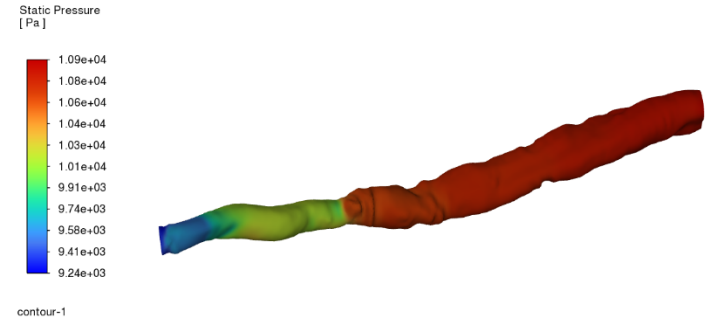

Case 9

Proximal Pressure : 82 mm Hg

Distal Pressure : 70 mm Hg

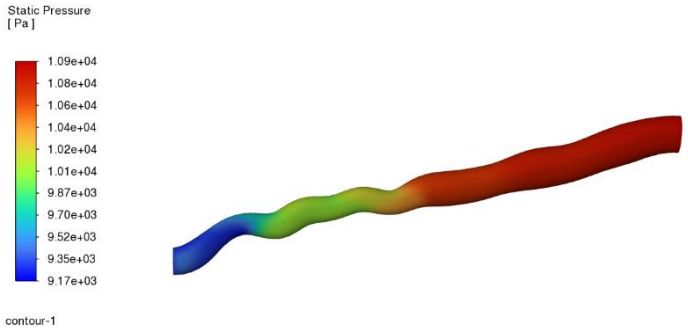

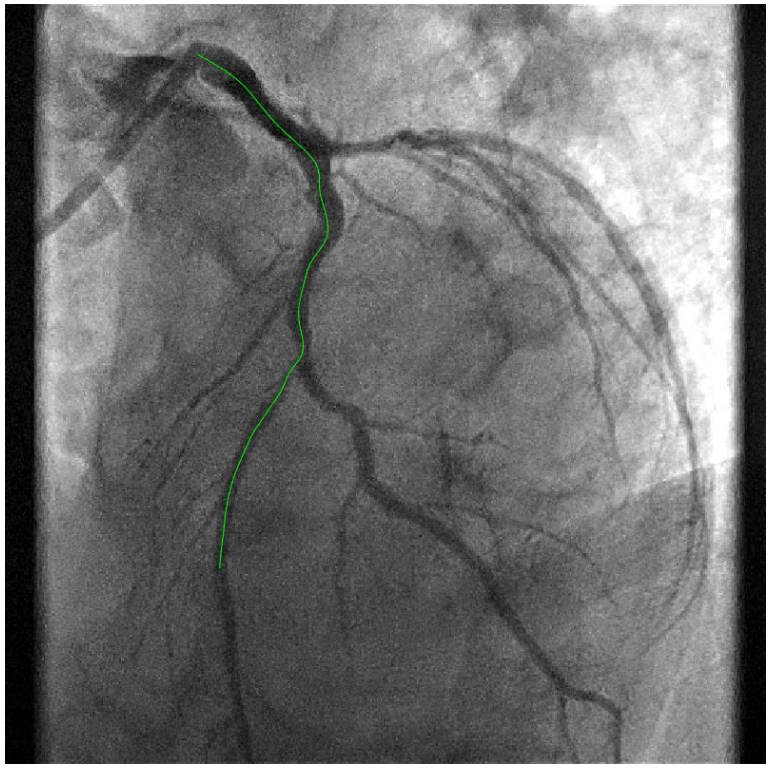

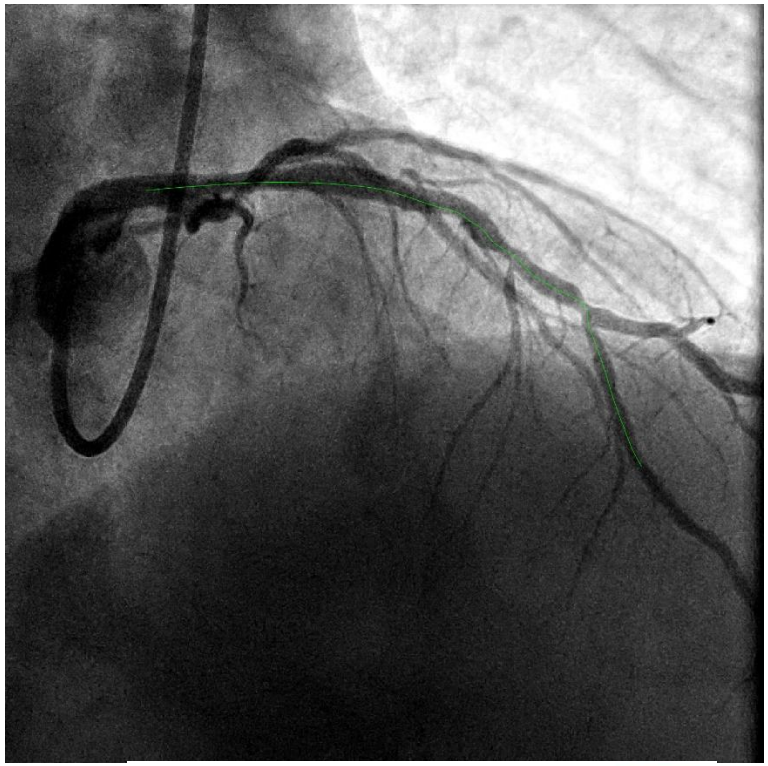

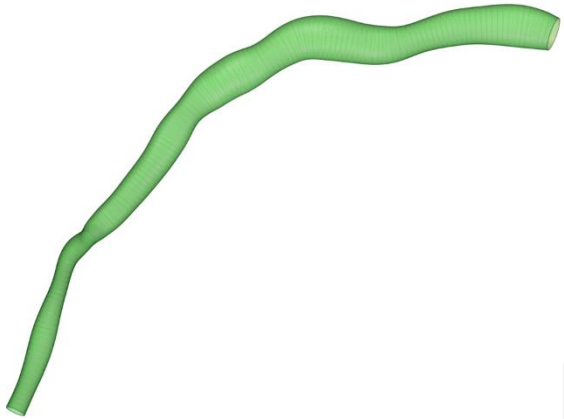

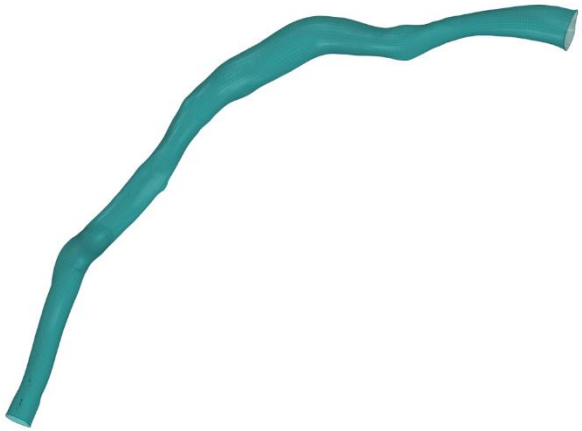

Case 10

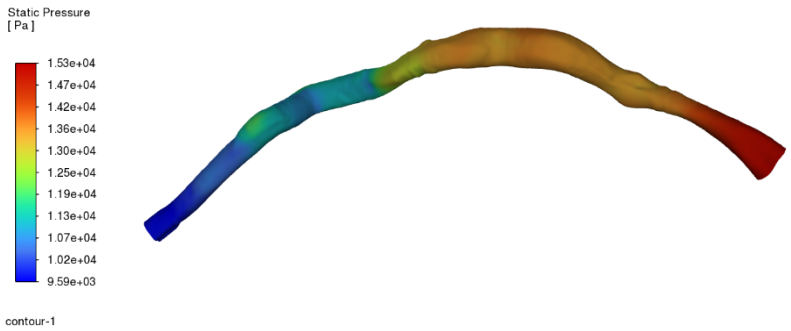

Case 10

Proximal Pressure : 115 mm Hg

Distal Pressure : 73 mm Hg

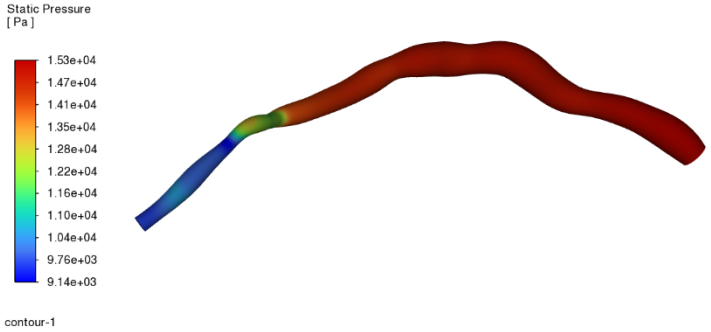

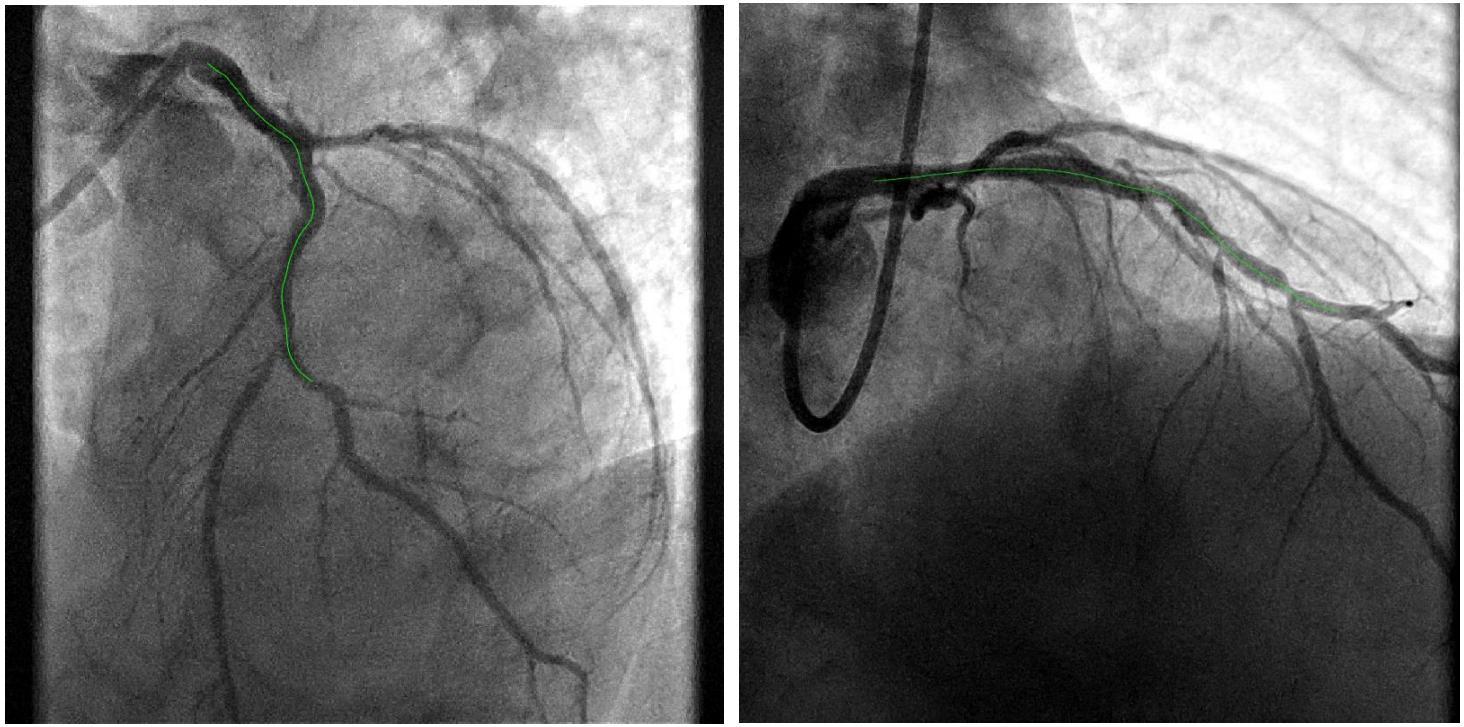

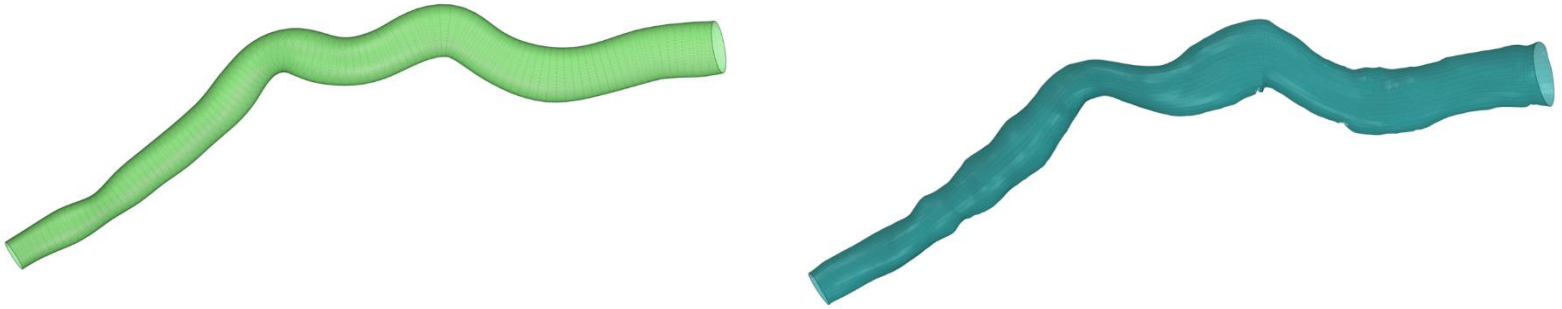

Case 11

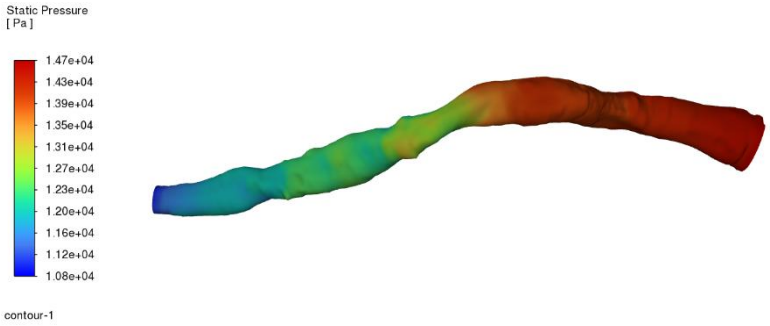

Case 11

Proximal Pressure : 110 mm Hg

Distal Pressure : 82 mm Hg

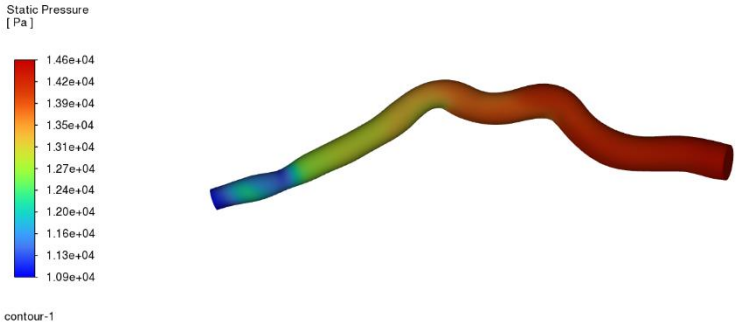

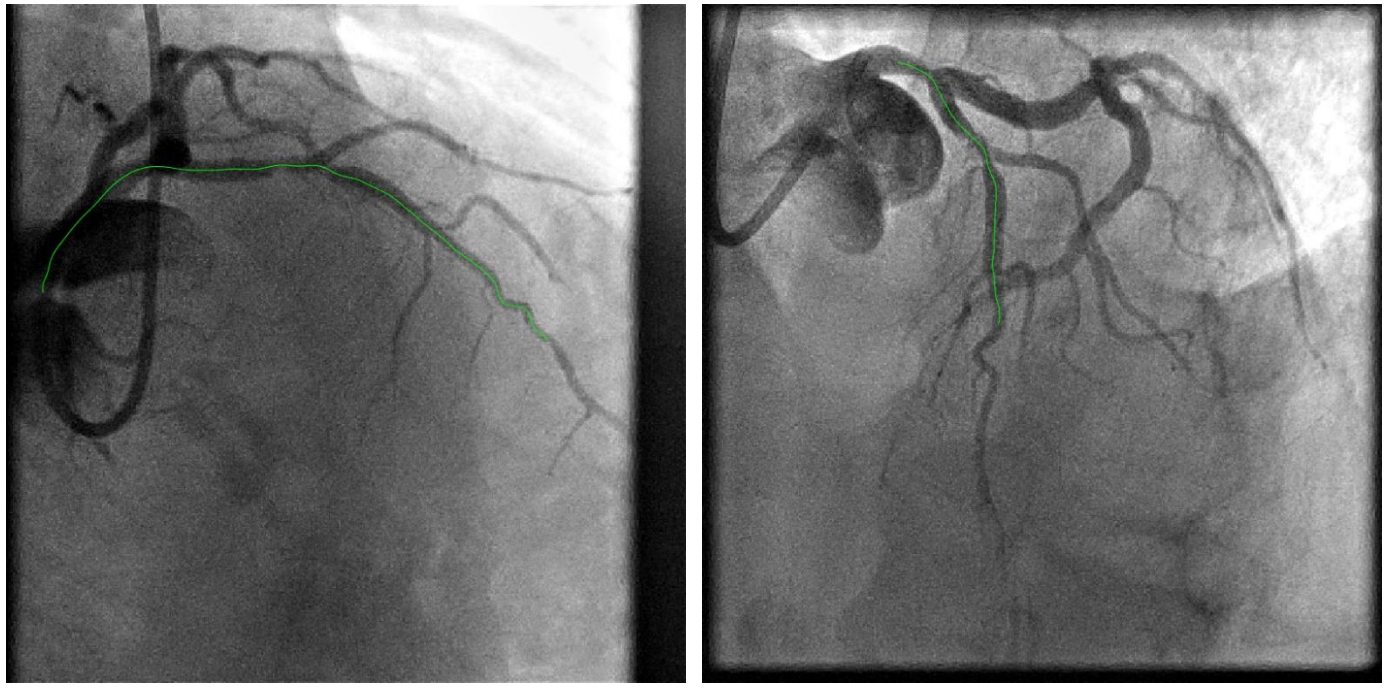

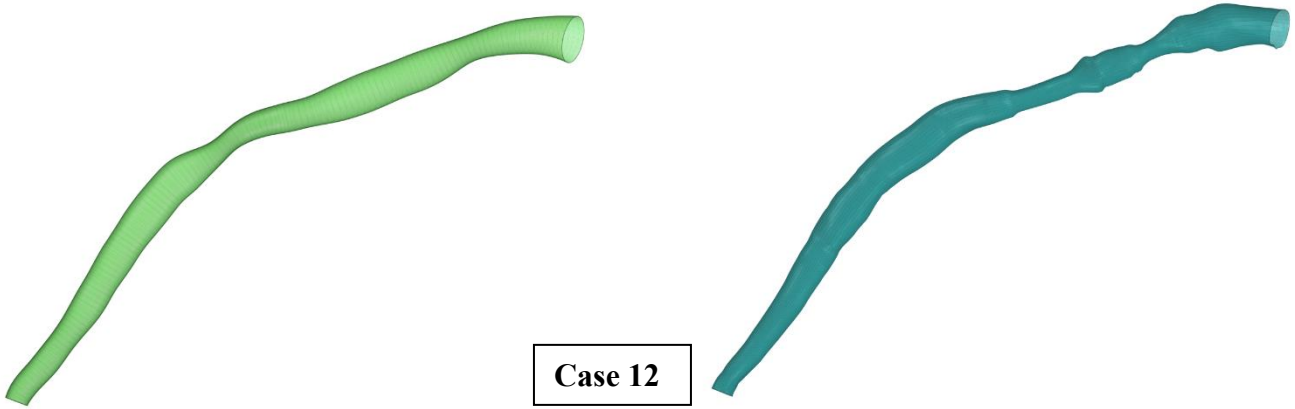

Case 12

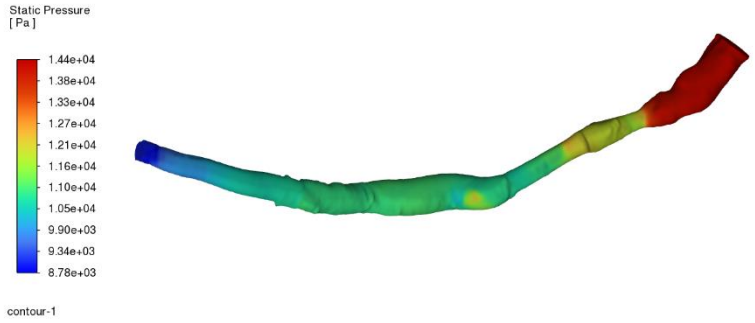

Case 12

Proximal Pressure : 108 mm Hg

Distal Pressure : 68 mm Hg

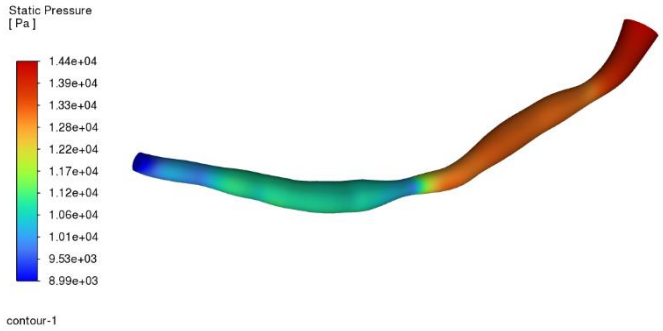

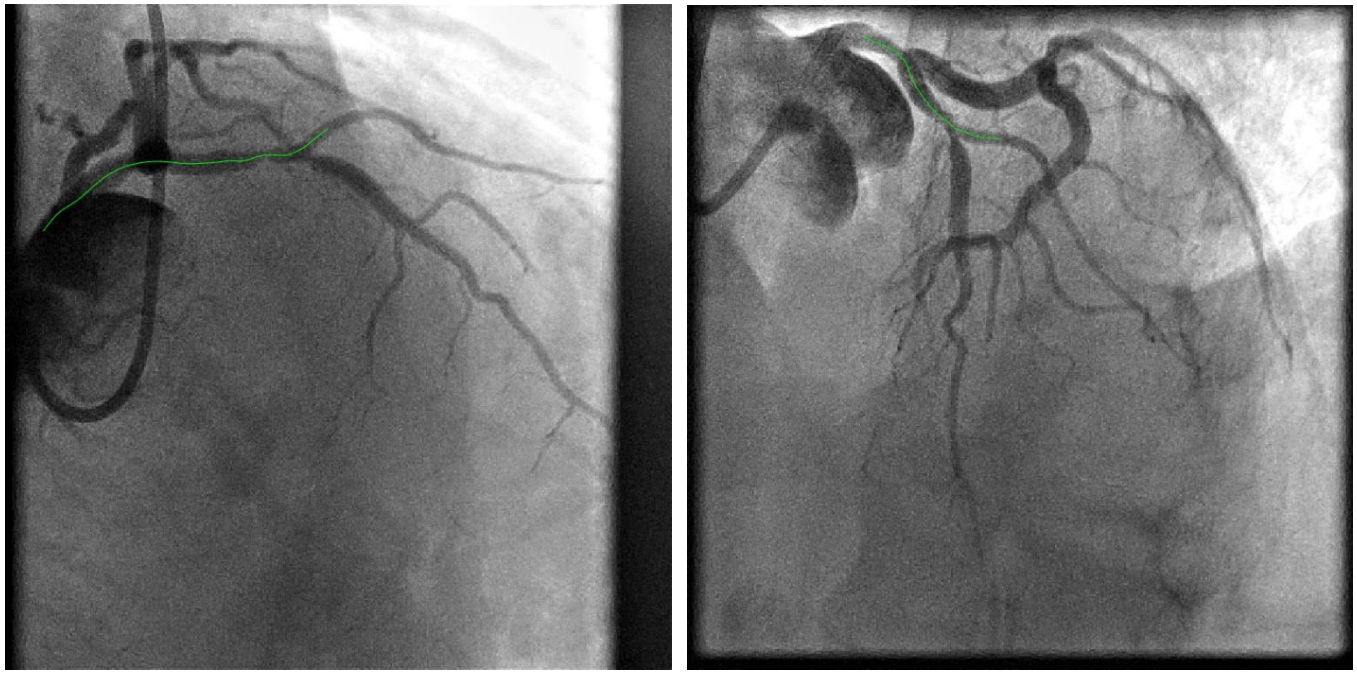

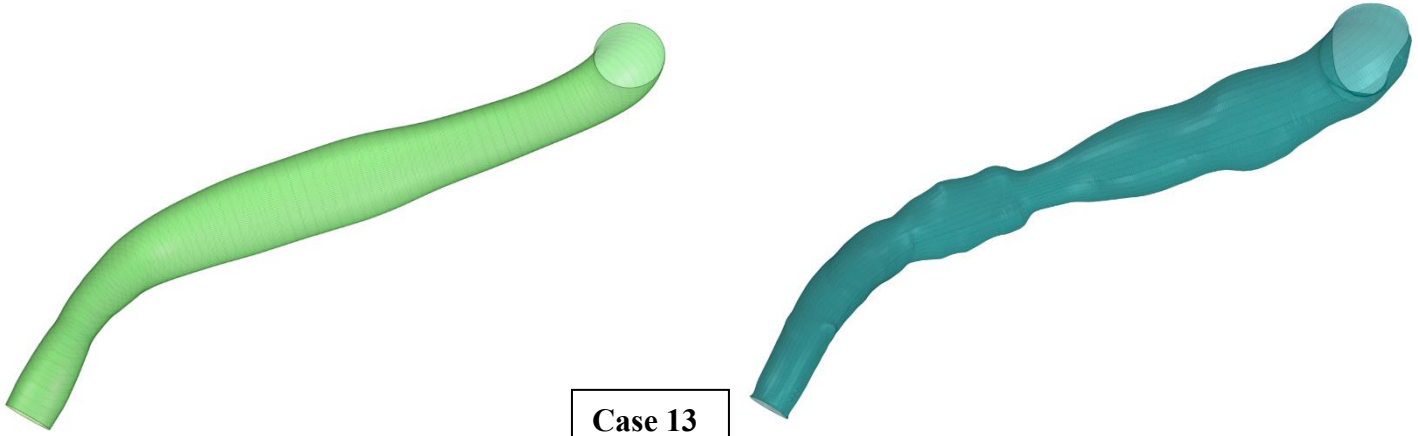

Case 13

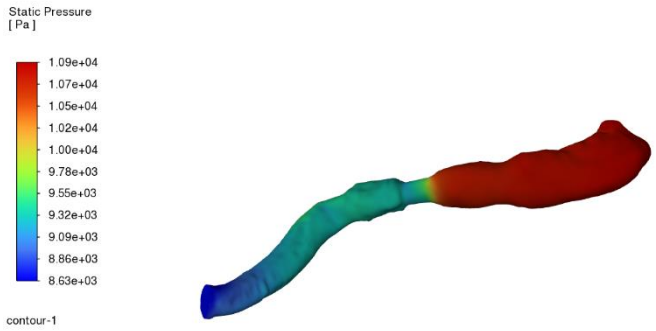

Case 13

Proximal Pressure : 82 mm Hg

Distal Pressure : 65 mm Hg

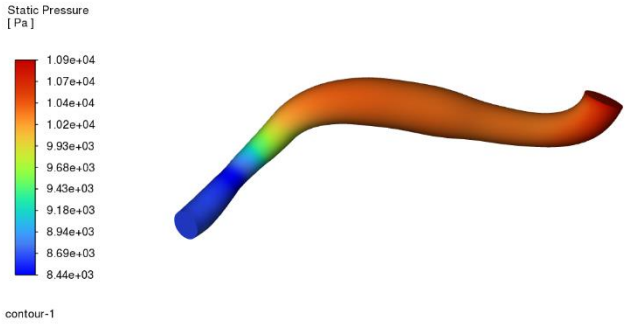

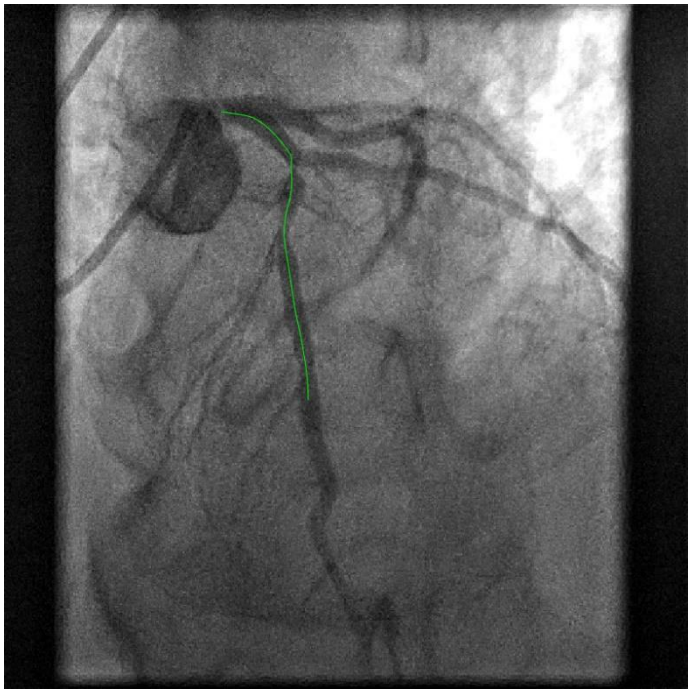

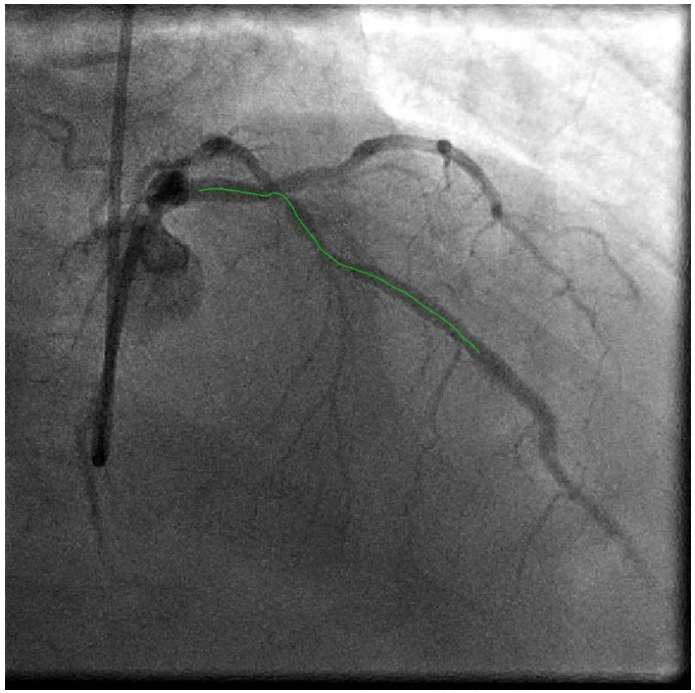

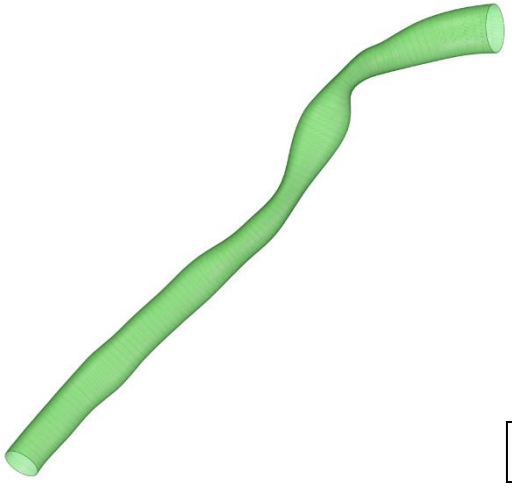

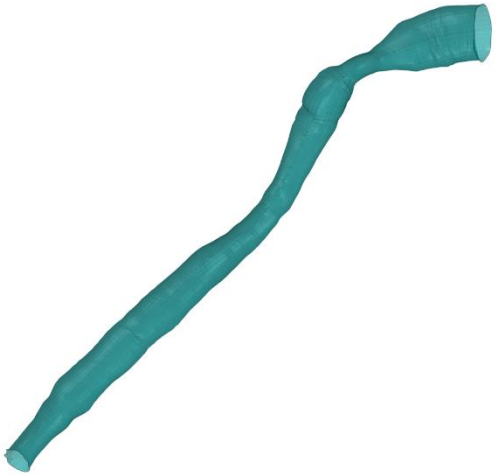

Case 14

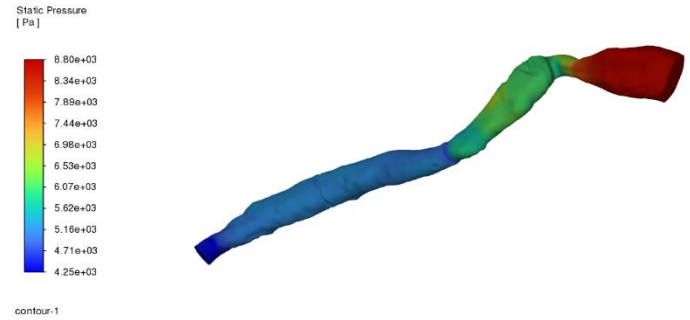

Case 14

Proximal Pressure : 66 mm Hg

Distal Pressure : 33 mm Hg

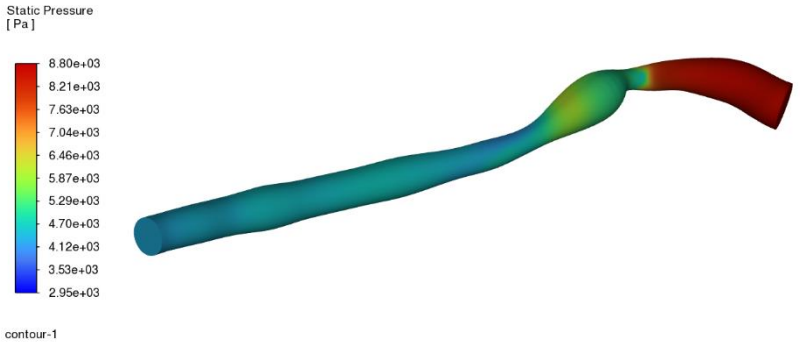

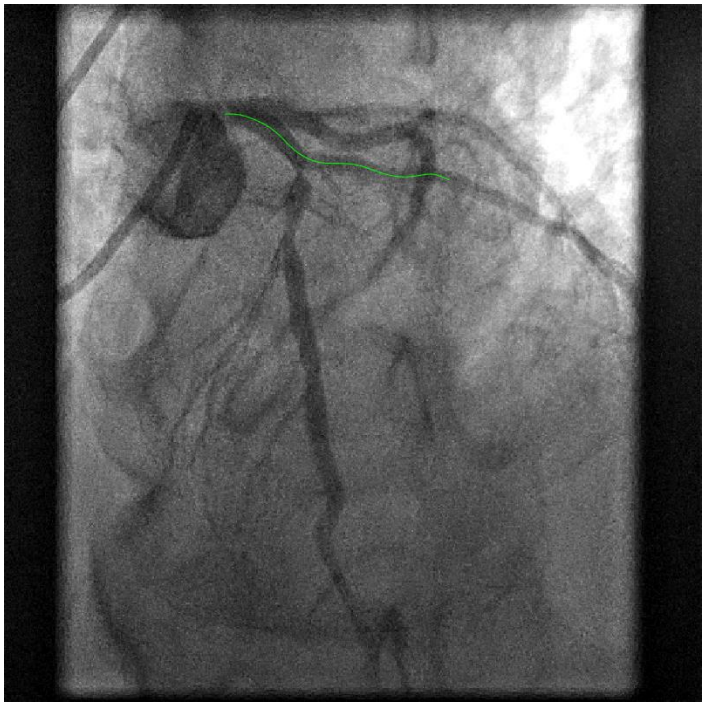

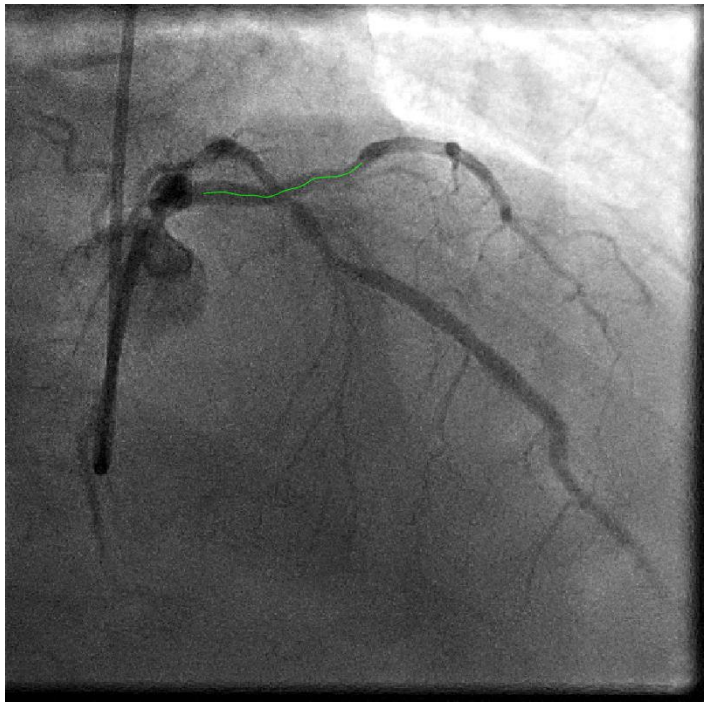

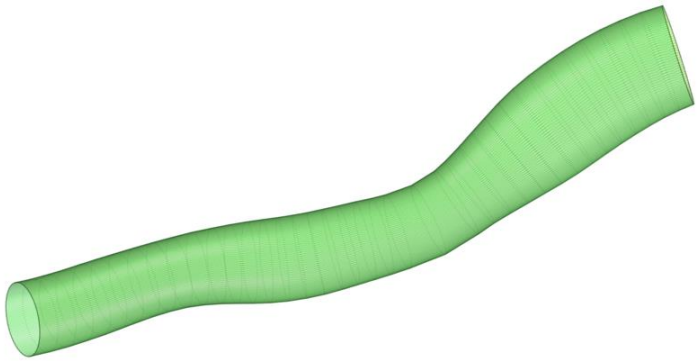

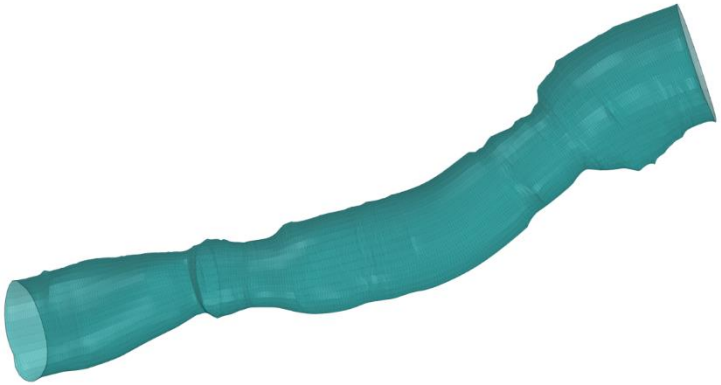

Case 15

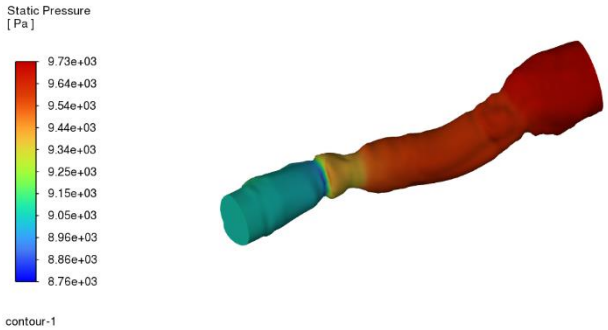

Case 15

Proximal Pressure : 73 mm Hg

Distal Pressure : 68 mm Hg

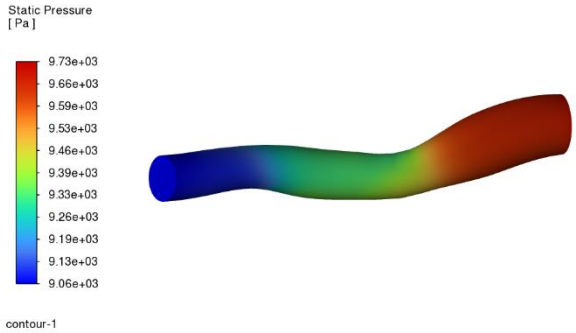

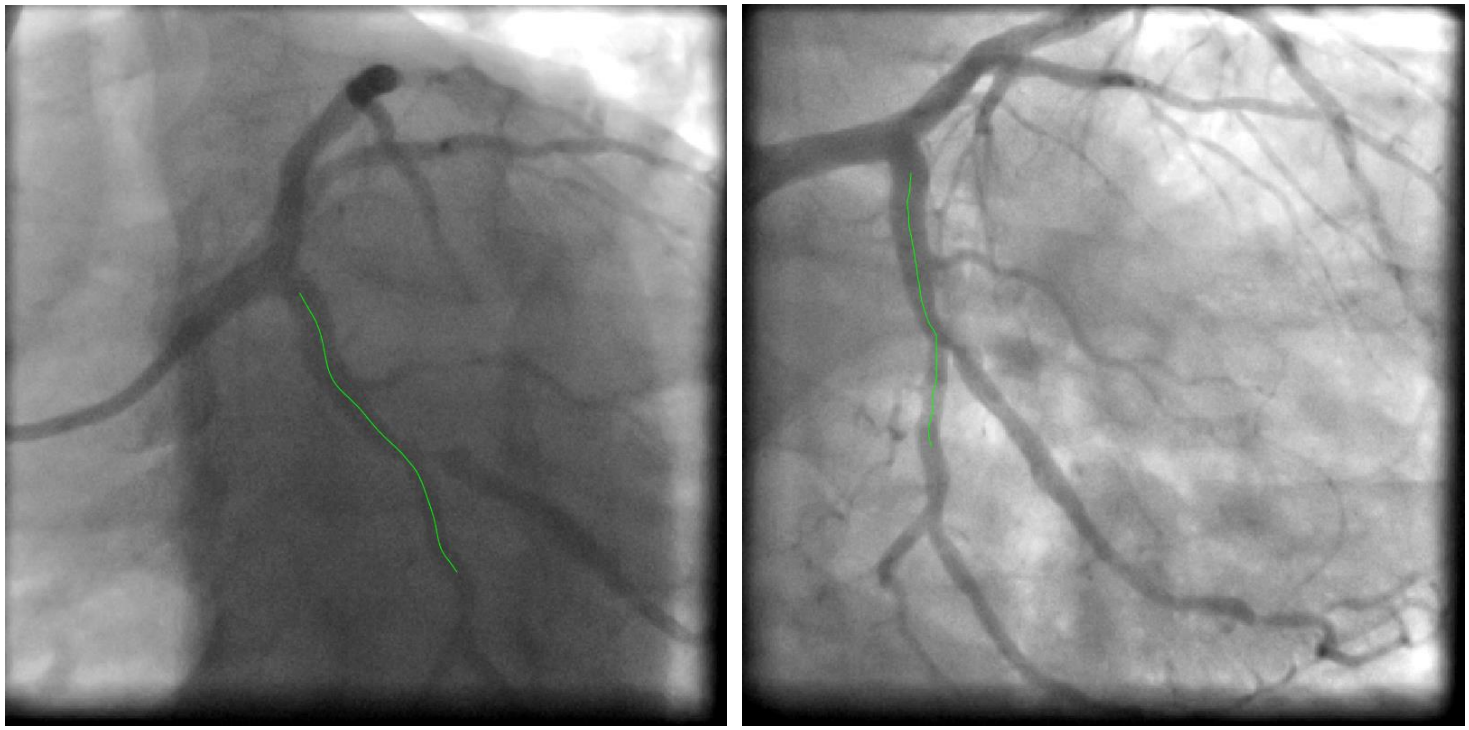

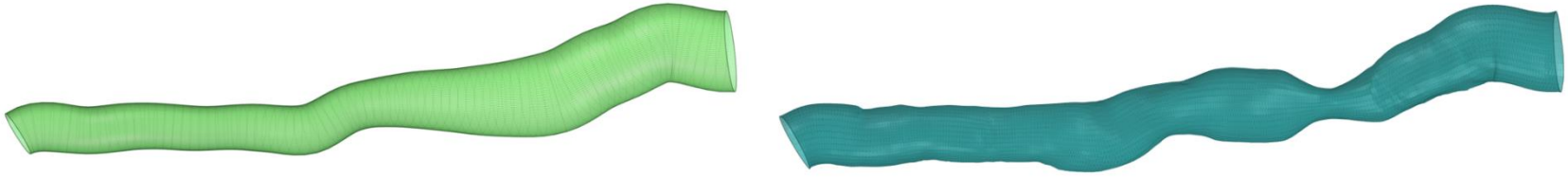

Case 16

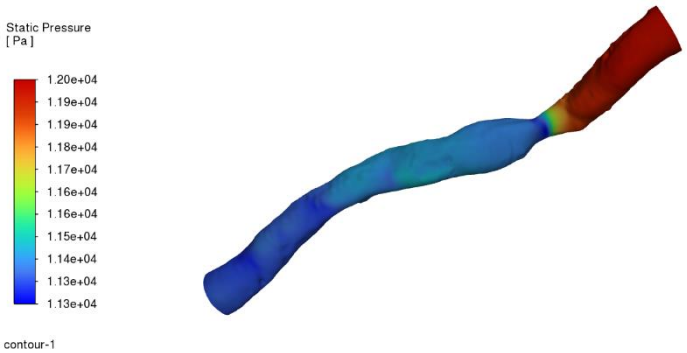

Case 16

Proximal Pressure : 90 mm Hg

Distal Pressure : 85 mm Hg

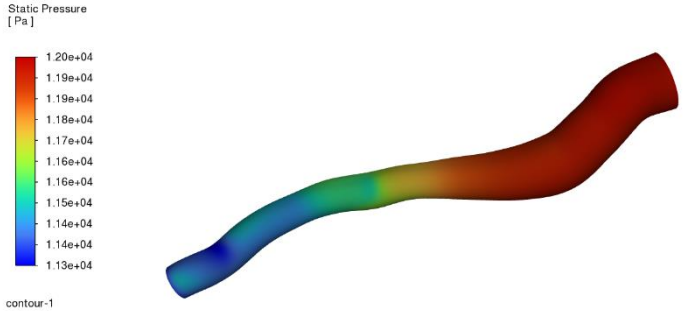

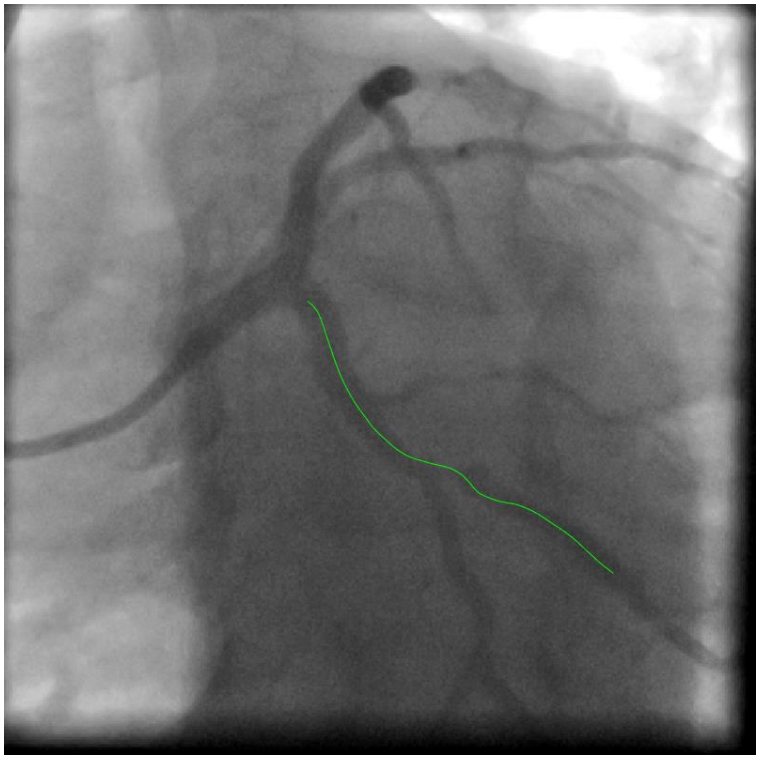

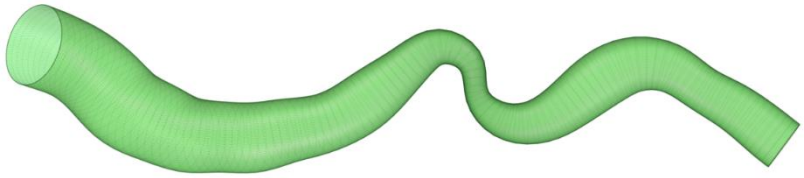

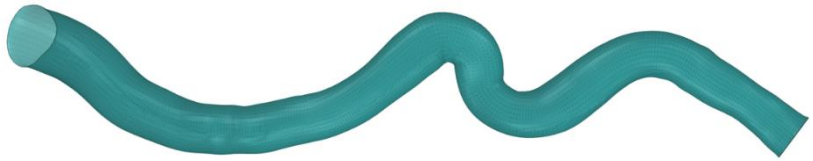

Case 17

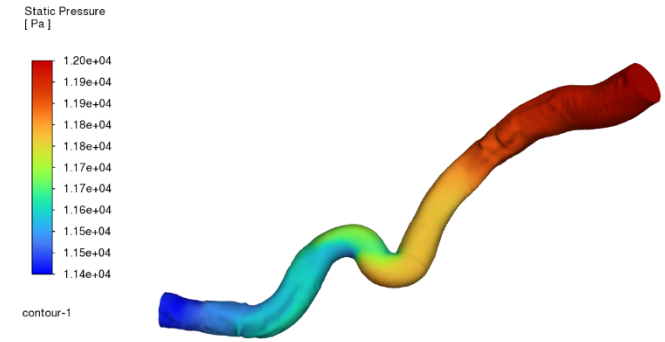

Case 17

Proximal Pressure : 90 mm Hg

Distal Pressure : 86 mm Hg

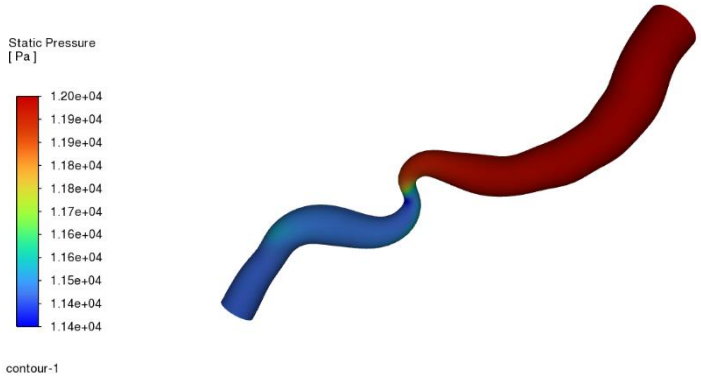

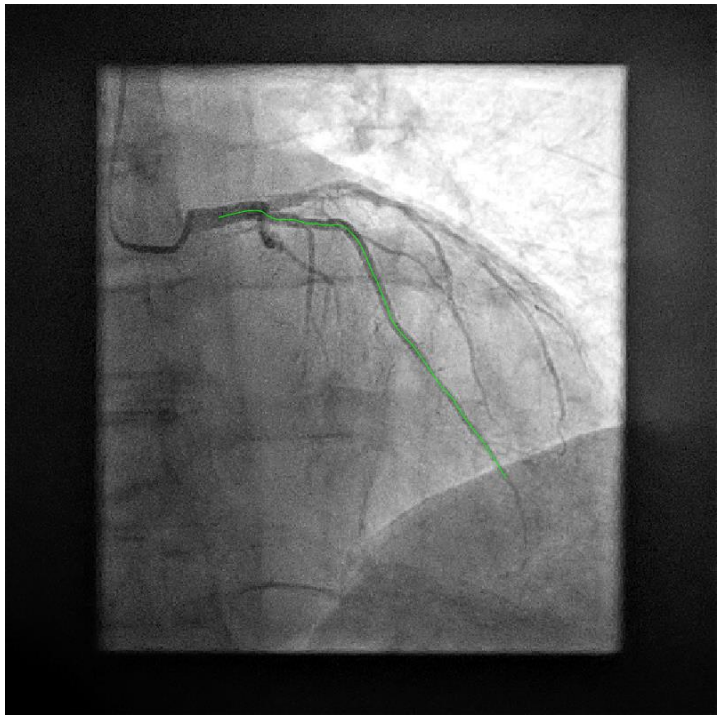

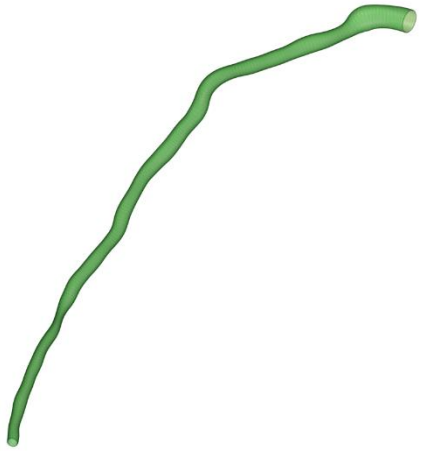

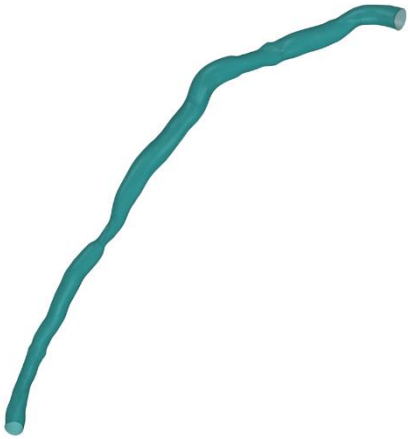

Case 18

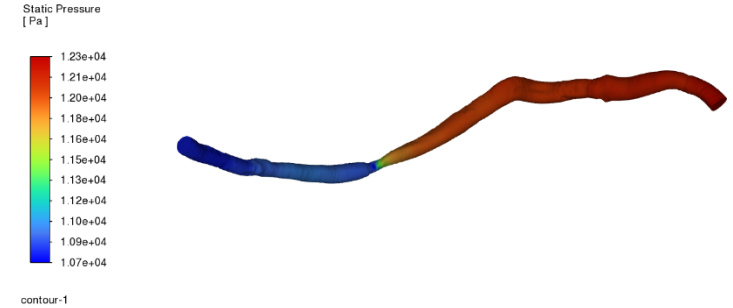

Case 18

Proximal Pressure : 92 mm Hg

Distal Pressure : 81 mm Hg

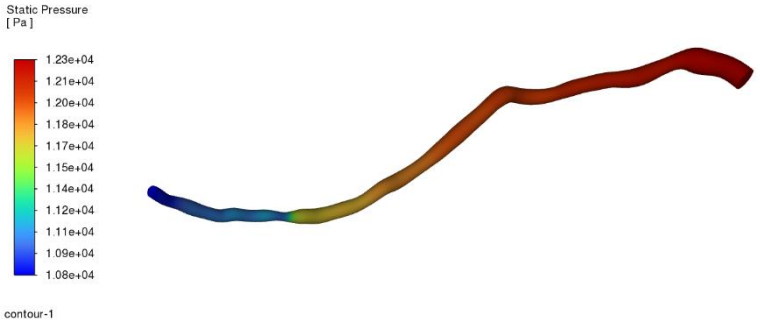

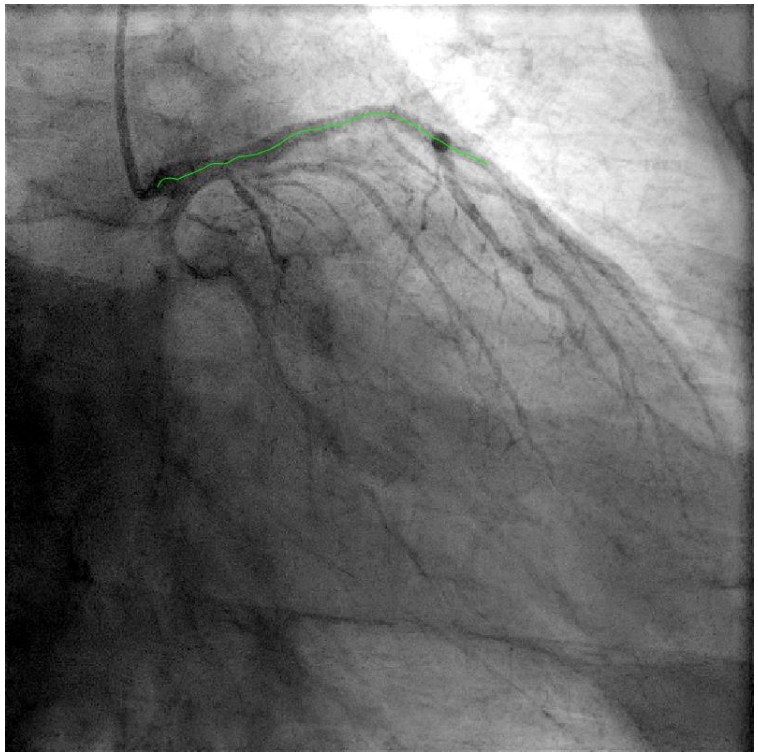

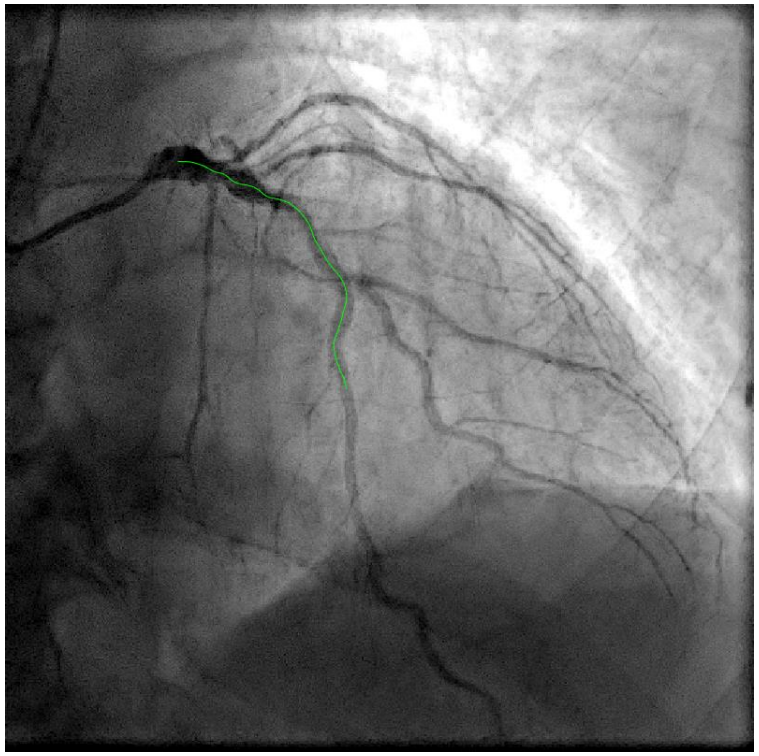

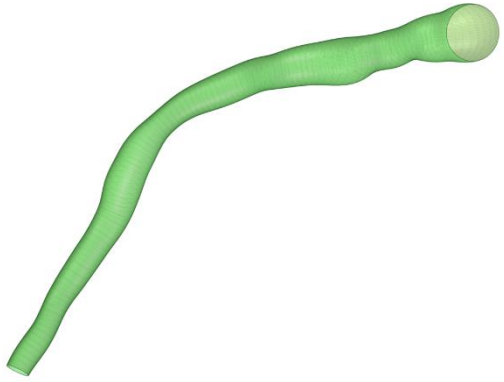

Case 19

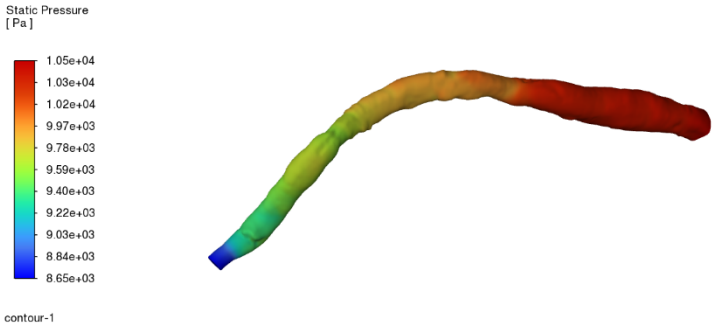

Case 19

Proximal Pressure : 79 mm Hg

Distal Pressure : 65 mm Hg

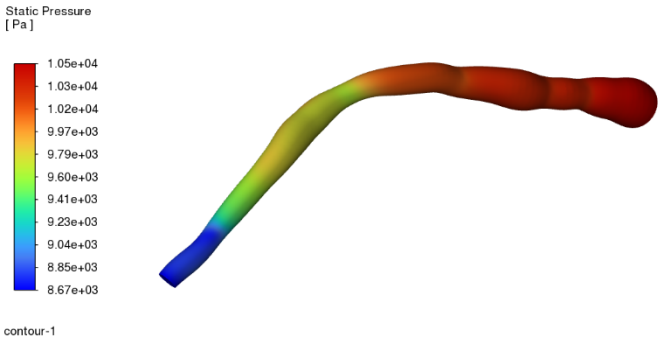

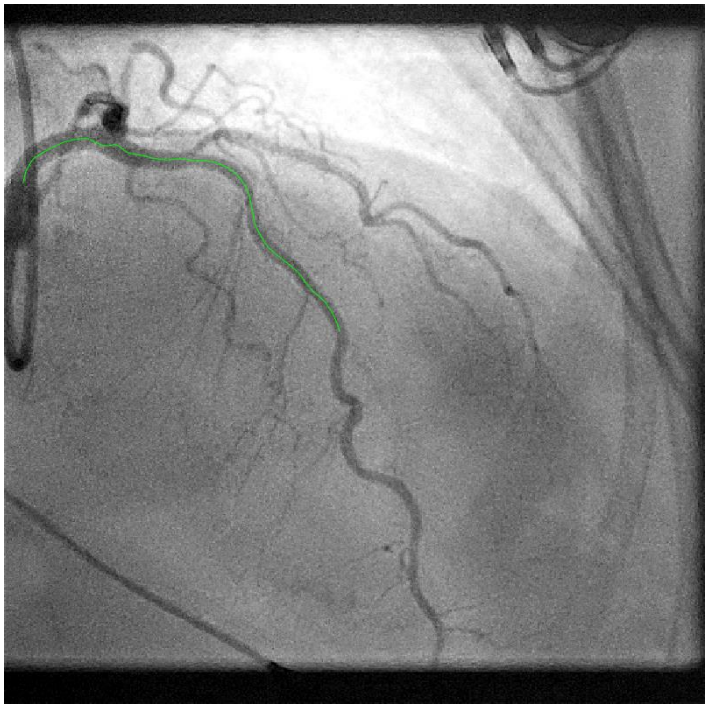

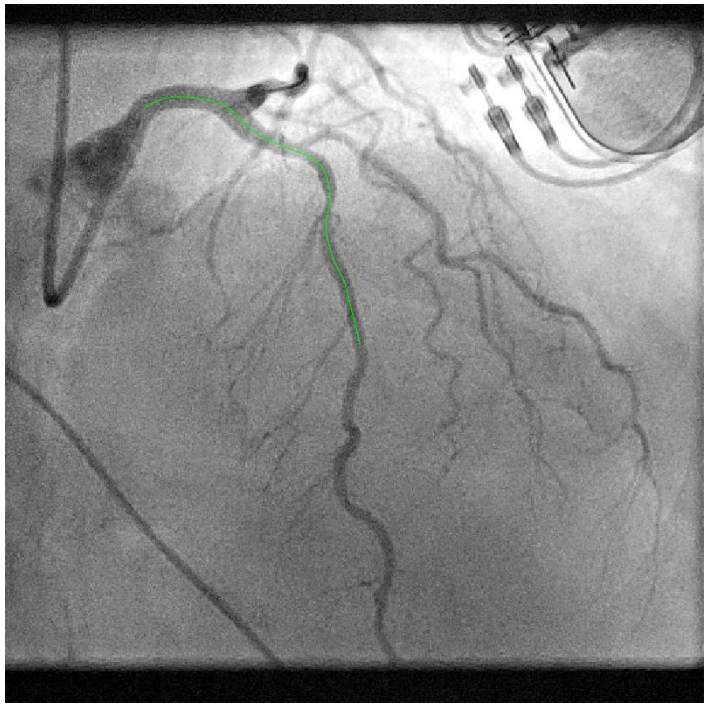

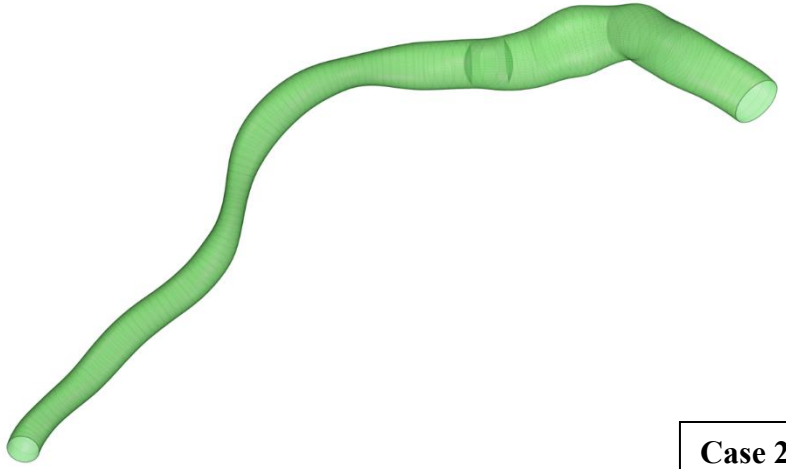

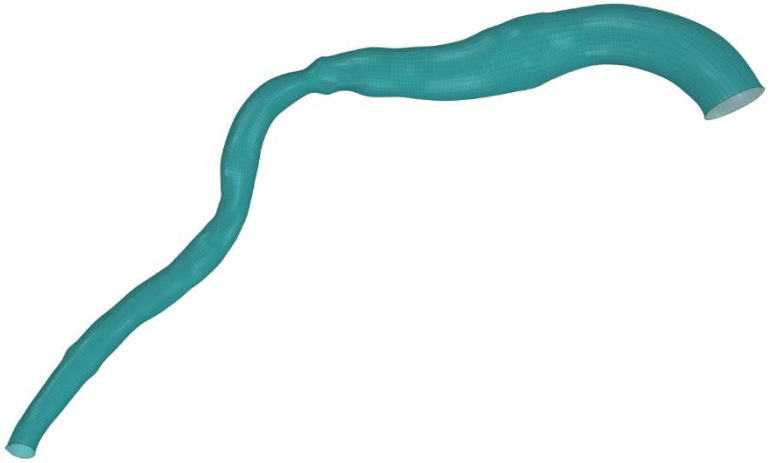

Case 20

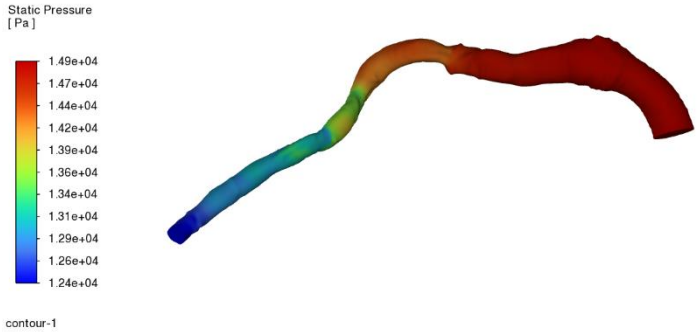

Case 20

Proximal Pressure : 112 mm Hg

Distal Pressure : 93 mm Hg

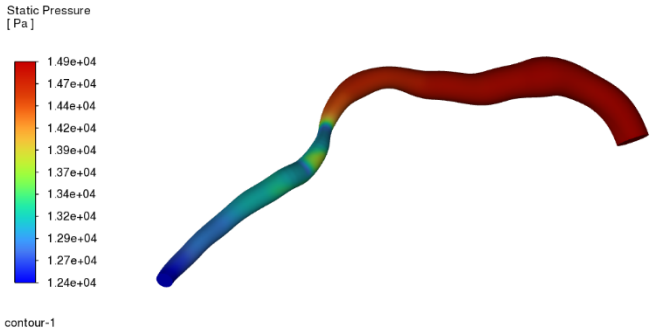

Appendix 2: Pressure Contours for the Eight Branching Reconstructions

Case 1

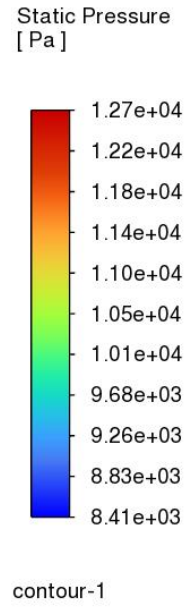

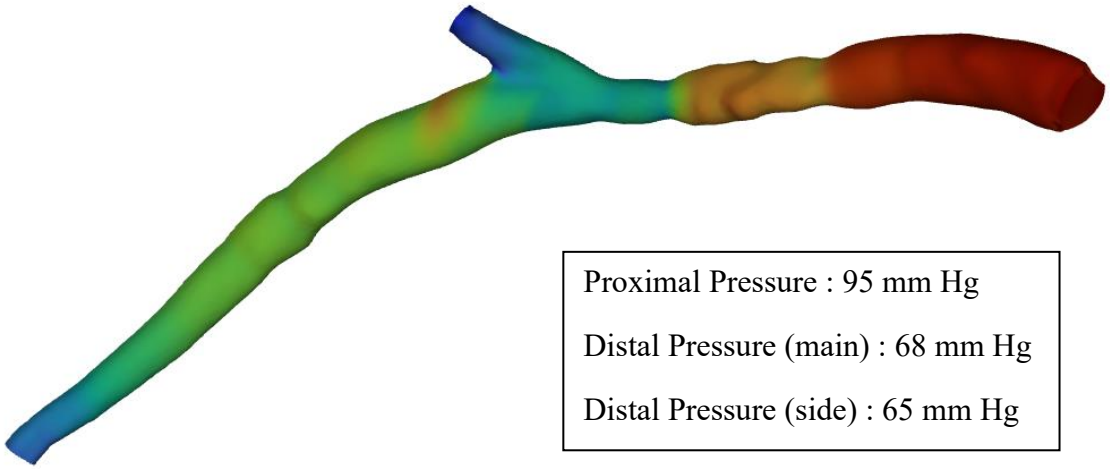

Proximal Pressure : 95 mm Hg

Distal Pressure (main) : 68 mm Hg

Distal Pressure (side) : 65 mm Hg

Case 2

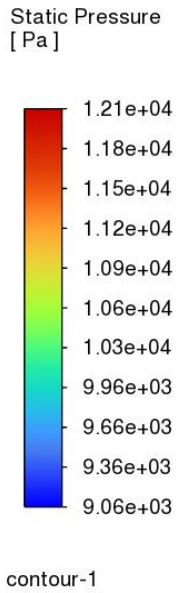

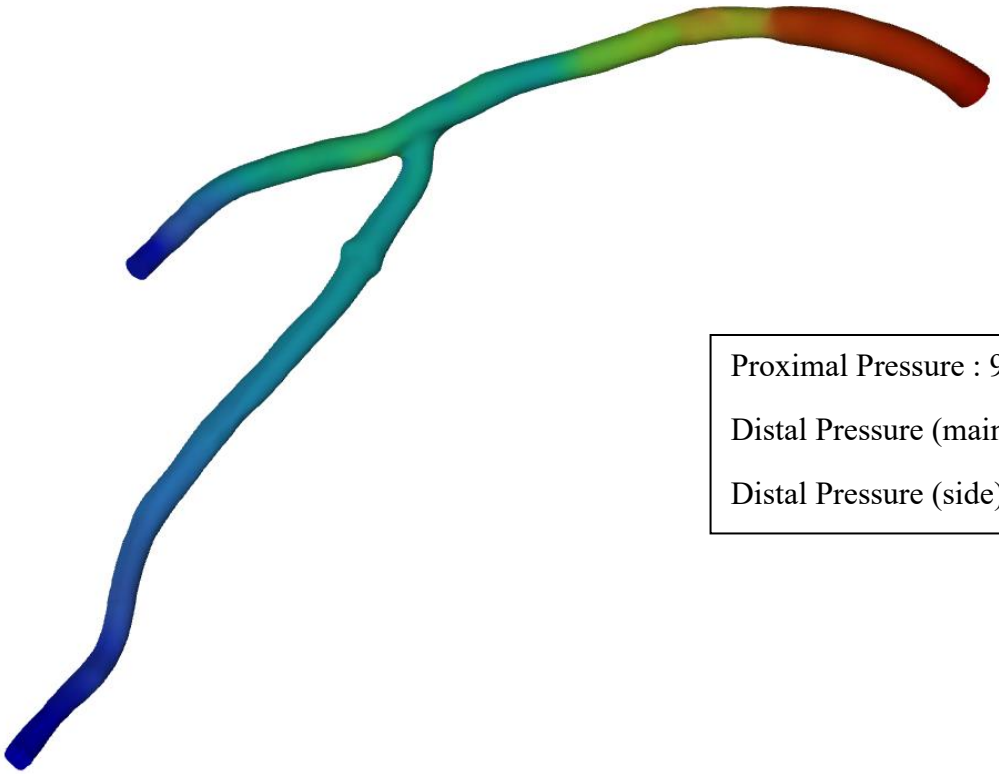

Proximal Pressure : 90.5 mm Hg

Distal Pressure (main) : 68 mm Hg

Distal Pressure (side) : 69 mm Hg

Case 3

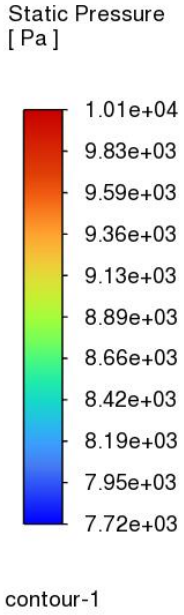

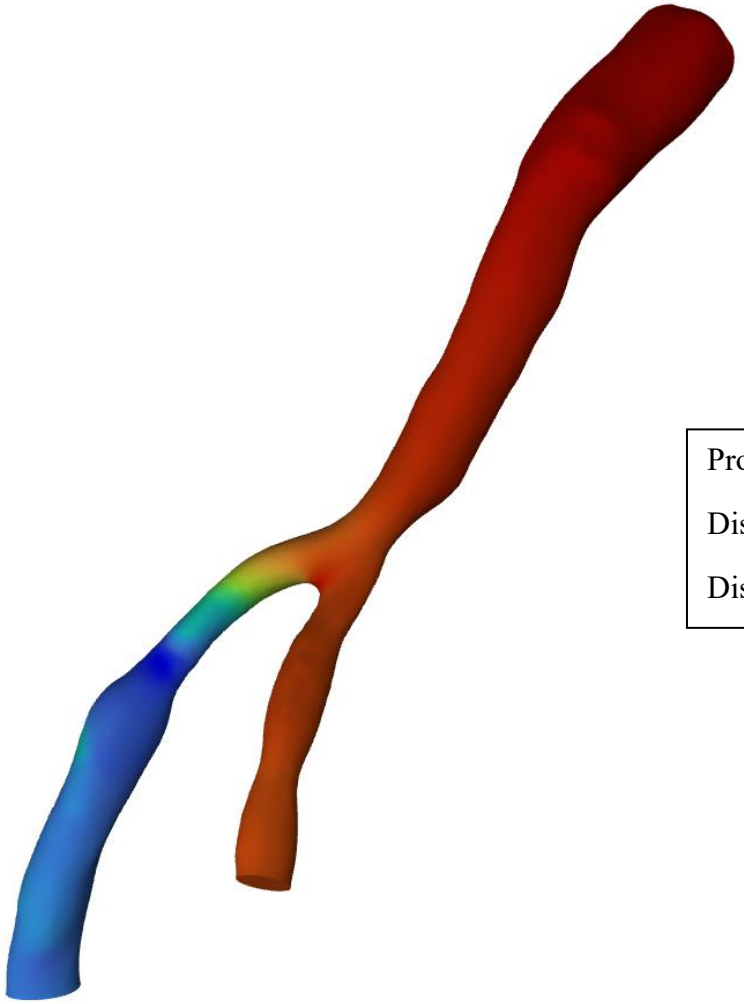

Proximal Pressure : 75.5 mm Hg

Distal Pressure (main) : 61 mm Hg

Distal Pressure (side) : 72 mm Hg

Case 4

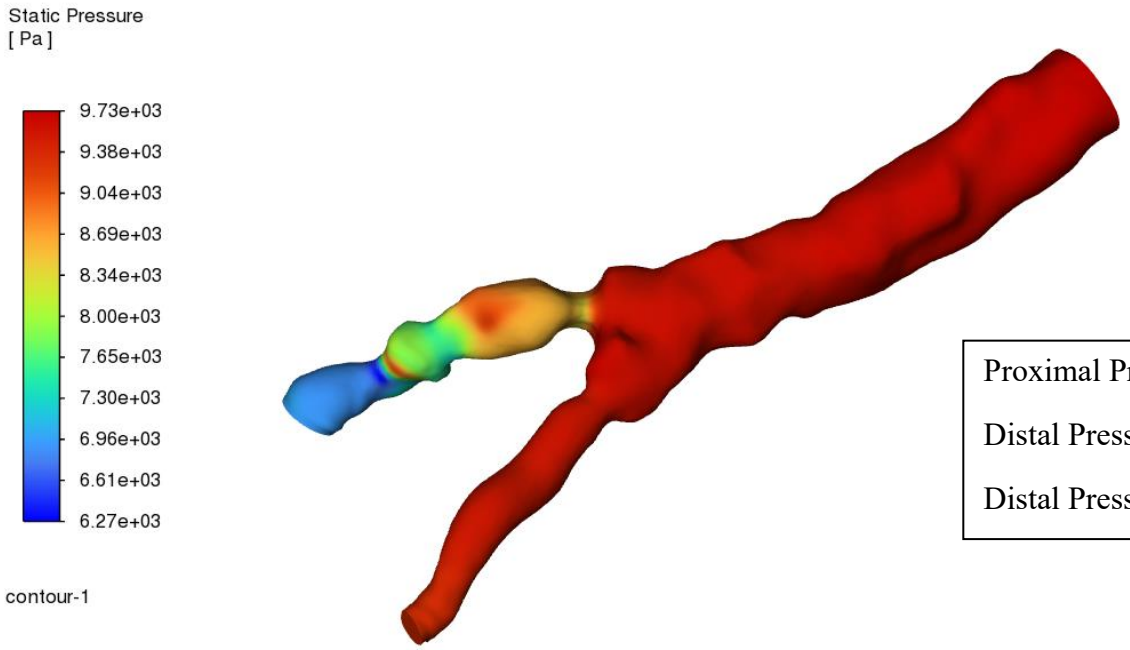

Non-converged plot

Proximal Pressure : 73 mm Hg

Distal Pressure (main) : 52 mm Hg

Distal Pressure (side) : 70 mm Hg

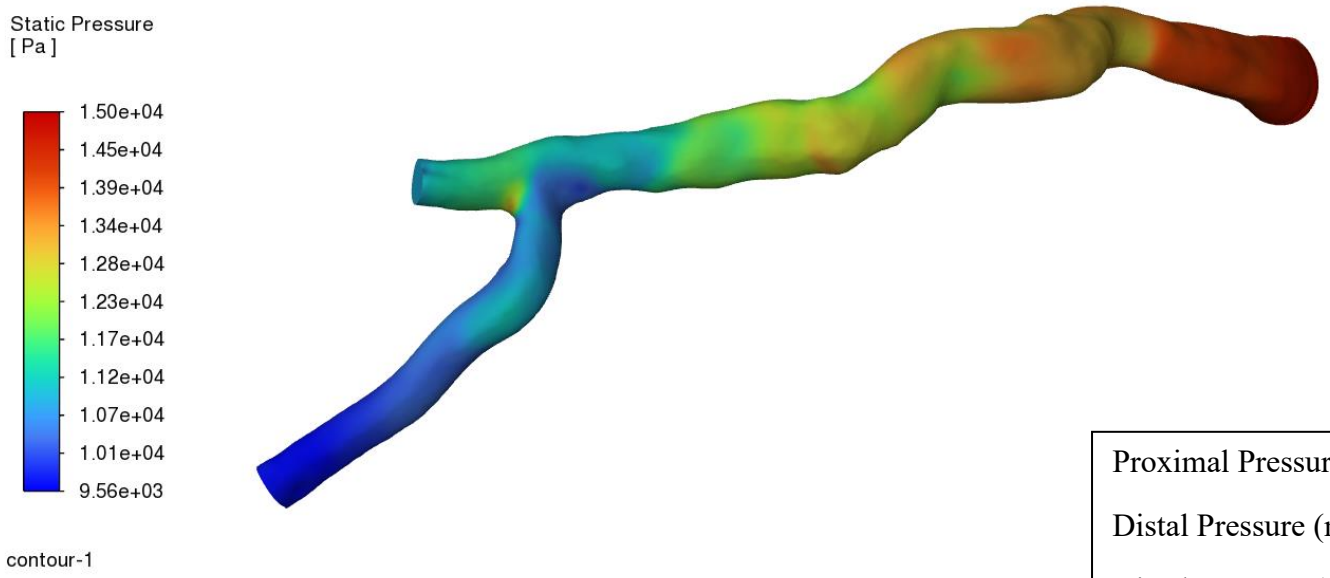

Case 5

Proximal Pressure : 112.5 mm Hg

Distal Pressure (main) : 73 mm Hg

Distal Pressure (side) : 82 mm Hg

Case 6

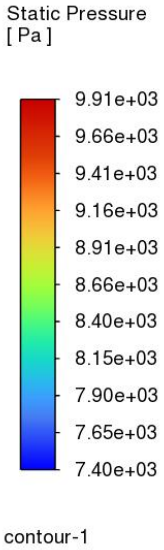

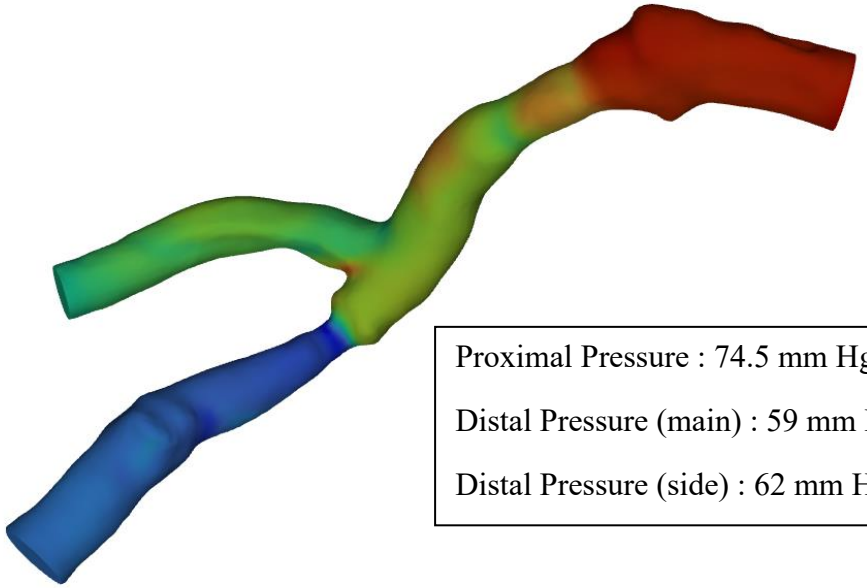

Proximal Pressure : 74.5 mm Hg

Distal Pressure (main) : 59 mm Hg

Distal Pressure (side) : 62 mm Hg

Case 7

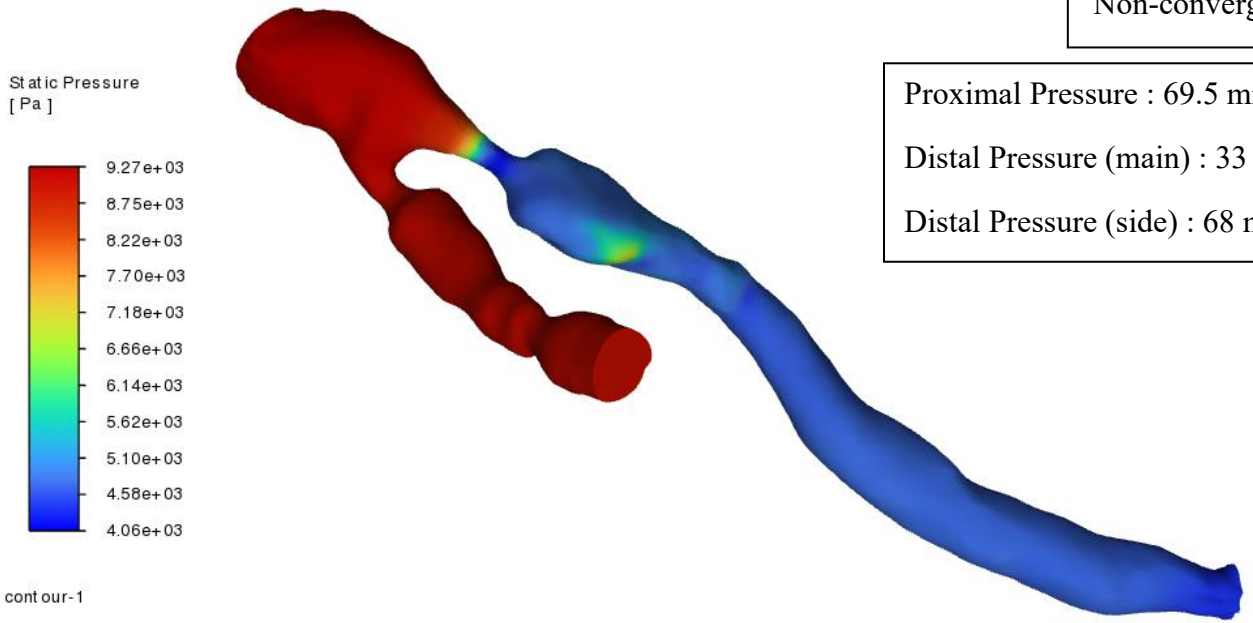

Non-converged plot

Proximal Pressure : 69.5 mm Hg

Distal Pressure (main) : 33 mm Hg

Distal Pressure (side) : 68 mm Hg

Case 8

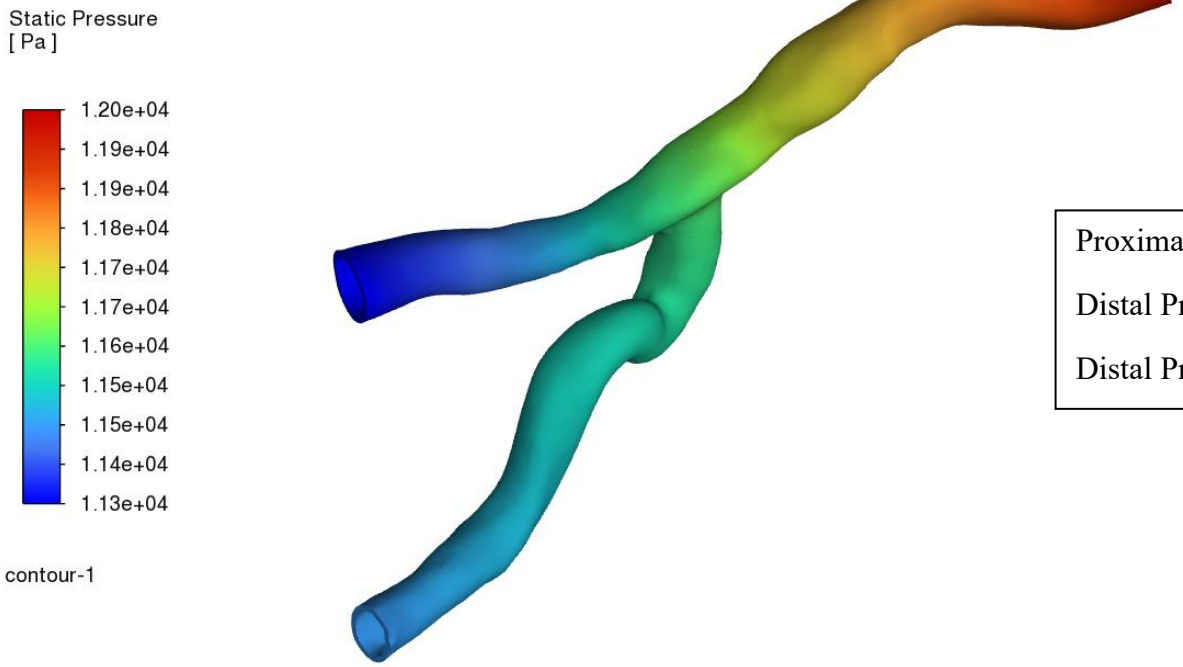

Proximal Pressure : 90 mm Hg

Distal Pressure (main) : 85 mm Hg

Distal Pressure (side) : 86 mm Hg

Bibliography

Ahadi, F., Biglari, M., Azadi, M. & Bodaghi, M. 2024. Computational fluid dynamics of coronary arteries with implanted stents: Effects of Newtonian and non-Newtonian blood flows. *Engineering Reports,* 6**,** e12779.

Alexander, Y., Osto, E., Schmidt-Trucksäss, A., Shechter, M., Trifunovic, D., Duncker, D. J., Aboyans, V., Bäck, M., Badimon, L., Cosentino, F., De Carlo, M., Dorobantu, M., Harrison, D. G., Guzik, T. J., Hoefer, I., Morris, P. D., Norata, G. D., Suades, R., Taddei, S., Vilahur, G., Waltenberger, J., Weber, C., Wilkinson, F., Bochaton-Piallat, M.-L. & Evans, P. C. 2020. Endothelial function in cardiovascular medicine: a consensus paper of the European Society of Cardiology Working Groups on Atherosclerosis and Vascular Biology, Aorta and Peripheral Vascular Diseases, Coronary Pathophysiology and Microcirculation, and Thrombosis. *Cardiovascular Research,* 117**,** 29-42.

Ali, Z. A., Karimi Galougahi, K., Mintz, G. S., Maehara, A., Shlofmitz, R. A. & Mattesini, A. 2021. Intracoronary optical coherence tomography: state of the art and future directions. *EuroIntervention,* 17**,** e105-e123.

Ali, Z. A., Landmesser, U., Maehara, A., Matsumura, M., Shlofmitz, R. A., Guagliumi, G., Price, M. J., Hill, J. M., Akasaka, T., Prati, F., Bezerra, H. G., Wijns, W., Leistner, D., Canova, P., Alfonso, F., Fabbiocchi, F., Dogan, O., Mcgreevy, R. J., Mcnutt, R. W., Nie, H., Buccola, J., West, N. E. J. & Stone, G. W. 2023. Optical Coherence Tomography–Guided versus Angiography-Guided PCI. *New England Journal of Medicine,* 389**,** 1466-1476.

Ali, Z. A., Maehara, A., Généreux, P., Shlofmitz, R. A., Fabbiocchi, F., Nazif, T. M., Guagliumi, G., Meraj, P. M., Alfonso, F., Samady, H., Akasaka, T., Carlson, E. B., Leesar, M. A., Matsumura, M., Ozan, M. O., Mintz, G. S., Ben-Yehuda, O. & Stone, G. W. 2016. Optical coherence tomography compared with intravascular ultrasound and with angiography to guide coronary stent implantation (ILUMIEN III: OPTIMIZE PCI): a randomised controlled trial. *Lancet,* 388**,** 2618-2628.

Andrikos, I. O., Sakellarios, A. I., Siogkas, P. K., Rigas, G., Exarchos, T. P., Athanasiou, L. S., Karanasos, A., Toutouzas, K., Tousoulis, D., Michalis, L. K. & Fotiadis, D. I. A novel

hybrid approach for reconstruction of coronary bifurcations using angiography and OCT. 2017 39th Annual International Conference of the IEEE Engineering in Medicine and Biology Society (EMBC), 11-15 July 2017 2017. 588-591.

Angelini, P. 1989. Normal and anomalous coronary arteries: Definitions and classification. *American Heart Journal,* 117**,** 418-434.

Antonsen, L., Thayssen, P., Maehara, A., Hansen, H. S., Junker, A., Veien, K. T., Hansen, K. N., Hougaard, M., Mintz, G. S. & Jensen, L. O. 2015. Optical Coherence Tomography Guided Percutaneous Coronary Intervention With Nobori Stent Implantation in Patients With Non–ST-Segment–Elevation Myocardial Infarction (OCTACS) Trial. *Circulation: Cardiovascular Interventions,* 8**,** e002446.

Araki, M., Park, S.-J., Dauerman, H. L., Uemura, S., Kim, J.-S., Di Mario, C., Johnson, T. W., Guagliumi, G., Kastrati, A., Joner, M., Holm, N. R., Alfonso, F., Wijns, W., Adriaenssens, T., Nef, H., Rioufol, G., Amabile, N., Souteyrand, G., Meneveau, N., Gerbaud, E., Opolski, M. P., Gonzalo, N., Tearney, G. J., Bouma, B., Aguirre, A. D., Mintz, G. S., Stone, G. W., Bourantas, C. V., Räber, L., Gili, S., Mizuno, K., Kimura, S., Shinke, T., Hong, M.-K., Jang, Y., Cho, J. M., Yan, B. P., Porto, I., Niccoli, G., Montone, R. A., Thondapu, V., Papafaklis, M. I., Michalis, L. K., Reynolds, H., Saw, J., Libby, P., Weisz, G., Iannaccone, M., Gori, T., Toutouzas, K., Yonetsu, T., Minami, Y., Takano, M., Raffel, O. C., Kurihara, O., Soeda, T., Sugiyama, T., Kim, H. O., Lee, T., Higuma, T., Nakajima, A., Yamamoto, E., Bryniarski, K. L., Di Vito, L., Vergallo, R., Fracassi, F., Russo, M., Seegers, L. M., Mcnulty, I., Park, S., Feldman, M., Escaned, J., Prati, F., Arbustini, E., Pinto, F. J., Waksman, R., Garcia-Garcia, H. M., Maehara, A., Ali, Z., Finn, A. V., Virmani, R., Kini, A. S., Daemen, J., Kume, T., Hibi, K., Tanaka, A., Akasaka, T., Kubo, T., Yasuda, S., Croce, K., Granada, J. F., Lerman, A., Prasad, A., Regar, E., Saito, Y., Sankardas, M. A., Subban, V., Weissman, N. J., Chen, Y., Yu, B., et al. 2022. Optical coherence tomography in coronary atherosclerosis assessment and intervention. *Nature Reviews Cardiology,* 19**,** 684-703.

Auricchio, F., Conti, M., Ferrazzano, C. & Sgueglia, G. A. 2014. A simple framework to generate 3D patient-specific model of coronary artery bifurcation from single-plane angiographic images. *Computers in Biology and Medicine,* 44**,** 97-109.

Avram, R., Olgin, J. E., Ahmed, Z., Verreault-Julien, L., Wan, A., Barrios, J., Abreau, S., Wan, D., Gonzalez, J. E., Tardif, J.-C., So, D. Y., Soni, K. & Tison, G. H. 2023. CathAI: fully automated coronary angiography interpretation and stenosis estimation. *npj Digital Medicine,* 6**,** 142.

Bavishi, C., Sardar, P., Chatterjee, S., Khan, A. R., Shah, A., Ather, S., Lemos, P. A., Moreno, P. & Stone, G. W. 2017. Intravascular ultrasound-guided vs angiography-guided drug-eluting stent implantation in complex coronary lesions: Meta-analysis of randomized trials. *Am Heart J,* 185**,** 26-34.

Beier, S., Ormiston, J., Webster, M., Cater, J., Norris, S., Medrano-Gracia, P., Young, A. & Cowan, B. 2016. Impact of bifurcation angle and other anatomical characteristics on blood flow – A computational study of non-stented and stented coronary arteries. *Journal of Biomechanics,* 49**,** 1570-1582.

Bhf 2025a. England Fact Sheet.

Bhf 2025b. Global Heart and Circulatory Diseases Factsheet.

Biglino, G., Capelli, C., Bruse, J., Bosi, G. M., Taylor, A. M. & Schievano, S. 2017. Computational modelling for congenital heart disease: how far are we from clinical translation? *Heart,* 103**,** 98.

Bourantas, C. V., Papafaklis, M. I., Athanasiou, L. S., Kalatzis, F. G., Naka, K. K., Siogkas, P. K., Takahashi, S., Saito, S., Fotiadis, D. I., Feldman, C. L., Stone, P. H. & Michalis, L. K. 2013. A new methodology for accurate 3-dimensional coronary artery reconstruction using routine intravascular ultrasound and angiographic data: implications for widespread assessment of endothelial shear stress in humans. *EuroIntervention,* 9**,** 582-593.

Bourantas, C. V., Papafaklis, M. I., Lakkas, L., Sakellarios, A., Onuma, Y., Zhang, Y. J., Muramatsu, T., Diletti, R., Bizopoulos, P., Kalatzis, F., Naka, K. K., Fotiadis, D. I., Wang, J., Garcia Garcia, H. M., Kimura, T., Michalis, L. K. & Serruys, P. W. 2014. Fusion of optical coherence tomographic and angiographic data for more accurate evaluation of the endothelial shear stress patterns and neointimal distribution after bioresorbable scaffold implantation:

comparison with intravascular ultrasound-derived reconstructions. *Int J Cardiovasc Imaging,* 30**,** 485-94.

Brezinski, M. E., Tearney, G. J., Bouma, B. E., Boppart, S. A., Hee, M. R., Swanson, E. A., Southern, J. F. & Fujimoto, J. G. 1996. Imaging of coronary artery microstructure (in vitro) with optical coherence tomography. *American Journal of Cardiology,* 77**,** 92-93.

Brown, B. G., Bolson, E., Frimer, M. & Dodge, H. T. 1977. Quantitative coronary arteriography: estimation of dimensions, hemodynamic resistance, and atheroma mass of coronary artery lesions using the arteriogram and digital computation. *Circulation,* 55**,** 329-337.

Bruyne, B. D., Pijls, N. H. J., Kalesan, B., Barbato, E., Tonino, P. A. L., Piroth, Z., Jagic, N., Möbius-Winkler, S., Rioufol, G., Witt, N., Kala, P., Maccarthy, P., Engström, T., Oldroyd, K. G., Mavromatis, K., Manoharan, G., Verlee, P., Frobert, O., Curzen, N., Johnson, J. B., Jüni, P. & Fearon, W. F. 2012. Fractional Flow Reserve–Guided PCI versus Medical Therapy in Stable Coronary Disease. *New England Journal of Medicine,* 367**,** 991-1001.

Candreva, A., Gallinoro, E., Van 'T Veer, M., Sonck, J., Collet, C., Di Gioia, G., Kodeboina, M., Mizukami, T., Nagumo, S., Keulards, D., Fournier, S., Pijls, N. H. J. & De Bruyne, B. 2021. Basics of Coronary Thermodilution. *JACC: Cardiovascular Interventions,* 14**,** 595-605.

Carpenter, H. J., Ghayesh, M. H., Zander, A. C., Li, J., Di Giovanni, G. & Psaltis, P. J. 2022. Automated Coronary Optical Coherence Tomography Feature Extraction with Application to Three-Dimensional Reconstruction. *Tomography,* 8**,** 1307-1349.

Carvalho, V., Rodrigues, N., Lima, R. A. & Teixeira, S. Numerical simulation of blood pulsatile flow in stenotic coronary arteries: The effect of turbulence modeling and non-Newtonian assumptions. 2020 24th International Conference on Circuits, Systems, Communications and Computers (CSCC), 2020. IEEE, 112-116.

Celeng, C., Leiner, T., Maurovich-Horvat, P., Merkely, B., De Jong, P., Dankbaar, J. W., Van Es, H. W., Ghoshhajra, B. B., Hoffmann, U. & Takx, R. A. P. 2019. Anatomical and Functional

Computed Tomography for Diagnosing Hemodynamically Significant Coronary Artery Disease: A Meta-Analysis. *JACC: Cardiovascular Imaging,* 12**,** 1316-1325.

Cervantes-Sanchez, F., Cruz-Aceves, I., Hernandez-Aguirre, A., Hernandez-Gonzalez, M. A. & Solorio-Meza, S. E. 2019. Automatic Segmentation of Coronary Arteries in X-ray Angiograms using Multiscale Analysis and Artificial Neural Networks. *Applied Sciences,* 9**,** 5507.

Chahour, K., Aboulaich, R., Habbal, A., Zemzemi, N. & Abdelkhirane, C. 2020. Virtual FFR Quantified with a Generalized Flow Model Using Windkessel Boundary Conditions. *Computational and Mathematical Methods in Medicine,* 2020**,** 3942152.

Chaichana, T., Sun, Z. & Jewkes, J. 2012. Computational fluid dynamics analysis of the effect of plaques in the left coronary artery. *Computational and mathematical methods in medicine,* 2012**,** 504367.

Chamié, D., Costa, J. R., Damiani, L. P., Siqueira, D., Braga, S., Costa, R., Seligman, H., Brito, F., Barreto, G., Staico, R., Feres, F., Petraco, R. & Abizaid, A. 2021. Optical Coherence Tomography Versus Intravascular Ultrasound and Angiography to Guide Percutaneous Coronary Interventions. *Circulation: Cardiovascular Interventions,* 14**,** e009452.

Chatzizisis, Y. S., Giannoglou, G. D., Parcharidis, G. E. & Louridas, G. E. 2007. Is left coronary system more susceptible to atherosclerosis than right?: A pathophysiological insight. *International Journal of Cardiology,* 116**,** 7-13.

Chiastra, C., Migliori, S., Burzotta, F., Dubini, G. & Migliavacca, F. 2018. Patient-Specific Modeling of Stented Coronary Arteries Reconstructed from Optical Coherence Tomography: Towards a Widespread Clinical Use of Fluid Dynamics Analyses. *J Cardiovasc Transl Res,* 11**,** 156-172.

Collet, C., Grundeken, M. J., Asano, T., Onuma, Y., Wijns, W. & Serruys, P. W. 2017. State of the art: coronary angiography. *EuroIntervention,* 13**,** 634-643.

Costa, M. 2024. *Statistical shape modelling of patient-specific coronary arteries.* Politecnico di Torino.

Crowhurst, J. A., Whitby, M., Thiele, D., Halligan, T., Westerink, A., Crown, S. & Milne, J. 2014. Radiation dose in coronary angiography and intervention: initial results from the establishment of a multi-centre diagnostic reference level in Queensland public hospitals. *Journal of Medical Radiation Sciences,* 61**,** 135-141.

Csippa, B., Sándor, L. & Paál, G. 2021. Decomposition of Velocity Field Along a Centerline Curve Using Frenet-Frames: Application to Arterial Blood Flow Simulations. *Periodica Polytechnica Mechanical Engineering,* 65**,** 374-384.

Cuisset, T., Quilici, J. & Cayla, G. 2013. Qu'est-ce que la FFR? Comment l'utiliser? *Réalités Cardiologiques*.

Curzen, N., Nicholas, Z., Stuart, B., Wilding, S., Hill, K., Shambrook, J., Eminton, Z., Ball, D., Barrett, C., Johnson, L., Nuttall, J., Fox, K., Connolly, D., O'kane, P., Hobson, A., Chauhan, A., Uren, N., Mccann, G., Berry, C., Carter, J., Roobottom, C., Mamas, M., Rajani, R., Ford, I., Douglas, P., Hlatky, M. & Investigators, o. B. o. t. F. 2021. Fractional flow reserve derived from computed tomography coronary angiography in the assessment and management of stable chest pain: the FORECAST randomized trial. *European Heart Journal,* 42**,** 3844-3852.

Daubert, M. A., Tailor, T., James, O., Shaw, L. J., Douglas, P. S. & Koweek, L. 2021. Multimodality cardiac imaging in the 21st century: evolution, advances and future opportunities for innovation. *Br J Radiol,* 94**,** 20200780.

Davies, J. E., Sen, S., Dehbi, H.-M., Al-Lamee, R., Petraco, R., Nijjer, S. S., Bhindi, R., Lehman, S. J., Walters, D., Sapontis, J., Janssens, L., Vrints, C. J., Khashaba, A., Laine, M., Belle, E. V., Krackhardt, F., Bojara, W., Going, O., Härle, T., Indolfi, C., Niccoli, G., Ribichini, F., Tanaka, N., Yokoi, H., Takashima, H., Kikuta, Y., Erglis, A., Vinhas, H., Silva, P. C., Baptista, S. B., Alghamdi, A., Hellig, F., Koo, B.-K., Nam, C.-W., Shin, E.-S., Doh, J.-H., Brugaletta, S., Alegria-Barrero, E., Meuwissen, M., Piek, J. J., Royen, N. v., Sezer, M., Mario, C. D., Gerber, R. T., Malik, I. S., Sharp, A. S. P., Talwar, S., Tang, K., Samady, H., Altman, J., Seto, A. H., Singh, J., Jeremias, A., Matsuo, H., Kharbanda, R. K., Patel, M. R., Serruys, P. & Escaned, J. 2017. Use of the Instantaneous Wave-free Ratio or Fractional Flow Reserve in PCI. *New England Journal of Medicine,* 376**,** 1824-1834.

Davies, P. F. 2009. Hemodynamic shear stress and the endothelium in cardiovascular pathophysiology. *Nat Clin Pract Cardiovasc Med,* 6**,** 16-26.

De Bruyne, B., Bartunek, J., Sys, S. U. & Heyndrickx, G. R. 1995. Relation between myocardial fractional flow reserve calculated from coronary pressure measurements and exercise-induced myocardial ischemia. *Circulation,* 92**,** 39-46.

De Bruyne, B., Pijls, N. H., Kalesan, B., Barbato, E., Tonino, P. A., Piroth, Z., Jagic, N., Möbius-Winkler, S., Rioufol, G., Witt, N., Kala, P., Maccarthy, P., Engström, T., Oldroyd, K. G., Mavromatis, K., Manoharan, G., Verlee, P., Frobert, O., Curzen, N., Johnson, J. B., Jüni, P. & Fearon, W. F. 2012. Fractional flow reserve-guided PCI versus medical therapy in stable coronary disease. *N Engl J Med,* 367**,** 991-1001.

De Oliveira Miranda, A. C., Lira, W. W. M., Marques, R. C., Pereira, A. M. B., Cavalcante-Neto, J. B. & Martha, L. F. 2015. Finite element mesh generation for subsurface simulation models. *Engineering with Computers,* 31**,** 305-324.

Devos, A. N., Reifart, J., Valenzuela, T. F., Cangemi, S. & Iaizzo, P. A. 2024. Percutaneous Coronary Intervention: Devices, Research, and Clinical Implications. *In:* IAIZZO, P. A. (ed.) *Handbook of Cardiac Anatomy, Physiology, and Devices.* Cham: Springer Nature Switzerland.

Eftekhari, A., Holck, E. N., Westra, J., Olsen, N. T., Bruun, N. H., Jensen, L. O., Engstrøm, T. & Christiansen, E. H. 2023. Instantaneous wave free ratio vs. fractional flow reserve and 5-year mortality: iFR SWEDEHEART and DEFINE FLAIR. *European Heart Journal,* 44**,** 4376-4384.

Elgendy, I. Y., Mahmoud, A. N., Elgendy, A. Y. & Bavry, A. A. 2016. Outcomes with intravascular ultrasound-guided stent implantation: a meta-analysis of randomized trials in the era of drug-eluting stents. *Circulation: Cardiovascular Interventions,* 9**,** e003700.

Elgendy, I. Y., Mahmoud, A. N., Elgendy, A. Y. & Mintz, G. S. 2019. Intravascular Ultrasound-Guidance Is Associated With Lower Cardiovascular Mortality and Myocardial Infarction for Drug-Eluting Stent Implantation ―Insights From an Updated Meta-Analysis of Randomized Trials―. *Circulation Journal,* 83**,** 1410-1413.

Ellwein, L. M., Otake, H., Gundert, T. J., Koo, B.-K., Shinke, T., Honda, Y., Shite, J. & Ladisa, J. F. 2011. Optical Coherence Tomography for Patient-specific 3D Artery Reconstruction and Evaluation of Wall Shear Stress in a Left Circumflex Coronary Artery. *Cardiovascular Engineering and Technology,* 2**,** 212-227.

Equbal, A. & Kalita, P. 2024. Numerical assessment of using various outlet boundary conditions on the hemodynamics of an idealized left coronary artery model. *Biomedical Physics & Engineering Express,* 10.

Everaars, H., De Waard, G. A., Schumacher, S. P., Zimmermann, F. M., Bom, M. J., Van De Ven, P. M., Raijmakers, P. G., Lammertsma, A. A., Götte, M. J., Van Rossum, A. C., Kurata, A., Marques, K. M. J., Pijls, N. H. J., Van Royen, N. & Knaapen, P. 2019. Continuous thermodilution to assess absolute flow and microvascular resistance: validation in humans using [15O]H2O positron emission tomography. *European Heart Journal,* 40**,** 2350-2359.

Fallavollita, P. & Cheriet, F. 2008. Optimal 3D reconstruction of coronary arteries for 3D clinical assessment. *Computerized Medical Imaging and Graphics,* 32**,** 476-487.

Fearon, W. F., Achenbach, S., Engstrom, T., Assali, A., Shlofmitz, R., Jeremias, A., Fournier, S., Kirtane, A. J., Kornowski, R. & Greenberg, G. 2019. Accuracy of fractional flow reserve derived from coronary angiography. *Circulation,* 139**,** 477-484.

Flohr, T., Schmidt, B., Ulzheimer, S. & Alkadhi, H. 2023. Cardiac imaging with photon counting CT. *British Journal of Radiology,* 96.

Frangi, A. F., Niessen, W. J., Vincken, K. L. & Viergever, M. A. Multiscale vessel enhancement filtering. Medical image computing and computer-assisted intervention—MICCAI'98: first international conference cambridge, MA, USA, october 11–13, 1998 proceedings 1, 1998. Springer, 130-137.

Frenet, F. 1852. Sur les courbes à double courbure. *Journal de Mathématiques Pures et Appliquées*

Frison, M. 2018a. *Effective Computational Coronary Haemodynamics for Clinical Application.* Doctor of Philosophy, The University of Sheffield.

Frison, M. 2018b. *Effective Computational Coronary Haemodynamics for Clinical Application.* PhD, University of Sheffield.

Galassi, F., Alkhalil, M., Lee, R., Martindale, P., Kharbanda, R. K., Channon, K. M., Grau, V. & Choudhury, R. P. 2018. 3D reconstruction of coronary arteries from 2D angiographic projections using non-uniform rational basis splines (NURBS) for accurate modelling of coronary stenoses. *PLOS ONE,* 13**,** e0190650.

Galbraith, J. E., Murphy, M. L. & De Soyza, N. 1978a. Coronary angiogram interpretation. Interobserver variability. *JAMA,* 240**,** 2053-6.

Galbraith, J. E., Murphy, M. L. & De Soyza, N. 1978b. Coronary Angiogram Interpretation: Interobserver Variability. *JAMA,* 240**,** 2053-2056.

Gamage, P. T., Dong, P., Lee, J., Gharaibeh, Y., Zimin, V. N., Bezerra, H. G., Wilson, D. L. & Gu, L. 2022. Fractional Flow Reserve (FFR) Estimation from OCT-Based CFD Simulations: Role of Side Branches. *Applied Sciences,* 12**,** 5573.

Garrone, P. B.-Z., Giuseppe Salvetti, Ilaria Sina, Noemi Sheiban, Imad Stella, Peter R. Agostoni, Pierfrancesco 2009. Quantitative Coronary Angiography in the Current Era: Principles and Applications. *Journal of Interventional Cardiology,* 22**,** 527-536.

Gaudio, L. T., Caruso, M. V., Rosa, S. D., Indolfi, C. & Fragomeni, G. Different Blood Flow Models in Coronary Artery Diseases: Effects on hemodynamic parameters. 2018 40th Annual International Conference of the IEEE Engineering in Medicine and Biology Society (EMBC), 18-21 July 2018 2018. 3185-3188.

Gessat, M., Altwegg, L., Frauenfelder, T., Plass, A. & Falk, V. 2011. Cubic Hermite Bezier spline based reconstruction of implanted aortic valve stents from CT images. *Annu Int Conf IEEE Eng Med Biol Soc,* 2011**,** 2667-70.

Ghobrial, M. 2021. *How Will Virtual (Computed) Fractional Flow Reserve (FFR) Impact the Management of Patients with Chronic Coronary Syndromes? The VIRTU-4 CCS Trial.* Doctor of Medicine, The University of Sheffield.

Ghobrial, M., Haley, H. A., Gosling, R., Rammohan, V., Lawford, P. V., Hose, D. R., Gunn, J. P. & Morris, P. D. 2021. The new role of diagnostic angiography in coronary physiological assessment. *Heart,* 107**,** 783.

Gosling, R. C., Sturdy, J., Morris, P. D., Fossan, F. E., Hellevik, L. R., Lawford, P., Hose, D. R. & Gunn, J. 2020. Effect of side branch flow upon physiological indices in coronary artery disease. *Journal of Biomechanics,* 103**,** 109698.

Götberg, M., Christiansen, E. H., Gudmundsdottir, I. J., Sandhall, L., Danielewicz, M., Jakobsen, L., Olsson, S.-E., Öhagen, P., Olsson, H., Omerovic, E., Calais, F., Lindroos, P., Maeng, M., Tödt, T., Venetsanos, D., James, S. K., Kåregren, A., Nilsson, M., Carlsson, J., Hauer, D., Jensen, J., Karlsson, A.-C., Panayi, G., Erlinge, D. & Fröbert, O. 2017. Instantaneous Wave-free Ratio versus Fractional Flow Reserve to Guide PCI. *New England Journal of Medicine,* 376**,** 1813-1823.

Green, N. E., Chen, S.-Y. J., Hansgen, A. R., Messenger, J. C., Groves, B. M. & Carroll, J. D. 2005a. Angiographic views used for percutaneous coronary interventions: A three-dimensional analysis of physician-determined vs. computer-generated views. *Catheterization and Cardiovascular Interventions,* 64**,** 451-459.

Green, N. E., Chen, S. Y. J., Hansgen, A. R., Messenger, J. C., Groves, B. M. & Carroll, J. D. 2005b. Angiographic views used for percutaneous coronary interventions: A three-dimensional analysis of physician-determined vs. computer-generated views. *Catheterization and Cardiovascular Interventions,* 64**,** 451-459.

Greulich, S. & Sechtem, U. 2015. Multimodality imaging in coronary artery disease – "The more the better?". *Cor et Vasa,* 57**,** e462-e469.

Gunn, J. & Morris, P. D. 2022. Revascularisation for the proximal left anterior descending artery: special case or part of the package? *Heart,* 108**,** 1754.

Guo, J., Sun, L., Chen, Y.-D., Tian, F., Liu, H.-B., Chen, L., Sun, Z.-J., Ren, Y.-H., Jin, Q.-H., Liu, C.-F., Han, B.-S., Gai, L.-Y. & Yang, T.-S. 2012. [Ex vivo assessment of coronary lesions

by optical coherence tomography and intravascular ultrasound in comparison with histology results]. *Zhonghua xin xue guan bing za zhi,* 40**,** 302-306.

Haft-Javaherian, M., Villiger, M., Otsuka, K., Daemen, J., Libby, P., Golland, P. & Bouma, B. E. 2024. Segmentation of anatomical layers and imaging artifacts in intravascular polarization sensitive optical coherence tomography using attending physician and boundary cardinality losses. *Biomedical Optics Express,* 15**,** 1719-1738.

Hebsgaard, L., Nielsen, T. M., Tu, S., Krusell, L. R., Maeng, M., Veien, K. T., Raungaard, B., Terkelsen, C. J., Kaltoft, A., Reiber, J. H., Lassen, J. F., Christiansen, E. H. & Holm, N. R. 2015. Co-registration of optical coherence tomography and X-ray angiography in percutaneous coronary intervention. the Does Optical Coherence Tomography Optimize Revascularization (DOCTOR) fusion study. *Int J Cardiol,* 182**,** 272-8.

Holm, N. R., Andreasen, L. N., Neghabat, O., Laanmets, P., Kumsars, I., Bennett, J., Olsen, N. T., Odenstedt, J., Hoffmann, P., Dens, J., Chowdhary, S., O'kane, P., Rasmussen, S.-H. B., Heigert, M., Havndrup, O., Kuijk, J. P. V., Biscaglia, S., Mogensen, L. J. H., Henareh, L., Burzotta, F., Eek, C. H., Mylotte, D., Llinas, M. S., Koltowski, L., Knaapen, P., Calic, S., Witt, N., Santos-Pardo, I., Watkins, S., Lønborg, J., Kristensen, A. T., Jensen, L. O., Calais, F., Cockburn, J., Mcneice, A., Kajander, O. A., Heestermans, T., Kische, S., Eftekhari, A., Spratt, J. C. & Christiansen, E. H. 2023. OCT or Angiography Guidance for PCI in Complex Bifurcation Lesions. *New England Journal of Medicine,* 389**,** 1477-1487.

Hong, S.-J., Mintz, G. S., Ahn, C.-M., Kim, J.-S., Kim, B.-K., Ko, Y.-G., Kang, T.-S., Kang, W.-C., Kim, Y. H., Hur, S.-H., Hong, B.-K., Choi, D., Kwon, H., Jang, Y. & Hong, M.-K. 2020. Effect of Intravascular Ultrasound–Guided Drug-Eluting Stent Implantation: 5-Year Follow-Up of the IVUS-XPL Randomized Trial. *JACC: Cardiovascular Interventions,* 13**,** 62-71.

Hong, S. J., Kim, B. K., Shin, D. H., Nam, C. M., Kim, J. S., Ko, Y. G., Choi, D., Kang, T. S., Kang, W. C., Her, A. Y., Kim, Y. H., Hur, S. H., Hong, B. K., Kwon, H., Jang, Y. & Hong, M. K. 2015. Effect of Intravascular Ultrasound-Guided vs Angiography-Guided Everolimus-Eluting Stent Implantation: The IVUS-XPL Randomized Clinical Trial. *Jama,* 314**,** 2155-63.

Huang, B., Zhang, S., Wu, P., Liu, X., Yu, W., Li, Y. & Tu, S. Segmentation of side branch regions in intravascular images using multi-modal information. *In:* BYRAM, B. C. & RUITER, N. V., eds. Medical Imaging 2021: Ultrasonic Imaging and Tomography, February 01, 2021 2021. 1160214.

Huang, D., Swanson, E. A., Lin, C. P., Schuman, J. S., Stinson, W. G., Chang, W., Hee, M. R., Flotte, T., Gregory, K., Puliafito, C. A. & Fujimoto, J. G. 1991. Optical Coherence Tomography. *Science,* 254**,** 1178-1181.

Ishibashi, Y., Grundeken, M. J., Nakatani, S., Iqbal, J., Morel, M. A., Genereux, P., Girasis, C., Wentzel, J. J., Garcia-Garcia, H. M., Onuma, Y. & Serruys, P. W. 2015. In Vitro Validation and Comparison of Different Software Packages or Algorithms for Coronary Bifurcation Analysis Using Calibrated Phantoms: Implications for Clinical Practice and Research of Bifurcation Stenting. *Catheterization and Cardiovascular Interventions,* 85**,** 554-563.

Jerman, T., Pernus, F., Likar, B. & Špiclin, Ž. Beyond Frangi: an improved multiscale vesselness filter. Medical Imaging, 2015.

Jiménez, J. J., Segura, R. J. & Feito, F. R. 2010. A robust segment/triangle intersection algorithm for interference tests. Efficiency study. *Computational Geometry,* 43**,** 474-492.

John Lampignano, L. E. K. 2017. *Bontrager's Textbook of Radiographic Positioning and Related Anatomy,* St. Louis, Missouri, Elsevier.

Johnston, B. M., Johnston, P. R., Corney, S. & Kilpatrick, D. 2006. Non-Newtonian blood flow in human right coronary arteries: Transient simulations. *Journal of Biomechanics,* 39**,** 1116-1128.

Jones, D. A., Rathod, K. S., Koganti, S., Hamshere, S., Astroulakis, Z., Lim, P., Sirker, A., O'mahony, C., Jain, A. K., Knight, C. J., Dalby, M. C., Malik, I. S., Mathur, A., Rakhit, R., Lockie, T., Redwood, S., Maccarthy, P. A., Desilva, R., Weerackody, R., Wragg, A., Smith, E. J. & Bourantas, C. V. 2018. Angiography Alone Versus Angiography Plus Optical Coherence Tomography to Guide Percutaneous Coronary Intervention: Outcomes From the Pan-London PCI Cohort. *JACC: Cardiovascular Interventions,* 11**,** 1313-1321.

Karanasos, A., Li, Y., Tu, S., Wentzel, J. J., Reiber, J. H., Van Geuns, R. J. & Regar, E. 2015. Is it safe to implant bioresorbable scaffolds in ostial side-branch lesions? Impact of 'neo-carina' formation on main-branch flow pattern. Longitudinal clinical observations. *Atherosclerosis,* 238**,** 22-5.

Kim, H. Y., Doh, J. H., Lim, H. S., Nam, C. W., Shin, E. S., Koo, B. K., Lee, J. M., Park, T. K., Yang, J. H., Song, Y. B., Hahn, J. Y., Choi, S. H., Gwon, H. C., Lee, S. H., Kim, S. M., Choe, Y. & Choi, J. H. 2017. Identification of Coronary Artery Side Branch Supplying Myocardial Mass That May Benefit From Revascularization. *JACC Cardiovasc Interv,* 10**,** 571-581.

Kim, I.-C., Nam, C.-W., Cho, Y.-K., Park, H.-S., Yoon, H.-J., Kim, H., Chung, I.-S., Han, S., Hur, S.-H., Kim, Y.-N. & Kim, K.-B. 2016. Discrepancy between frequency domain optical coherence tomography and intravascular ultrasound in human coronary arteries and in a phantom in vitro coronary model. *International Journal of Cardiology,* 221**,** 860-866.

Koyama, K., Fujino, A., Maehara, A., Yamamoto, M. H., Alexandru, D., Jennings, J., Krug, P., Santiago, L. M., Murray, M., Bongiovanni, L., Lee, T., Kim, S. Y., Wang, X., Lin, Y., Matsumura, M., Ali, Z. A., Sosa, F., Haag, E., Mintz, G. S. & Shlofmitz, R. A. 2019. A prospective, single-center, randomized study to assess whether automated coregistration of optical coherence tomography with angiography can reduce geographic miss. *Catheter Cardiovasc Interv,* 93**,** 411-418.

Krams, R., Wentzel, J. J., Oomen, J. A., Vinke, R., Schuurbiers, J. C., De Feyter, P. J., Serruys, P. W. & Slager, C. J. 1997. Evaluation of endothelial shear stress and 3D geometry as factors determining the development of atherosclerosis and remodeling in human coronary arteries in vivo. Combining 3D reconstruction from angiography and IVUS (ANGUS) with computational fluid dynamics. *Arterioscler Thromb Vasc Biol,* 17**,** 2061-5.

Krishnamurthy, A., Gonzales, M. J., Sturgeon, G., Segars, W. P. & Mcculloch, A. D. 2016. Biomechanics simulations using cubic Hermite meshes with extraordinary nodes for isogeometric cardiac modeling. *Computer Aided Geometric Design,* 43**,** 27-38.

Kubo, T., Akasaka, T., Shite, J., Suzuki, T., Uemura, S., Yu, B., Kozuma, K., Kitabata, H., Shinke, T., Habara, M., Saito, Y., Hou, J., Suzuki, N. & Zhang, S. 2013. OCT Compared With IVUS in a Coronary Lesion Assessment: The OPUS-CLASS Study. *JACC: Cardiovascular Imaging,* 6**,** 1095-1104.

Kubo, T., Ino, Y., Shiono, Y., Terada, K., Emori, H., Higashioka, D., Takahata, M., Wada, T., Shimamura, K., Khalifa, A. K. M., Tu, S. & Akasaka, T. 2021. Usefulness of optical coherence tomography with angiographic coregistration in the guidance of coronary stent implantation. *Heart Vessels*.

Kuno, T., Kiyohara, Y., Maehara, A., Ueyama, H. A., Kampaktsis, P. N., Takagi, H., Mehran, R., Stone, G. W., Bhatt, D. L., Mintz, G. S. & Bangalore, S. 2023. Comparison of Intravascular Imaging, Functional, or Angiographically Guided Coronary Intervention. *Journal of the American College of Cardiology,* 82**,** 2167-2176.

Kwak, B. R., Bäck, M., Bochaton-Piallat, M. L., Caligiuri, G., Daemen, M. J., Davies, P. F., Hoefer, I. E., Holvoet, P., Jo, H., Krams, R., Lehoux, S., Monaco, C., Steffens, S., Virmani, R., Weber, C., Wentzel, J. J. & Evans, P. C. 2014. Biomechanical factors in atherosclerosis: mechanisms and clinical implications. *Eur Heart J,* 35**,** 3013-20, 3020a-3020d.

Lee, J. M., Choi, K. H., Song, Y. B., Lee, J.-Y., Lee, S.-J., Lee, S. Y., Kim, S. M., Yun, K. H., Cho, J. Y., Kim, C. J., Ahn, H.-S., Nam, C.-W., Yoon, H.-J., Park, Y. H., Lee, W. S., Jeong, J.-O., Song, P. S., Doh, J.-H., Jo, S.-H., Yoon, C.-H., Kang, M. G., Koh, J.-S., Lee, K. Y., Lim, Y.-H., Cho, Y.-H., Cho, J.-M., Jang, W. J., Chun, K.-J., Hong, D., Park, T. K., Yang, J. H., Choi, S.-H., Gwon, H.-C. & Hahn, J.-Y. 2023. Intravascular Imaging–Guided or Angiography-Guided Complex PCI. *New England Journal of Medicine,* 388**,** 1668-1679.

Lefevre, T. L., Yves Morice, Marie-Claude, Loubeyre, Christophe Piechaud, Jean-Francois Dumas, Pierre 2001. Stenting of Bifurcation Lesions: A Rational Approach. *Journal of Interventional Cardiology,* 14**,** 573-585.

Li, Y., Gutiérrez-Chico, J. L., Holm, N. R., Yang, W., Hebsgaard, L., Christiansen, E. H., Mæng, M., Lassen, J. F., Yan, F., Reiber, J. H. C. & Tu, S. 2015. Impact of Side Branch Modeling on Computation of Endothelial Shear Stress in Coronary Artery Disease: Coronary

Tree Reconstruction by Fusion of 3D Angiography and OCT. *Journal of the American College of Cardiology,* 66**,** 125-135.

Li, Y., Nagoshi, R., Kozuki, A., Kijima, Y., Han, Y. & Shite, J. 2024. Three-dimensional optical coherence tomography for guidance of percutaneous coronary intervention for coronary bifurcation disease: a review of current clinical applications. *Cardiovascular Diagnosis and Therapy,* 14**,** 949.

Liu, C.-C., Tang, Q., Cai, L., Yu, Z. & Zhou, J. 2023. *Automated right coronary artery localizer using deep learning for optimal cardiac phase selection*, SPIE.

Lo, S. H. 1995. Automatic mesh generation over intersecting surfaces. *International Journal for Numerical Methods in Engineering,* 38**,** 943-954.

Lodi Rizzini, M., Gallo, D., De Nisco, G., D'ascenzo, F., Chiastra, C., Bocchino, P. P., Piroli, F., De Ferrari, G. M. & Morbiducci, U. 2020. Does the inflow velocity profile influence physiologically relevant flow patterns in computational hemodynamic models of left anterior descending coronary artery? *Medical Engineering & Physics,* 82**,** 58-69.

Lyu, C., Hu, G. & Wang, D. 2020. HRED-Net: High-Resolution Encoder-Decoder Network for Fine-Grained Image Segmentation. *IEEE Access,* 8**,** 38210-38220.

Malota, Z., Glowacki, J., Sadowski, W. & Kostur, M. 2018. Numerical analysis of the impact of flow rate, heart rate, vessel geometry, and degree of stenosis on coronary hemodynamic indices. *BMC Cardiovascular Disorders,* 18**,** 132.

Mamas A, M. 2023. National Audit Presentation BCIS. Britsh Cardiovascular Intervention Society.

Marcinnó, F., Hinz, J., Buffa, A. & Deparis, S. 2025. A spline-based hexahedral mesh generator for patient-specific coronary arteries. *arXiv preprint arXiv:2501.12965*.

Marin, F., Fawaz, S., Kotronias, R. A., Chai, J., Chu, M., Karamasis, G. V., Cook, C. M., Khan, S., Davies, J. R., Channon, K., Banning, A. P., Keeble, T. R. & De Maria, G. L. 2024.

Development and validation of a novel angiography-derived index of absolute coronary blood flow and resistance. *The International Journal of Cardiovascular Imaging,* 40**,** 2103-2115.

Masdjedi, K., Tanaka, N., Van Belle, E., Porouchani, S., Linke, A., Woitek, F. J., Bartorelli, A. L., Ali, Z. A., Den Dekker, W. K., Wilschut, J., Diletti, R., Zijlstra, F., Boersma, E., Van Mieghem, N. M., Spitzer, E. & Daemen, J. 2022. Vessel fractional flow reserve (vFFR) for the assessment of stenosis severity: the FAST II study. *EuroIntervention,* 17**,** 1498-1505.

Masdjedi, K., Van Zandvoort, L. J., Balbi, M. M., Gijsen, F. J., Ligthart, J. M., Rutten, M. C., Lemmert, M. E., Wilschut, J. M., Diletti, R. & De Jaegere, P. 2020. Validation of a three-dimensional quantitative coronary angiography-based software to calculate fractional flow reserve: the FAST study. *EuroIntervention: journal of EuroPCR in collaboration with the Working Group on Interventional Cardiology of the European Society of Cardiology,* 16**,** 591-599.

Medrano-Gracia, P., Ormiston, A. J., Webster Mark, W. I., Beier, S., Young, A., Ellis, C., Wang, C., Smedby, O. & Cowan, B. 2016a. A computational atlas of normal coronary artery anatomy. *EuroIntervention,* 12**,** 845-854.

Medrano-Gracia, P., Ormiston, J., Webster, M., Beier, S., Young, A., Ellis, C., Wang, C., Smedby, Ö. & Cowan, B. 2016b. A computational atlas of normal coronary artery anatomy. *EuroIntervention,* 12**,** 845-54.

Mehta, P. K., Quesada, O., Al-Badri, A., Fleg, J. L., Volgman, A. S., Pepine, C. J., Merz, C. N. B. & Shaw, L. J. 2022. Ischemia and no obstructive coronary arteries in patients with stable ischemic heart disease. *Int J Cardiol,* 348**,** 1-8.

Mieres, J. H., Gulati, M., Bairey Merz, N., Berman, D. S., Gerber, T. C., Hayes, S. N., Kramer, C. M., Min, J. K., Newby, L. K., Nixon, J. V., Srichai, M. B., Pellikka, P. A., Redberg, R. F., Wenger, N. K., Shaw, L. J., American Heart Association Cardiac Imaging Committee of the Council on Clinical, C., Cardiovascular, I., Intervention Committee of the Council on Cardiovascular, R. & Intervention 2014. Role of noninvasive testing in the clinical evaluation of women with suspected ischemic heart disease: a consensus statement from the American Heart Association. *Circulation,* 130**,** 350-79.

Migliori, S., Chiastra, C., Bologna, M., Montin, E., Dubini, G., Aurigemma, C., Fedele, R., Burzotta, F., Mainardi, L. & Migliavacca, F. 2017. A framework for computational fluid dynamic analyses of patient-specific stented coronary arteries from optical coherence tomography images. *Medical Engineering & Physics,* 47**,** 105-116.

Miller, J. M., Rochitte, C. E., Dewey, M., Arbab-Zadeh, A., Niinuma, H., Gottlieb, I., Paul, N., Clouse, M. E., Shapiro, E. P., Hoe, J., Lardo, A. C., Bush, D. E., Roos, A. d., Cox, C., Brinker, J. & Lima, J. A. C. 2008. Diagnostic Performance of Coronary Angiography by 64-Row CT. *New England Journal of Medicine,* 359**,** 2324-2336.

Min, J. K., Shaw, L. J. & Berman, D. S. 2010. The Present State of Coronary Computed Tomography Angiography: A Process in Evolution. *Journal of the American College of Cardiology,* 55**,** 957-965.

Mintz, G. S. & Guagliumi, G. 2017. Intravascular imaging in coronary artery disease. *The Lancet,* 390**,** 793-809.

Morlacchi, S. & Migliavacca, F. 2013. Modeling Stented Coronary Arteries: Where We are, Where to Go. *Annals of Biomedical Engineering,* 41**,** 1428-1444.

Morris, P. D., Al-Lamee, R. K. & Berry, C. 2022. Coronary physiological assessment in the catheter laboratory: haemodynamics, clinical assessment and future perspectives. *Heart,* 108**,** 1737.

Morris, P. D., Curzen, N. & Gunn, J. P. 2020a. Angiography-Derived Fractional Flow Reserve: More or Less Physiology? *Journal of the American Heart Association,* 9**,** e015586.

Morris, P. D., Gosling, R., Zwierzak, I., Evans, H., Aubiniere-Robb, L., Czechowicz, K., Evans, P. C., Hose, D. R., Lawford, P. V., Narracott, A. J. & Gunn, J. P. 2020b. A novel method for measuring absolute coronary blood flow and microvascular resistance in patients with ischaemic heart disease. *Cardiovascular Research,* 117**,** 1567-1577.

Morris, P. D., Narracott, A., Von Tengg-Kobligk, H., Silva Soto, D. A., Hsiao, S., Lungu, A., Evans, P., Bressloff, N. W., Lawford, P. V., Hose, D. R. & Gunn, J. P. 2016. Computational fluid dynamics modelling in cardiovascular medicine. *Heart,* 102**,** 18.

Morris, P. D., Ryan, D., Morton, A. C., Lycett, R., Lawford, P. V., Hose, D. R. & Gunn, J. P. 2013. Virtual Fractional Flow Reserve From Coronary Angiography: Modeling the Significance of Coronary Lesions: Results From the VIRTU-1 (VIRTUal Fractional Flow Reserve From Coronary Angiography) Study. *JACC: Cardiovascular Interventions,* 6**,** 149-157.

Morris, P. D., Silva Soto, D. A., Feher, J. F. A., Rafiroiu, D., Lungu, A., Varma, S., Lawford, P. V., Hose, D. R. & Gunn, J. P. 2017. Fast Virtual Fractional Flow Reserve Based Upon Steady-State Computational Fluid Dynamics Analysis: Results From the VIRTU-Fast Study. *JACC: Basic to Translational Science,* 2**,** 434-446.

Murasato, Y., Meno, K., Mori, T. & Tanenaka, K. 2022. Impact of coronary bifurcation angle on the pathogenesis of atherosclerosis and clinical outcome of coronary bifurcation intervention–A scoping review. *PLOS ONE,* 17**,** e0273157.

Mutha, V., Ul Haq, M. A., Ooi, A., Monty, J., Moore, S. & Barlis, P. 2013. 3D Reconstruction of Coronary Arteries Using Multiplane Angiography and Optical Coherence Tomography to Improve Stent Visualisation. *Heart, Lung and Circulation,* 22**,** S126.

Narula, J., Chandrashekhar, Y., Ahmadi, A., Abbara, S., Berman, D. S., Blankstein, R., Leipsic, J., Newby, D., Nicol, E. D., Nieman, K., Shaw, L., Villines, T. C., Williams, M. & Hecht, H. S. 2021. SCCT 2021 Expert Consensus Document on Coronary Computed Tomographic Angiography: A Report of the Society of Cardiovascular Computed Tomography. *J Cardiovasc Comput Tomogr,* 15**,** 192-217.

Neumann, F.-J., Sousa-Uva, M., Ahlsson, A., Alfonso, F., Banning, A. P., Benedetto, U., Byrne, R. A., Collet, J.-P., Falk, V., Head, S. J., Jüni, P., Kastrati, A., Koller, A., Kristensen, S. D., Niebauer, J., Richter, D. J., Seferović, P. M., Sibbing, D., Stefanini, G. G., Windecker, S., Yadav, R., Zembala, M. O. & Group, E. S. D. 2018. 2018 ESC/EACTS Guidelines on myocardial revascularization. *European Heart Journal,* 40**,** 87-165.

Nice. 2010. *Recent-onset chest pain of suspected cardiac origin: assessment and diagnosis* [Online]. NICE - National Institute for Health and Care Excellence. Available: https://www.nice.org.uk/guidance/cg95 [Accessed 23/10/2024 2024].

Ono, M., Kawashima, H., Hara, H., Gao, C., Wang, R., Kogame, N., Takahashi, K., Chichareon, P., Modolo, R., Tomaniak, M., Wykrzykowska, J. J., Piek, J. J., Mori, I., Courtney, B. K., Wijns, W., Sharif, F., Bourantas, C., Onuma, Y. & Serruys, P. W. 2020. Advances in IVUS/OCT and Future Clinical Perspective of Novel Hybrid Catheter System in Coronary Imaging. *Front Cardiovasc Med,* 7**,** 119.

Park, H., Ahn, J.-M., Kang, D.-Y., Lee, J.-B., Park, S., Ko, E., Cho, S.-C., Lee, P. H., Park, D.-W., Kang, S.-J., Lee, S.-W., Kim, Y.-H., Lee, C. W., Park, S.-W. & Park, S.-J. 2020. Optimal Stenting Technique for Complex Coronary Lesions: Intracoronary Imaging-Guided Pre-Dilation, Stent Sizing, and Post-Dilation. *JACC: Cardiovascular Interventions,* 13**,** 1403-1413.

Pederzani, G., Czechowicz, K., Ghorab, N., Morris, P. D., Gunn, J. P., Narracott, A. J., Hose, D. R. & Halliday, I. 2022. The Use of Digital Coronary Phantoms for the Validation of Arterial Geometry Reconstruction and Computation of Virtual FFR. *Fluids,* 7**,** 201.

Perera, D., Berry, C., Hoole, S. P., Sinha, A., Rahman, H., Morris, P. D., Kharbanda, R. K., Petraco, R. & Channon, K. 2023. Invasive coronary physiology in patients with angina and non-obstructive coronary artery disease: a consensus document from the coronary microvascular dysfunction workstream of the British Heart Foundation/National Institute for Health Research Partnership. *Heart,* 109**,** 88.

Peters, R. J., Kok, W. E., Di Mario, C., Serruys, P. W., Bär, F. W., Pasterkamp, G., Borst, C., Kamp, O., Bronzwaer, J. G., Visser, C. A., Piek, J. J., Panday, R. N., Jaarsma, W., Savalle, L. & Bom, N. 1997. Prediction of restenosis after coronary balloon angioplasty. Results of PICTURE (Post-IntraCoronary Treatment Ultrasound Result Evaluation), a prospective multicenter intracoronary ultrasound imaging study. *Circulation,* 95**,** 2254-61.

Phe. 2019. *Health matters: preventing cardiovascular disease* [Online]. Available: https://www.gov.uk/government/publications/health-matters-preventing-cardiovascular-disease/health-matters-preventing-cardiovascular-disease [Accessed 01/04/2025 2025].

Pijls, N. H., De Bruyne, B., Peels, K., Van Der Voort, P. H., Bonnier, H. J., Bartunek, J. & Koolen, J. J. 1996. Measurement of fractional flow reserve to assess the functional severity of coronary-artery stenoses. *New England Journal of Medicine,* 334**,** 1703-1708.

Pijls, N. H. J., Fearon, W. F., Tonino, P. A. L., Siebert, U., Ikeno, F., Bornschein, B., Van't Veer, M., Klauss, V., Manoharan, G., Engstrøm, T., Oldroyd, K. G., Ver Lee, P. N., Maccarthy, P. A. & De Bruyne, B. 2010. Fractional Flow Reserve Versus Angiography for Guiding Percutaneous Coronary Intervention in Patients With Multivessel Coronary Artery Disease: 2-Year Follow-Up of the FAME (Fractional Flow Reserve Versus Angiography for Multivessel Evaluation) Study. *Journal of the American College of Cardiology,* 56**,** 177-184.

Prati, F., Romagnoli, E., Gatto, L., La Manna, A., Burzotta, F., Limbruno, U., Versaci, F., Fabbiocchi, F., Di Giorgio, A., Marco, V., Ramazzotti, V., Di Vito, L., Trani, C., Porto, I., Boi, A., Tavazzi, L. & Mintz, G. S. 2016. Clinical Impact of Suboptimal Stenting and Residual Intrastent Plaque/Thrombus Protrusion in Patients With Acute Coronary Syndrome: The CLI-OPCI ACS Substudy (Centro per la Lotta Contro L'Infarto-Optimization of Percutaneous Coronary Intervention in Acute Coronary Syndrome). *Circ Cardiovasc Interv,* 9.

Prati, F., Romagnoli, E., La Manna, A., Burzotta, F., Gatto, L., Marco, V., Fineschi, M., Fabbiocchi, F., Versaci, F., Trani, C., Tamburino, C., Alfonso, F. & Mintz, G. S. 2018. Long-term consequences of optical coherence tomography findings during percutaneous coronary intervention: the Centro Per La Lotta Contro L'infarto - Optimization Of Percutaneous Coronary Intervention (CLI-OPCI) LATE study. *EuroIntervention,* 14**,** e443-e451.

Räber, L., Mintz, G. S., Koskinas, K. C., Johnson, T. W., Holm, N. R., Onuma, Y., Radu, M. D., Joner, M., Yu, B., Jia, H., Meneveau, N., De La Torre Hernandez, J. M., Escaned, J., Hill, J., Prati, F., Colombo, A., Di Mario, C., Regar, E., Capodanno, D., Wijns, W., Byrne, R. A., Guagliumi, G. & Group, E. S. D. 2018. Clinical use of intracoronary imaging. Part 1: guidance and optimization of coronary interventions. An expert consensus document of the European Association of Percutaneous Cardiovascular Interventions. *European Heart Journal,* 39**,** 3281-3300.

Razavi, A., Shirani, E. & Sadeghi, M. 2011. Numerical simulation of blood pulsatile flow in a stenosed carotid artery using different rheological models. *Journal of biomechanics,* 44**,** 2021-2030.

Reiber, J. H., Tu, S., Tuinenburg, J. C., Koning, G., Janssen, J. P. & Dijkstra, J. 2011. QCA, IVUS and OCT in interventional cardiology in 2011. *Cardiovasc Diagn Ther,* 1**,** 57-70.

Rieber, J., Meissner, O., Babaryka, G., Reim, S., Oswald, M., Koenig, A., Schiele, T. M., Shapiro, M., Theisen, K., Reiser, M. F., Klauss, V. & Hoffmann, U. 2006. Diagnostic accuracy of optical coherence tomography and intravascular ultrasound for the detection and characterization of atherosclerotic plaque composition in ex-vivo coronary specimens: a comparison with histology. *Coronary Artery Disease,* 17.

Sadick, V., Reed, W., Collins, L., Sadick, N., Heard, R. & Robinson, J. 2014. Impact of biplane versus single-plane imaging on radiation dose, contrast load and procedural time in coronary angioplasty. *British Journal of Radiology,* 83**,** 379-394.

Schneider, V. S., Böhm, F., Blum, K., Riedel, M., Abdelwahed, Y. S., Klotsche, J., Steiner, J. K., Heuberger, A., Skurk, C., Mochmann, H. C., Lauten, A., Fröhlich, G., Rauch-Kröhnert, U., Haghikia, A., Sinning, D., Stähli, B. E., Landmesser, U. & Leistner, D. M. 2021. Impact of real-time angiographic co-registered optical coherence tomography on percutaneous coronary intervention: the OPTICO-integration II trial. *Clin Res Cardiol,* 110**,** 249-257.

Segura, R. J. & Feito, F. R. 1998. An algorithm for determining intersection segment-polygon in 3D. *Computers & Graphics,* 22**,** 587-592.

Sheth, T. N., Pinilla-Echeverri, N., Mehta, S. R. & Courtney, B. K. 2018. First-in-Human Images of Coronary Atherosclerosis and Coronary Stents Using a Novel Hybrid Intravascular Ultrasound and Optical Coherence Tomographic Catheter. *JACC Cardiovasc Interv,* 11**,** 2427-2430.

Shimokado, A., Kubo, T., Matsuo, Y., Ino, Y., Shiono, Y., Shimamura, K., Katayama, Y., Taruya, A., Nishiguchi, T., Kashiwagi, M., Kitabata, H., Tanaka, A., Hozumi, T. & Akasaka, T. 2019. Imaging assessment and accuracy in coronary artery autopsy: comparison of frequency-domain optical coherence tomography with intravascular ultrasound and histology. *The International Journal of Cardiovascular Imaging,* 35**,** 1785-1790.

Solanki, R., Gosling, R., Rammohan, V., Pederzani, G., Garg, P., Heppenstall, J., Hose, D. R., Lawford, P. V., Narracott, A. J., Fenner, J., Gunn, J. P. & Morris, P. D. 2021. The importance of three dimensional coronary artery reconstruction accuracy when computing virtual fractional flow reserve from invasive angiography. *Scientific Reports,* 11**,** 19694.

Song, L., Xu, B., Tu, S., Guan, C., Jin, Z., Yu, B., Fu, G., Zhou, Y., Wang, J. a., Chen, Y., Pu, J., Chen, L., Qu, X., Yang, J., Liu, X., Guo, L., Shen, C., Zhang, Y., Zhang, Q., Pan, H., Zhang, R., Liu, J., Zhao, Y., Wang, Y., Dou, K., Kirtane, A. J., Wu, Y., Wijns, W., Yang, W., Leon, M. B., Qiao, S. & Stone, G. W. 2022. 2-Year Outcomes of Angiographic Quantitative Flow Ratio-Guided Coronary Interventions. *Journal of the American College of Cardiology,* 80**,** 2089-2101.

Stähli, B. E., Erbay, A., Steiner, J., Klotsche, J., Mochmann, H.-C., Skurk, C., Lauten, A., Landmesser, U. & Leistner, D. M. 2019. Comparison of resting distal to aortic coronary pressure with angiography-based quantitative flow ratio. *International Journal of Cardiology,* 279**,** 12-17.

Stone, G. W., Christiansen, E. H., Ali, Z. A., Andreasen, L. N., Maehara, A., Ahmad, Y., Landmesser, U. & Holm, N. R. 2024. Intravascular imaging-guided coronary drug-eluting stent implantation: an updated network meta-analysis. *The Lancet,* 403**,** 824-837.

Su, B., Huo, Y., Kassab, G. S., Kabinejadian, F., Kim, S., Leo, H. L. & Zhong, L. 2014. Numerical investigation of blood flow in three-dimensional porcine left anterior descending artery with various stenoses. *Computers in biology and medicine,* 47**,** 130-138.

Tafti, A. & Byerly, D. W. 2025. X-ray Radiographic Patient Positioning. *StatPearls.* Treasure Island (FL): StatPearls Publishing

Tan, Q., Wang, Q., Liu, D., Zhang, S., Zhang, Y. & Li, Y. 2015. Intravascular ultrasound-guided unprotected left main coronary artery stenting in the elderly. *Saudi Med J,* 36**,** 549-53.

Taylor, D. J., Aubiniere-Robb, L., Gosling, R., Newman, T., Hose, D. R., Halliday, I., Lawford, P. V., Narracott, A. J., Gunn, J. P. & Morris, P. D. 2023. Sex differences in coronary microvascular resistance measured by a computational fluid dynamics model. *Frontiers in Cardiovascular Medicine,* Volume 10 - 2023.

Taylor, D. J., Saxton, H., Halliday, I., Newman, T., Feher, J., Gosling, R., Narracott, A. J., Van Kemenade, D., Van't Veer, M., Tonino, P. A. L., Rochette, M., Hose, D. R., Gunn, J. P. &

Morris, P. D. 2024. Evaluation of models of sequestration flow in coronary arteries—Physiology versus anatomy? *Computers in Biology and Medicine,* 173**,** 108299.

Tekle, M. 2025. *Statistical Shape Modeling of Diseased Coronary Arteries.* Politecnico di Torino.

Terashima, M., Kaneda, H. & Suzuki, T. 2012. The role of optical coherence tomography in coronary intervention. *Korean J Intern Med,* 27**,** 1-12.

Thondapu, V., Bourantas, C. V., Foin, N., Jang, I.-K., Serruys, P. W. & Barlis, P. 2016. Biomechanical stress in coronary atherosclerosis: emerging insights from computational modelling. *European Heart Journal,* 38**,** 81-92.

Tonino, P. A. L., De Bruyne, B., Pijls, N. H. J., Siebert, U., Ikeno, F., Van `T Veer, M., Klauss, V., Manoharan, G., Engstrøm, T., Oldroyd, K. G., Ver Lee, P. N., Maccarthy, P. A. & Fearon, W. F. 2009. Fractional Flow Reserve versus Angiography for Guiding Percutaneous Coronary Intervention. *New England Journal of Medicine,* 360**,** 213-224.

Van Belle, E., Baptista, S.-B., Raposo, L., Henderson, J., Rioufol, G., Santos, L., Pouillot, C., Ramos, R., Cuisset, T., Calé, R., Teiger, E., Jorge, E., Belle, L., Machado, C., Barreau, D., Costa, M., Hanssen, M., Oliveira, E., Besnard, C., Costa, J., Dallongeville, J., Pipa, J., Sideris, G., Fonseca, N., Bretelle, C., Guardado, J., Lhoest, N., Silva, B., Barnay, P., Sousa, M.-J., Leborgne, L., Silva, J. C., Vincent, F., Rodrigues, A., Seca, L., Fernandes, R. & Dupouy, P. 2017. Impact of Routine Fractional Flow Reserve on Management Decision and 1-Year Clinical Outcome of Patients With Acute Coronary Syndromes. *Circulation: Cardiovascular Interventions,* 10**,** e004296.

Van Mieghem, C. A. G. 2017. CT as gatekeeper of invasive coronary angiography in patients with suspected CAD. *Cardiovascular Diagnosis and Therapy,* 7**,** 189-195.

Van Nunen, L. X., Zimmermann, F. M., Tonino, P. A. L., Barbato, E., Baumbach, A., Engstrøm, T., Klauss, V., Maccarthy, P. A., Manoharan, G., Oldroyd, K. G., Ver Lee, P. N., Van't Veer, M., Fearon, W. F., De Bruyne, B. & Pijls, N. H. J. 2015. Fractional flow reserve

versus angiography for guidance of PCI in patients with multivessel coronary artery disease (FAME): 5-year follow-up of a randomised controlled trial. *The Lancet*, 386**,** 1853-1860.

Van Zandvoort, L. J. C., Tomaniak, M., Tovar Forero, M. N., Masdjedi, K., Visseren, L., Witberg, K., Ligthart, J., Kardys, I., Lemmert, M. E., Diletti, R., Wilschut, J., De Jaegere, P., Zijlstra, F., Van Mieghem, N. M. & Daemen, J. 2020. Predictors for Clinical Outcome of Untreated Stent Edge Dissections as Detected by Optical Coherence Tomography. *Circ Cardiovasc Interv*, 13**,** e008685.

Vrints, C., Andreotti, F., Koskinas, K. C., Rossello, X., Adamo, M., Ainslie, J., Banning, A. P., Budaj, A., Buechel, R. R., Chiariello, G. A., Chieffo, A., Christodorescu, R. M., Deaton, C., Doenst, T., Jones, H. W., Kunadian, V., Mehilli, J., Milojevic, M., Piek, J. J., Pugliese, F., Rubboli, A., Semb, A. G., Senior, R., Ten Berg, J. M., Van Belle, E., Van Craenenbroeck, E. M., Vidal-Perez, R., Winther, S. & Group, E. S. D. 2024. 2024 ESC Guidelines for the management of chronic coronary syndromes: Developed by the task force for the management of chronic coronary syndromes of the European Society of Cardiology (ESC) Endorsed by the European Association for Cardio-Thoracic Surgery (EACTS). *European Heart Journal*, 45**,** 3415-3537.

Wang, Q., Ouyang, H., Lv, L., Gui, L., Yang, S. & Hua, P. 2024. Left main coronary artery morphological phenotypes and its hemodynamic properties. *BioMedical Engineering OnLine*, 23**,** 9.

Wellnhofer, E., Osman, J., Kertzscher, U., Affeld, K., Fleck, E. & Goubergrits, L. 2010. Flow simulation studies in coronary arteries--impact of side-branches. *Atherosclerosis*, 213**,** 475-81.

Windecker, S., Kolh, P., Alfonso, F., Collet, J. P., Cremer, J., Falk, V., Filippatos, G., Hamm, C., Head, S. J., Jüni, P., Kappetein, A. P., Kastrati, A., Knuuti, J., Landmesser, U., Laufer, G., Neumann, F. J., Richter, D. J., Schauerte, P., Sousa Uva, M., Stefanini, G. G., Taggart, D. P., Torracca, L., Valgimigli, M., Wijns, W. & Witkowski, A. 2014. 2014 ESC/EACTS Guidelines on myocardial revascularization: The Task Force on Myocardial Revascularization of the European Society of Cardiology (ESC) and the European Association for Cardio-Thoracic Surgery (EACTS)Developed with the special contribution of the European Association of Percutaneous Cardiovascular Interventions (EAPCI). *Eur Heart J*, 35**,** 2541-619.

Wu, W., Samant, S., De Zwart, G., Zhao, S., Khan, B., Ahmad, M., Bologna, M., Watanabe, Y., Murasato, Y., Burzotta, F., Brilakis, E. S., Dangas, G., Louvard, Y., Stankovic, G., Kassab, G. S., Migliavacca, F., Chiastra, C. & Chatzizisis, Y. S. 2020. 3D reconstruction of coronary artery bifurcations from coronary angiography and optical coherence tomography: feasibility, validation, and reproducibility. *Scientific Reports,* 10**,** 18049.

Yamagishi, M., Terashima, M., Awano, K., Kijima, M., Nakatani, S., Daikoku, S., Ito, K., Yasumura, Y. & Miyatake, K. 2000. Morphology of vulnerable coronary plaque: insights from follow-up of patients examined by intravascular ultrasound before an acute coronary syndrome. *Journal of the American College of Cardiology,* 35**,** 106-111.

Yamamoto, M., Okura, Y., Ishihara, M., Kagemoto, M., Harada, K. & Ishida, T. 2009. Development of digital subtraction angiography for coronary artery. *Journal of digital imaging,* 22**,** 319-325.

Yan, Z., Yao, Z., Guo, W., Shang, D., Chen, R., Liu, J., Cai, X. C. & Ge, J. 2023. Impact of Pressure Wire on Fractional Flow Reserve and Hemodynamics of the Coronary Arteries: A Computational and Clinical Study. *IEEE Transactions on Biomedical Engineering,* 70**,** 1683-1691.

Yock, P. G., Linker, D. T., Angelsen, B. A. J. & Tech 1989. Two-Dimensional Intravascular Ultrasound: Technical Development and Initial Clinical Experience. *Journal of the American Society of Echocardiography,* 2**,** 296-304.

Zeng, D., Boutsianis, E., Ammann, M., Boomsma, K., Wildermuth, S. & Poulikakos, D. 2008. A Study on the Compliance of a Right Coronary Artery and Its Impact on Wall Shear Stress. *Journal of Biomechanical Engineering,* 130.

Zhang, J., Gao, X., Kan, J., Ge, Z., Han, L., Lu, S., Tian, N., Lin, S., Lu, Q., Wu, X., Li, Q., Liu, Z., Chen, Y., Qian, X., Wang, J., Chai, D., Chen, C., Li, X., Gogas, B. D., Pan, T., Shan, S., Ye, F. & Chen, S.-L. 2018. Intravascular Ultrasound Versus Angiography-Guided Drug-Eluting Stent Implantation: The ULTIMATE Trial. *Journal of the American College of Cardiology,* 72**,** 3126-3137.

Zhu, Y., Zhao, C., Wu, Z., Maehara, A., Tang, D., Wang, L., Gao, Z., Xu, Y., Lv, R., Huang, M., Zhang, X., Zhu, J., Jia, H., Yu, B., Chen, M. & Mintz, G. S. 2025. Comparison and identification of human coronary plaques with/without erosion using patient-specific optical coherence tomography-based fluid–structure interaction models: a pilot study. *Biomechanics and Modeling in Mechanobiology*, 24**,** 213-231.

Zhu, Y., Zhu, F., Ding, Z., Tao, K., Lai, T., Kuang, H., Hua, P., Shang, M., Hu, J., Yu, Y. & Liu, T. 2021. Three-dimensional spatial reconstruction of coronary arteries based on fusion of intravascular optical coherence tomography and coronary angiography. *Journal of Biophotonics*, 14**,** e202000370.

Zir, L. M., Miller, S. W., Dinsmore, R. E., Gilbert, J. P. & Harthorne, J. W. 1976a. Interobserver variability in coronary angiography. *Circulation*, 53**,** 627-632.

Zir, L. M., Miller, S. W., Dinsmore, R. E., Gilbert, J. P. & Harthorne, J. W. 1976b. Interobserver variability in coronary angiography. *Circulation*, 53**,** 627-32.